Mid-America Earthquake Center

Headquartered at the University of Illinois at Urbana-Champaign

Probabilistic Seismic Assessment of Structure, Foundation, and Soil Interacting Systems

by

Oh-Sung Kwon and Amr S. Elnashai

Department of Civil and Environmental Engineering
University of Illinois at Urbana-Champaign
Urbana, Illinois

September, 2007

This research is supported by the Mid-America Earthquake Center
under National Science Foundation Grant EEC-9701785

ABSTRACT

This report presents research on the probabilistic seismic performance evaluation of a structural-geotechnical interacting system. The system comprises a bridge, its foundation, and the supporting soil. The investigation includes a study on probabilistic performance evaluation methodologies, development of a multiplatform and hybrid simulation framework, and verifications of numerical models of structural and geotechnical systems in comparison with measured data. The developments are demonstrated through a reference application concerning the probabilistic performance evaluation and the analytical models required for seismic vulnerability assessment of a bridge-foundation-soil system.

Seismic performance evaluation procedures are studied using a benchmark three-story, reinforced concrete (RC) building structure. The benchmark is selected for the high-quality experimental (shaking table) results that would lend weight to the comparative study of different probabilistic models and random fields. Throughout the study, three probabilistic performance evaluation methods are applied: the Monte Carlo simulation, response surface, and SAC-FEMA methods. In addition, effects of uncertainties in structural materials and ground motion are thoroughly investigated. The analysis of benchmark structure shows that the effect of random variability in structural materials is small compared to the effect of input ground motion. When Peak Ground Acceleration (PGA) is used as an intensity measure, the derived vulnerability curves highly depend on ground motion sets. Hence, scrupulous consideration is required when ground motions are selected for vulnerability analysis. The comparisons of shaking table test results with responses from the analytical model show that different damping levels need to be assigned for low- and high-intensity ground motions. The comparison verifies that fiber-based beam-column elements in ZEUS-NL can replicate the behavior of real structure with acceptable accuracy. Three different simulation methods results in similar vulnerability curves. The computational cost are the most expensive when the Monte Carlo simulation is adopted.

Methodologies for soil-structure-interaction analysis are introduced, including the newly developed multiplatform, multiresolution hybrid simulation framework. These

methodologies and numerical models of soil-structure-interaction systems are verified through comparison with field measurements and experimental results. The main structural analysis platform for the thesis, ZEUS-NL, is verified against shaking table test result of the above three-story RC frame. The main geotechnical analysis platform for the thesis, OpenSees, is verified through in-situ lateral load tests of piles in sand and clay. The soil-structure interacting system is verified through analyses of a heavily instrumented bridge which recorded several sets of ground motions. The verification study of soil-structure interacting system shows that detailed and meticulously developed analytical models are capable of replicating measurements of the response of complex bridge systems subjected to strong ground motion.

Seismic vulnerability curves of a reference bridge in the Central and Eastern United States (CEUS) are derived employing the aforementioned methods with and without soil-structure interaction. A typical highway over-crossing bridge representing one of the most common bridge types in the CEUS is selected. Four different approaches of Soil-Structure Interaction (SSI) are tried: (a) Abutments and foundations are assumed to be fixed, (b) Conventional lumped spring approaches are adopted to model abutments and foundations, (c) Lumped springs for abutments and foundations are estimated from Finite Element (FE) analysis of geotechnical system, and (d) Multiplatform simulation is conducted. All four of the methods shows that abutment bearings in transverse direction are most vulnerable components. Failure probability of the bridge system is highly dependent on the failure probability of abutment bearings. Among the four approaches, the fixed foundation approach underestimated the failure probability of all bridge components except abutment bearings in transverse direction. Approaches (b), (c), and (d) show similar trends in derived vulnerability functions. Considering that simplified methods for SSI analysis include larger assumptions than fully coupled methods and that the multiplatform simulation is verified with measured responses from instrumented bridge, the use of multiplatform simulation is suggested if computational power and resources for FE modeling are affordable.

ACKNOWLEDGMENTS

This report is a deliverable of project EE-3: Advanced Simulation Tools, part of the Mid-America Earthquake Center Core Research Program under the Thrust Area Engineering Engines. This work was supported primarily by the Mid-America Earthquake Center through the Earthquake Engineering Research Centers Program of the National Science Foundation under NSF Award No. EEC-9701785. Any opinions, findings and conclusions or recommendations expressed in this material are those of the authors and do not necessarily reflect those of the National Science Foundation.

TABLE OF CONTENTS

LIST OF TABLES

LIST OF FIGURES

LIST OF ABBREVIATIONS

3D	Three-dimension
CCD	Central Composite Design
COV	Coefficient of Variation
CQC	Complete Quadratic Combination
DOF	Degree Of Freedom
DSDSS	Dual Specimen Direct Simple Shear
FE	Finite Element
FORM	First Order Reliability Method
GUI	Graphic User Interface
ISD	InterStory Drift
ISD_{max}	Maximum interstory drift
MCS	Monte-Carlo Simulation
MISST	Multi-Site Soil-Structure-Foundation Interaction
MRO	Meloland Road Overcrossing
NEES	Network for Earthquake Engineering Simulation
NHCP	NEES Hybrid Simulation Communications Protocol
NTCP	NEESgrid Teleoperation Control Protocol
OMRCF	Ordinary Moment Resisting Reinforced Concrete Frame
PGA	Peak Ground Acceleration
PGD	Peak Ground Displacement
PGV	Peak Ground Velocity
RC	Reinforced Concrete
RC/CT	Resonant Column/Cyclic Torsional Shear
RHA	Response History Analysis
ROSRINE	ResOlution of Site Response Issues from the Northridge Earthquake
RSM	Response Surface Method
PSD	PSeudo-Dynamic
SDOF	Single Degree Of Freedom
SORM	Second Order Reliability Method
SPT	Standard Penetration Test
SSI	Soil-Structure-Interaction

LIST OF SYMBOLS

β_C	Dispersion of capacity (standard deviation of the natural logarithm of capacity, C)
β_D	Dispersion of demand (standard deviation of the natural logarithm of demand, D)
γ	Shear strain of soil
δ	Random variable representing uncertainties in ground motion
ε	Random variable with unit mean representing the uncertainties of seismic demand, Eq. (2.5)
ε	Random variable with zero mean representing the fitness of response surface on experimental results, Eq. (2.15)
$\bar{\varepsilon}$	Random variable with zero mean representing the combined effect of uncertainties in ground motion and the fitness of response surface, Eq. (2.16)
$\sigma_{[\bullet]}$	Standard deviation of a variable in the brackets
τ	Shear stress of soil
ϕ	Friction angle of soil
$\mathbf{\Phi}$	Eigen matrix
a	A coefficient in seismic intensity-demand relationship, Eq. (2.4)
a	Peak ground acceleration, Section 2.3.4.2
b	A coefficient in seismic intensity-demand relationship, Eq. (2.4)
c	Cohesion of soil
d	Realization of seismic demand, D
$g(\mathbf{x})$	Limit state function of random variables, $\mathbf{x}$
k_0	A coefficient in hazard definition, Eq. (2.3)
k	A coefficient in hazard definition, Eq. (2.3)
n	Total number of samples in Monte Carlo Simulation
n_f	Number of samples that do not satisfy limit state
q_i	Modal response of i^{th} mode
$\mathbf{r}(t)$	Restoring force vector as a function of time
t	Time
v	Peak ground velocity, Section 2.3.4.2

v_s	Shear wave velocity of soil medium
$\mathbf{x}$	Vector of random variables
$\mathbf{z}(\mathbf{x})\ \boldsymbol{\beta}$	Response surface of random variables, $\mathbf{x}$, and coefficients of $\boldsymbol{\beta}$
f_c'	Concrete ultimate stress
s	Realization of intensity measure, *IM*
C	Structural capacity, random variable
$\hat{C}$	Median structural capacity
$\mathbf{C}$	Damping matrix
D	Seismic demand, random variable
$\hat{D}$	Median seismic demand
$E[\blacksquare]$	Expected values of the variable in the brackets
F_y	Steel yield stress
$F(\bar{\omega})$	Transfer function as a function of $\bar{\omega}$
G	Shear modulus of soil
H	Hazard at a site
I	Ground motion intensity
I_f	Ground motion intensity at structural failure
$\mathbf{K}$	Stiffness matrix
$\mathbf{M}$	Mass matrix
IM	Intensity measure, random variable
$P[\blacksquare]$	Probability of the event in the brackets
P_f	Probability of failure
P_{PL}	Annual probability of the performance level not being met
S_a	Spectral acceleration
S_d	Spectral displacement
S_v	Spectral velocity
T	Fundamental period of a structure
Var[▪]	Variance of the variable in the brackets

CHAPTER 1

INTRODUCTION

1.1 Problem Description

Seismic risk assessment is a critical component of estimating social and economical loss from earthquakes and to mitigate losses when earthquakes occur. Decision makers in emergency management organizations, insurance companies, engineers, seismologists, and social scientists, among others, are most interested in risk assessment. Seismic risk assessment consists of hazard definition, vulnerability curves, inventory data, and integration of the three. Among these ingredients, the vulnerability relationships of a facility associate the level of ground motion with structural damage. The derivation of vulnerability curves requires probabilistic seismic performance analysis of structures. There have been numerous studies regarding the vulnerability analysis of structures. Some of the vulnerability curves were derived based on observed damage from past earthquakes (Orsini, 1999; Rossetto and Elnashai, 2003), while others were derived from analytical simulation (Mosalam et al., 1997; Reinhorn et al., 2001; Chryssanthopoulos et al., 2000). Vulnerability curves from observed damage data are the most realistic, but lack generality. Those vulnerability curves also include large uncertainty because the damage assessment is based on the subjective observation of field investigators. Moreover, few seismic regions have well-organized structural damage reports that can be utilized for the derivation of vulnerability curves.

The analytical derivation of vulnerability curves requires a realistic analytical model of every component of a structural system, such as piers, bearings, gaps, abutments, and foundations. There have been many studies for the derivation of analytical vulnerability curves. Most, however, have been derived based on the assumption that structures are supported on rigid foundations even though the soil-foundation systems have considerable effects on the response of the structure. A recent attempt to include the effect of flexible foundation on bridges by using lumped spring

was made (Nielson, 2005), which is the most commonly adopted approach to model soil-foundation system. However, the lumped spring approach cannot represent the complexity of soil behavior as well as the uncertainties associated with soil properties. Such very simple representation may give a false impression of comprehensiveness and accuracy.

There are various effects of soft soil deposits on structural response in the event of an earthquake. The most considered effect is that the soil deposits modify frequency contents of waves propagating from bedrock to surface. This effect is usually considered by using propagated ground motions at the layer of the structure's foundation. When a structural mass and stiffness are significant in comparison with those of supporting soil, the foundation input motion may also be altered due to inertial interaction between the soil and structure. In that case, a wave propagation analysis should be conducted including structural mass and stiffness. Another important effect of soil deposit is that flexible structural foundations elongate the overall structural period, which in general decreases force demand and increases displacement demand on the structure, depending on input motion. In addition, support failure is frequently observed during an earthquake, which significantly reduces usability of structures even though it may not lead to collapse. In comparison with the quality-controlled structural materials, the subsurface condition of soil deposits includes much more uncertainties. Consequently, the seismic performance analysis of a structure without consideration of its foundation may be misleading.

1.2 Objectives and Scope of Research

The main goal of this research is to investigate the effect of soil-structure interaction (SSI) on seismic performance of structures, using state-of-the-art platforms for structural models as well as geotechnical models, and to give guidance as to its effect and required level of modeling rigor, as follows:

- Verify structural analysis platform through experimental data
- Verify geotechnical analysis platform and SSI system through comparison with measurement from earthquakes and with in-situ experiment data

- Develop a framework for multiplatform analysis for SSI study
- Examine various aspects of vulnerability derivation process
- Apply SSI analysis on a major highway overcrossing bridge
- Conduct a vulnerability analysis of a reference bridge in mid-America with several approaches of SSI consideration

This research focuses on the effect of SSI on derived vulnerability curves. Hence, rather than deriving a set of vulnerability curves for numerous structural configurations, vulnerability curves for the most typical bridge type in mid-America are derived, using several levels of modeling. Thereafter, conclusions are drawn from the comparisons.

1.3 Outline of Report

The probabilistic seismic evaluation of a structure considering soil-structure interaction comprises several fields of study, including nonlinear structural models, geotechnical models, soil-structure interaction analyses, probabilistic simulation methods, and verification of these components. Figure 1.1 illustrates how these components are combined to achieve the main goal of this research.

This report consists of six chapters. Chapter 1 introduces the background and objectives of this study. Chapter 2 focuses on the seismic vulnerability analysis of structures. Several methods for probabilistic seismic performance evaluation are introduced. Chapter 2 also introduces a cluster simulation application that runs on a supercomputing facility. The application is developed for mass-simulation typically required for vulnerability analysis. In addition, a benchmark study of a three-story reinforced concrete (RC) structure is presented. Through the benchmark study, several aspects of seismic vulnerability analysis are discussed, including the effects of analysis procedures and intensity measure of ground motions.

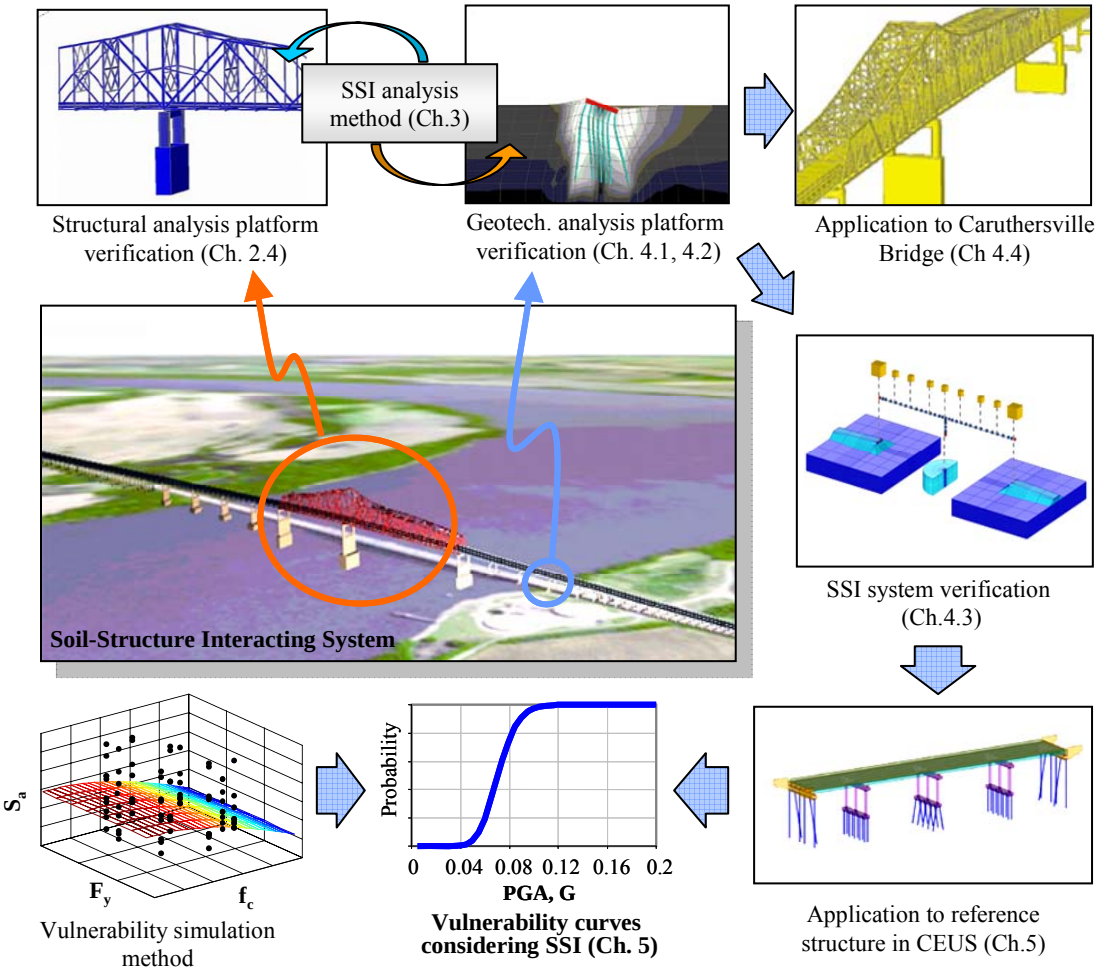

Figure 1.1 Probabilistic seismic assessment of a soil-structure-interaction system

Chapter 3 introduces analysis methods for SSI study. The first section of the chapter is devoted to introductions on conventional methods for SSI analysis. Representative methods for the analysis of mat foundations and pile foundations are briefly introduced. The SSI analysis always involves approximation, except in the case where the whole geotechnical-structural system is modeled as numerical model. Therefore, the applicability of approximate methods is investigated with transfer function of soil-structure system. The second section of Chapter 3 introduces a multiplatform hybrid simulation framework that can be utilized for analysis or experiment of complex structural systems. A few application examples of the developed framework are also briefly presented.

Chapter 4 introduces verification studies of SSI systems. The analytical models of SSI systems are compared with in-situ experimental results as well as previous research results. For a verification of a simple SSI system, lateral load tests of a single pile in cohesionless soil and cohesive soil are analyzed, using a three-dimensional nonlinear soil material model. For verification of more complex system under earthquake loading, a highway overcrossing bridge that was heavily instrumented and recorded several sets of earthquake ground motions is modeled in two different analysis platforms. The models are analyzed through multiplatform simulation framework. The last section of the chapter introduces the Caruthersville Bridge Project, in which foundation properties are evaluated from nonlinear soil-pile-foundation model.

Chapter 5 introduces a reference application of SSI simulation on a bridge in the Central and Eastern U.S. The bridge is carefully modeled, and extensive seismic response analyses are conducted using the analysis platforms introduced in Chapter 3. Vulnerability curves of the reference bridge are derived with consideration of SSI.

Chapter 6 summarizes the findings from this study followed by recommendations for future research.

CHAPTER 2

SEISMIC VULNERABILITY ANALYSIS OF STRUCTURES

This chapter introduces seismic vulnerability relationships, methods for seismic vulnerability analysis of structures, a cluster simulation tool developed for a large amount of analyses, and example vulnerability curves of a three-story Ordinary Moment-Resisting Reinforce Concrete Frame (OMRCF), used as a benchmark application. The benchmark application is steered by the requirement to have access to verify dynamic testing results for verification of the analysis platform. Throughout the benchmark study, various aspects of vulnerability analyses are discussed and vulnerability curves derived from different methods are compared.

2.1 Seismic Vulnerability Relationships

Regional seismic risk and loss estimations are essential for disaster planning and formulating risk-reduction policies. According to a study by Elnashai (2003), the driving technical engines of a regional seismic risk and loss estimation system are:

- Seismic hazard maps in terms of peak ground parameters or spectral ordinates
- Vulnerability functions (i.e., relationships of conditional probability of reaching or exceeding a performance limit state given the measure of earthquake shaking)
- Inventory data (i.e., numbers, location, and characteristics of the exposed system or elements of a system)
- Integration and visualization capabilities (i.e., data management framework, integration of seismic risk, and graphical projection of the results)

Regional loss estimation can be mathematically described through Equation (2.1) (Ellingwood and Wen, 2005).

$$P[Loss] = \sum_{s}\sum_{LS}\sum_{d} P[Loss \mid D = d] \cdot P[D = d \mid LS] \cdot P[LS \mid IM = s] \cdot P[IM = s] \qquad (2.1)$$

in which $P[\blacksquare]$ = probability of the event in the brackets. The term 'loss' refers to direct or indirect losses from a seismic event; *IM* is an intensity measure of a seismic hazard such

as spectral acceleration or peak ground acceleration; and s is a realization of the intensity measure. P[$LS \mid IM = s$] is a conditional probability of attaining structural limit states, and P[$D = d \mid LS$] is a conditional probability of attaining damage (minor, moderate, or major), which is qualitative measure. The loss of a region is determined based on the damage state. Among these ingredients, the term, P[$LS \mid IM = s$], refers to strong, motion-shaking severity to the probability of reaching or exceeding a specified performance limit state. This term is referred as *vulnerability* or *fragility*. The strong, motion-shaking severity may be expressed as an intensity, peak ground parameters (PGA, PGV, or PGD), or spectral ordinates (S_a, S_v, or S_d) corresponding to a fundamental structural period.

Vulnerability curves may be subdivided into four categories (Rossetto and Elnashai, 2003), based on the sources of data as summarized in Table 2.1. A class of the vulnerability curves is based on observational data from postearthquake surveys, while others are based on analytical simulation. Observational data are realistic, but are often neither statistically viable nor homogeneous. Empirical vulnerability curves based on these observational data should be inherently more realistic than their analytical counterparts, because they are based on the observed damage of actual structures subjected to strong motion. However, there are limitations in their general application because the curves are derived for a specific seismic region and a sample that is not necessarily similar to that sought. On the other hand, analytical vulnerability curves can be derived for general purposes, but the choice of analytical model, simulation method, and required computational power pose challenges for the development of the required relationship. With the expansion of computational power and the development of reliable analysis tools, the limitations in the analytical derivation of vulnerability curves are diminishing.

For the analytical derivation of vulnerability curves, Mosalam et al. (1997) used Single Degree Of Freedom (SDOF) systems, representations of the pushover curves of infilled and bare frames. In HAZUS (NIBS, 1999), the variability in seismic demand are provided without explicit consideration of the influence of structural parameters, such as damping, period and yield strength level. Reinhorn et al. (2001) used constant yield-reduction-factor inelastic spectra with the capacity spectrum method to evaluate inelastic response. The above-referenced studies used simplified methods because the derivation

of vulnerability curves required large amount of simulation. Thus, the results were approximate as these methods neglected the effect of higher modes, hysteretic damping, and limit states based on local failure. Due to the computational limitation in deriving fragility curves from nonlinear response history analysis of a full structural model, Jeong and Elnashai (2006) developed parameterized fragility curves that require only stiffness, strength, and ductility of a structure in order to estimate fragility curves. There have been also many attempts to derive fragility curves from full nonlinear response history analysis (e.g., Elnashai et al., 2004; Erberik and Elnashai, 2004).

Analytical derivation of a vulnerability relationship includes hazard definition, reference structure, limit state definition, analysis method, uncertainty quantification, and probabilistic simulation method, as shown in Figure 2.1. The seismic hazard used as an input to a structure should be defined considering the seismic nature of the region where the derived vulnerability curves will be applied. The reference structure should be selected such that it represents large population of building stocks of a considered region. Analysis methods must be chosen carefully, because an overly simplified method, such as SDOF analysis or static analysis, rather than a nonlinear response history analysis, will not properly capture structural failure. Furthermore, an overly sophisticated method will be quite expensive to run simulations. The computational cost and reliability of vulnerability curves are also affected by the simulation method chosen. These components in the vulnerability simulation are discussed in Section 2.4.

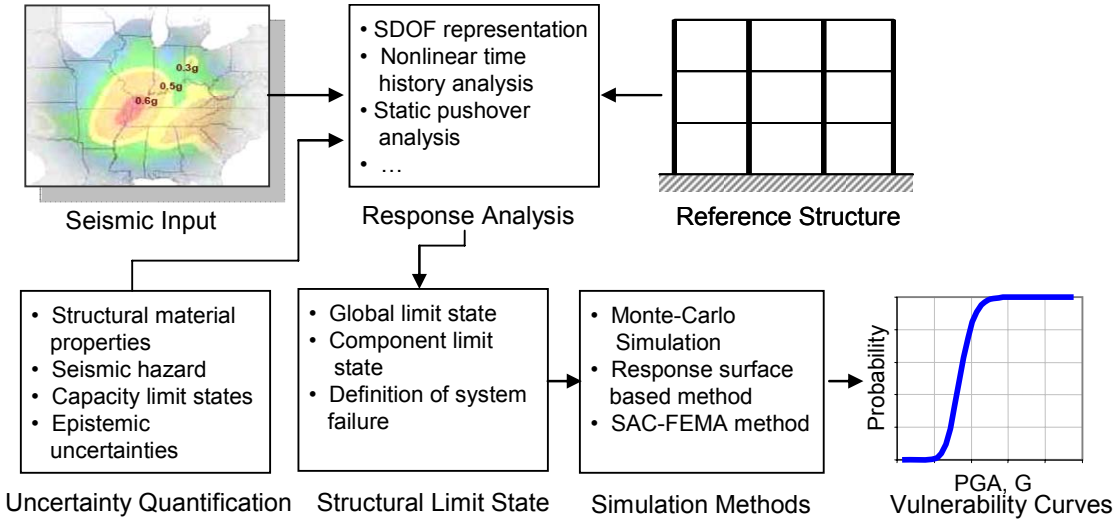

Figure 2.1 Components of seismic vulnerability simulation

Table 2.1 Categorization of vulnerability curves

Category	Characteristics	
Empirical vulnerability curve	Feature	Based on postearthquake survey Most realistic
	Limitation	Highly specific to a particular seismo-tectonic, geotechnical and built-environment The observational data used tend to be scarce and highly clustered in the low-damage, low-ground-motion severity range Include errors in building damage classification Damage due to multiple earthquakes may be aggregated
	Sample Ref.	Orsini, 1999
Judgmental vulnerability curve	Feature	Based on expert opinion The curves can be easily made to include all the factors
	Limitation	The reliability of the curves depends on the individual experience of the experts consulted A consideration of local structural types, typical configurations, detailing and materials inherent in the expert vulnerability predictions
	Sample Ref.	ATC-13, 1985
Analytical vulnerability curve	Feature	Based on damage distributions simulated from the analyses Reduced bias and increased reliability of the vulnerability estimate for different structures
	Limitation	Substantial computational effort involved and limitations in modeling capabilities The choices of the analysis method, idealization, seismic hazard, and damage models influence the derived curves and have been seen to cause significant discrepancies in seismic risk assessments
	Sample Ref.	Chryssanthopoulos et al., 2000; Mosalam et al., 1997; Reinhorn et al., 2001
Hybrid vulnerability curve	Feature	Compensate for the scarcity of observational data, subjectivity of judgmental data, and modeling deficiencies of analytical procedures Modification of analytical or judgment-based relationships with observational data and experimental results
	Limitation	The consideration of multiple data sources is necessary for the correct determination of vulnerability curve reliability
	Sample Ref.	Kappos et al., 1995

Mainly excerpted from Rossetto and Elnashai (2003)

2.2 Methods for Seismic Vulnerability Analysis

There are several methods that estimate the failure probability of a system with time-invariant reliability problem. Those methods include: the First Order Reliability Method (FORM), Second Order Reliability Method (SORM), and Monte Carlo Simulations (MCS) with various sampling techniques.

The seismic vulnerability analysis is a time-variant problem. For time-variant problems it is not readily possible to rigorously formulate limit state functions as capacity and demand depend on random variable at each time instant. There are rigorous approaches for time-variant problems based on the classical random vibration theory, which resulted in the concept of isoprobable response spectrum, the derivation of spectrum-compatible accelerograms, and the rules for combining the modal maxima (Pinto et al., 2004). Those approaches focus on the random vibration itself rather than failure probability based on the relationship between seismic demand and structural capacity.

Some practical approaches transform time-variant problems into time-invariant ones by considering maximum response during the seismic action. These methods include the SAC-FEMA Method (Cornell et al., 2002), the Effective Fragility Analysis Method (de Felice et al., 2002; Lupoi et al., 2004), and Response Surface Based Approaches (Schotanus et al., 2004). Also available for time-variant problem analysis is MCS: however, the computational cost is typically expensive when the probability of failure is low and there are several random variables. This section briefly introduces approaches for the probabilistic assessment of seismic performance of structures. Reference is made to Wen et al. (2004) and Pinto et al. (2004) for details on these methods.

2.2.1 The SAC-FEMA Method

This section presents a method by Cornell et al. (2002), which is the basis for the SAC-FEMA-350 (2000) guidelines for seismic design and assessment of steel moment-resisting frames. In the SAC-FEMA method, the hazard at a site, $P[IM = s]$ in Equation

(2.1), is defined in terms of the acceleration spectral ordinate $S_a(T)$ corresponding to a period, T, close to the fundamental period of the structure T_f. In this method, it is assumed that failure occurs when the maximum demand over the duration of the seismic excitation exceeds the corresponding capacity. In the SAC-FEMA approach, seismic hazard is combined with drift demand to define drift hazard:

$$H_D(d) = \int P[D \geq d \mid S_a = x] \mid dH(x) \mid \tag{2.2}$$

where $|dH(x)|$ means the absolute value of the derivative of the site's spectral acceleration hazard curve times dx, i.e., loosely likelihood that $S_a = x$. The hazard at a site is expressed as:

$$H(S_a) = \Pr(S_a \geq s_a, 1\ year) = k_0 s_a^{-k} \tag{2.3}$$

which is determined from the hazard analysis in several cases. Seismic demand is related to the hazard with following relationships:

$$\hat{D} = a s_a^b \tag{2.4}$$

where $\hat{D}$ is the median value of demand, D. The constants, a and b, are determined from a regression analysis of structural demands calculated from nonlinear dynamic analyses. The β_D, standard deviation of the natural logarithm of demand, D, is calculated about median value of demand. The constant, b, in general, is not far from 1 for deformation-based demand. For force-based demand, b, is rather low, in which case the closed form approach may not appropriate as Equation (2.4) generally cannot fit the relationship between spectral acceleration and forced demand on structures, Pinto et al. (2004). To consider the dispersion of Equation (2.4), random variable, ε, with unit median and dispersion equal to β_D is introduced:

$$D = \left(a s_a^b\right) \varepsilon \tag{2.5}$$

The demand, D, is assumed to be log-normally distributed about the median, with standard deviation of the natural logarithm equal to β_D. For a given intensity level, the probability of reaching structural demand, d, can be calculated as follows:

$$P[d \leq D \mid S_a = x] = 1 - \Phi(\ln[d / a x^b] / \beta_{D|Sa}) \tag{2.6}$$

in which Φ is standardized Gaussian distribution function. Equations (2.2) and (2.6) result in a closed form solution of drift hazard:

$$H_D(d) = P[D \geq d] = H(s_a^d) \exp\left[\frac{1}{2}\frac{k^2}{b^2}\beta_{D|S_a}^2\right] \tag{2.7}$$

The drift hazard should be combined with drift capacity, *C*, to evaluate the annual probability of the performance level not being met, P_{PL}.

$$P_{\mathrm{PL}} = \int P[C \leq d] \, | dH_D(d) | \tag{2.8}$$

The drift capacity, *C*, is assumed to be lognormally distributed with a median value, $\hat{C}$, and dispersion, β_C. Therefore, the probability of the capacity, *C*, being lower than the demand, *d*, is expressed as:

$$P[C \leq d] = \Phi(\ln[d / \hat{C}] / \beta_C) \tag{2.9}$$

Substituting Equations (2.9) and (2.7) into Equation (2.8) results in probability of annual failure as:

$$P_{\mathrm{PL}} = H(s_a^{\hat{C}}) \exp\left[\frac{1}{2}\frac{k^2}{b^2}(\beta_{D|S_a}^2 + \beta_C^2)\right] \tag{2.10}$$

Parametric study by Pinto et al. (2004) showed that the order of magnitude of P_{PL} is dictated by the hazard, and not by the uncertainties/randomness in both input-output relationship and in the capacity.

The SAC-FEMA method is efficient when the response is predominantly contributed by the first mode [due to the choice of $S_a(T)$ as intensity parameter] and when failure is controlled by a single scalar variable, e.g., the maximum inter-story drift. However, it is difficult to account for the possible correlation between multiple failure modes. In addition, the outcome of the SAC-FEMA method is the total risk, rather than the vulnerability for given intensity level.

In the SAC-FEMA method, the seismic hazard combined with drift demand is referred as drift hazard, Equation (2.2). The drift hazard and structural capacity are combined to estimate annual probability of failure. This procedure fully couples hazard, demand, and capacity. The uncoupled vulnerability curves, $P[LS \mid IM = s]$ in Equation

(2.1), are a less informative measure than that obtained from fully coupled risk analysis in Equation (2.1). Wet et al. (2004) noted that the derivation of vulnerability curves rather than fully coupled risks has following advantages:

- The probabilistic system analysis is effectively uncoupled from the hazard analysis
- A properly conducted vulnerability analysis is less complex, less costly, and involves fewer disciplines than a fully coupled risk analysis.
- The vulnerability analysis can be used to determine probabilistic safety margins against specifically identified events for decision purposes.

With the advantages of uncoupling fragilities and hazards, Nielson (2005) derived vulnerability curves combining structural capacity with drift demand, i.e., Equation (2.6) and Equation (2.9) were combined without introduction of seismic hazard as in Equation (2.8).

$$P[C < D \mid S_a = x] = \Phi\left(\frac{\ln(\hat{D}/\hat{C})}{\sqrt{\beta_{D/S_a}^2 + \beta_C^2}}\right) \tag{2.11}$$

In this approach, the relationship between seismic demand and seismic intensity, Equation (2.4), was based on the SAC-FEMA approach. Other than that the procedure followed standard reliability assessment procedure. The failure probability in Equation (2.11) considers a single mode failure. To estimate a failure probability of a system with several components, numerical approach should be adopted as closed-form estimation of failure probability of multivariate system is not readily possible.

In Chapter 5, the relationship between drift demand of structural components and ground motion intensity, Equation (2.4), is determined from nonlinear response history analyses, with recorded and artificial ground motions carefully chosen for the bridge site. The capacity of structural components and its dispersions are determined from literature reviews, pushover analysis of bents, and engineering judgment. The seismic demands of components are correlated to define systemic seismic demand. System vulnerability is derived from numerical evaluation of failure probability from the seismic demands of components.

2.2.2 Monte-Carlo Simulation Method

Vulnerability curves of a structural component may be easily derived if a probabilistic seismic demand function, such as Equation (2.5), and the structural capacity can be explicitly defined. The derivation of vulnerability curves of a system consisting of many of these components is not straightforward as the closed-form solution of multivariate limit state function is not readily available.

The MCS is a useful simulation method for complex systems with several random variables, $\mathbf{x}$, and several failure modes. For such systems, it is difficult to derive a limit state function, $g(\mathbf{x})$, and to evaluate the failure probability from the closed-form integration of $g(\mathbf{x})$ over the failure domain. The MCS may be used to estimate reliability of such systems by sampling sets of random numbers and running simulations for each set.

The MCS is conceptually straightforward. To estimate failure probability of a system, it needs to generate n sets of random variables, x_i, $i = 1, 2, ..., m$, according to joint probability density, $f_{\mathbf{x}}(\mathbf{x})$. Each set of random variables is used to run simulation and to check whether the system is failed or not. The probability of failure is

$$P_f = n_f / n \tag{2.12}$$

where n_f is number of simulation with $g(\mathbf{x}) < 0$. With the increasing number of simulations, the result from the MCS converges to closed form solution. As the number of simulation cannot be infinite, the MCS is always subject to sampling error. The MCS can be computationally very expensive, depending on the number of random variables. Convergence of the MCS in terms of standard deviation of failure probability is slow ($\propto n^{-1/2}$). To reduce the variance of estimated probability, diverse sampling techniques such as Importance and Latin Hypercube may be applied.

In Chapter 5, the seismic intensity–demand relationships of components are estimated based on the SAC-FEMA method. Assuming that the seismic demands of components are jointly normal in log-log space, the covariance matrix of the random variables, ε in Equation (2.5), is evaluated. The vulnerability curves of a system are

derived through the MCS, in which the random numbers are generated based on the covariance matrix.

2.2.3 Response-Surface Approach

The Response-Surface Method (RSM) approximates the response of a complex system whose limit state functions cannot be easily derived in a closed-form that is amenable to reliability analysis. A limit state function is defined as the boundary between failure and safe domains which is often formulated as the capacity subtracted by demand:

$$g(\mathbf{x}) = C(\mathbf{x}) - D(\mathbf{x}) \tag{2.13}$$

In time-variant problems, such as a structure subjected to ground motions, demand varies with time. When capacity is assumed to be constant, the maximum of seismic demand over time may be used in the limit-state function. If both the capacity and the demand vary with time, the limit-state function may be defined as the minimum of $C(\mathbf{x}, t) - D(\mathbf{x}, t)$ in time domain. Alternatively, Veneziano et al. (1983) defined the limit-state function as a difference between the ground motion intensity, $I_f(\mathbf{x})$, at which a structure fails and the intensity of ground motion.

$$g(\mathbf{x}) = I_f(\mathbf{x}) - I \tag{2.14}$$

Schotanus et al. (2004) proposed to use a response surface to represent the capacity part in an analytical limit-state function, Equation (2.14), as input for FORM analysis. The following are the advantages of the procedure (Schotanus et al., 2004):

- The procedure is general in the sense that it can be used in conjunction with state-of-the-art mechanical models, and that the variability in the response due to uncertainty in the input ground motion is realistically represented.
- The method is computationally affordable.
- A second order polynomial for response surface yields vulnerability values that satisfy criteria of accuracy in the reliability analysis.

The random variables for RSM can be categorized into two groups; controllable random variables, denoted as $\mathbf{x}_1$, and uncontrollable, random variables, denoted as $\mathbf{x}_2$.

For example, the strengths of materials belong to $\mathbf{x}_1$ as mean and standard deviation of the random variables allow the selection of sampling points for response surface generation. Ground motions, however, just add uncertainty on the response for given intensity level. A response surface may be modeled as a function of $\mathbf{x}_1$ and $\mathbf{x}_2$:

$$I_f(\mathbf{x}_1, \mathbf{x}_2) = \mathbf{z}(\mathbf{x}_1)\boldsymbol{\beta} + \delta(\mathbf{x}_2) + \varepsilon \tag{2.15}$$

where I_f is ground motion intensity at failure, $\mathbf{z}(\mathbf{x}_1)\boldsymbol{\beta}$ is called the fixed-effect part of the model, δ is the effect of the random vector $\mathbf{x}_2$, and ε is a random deviation term that represents the fitness of the response surface on experimental results. If the response surface goes through all of the experimented responses, i.e., interpolation rather than regression, the standard deviation of ε becomes zero. Both δ and ε are assumed to be Gaussian with zero mean. To determine the values of δ and ε, simulation must be carefully designed following orthogonal blocking of the sampling points. Orthogonal blocking of experiments, which assures the independence of $\boldsymbol{\beta}$, δ, and ε, is not always possible, depending on the number of random variables. Fortunately, if one is interested solely in overall uncertainty rather than the relative values of δ and ε, complicated simulation design procedure with orthogonal blocking can be avoided. The combined effect of uncertainties in random variables, $\mathbf{x}_2$, represented by δ and the random deviation term, ε, can be accounted for using a single random variable, $\bar{\varepsilon}$, with second-moments expressed as a function of those of δ and ε, $\sigma_{\bar{\varepsilon}}^2 = \sigma_{\varepsilon}^2 + \sigma_{\delta}^2$. Then, Equation (2.15) can be rewritten as:

$$I_f(\mathbf{x}_1, \mathbf{x}_2) = \mathbf{z}(\mathbf{x}_1)\boldsymbol{\beta} + \bar{\varepsilon} \tag{2.16}$$

The second moment may be evaluated through the ordinary least-square method. The procedure for applying RSM on the seismic vulnerability analysis is illustrated in Figure 2.2. FORM analysis of general response surface function may be conducted using components of the reliability package, such as FERUM (Haukaas, 2003). For further information regarding experimental design and blocking, refer to Pinto et al. (2004).

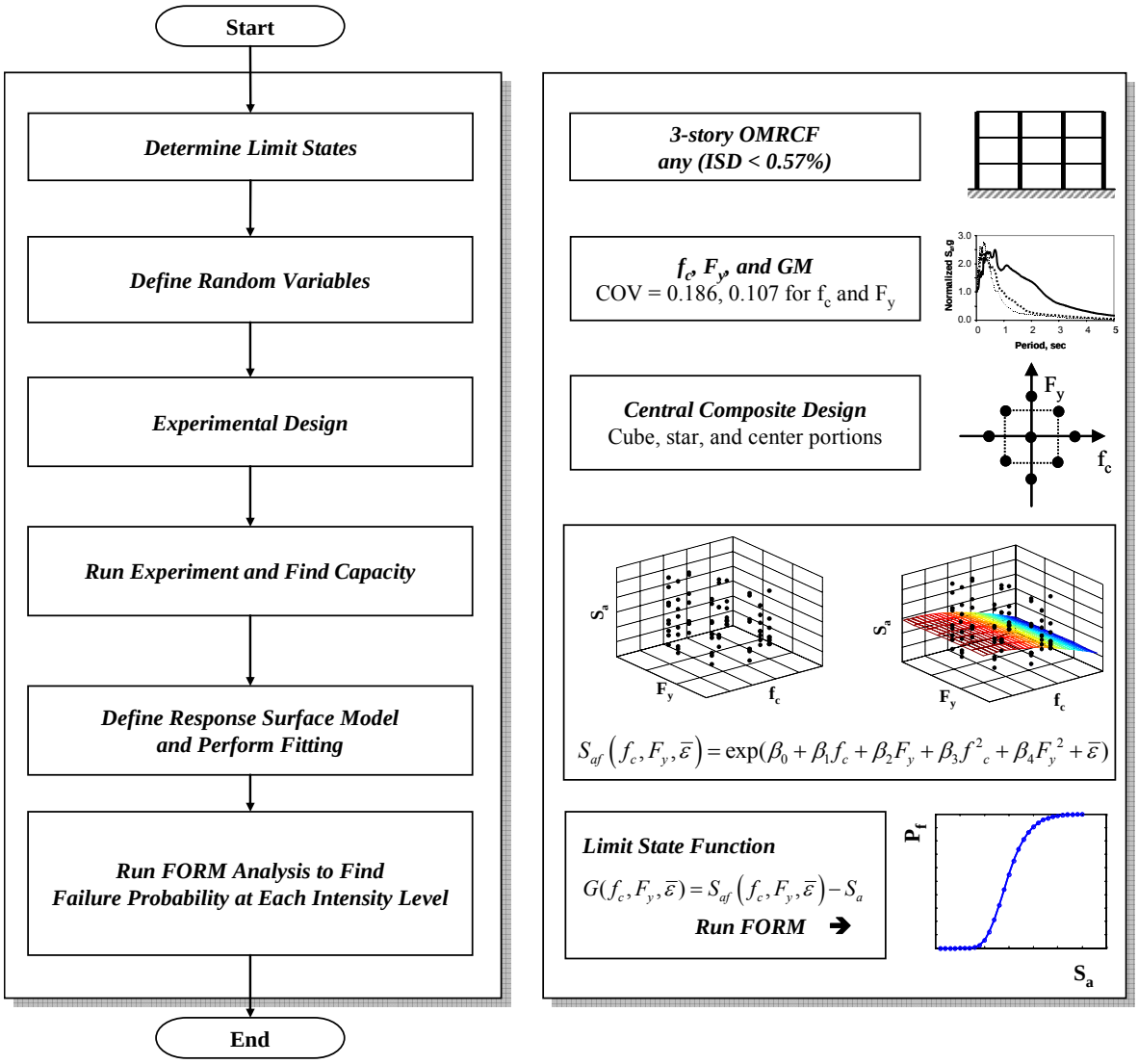

(a) Flow chart (b) Application to 3-story OMRCF

Figure 2.2 Flowchart of RSM for seismic vulnerability analysis

2.3 Application for Cluster Simulation

Vulnerability analysis of structures subjected to seismic loading is a time-variant reliability problem in which a closed-form solution does not exist and, therefore, simulation is inevitable. Full MCS can represent reality most accurately, although it involves a tremendous amount of computational cost. Simulation methods with advanced sampling techniques consume large amounts of computational time when inelastic dynamic analyses are involved.

The nature of computational time required for vulnerability analysis is different from the one required for a single finite element (FE) analysis with a large number of elements. For vulnerability analysis of framed structures, the computational cost for a single inelastic response history analysis is not costly. Each simulation may be conducted easily on moderate-speed processors. Fortunately, computational cost is directly related to the number of simulations. Hence, the computational time may be reduced by distributing each simulation among multiple processors and collecting the required output for vulnerability analysis. The latter approach does not reduce total computational cost, but the time required to conduct the vulnerability analysis may be significantly reduced.

The idea of utilizing multiple processors is implemented in the supercomputer, IBM p690, at the National Center for Supercomputing Applications (NCSA), as shown in Figure 2.3. Open specification for Multiple Processing (OpenMP) directives are used in the preprocessor to handle multiple processors. The computing environment of IBM p690 allows maximum use of 32 processors at the same time. ZEUS-NL (Elnashai et al., 2002) is ported to the UNIX platform and used as a main solver of the simulation tool. Figure 2.4 shows the relative computational time to finish a total of 250 analyses, consisting of 5 frames and 5 ground motions at 10 PGA steps. Analyses using 1 to 50 threads with 16 processors, 32 threads with 32 processors, and the personal computer, Pentium IV 2.65 GHz, are compared. The result shows that the utilization of multiple processors can reduce computational time up to 1/0.037 = 27 times, in comparison with the personal computer. The application is utilized for vulnerability analysis using the Monte-Carlo simulation for the three-story OMRCF.

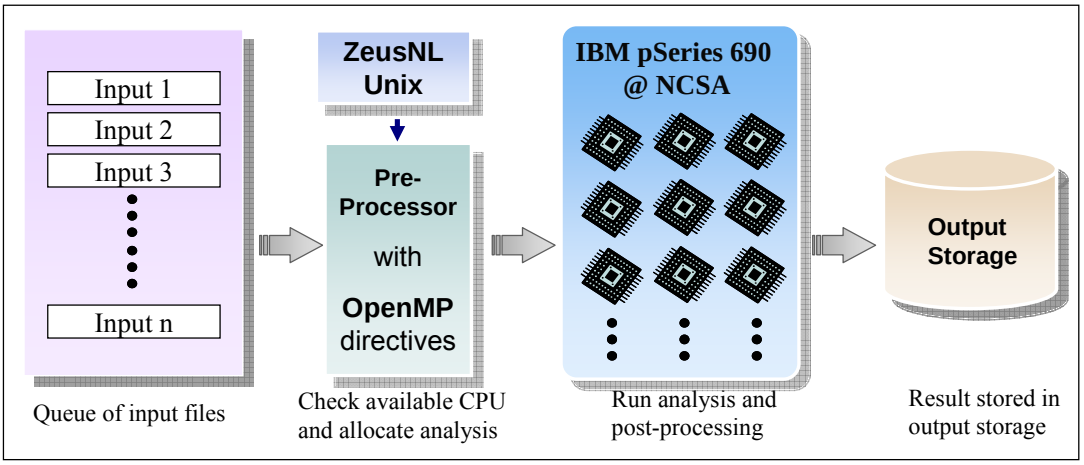

Figure 2.3 Architecture of mass-simulation application

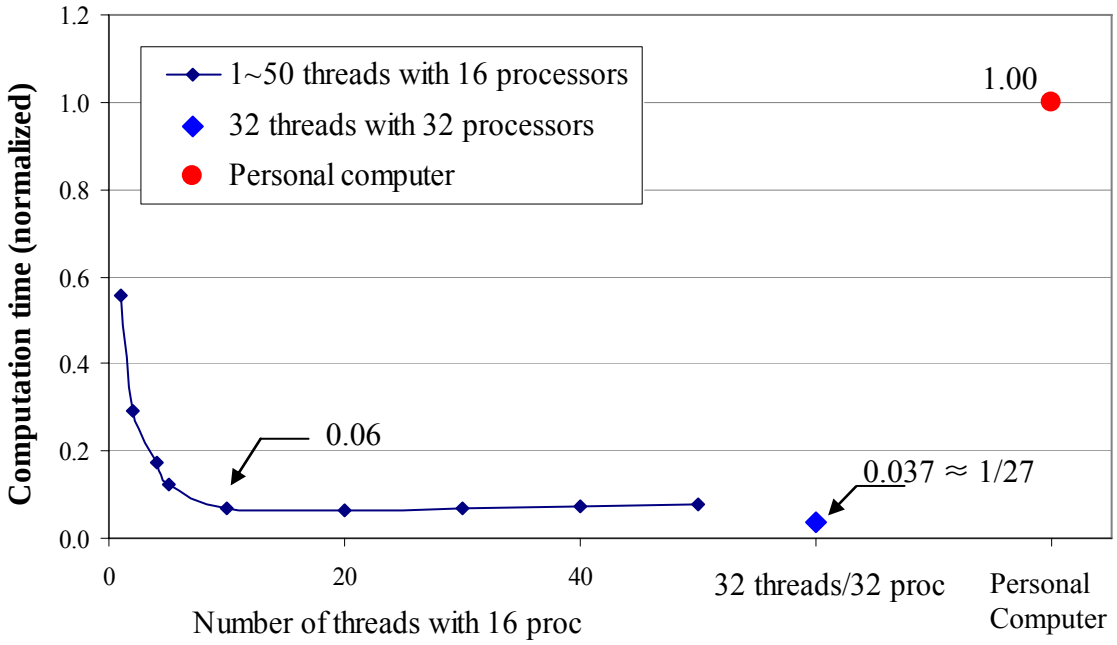

Figure 2.4 Comparison of computational time of cluster simulation

2.4 Benchmark Study on Seismic Vulnerability Evaluation

In this section, vulnerability curves are derived for a typical RC frame structure in mid-America. Various aspects of vulnerability derivation are discussed, such as the selection of reference structures, verification of analytical model, definition of limit states, influential random variables and simulation methods, and derived vulnerability curves from different simulation methods (MCS, SAC-FEMA, and RSM). In addition, this benchmark study verifies the structural analysis platform through comparison of analysis result with the result from shaking table tests.

2.4.1 Reference Structure for Simulation

The main objective of the benchmark study is to verify the structural analysis platform for RC structures, to compare several vulnerability derivation methods, and to estimate important parameters that affect derived fragility curves most sensitively. To achieve this objective, the reference structure should have realistic data with which the analytical model may be compared. The structure must also be simple enough to conduct parametric studies. To fulfill these requirements, a three-story, ordinary, moment- resisting concrete frame (OMRCF) is chosen. The selected structure is a building structure, but it ideally serves the main objective because it is an RC structure. In addition, the structure was previously shaking table-tested, which provides an excellent data set for the verification of an analytical model. Thusfar, no bridges have been tested in a complete system manner on shaking tables.

It is appreciated that the curves developed for this specific building may not be generally applicable to the loss estimation of all RC buildings. Nonetheless, it is postulated that the curves derived could be applicable to the subclass of medium-rise RC buildings with limited ductility and no seismic design provisions; this might be applicable to many areas in the Midwest and in Central/Northern Europe.

The prototype structure was originally designed for the purpose of an experimental study (Bracci et al., 1992). The building features three and four bays in east-west and north-south directions, respectively. The story height is 3.7 m (12 ft) and

the bay width is 5.5 m (18 ft). The total building height is 11m (36 ft). It is designed for gravity loads since wind loads seldom govern for low-rise buildings, and is non-seismically detailed. The provisions of ACI 318-89 (ACI, 1989) code, with Grade 40 steel (F_y = 276 MPa, 40 ksi) and ordinary Portland cement ($f_c^{'}$ = 24 MPa, 3.5 ksi), was employed. The plan and elevation layouts of the structure are given in Figure 2.5. The analyzed frame is shaded in the figure. For detailed design information, reference is made to Bracci et al. (1992).

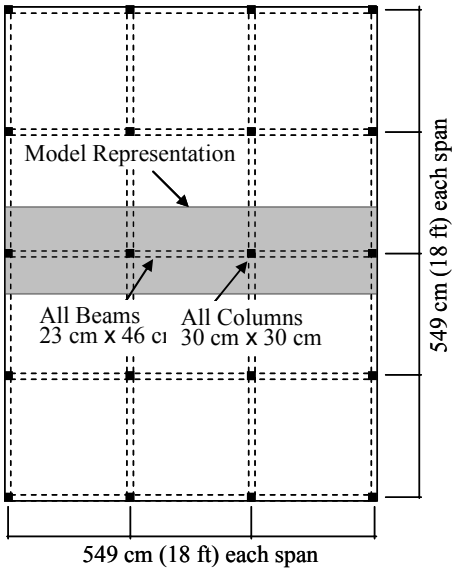

(a) Plan view

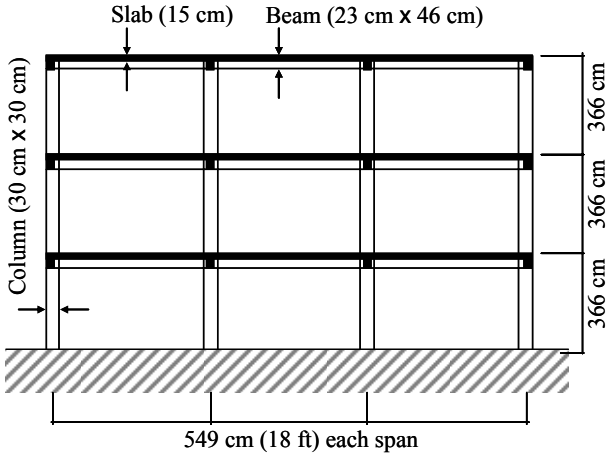

(b) Elevation

Figure 2.5 Configuration of reference RC frame

2.4.2 Analysis Environment

Several methods of analysis have been utilized to determine the seismic demand of structures subjected to earthquake loading. Static pushover analysis, conventional, modal, or adaptive, yields the capacity and collapse mechanism of a structure. For seismic response assessment, though, a seismic demand procedure is required, where effective damping or equivalent ductility is accounted for. Such equivalence may introduce approximations in the analysis results. In addition, the more irregular the structure and the more peculiar the strong-motion records, the less representative the pushover results of dynamic response. This limitation lends weight to the use of dynamic analysis which deals with the coupled demand-capacity problem (Elnashai, 2002), especially for irregular structure.

Because structures not designed to resist seismic loads usually fail in localized modes, their response is not likely to be well-estimated by static methods. Moreover, in order to focus attention on other approximations in the vulnerability functions derivation, it is decided to deploy the most accurate and generally applicable method available for seismic demand and supply evaluation, that is, inelastic dynamic response-history analysis. Use is made of the Mid-America Earthquake Center analysis environment ZEUS-NL (Elnashai et al., 2002). Elements capable of modeling material and geometric nonlinearity are available in the program. The sectional stress-strain state is obtained through the integration of the inelastic material response of the individual fibers describing the section. The Eularian approach of geometric nonlinearity is employed on the element level. Therefore, full account is taken of the spread of inelasticity along the member length and across the section depth as well as the effect of the large member deformations. Because the sectional response is calculated at each loading step from inelastic material models that account for stiffness and strength degradation, there is no need for sweeping assumptions on the moment-curvature relationships required by other analysis approaches. In ZEUS-NL, conventional pushover, adaptive pushover, Eigen analysis, and dynamic analyses are available and have been tested on the member and structural levels (Elnashai and Elghazouli, 1993; Elnashai and Izzuddin, 1993; Broderick and Elnashai, 1994; Martinez-Rueda and Elnashai, 1997; Pinho, 2000; et al.). Recently, ZEUS-NL was used to steer a full-scale, three-dimensional (3D), RC frame testing

campaign, and the a priori predictions were shown to be accurate and representative of the subsequently undertaken, pseudo-dynamic tests (Jeong and Elnashai, 2004a and 2004b). In the following section, the verification of the analysis model and environment through comparison with shaking table experiments are undertaken.

2.4.3 Verification of Analytical Model

The structural model and analysis environment are verified through comparison of response history analysis with shaking table test results by Bracci et al. (1992). In response history analysis, damping, mass, and stiffness are key parameters that affect the assessment result. The verification is undertaken in terms of structural periods and global displacement time histories, because local stress-strain measurements are not available in the published literature.

2.4.3.1 Structural Period

Columns and beams are divided into six and seven elements, respectively, in the numerical model. Mass is deposited at the beam and column connections, as shown in Figure 2.6. Material properties are taken from the reported test results of the experimental model. The elastic structural periods from Eigen value analysis are 0.898, 0.305, and 0.200 sec. for the 1^{st}, 2^{nd}, and 3^{rd} modes, respectively. Bracci et al. (1992) conducted a snap-back test before running shaking-table experiments to estimate the natural periods of the 1/3 scale specimen and found that the periods, after conversion to full scale using similitude laws, were 0.932, 0.307, and 0.206 sec. The experimental values under small amplitude testing are 3~4% longer than the analytical values, which might have resulted from minor cracking in the test specimen. These values give credence to the analytical model.

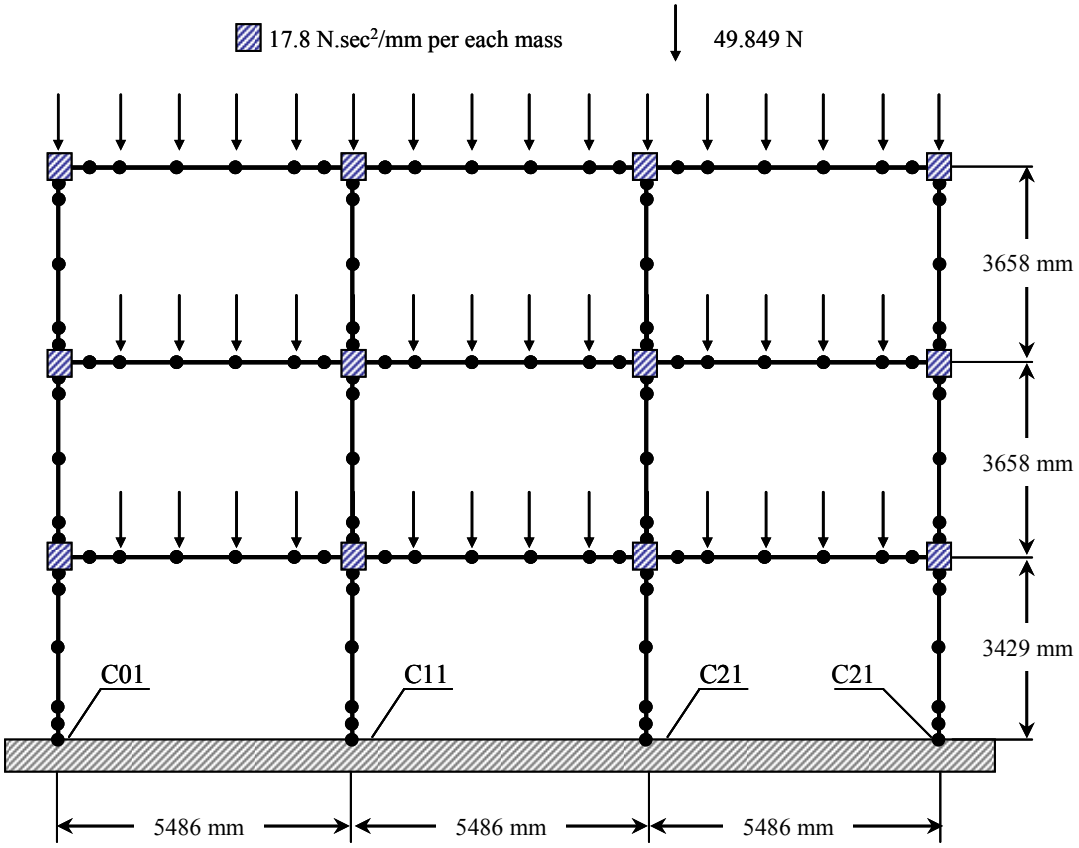

Figure 2.6 Configuration of analytical model

2.4.3.2 Displacement Response History Verification

Figure 2.7 depicts the comparison of the 3rd story displacements of the 1/3 scale specimen and analysis using a 1/3 scale analytical model. For the analysis, Rayleigh damping is used for small amplitude ground excitation with PGA of 0.05g, in which the damping ratio was taken from the snap-back test, (Bracci et al., 1992). For moderate and severe ground motions of 0.20 and 0.30g, damping other than hysteretic is not included. Figure 2.7 (a) does not show good agreement, while Figure 2.7(b) and 2.5(c) show very good agreement between experimental and analytical results. These results are attributed to the fact that at low-level ground motion, it is difficult to accurately estimate the level of damping and to model initial cracks due to curing and experimental setup. On the contrary, at medium-to-high earthquake motion, inelastic response from fully cracked section mainly governs the behavior, thus reducing the effect of cracking and small

amplitude damping. Good agreement in the moderate-to-large amplitude shaking verifies that the analytical model represents the experimented structure well. It is also observed that assuming the same level of damping from the low amplitude to the collapse level, ground motion could result in nonconservative vulnerability curves at medium-to-high ground motion intensities. In this study, it is assumed that there is no source of damping other than hysteretic. Thus, for low-level ground motions, the vulnerability curves might be on the conservative side. Assuming no viscous damping may cause spurious, higher-mode oscillation in a structure without any other sources of energy dissipation. In the studied structure, however, this is not a significant issue because (a) the shaking-table experiment confirmed that the numerical model is of good accuracy; (b) the height of the structure is short, with no irregularity; therefore, there are limited possibilities for spurious modes; and (c) the inelastic concrete material used in the analysis shows hysteretic damping even under small magnitude of vibrations; therefore damping out short-period, spurious modes.

The current and previous verification of the modeling approach and analysis platform lend weight to the confident use of the analytical tools to investigate the effects of parameter variation within the vulnerability analysis.

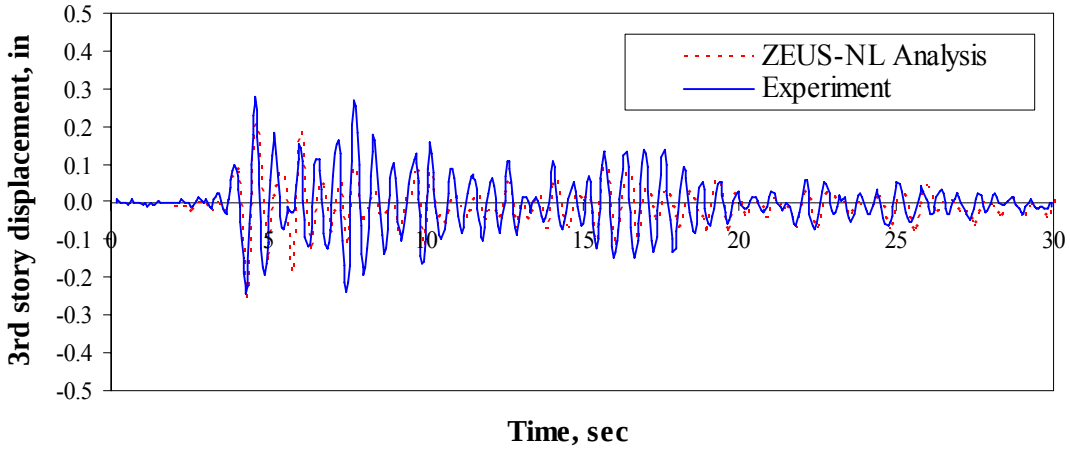

(a) 3rd story displacement —Taft 0.05g

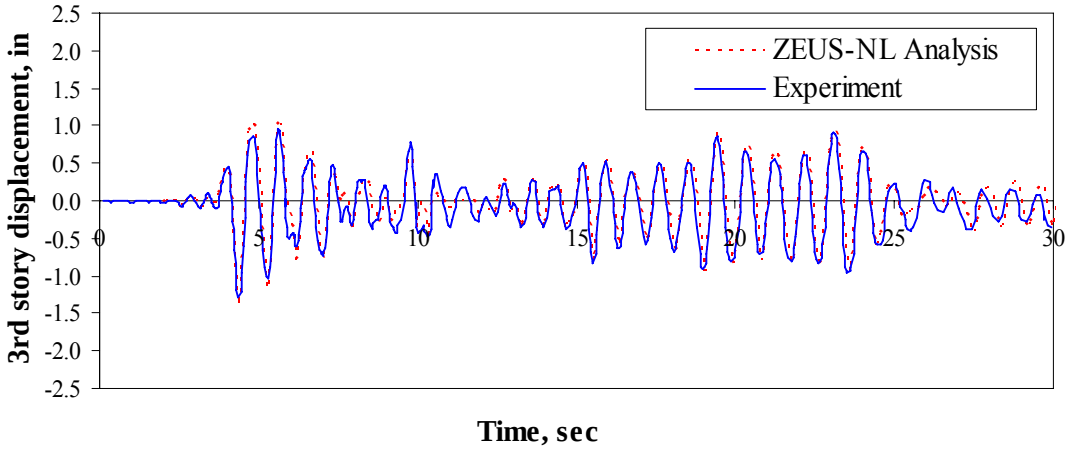

(b) 3rd story displacement —Taft 0.20g

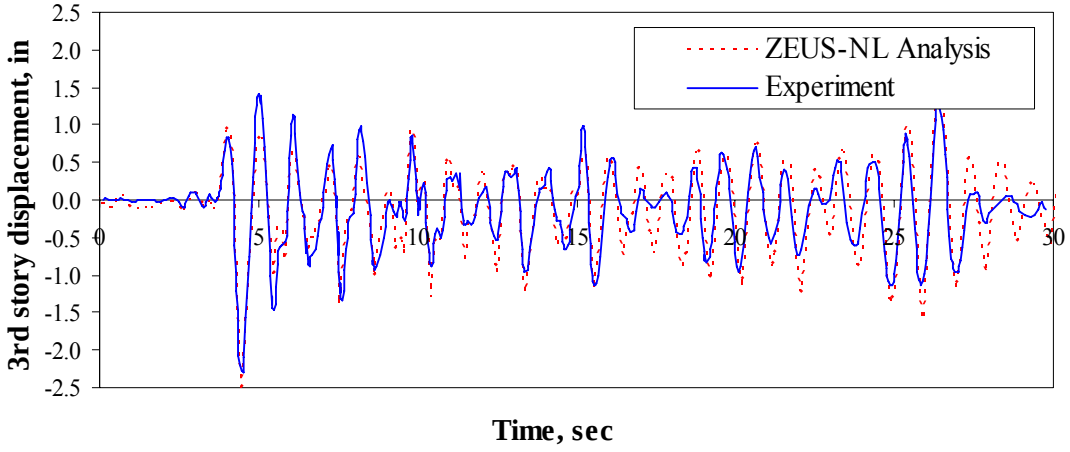

(c) 3rd story displacement —Taft 0.30g

Figure 2.7 Comparison of dynamic analysis with shaking-table test

2.4.4 Uncertainties in Capacity and Demand

In the derivation of vulnerability functions, a probabilistic approach is adopted due to uncertainties in the hazard (demand) as well as the structural supply (capacity). Some of those uncertainties stem from factors that are inherently random (referred to as aleatory uncertainty) or from lack of knowledge (referred to as epistemic uncertainty) (Wen et al., 2003). In this section, the effects of aleatory uncertainties from material strengths and ground motion on the vulnerability curves are investigated.

2.4.4.1 Material Uncertainty

i - Concrete strength

Barlett and MacGregor (1996) investigated the relationship between the strength of cast-in-place concrete and specified concrete strength. When concrete was 1 year old, the ratio of the average in-place strength to the specified strength was 1.33 and 1.44, for short and long elements, respectively, with a coefficient of variation (COV) of 18.6%. The variation of strength throughout the structure for a given mean in-place strength depended on the number of members, number of batches, and type of construction. In this study, it is assumed that there is no variability of concrete strength because the structure is a low-rise building of limited volume that would have been constructed in a relatively short period. Thus, a COV of 18.6% is adopted. The specified concrete strength (or design strength) of the considered structure was 24 MPa. In-place concrete strength is assumed to be 1.40 times larger than the specified strength (33.6 MPa). Normal distribution assumption is adopted for the concrete strength.

ii - Steel strength

Mirza and MacGregor (1979) reported results of about 4000 tests on Grade 40 and 60 bars. The mean values and COV of the yield strength were 337 MPa (48.8 ksi) and 10.7 %, respectively. The probability distribution of modulus of elasticity of Grade 40 reinforcing steel followed a normal distribution, with a mean value 201,327 MPa (29,200 ksi) and a COV of 3.3%. Due to the low level of variability observed, the modulus of elasticity is assumed deterministic (201,327 MPa) in this study. The structure was

designed with grade 40 steel; thus, the mean steel strength is assumed to be 337 MPa. The steel strength is assumed to follow a normal distribution.

2.4.4.2 Input Motion Uncertainty

i - Selection of ground motion

Nine sets of ground motions are used for the derivation of vulnerability curves. Derived vulnerability curves for each set are compared to gain insight into the effect of ground motion variation on vulnerability analysis.

The first three sets of ground motions are based on the ratio of peak ground acceleration-to-peak ground velocity (a/v). Zhu et al. (1988) discussed these three categories of earthquake ground motions and their engineering and seismological significance. The a/v ratio implicitly accounts for many seismo-tectonic features and site characteristics of earthquake ground motion records. Sawada et al. (1992) concluded that low a/v ratios signify earthquakes with low predominant frequencies, broader response spectra, longer durations and medium-to-high magnitudes, long epicentral distances and site periods. Conversely, high a/v ratios represent high predominant frequencies, narrow band spectra, short duration, and small-medium magnitudes, short epicentral distance and site periods. Ground motions were classified in the following ranges:

Low	$: a/v < 0.8\, g/ms^{-1}$
Intermediate	$: 0.8\, g/ms^{-1} \le a/v \le 1.2 g/ms^{-1}$
High	$: 1.2 g/ms^{-1} < a/v$

Based on the above categorization, three sets of ground motions are selected in this study, as shown in Table 2.2. The average response spectra of selected ground motion sets (Figure 2.8) show distinctive difference among each ground motion set.

The remaining six sets used in this study are artificial ground motions generated by Drosos (2003). Drosos (2003) generated the bedrock motion for the Mississippi Embayment in the New Madrid Seismic Zone. Equivalent linear site response analyses were conducted to evaluate the ground motions at soil surface. During the site response

analysis, shear wave velocity profiles were randomized to account for the uncertainties in shear wave velocity and layer thickness. Three of the sets, L-1, L-2, and L-3, were generated based on a Lowlands soil profile in the Memphis area. The other three sets, U-1, U-2, and U-3, were generated based on an Uplands soil profile in the same region. Each of the three sets of ground motions were based on three scenario earthquakes: small, medium, and large; at three epicenter distances: short, medium, and long. Each set contains 10 ground motions. Table 2.3 shows the ground motion parameters for Memphis, Tennessee.

Table 2.2 Properties of selected ground motions based on a/v ratio

a/v ratio	Earthquake event / Location	M_L	Date	Soil Type	Distance [km]	PGA [m/s^2]	a/v ratio [g/ms^{-1}]
Low (AV-1)	Bucharest / Romania	6.40	3/4/1977	rock	4	-1.906	0.275
	Erzincan / Turkey	unknown	3/13/1992	stiff soil	13	-3.816	0.382
	aftershock of Montenegro / Yugoslavia	6.20	5/24/1979	alluvium	8	-1.173	0.634
	Kalamata / Greece	5.50	9/13/1986	stiff soil	9	-2.109	0.657
	Kocaeli / Turkey	unknown	8/17/1999	unknown	101	-3.039	0.750
Inter-mediate (AV-2)	aftershock of Friuli / Italy	6.10	9/15/1976	soft soil	12	-0.811	1.040
	Athens / Greece	unknown	9/7/1999	unknown	24	-1.088	1.090
	Umbra-Marche / Italy	5.80	9/26/1997	stiff soil	27	-0.992	1.108
	Lazio Abruzzo / Italy	5.70	5/7/1984	rock	31	-0.628	1.136
	Basso Tirreno / Italy	5.60	4/15/1978	soft soil	18	0.719	1.183
High (AV-3)	Gulf of Corinth / Greece	4.70	11/4/1993	stiff soil	10	-0.673	1.432
	aftershock of Montenegro / Yugoslavia	6.20	5/24/1979	rock	32	-0.667	1.526
	aftershock of Montenegro / Yugoslavia	6.20	5/24/1979	alluvium	16	-1.709	1.564
	aftershock of Umbria-Marche / Italy	5.00	11/9/1997	rock	2	0.412	1.902
	Friuli / Italy	6.30	5/6/1976	rock	27	3.500	1.730

Table 2.3 Properties of artificial ground motions for Memphis, TN

	EQ Scenario	Scenario 1 7.5 @ Blytheville, AR	Scenario 2 6.5 @ Marked Tree, AR	Scenario 3 5.5 @ Memphis, TN
Memphis, TN (Lowlands)	Set ID	Set L-1	Set L-2	Set L-3
	PGA (g)	0.1427	0.0632	0.0958
	PGV (m/s)	0.1520	0.0576	0.0665
	PGD (m)	0.0606	0.0202	0.0138
Memphis, TN (Uplands)	Set ID	Set U-1	Set U-2	Set U-3
	PGA (g)	0.1407	0.0676	0.1030
	PGV (m/s)	0.1290	0.0516	0.0609
	PGD (m)	0.0537	0.0178	0.0118

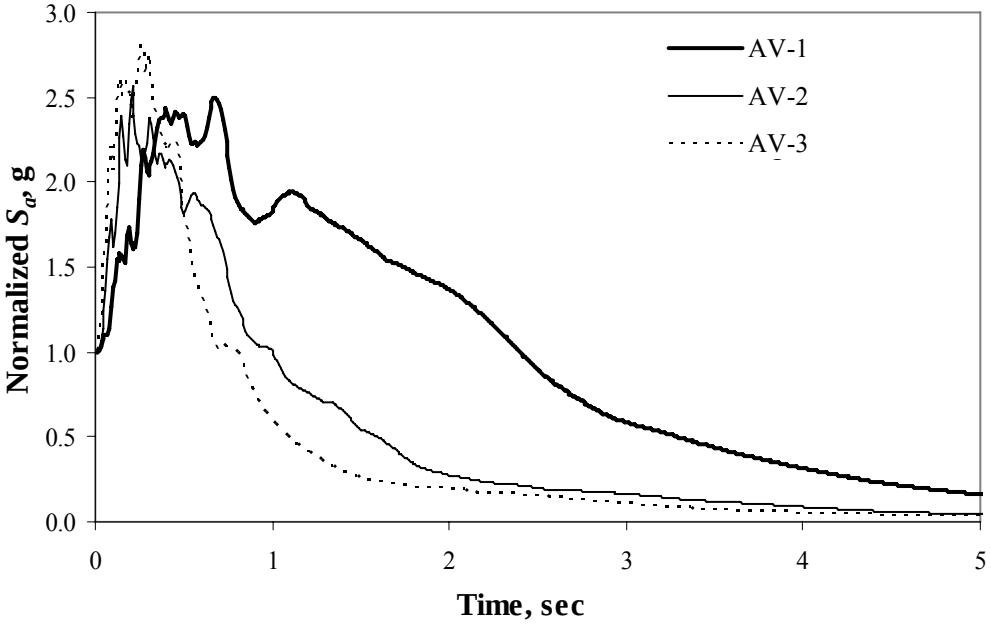

Figure 2.8 Average response spectrum of selected ground motion sets

2.4.4.3 Random Variables

Three different ground motion sets are combined with different material properties. For ground motion sets AV-1, AV-2, and AV-3, 10 ultimate concrete strengths, f_c, and 10 steel yield strengths, F_y, are generated and a full combination of material strengths are used, resulting in a total of 100 frames. The analysis results are used to study the effect of material properties on the structural response. For ground motion set L-1, L-2, and L-3, which are artificial ground motions based on Lowlands profile, 50 concrete and steel strengths are generated following the mean and standard deviation given in Section 2.4.4.1, resulting in 50 different frames. For ground motion set U-1, U-2, and U-3 based on Uplands profile, 100 concrete and steel strengths are generated. From the analysis result of these frames, the effect of sample size is investigated.

2.4.5 Ground Motion Duration and Scale Factors

2.4.5.1 Ground Motion Duration

The duration of the significant part of strong-motion affects the maximum response when a structure undergoes inelastic deformations. There are numerous studies aimed at defining the duration of strong ground motion. Bommer and Martinez-Pereira (1999) assembled 30 definitions of strong-motion duration suggested by previous researchers, and divided them into four categories: bracketed, uniform, significant, and structural response-based definitions. Because the selected motions in this study are to be scaled for vulnerability curve generation, the duration should be defined in a relative manner as in the 'significant duration' option. Trifunac and Brady (1975) used significant duration concepts based on the integral of the square of acceleration, velocity, and displacement in which the duration was defined as the interval between the times at which 5% and 95% of the total integral was attained. The latter range of duration is meaningful in characterizing ground motions. From a structural analysis point of view, however, this duration may not be practical. For instance, if the above-mentioned interval of total integral is used, as shown in the Figure 2.9, the ground motion acceleration could start at very large values, which may apply an unrealistic pulse to the structure. Moreover, because the major part of ground motion energy is skewed to the early part of the motion, using identical margins for the start and the end of the duration is not a reasonable approach. Based on the above argument, for the current study, the interval between 0.5% and 95% of the arias intensity is used.

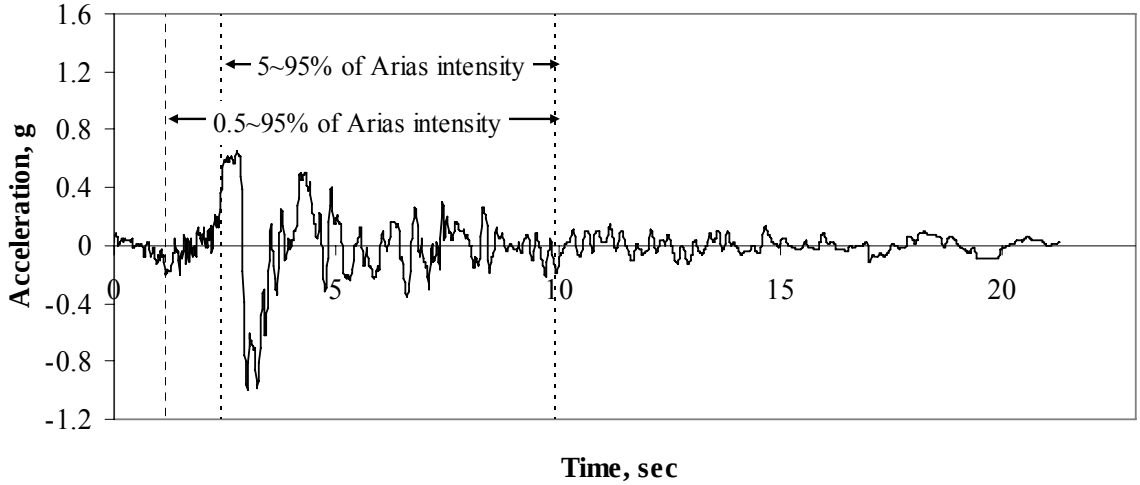

Figure 2.9 Significant duration of a ground motion

2.4.5.2 Selection of Scale Factors

The computational demand for derivation of the vulnerability curve is very large. Analysis time for 100 frames (combination of 10 concrete and 10 steel strengths) subjected to 5 ground motions (i.e., intermediate a/v ratio ground motion set) that are scaled from PGA of 0.05 to 0.5g at 0.05g interval, is about 121 hours on a fast PC (Pentium IV 2.65 GHz, 1 GByte of RAM) at the time of the current study. Thus, a reasonable range of PGA levels should be selected to most effectively utilize the computational power, because each ground motion set has different spectral acceleration at the fundamental period of the structure. For example, for the low a/v ratio ground motion set, a PGA of 0.50g is too large because most structures collapse at a PGA of 0.2g. Conversely, for high a/v ratio ground motion set, 0.50g PGA level is not large enough to derive vulnerability curve for the collapse limit state. Thus, for low and high a/v ratios, additional selective analyses have to be performed to improve the resolution of the vulnerability curves.

To determine the range of reasonable PGA scaling, the capacity spectrum method is utilized. The capacity curves are obtained from adaptive pushover analysis, and demand curves are converted from the elastic displacement and acceleration spectra of each ground motion set. For accurate estimation of maximum PGA scaling at which the structure collapses, elastic demand should be decreased to consider inelasticity using effective damping (ATC 40, 1997; Borzi et al., 2001) or ductility ratio (Chopra and Goel, 1999). In this analysis, however, rough estimation of PGA scales is undertaken using elastic demand spectra and inelastic capacity spectra.

2.4.6 Capacity Limit States

In ATC 40 (1997) and FEMA-273 (1997), four limit states were defined based on global behavior (interstory drift) as well as element deformation (plastic hinge rotation). Rossetto and Elnashai (2003) used five limit states for derivation of vulnerability curves based on observational data, while Chryssanthopoulos et al. (2000) used only two limit states. In the latter studies, the global limit states were independent of the specific response of the structure. For example, the FEMA-273 (1997) 'life safety level' limit

state of InterStory Drift (ISD) for nonductile moment resisting frame is 1.00% regardless of gravity force levels or the details of structural configuration within the subclass of structure.

For rigorous analysis, it is necessary to define limit states for each individual structure, because the deformational capacity could be affected by many other factors, such as gravity force level, irregularity, anticipated plastic hinging mechanism, etc. In this study, three limit states are defined for the prototype structure based on the first yielding of steel, attainment of maximum element strength, and maximum confined concrete strain during the adaptive pushover analysis. These are termed, 'serviceability', 'damage control', and 'collapse prevention', limit states, respectively. In this study, the local damage of individual structural element, such as beam, column, or beam-column joint, is not accounted for. Only interstory drift is used as a global measure of damage. The 1st story drift which corresponds to each limit state, for the prototype structure, is 0.57%, 1.2%, and 2.3% for the selected three limit states, respectively, as shown in Figure 2.10. In the figure, c01 through c31 represent the bottom element of the 1st story columns as indicated in Figure 2.6. It is assumed that theses limit states are also applicable to the 2nd and 3rd stories.

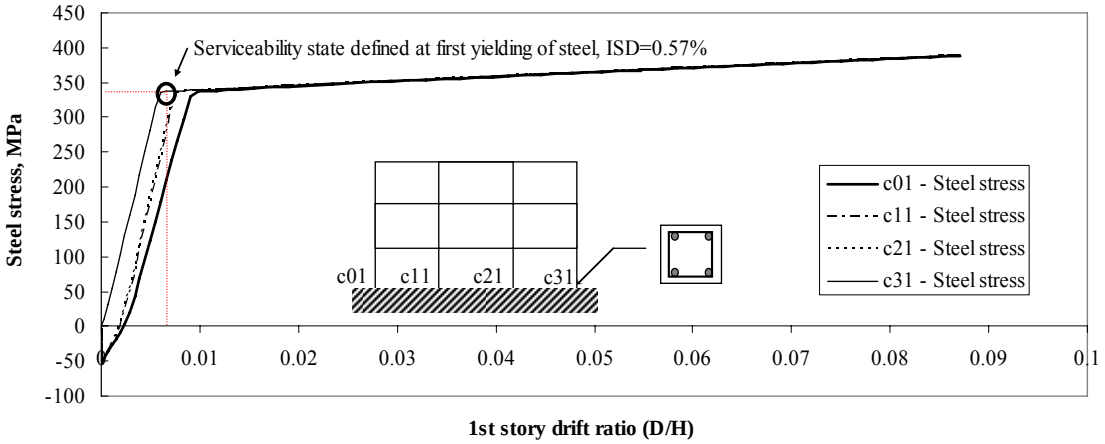

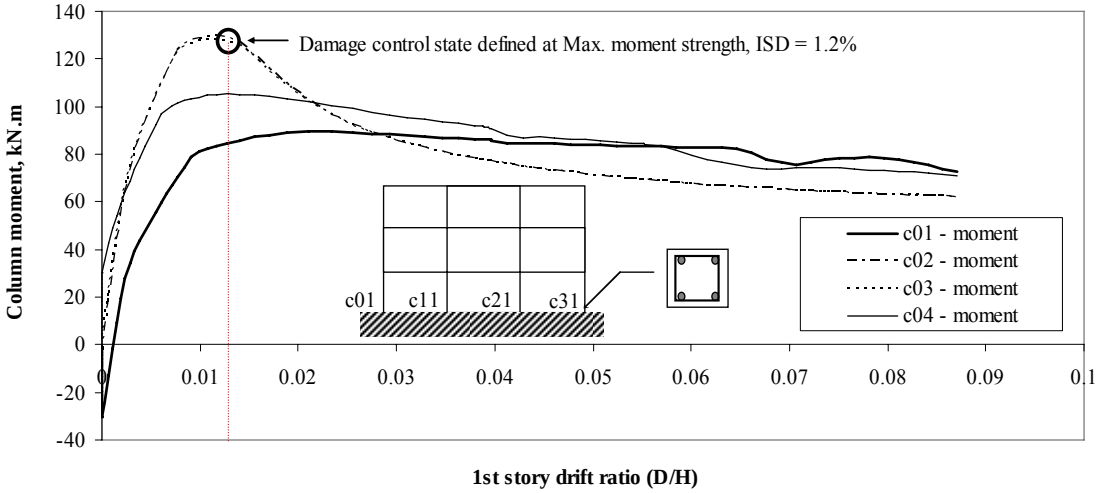

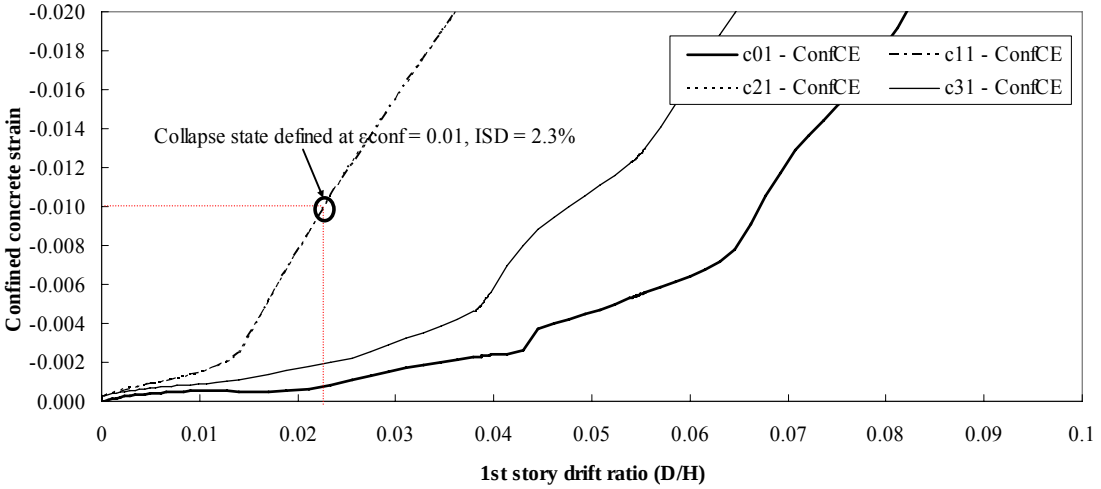

Figure 2.10 Definition of limit states

2.4.7 Simulation and Vulnerability Curve Derivation

There are many available methods to analytically derive vulnerability functions. The most realistic method with the least assumption might be an MCS, which requires a huge amount of computational cost. The SAC-FEMA method (Cornell et al., 2002) is the basis for the FEMA-350 (2000) guidelines. The SAC-FEMA method provides a closed- form expression for the risk rather than vulnerability. The effectiveness of the SAC-FEMA method is better when the response is predominantly contributed by the first mode (due to the choice of $S_a(T)$ as intensity parameter) and when failure is controlled by a single scalar variable, as for example the maximum interstory drift. The method is difficult to account for the possible correlation between failure modes. The RSM introduced in Section 2.2.3 is efficient, but assumes that there exists a smooth response surface.

In this benchmark study, the vulnerability curves from the MCS, the SAC-FEMA method, and the RSM are compared. In the SAC-FEMA method introduced in Section 2.2.1, the seismic intensity measure is related to seismic demand with Equation (2.4) and the dispersion of the seismic demand is estimated from the standard deviation about median seismic demand in log-log space. In the MCS approach taken in this section, an MCS is conducted at each intensity level, and probabilistic distribution of seismic demand is assumed to be lognormal at each intensity level. Strictly speaking, this method is not a rigorous MCS, as probabilistic distribution of structural responses is assumed. But in comparison with the SAC-FEMA method and RSM, the relationship between seismic intensity and structural demand is not assumed. Figure 2.11 highlights the subtle differences between the methods in Section 2.2.1 and the MCS in this example. In RSM, both spectral acceleration and peak ground acceleration are used to compare the effect of intensity measure. Table 2.4 shows the combination of ground motion sets, simulation methods, and intensity measures that are used in the simulation.

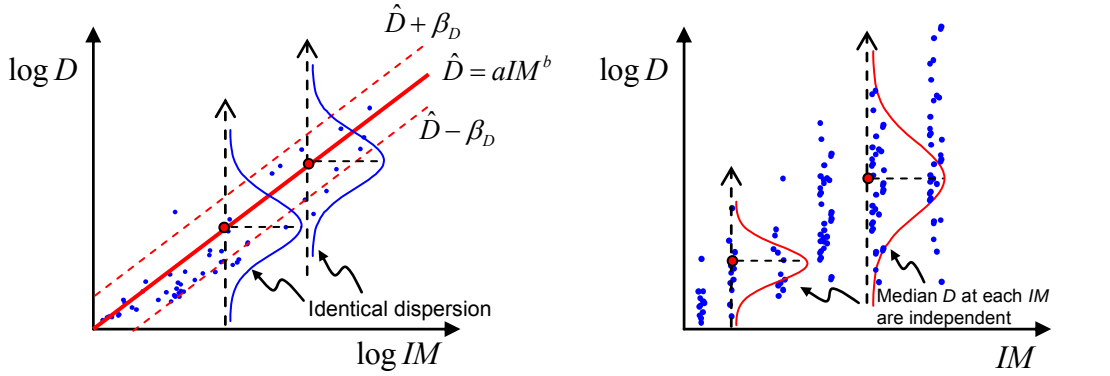

(a) Intensity measure- demand relationship in SAC/FEMA method

(b) The MCS based approximation

Figure 2.11 MCS method adopted for vulnerability curve derivation

Table 2.4 Simulation method, intensity measures, and ground motion sets

Simulation method \ Intensity measure	Peak ground acceleration	Spectral acceleration
Monte Carlo simulation	Set AV-1, Set AV-2, Set AV-3 Set L-1, Set L-2, Set L-3 Set U-1, Set U-2, Set U-3	N/A
Response surface method	Set U-1, Set U-2, Set U-3	Set U-1, Set U-2, Set U-3
SAC-FEMA method	Set U-1	N/A

2.4.7.1 Monte-Carlo Simulation

For ground motion sets, AV-1, AV-2, and AV-3, and 100 frames (full combination of 10 steel and 10 concrete properties) are used at each PGA level. The generated frames represent uncertainties in material strengths following the distribution in Section 2.4.4.1. The maximum interstory drift (ISD_{max}) of the OMRCF is collected from the simulations. The distribution parameters of ISD_{max} at each intensity level are calculated assuming log-normal distribution. The total simulations of the frame using ground motion set AV-1, AV-2, and AV-3 required 456 hours using a Pentium 4-2.65 GHz system, for a total of 23,000 response history analyses. For the analysis of frames using ground motion set L-1

through U-3, 50 frames (randomly generated 50 frames) are generated and the mass-simulation environment introduced in Section 2.3 is utilized.

The platform used for the simulation accounts for geometric nonlinearity as well as material inelasticity. Therefore, when the structure is subjected to large seismic demands, instability under gravity loading may ensue. Because the drift of unstable structures depends on the convergence criteria of the analysis tool, it is concluded that interstory drift at such response status should not be included in the estimation of mean and standard deviation at each intensity level. Thus, it is assumed that the structure is in the collapse state if the ISD_{max} is larger than 2.3%, as discussed in Section 2.4.6. To include the statistics of collapsed frames, the total probability theorem is adopted. The probability where a frame ISD_{max} will be larger than a certain limit state can be calculated as below:

$$\begin{aligned} P(\mathrm{ISD} > \mathrm{ISD}_{Limit}) &= P(\mathrm{ISD} > \mathrm{ISD}_{Limit} \mid E_1) \cdot P(E_1) + P(\mathrm{ISD} > \mathrm{ISD}_{Limit} \mid E_2) \cdot P(E_2) \\ &= P(\mathrm{ISD} > \mathrm{ISD}_{Limit} \mid E_1) \cdot P(E_1) + 1.0 \cdot P(E_2) \end{aligned} \tag{2.17}$$

where $P(E_1)$ and $P(E_2)$ represent the probability that the structure is in a stable or in a collapsed state, respectively. As shown in Figure 2.12, a lognormal distribution is assumed for structures with ISD < 2.3%, and the structures are considered to have collapsed if ISD ≥ 2.3%. Figure 2.13 shows a sample vulnerability curve for 0.57% ISD limit states using ground motion set AV-2. Without considering collapse state ISD, normal and lognormal distribution assumptions show lower probability of attaining the limit states at larger PGA levels, which is due to the misleading average and coefficient of variance of unstable structures.

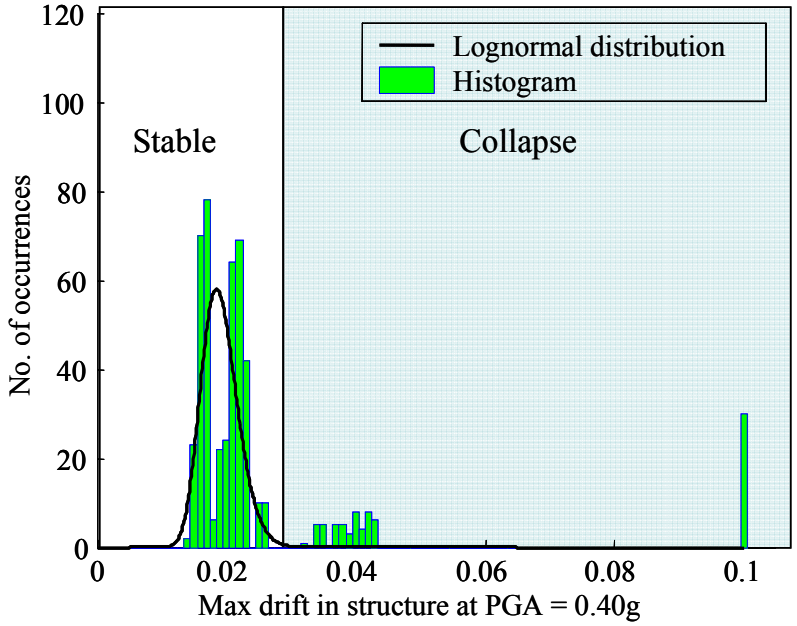

Figure 2.12 Lognormal distribution of seismic demand before collapse
(Ground motion – Set AV-2, PGA = 0.40g)

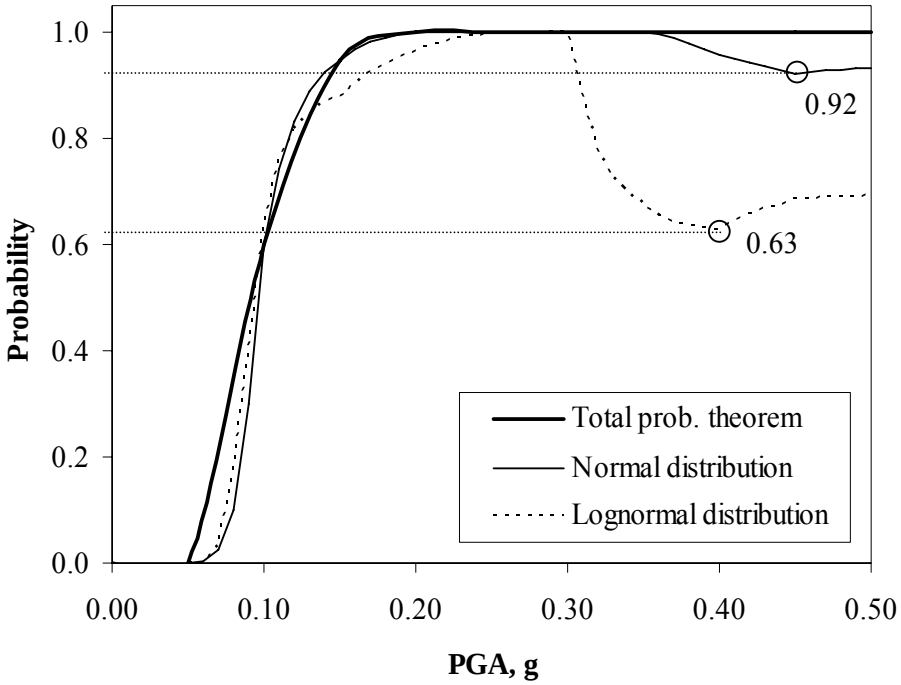

Figure 2.13 Vulnerability curves from various methods
(Ground motion – Set AV-2, Limit state = ISD 0.57%)

2.4.7.2 Response Surface Method

The response surface method (RSM) introduced in Section 2.2.3 is applied to ground motion Set U-1, U-2, and U-3. In this approach, the response surface is defined as the ground motion intensity, either PGA or S_a, where structural response exceeds predefined limit states. To determine this intensity level, five to nine iterations were necessary. Experimental points are chosen using Central Composite Design (CCD), as shown in Figure 2.14. As there are two random variables in the structure, concrete ultimate strength and steel yield strength, CCD results in 9 experimental points per ground motion. Each ground motion set consists of 10 ground motions. Thus, a total of 90 response points are evaluated. The dots in Figure 2.15 show the response points from the experiment for ground motion Set U-1.

The response surface is assumed to be an exponential of a second order polynomial. The exponential function is used because the ground motion intensity cannot be negative. The coupled terms between f_c and F_y are not considered because it is assumed that concrete and steel strength affect the structural response independently.

$$S_{af}\left(f_c, F_y, \bar{\varepsilon}\right) = \exp(\beta_0 + \beta_1 f_c + \beta_2 F_y + \beta_3 f^2{}_c + \beta_4 F_y{}^2 + \bar{\varepsilon}) \qquad (2.18)$$

The coefficients, β, determine mean response for given f_c and F_y. The error term $\bar{\varepsilon}$ is a random variable with zero mean and standard deviation of $\sigma_{\bar{\varepsilon}}$, which represents the lack of fitness of the response function and the inherent uncertainty in ground motion. The unknowns, β, can be determined from ordinary least square method. The error term $\bar{\varepsilon}$ can be evaluated from the residual of the least square method. The response surface function, Equation (2.18), with the random variables, f_c, F_y, and $\bar{\varepsilon}$, represents the capacity of the structure, which can be substituted into Equation (2.14), the limit-state function. The FORM analysis is conducted for the limit-state function using a reliability package, FERUM (Haukaas, 2003).

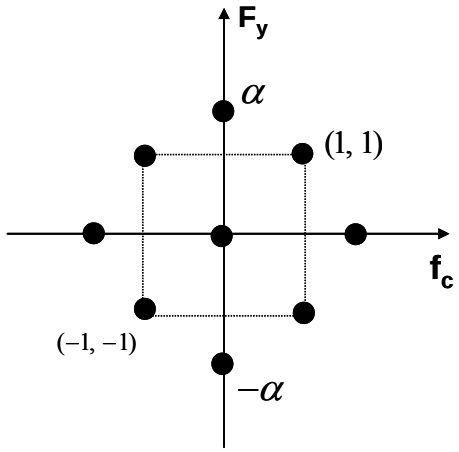

Figure 2.14 Central composite design of experiments

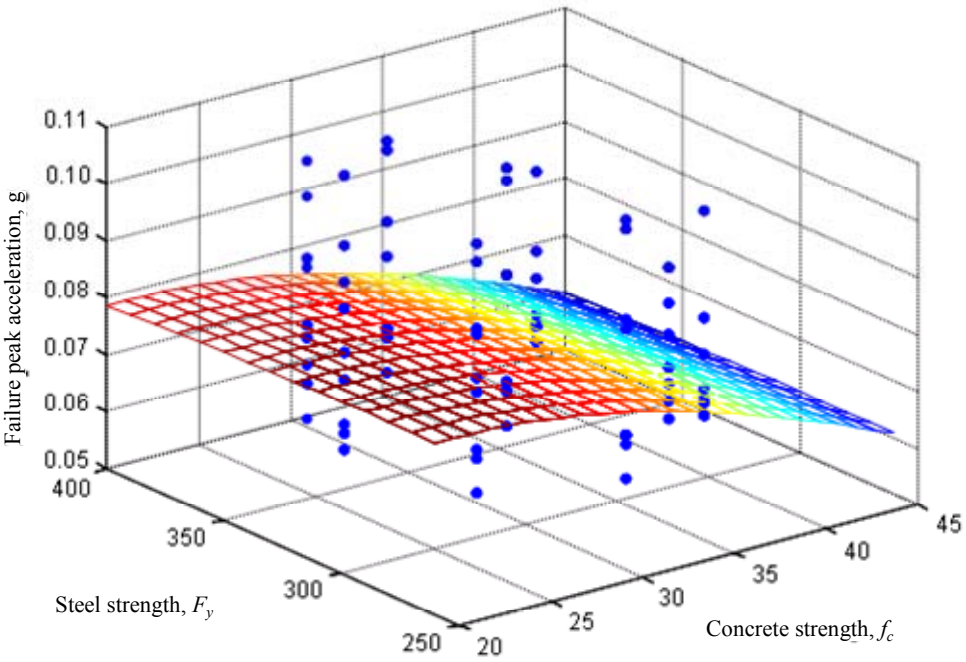

Figure 2.15 Response points and response surface for Set U-1, ISD=0.57%

2.4.7.3 The SAC-FEMA Method

A variation of the SAC-FEMA method is applied to derive vulnerability curves. In this verification example, PGA is used as an intensity measure and interstory drift at each story is used as a measure of seismic demand. It is assumed that the seismic intensity and seismic demand is related with following equation.

$$ISD_i = (a_i PGA^{b_i})\varepsilon_i \tag{2.19}$$

where ISD_i is the maximum interstory drift at i^{th} story, a_i and b_i define the relationship between intensity measure and seismic demand, and ε_i is a random parameter with mean of one. Equation (2.19) is identical to Equation (2.5) except PGA is used as an intensity measure. In this example, there are three failure modes; 1^{st} , 2^{nd} , and 3^{rd} story failure. The failure probability of each story can be estimated using Equation (2.11). The structure is assumed to be failed when any of three stories reaches a limit state.

$$P(\text{System Failure} \mid \text{IM=PGA}) = P(ISD_1>LS \text{ or } ISD_2>LS \text{ or } ISD_3>LS \mid \text{IM=PGA}) \tag{2.20}$$

Closed-form estimation of failure probability of a system from Equation (2.20) is not straightforward. The natural log of Equation (2.19) yields:

$$\ln(ISD_i) = \ln(a_i PGA^{b_i}) + \ln(\varepsilon_i) \tag{2.21}$$

where $\ln(\varepsilon_i)$ is a random variable with zero mean and the a_i and b_i are deterministic variables. From structural response data, these variables can be determined for each story and also the covariance of random variables, $\ln(\varepsilon_i)$, can be estimated. Because seismic demand at every story and their correlation can be probabilistically described, the system probability in Equation (2.20) can be estimated using the MCS following the probabilistic distribution of seismic demands. Note that the MCS at this procedure implies generation of seismic demands following the probabilistic distribution and correlation of each failure mode. It does not mean that the nonlinear structural response analyses are conducted with MCS to estimate system probability. Figure 2.16 compares the component failure probability with system failure probability for ground motion set U-1 and for damage control limit state (ISD > 1.2%). The component failure probabilities are estimated in Equation (2.11). The system failure probabilities are estimated with generation of seismic

demand and comparison of those with structural capacity. Note that the probability of system failure is always higher than the probability of component failure.

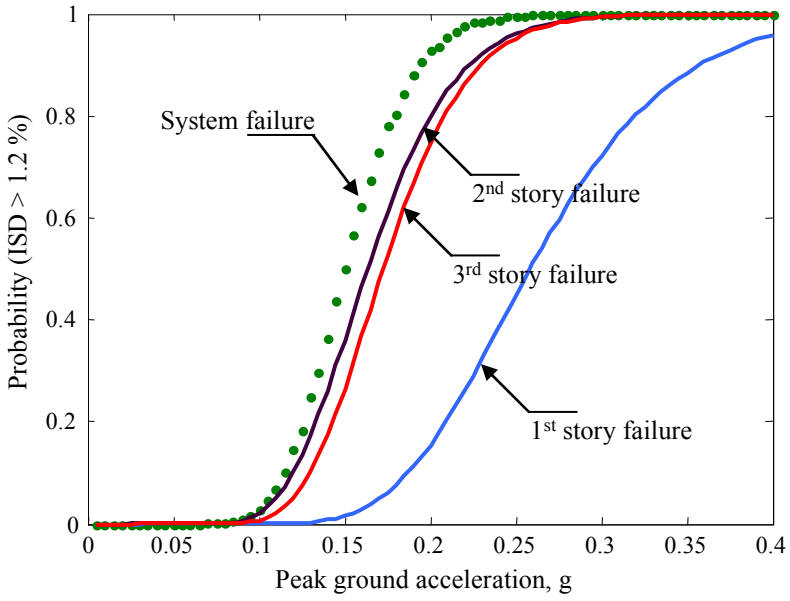

Figure 2.16 Comparison of failure probabilities of components and a system

2.4.8 Comparison of Vulnerability Curves

2.4.8.1 Effects of Derivation Methods

Vulnerability curves derived using the MCS, RSM, and SAC-FEMA methods for ground motion set U-1 are compared in Figure 2.17. The comparison shows that the three methods give practically identical vulnerability curves. When utilizing the MCS, it was difficult to ascertain appropriate steps and range of PGA levels. Therefore, a significant amount of computational time was wasted in calculating the probability of failure close to zero or close to one without getting high-resolution vulnerabilities at sensitive PGA levels.

The number of analyses required for the RSM was much smaller than that for the MCS. To find failure PGA using the RSM, it took 4 to 8 iterations. Therefore, approximately 540 analyses were run to generate response surface (6 iterations, 9 sample points, and 10 ground motions). On the contrary, 100 frames were used for each intensity

level for the MCS. As 10 ground motions and approximately 15 PGA levels are used, at least total 15,000 analyses were required for the MCS. Even if this number may be reduced by using an optimal number of frames that can represent the uncertainties of random variables, the computational cost for the MCS is much larger than that of the RSM. For the SAC-FEMA method, the structural responses from the simulation set for the MCS is used. Therefore, it is difficult to make a direct comparison of computational cost between the MCS and SAC-FEMA approaches. As the SAC-FEMA approach does not require a fixed step of intensity level, which is a necessity for the MCS, and the dispersion is estimated about the median demand curve over the full-intensity range rather than individual-intensity level, it is obvious that the SAC-FEMA method requires fewer simulations than does the MCS. In terms of accuracy of vulnerability curves, those from the MCS are most accurate, because the method does not assume a sweeping, intensity-demand relationship. Nonetheless, the slight improvement in accuracy does not justify the huge computational demands.

The RSM requires scaling of ground motion to achieve a failure surface. In reality, a ground motion with large intensity has different characteristics than ground motion with small intensity. Therefore, finding the failure surface by scaling up and down the ground motion intensity is not acceptable. Furthermore, the response surface generated for a set of ground motions are used to estimate failure probability at every intensity level, which is not logically correct. On the contrary, in the SAC-FEMA approach, ground motions do not need to be scaled, because the dispersion is measured around the median demand curve, which represents the entire range of intensity level. This approach is approximate but most practical. The comparison of vulnerability with an emphasis on accuracy and computational cost lends weight to the use of the SAC-FEMA method.

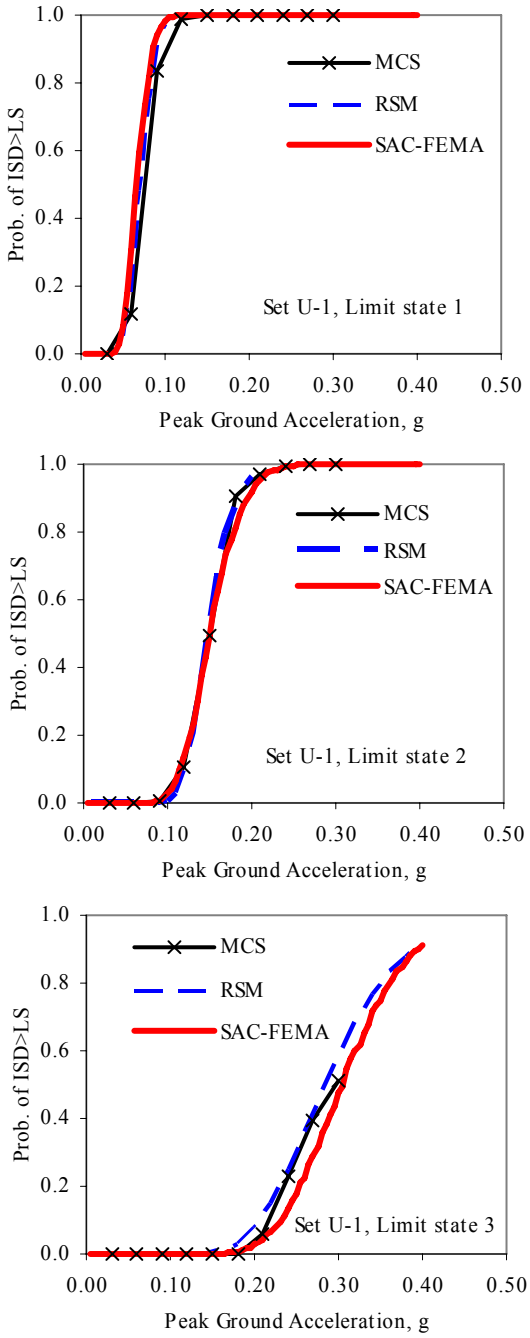

Figure 2.17 Vulnerability curves from MCS, RSM, and SAC-FEMA method

2.4.8.2 Effects of Ground Motion Intensity Measures, PGA and S_a

There are pros and cons in using PGA or S_a as intensity measures of ground motion. If PGA is adopted, it is not necessary to have frequency domain information on ground motion. Vulnerability curves may be applicable to structures with various frequency ranges. The dynamic responses of structures, however, depend largely on the frequency content of imposing excitation. Thus, using PGA as an intensity measure can increase the scatter of the response. If S_a is adopted, the scatter of the structural response decreases. But it is necessary to define several vulnerability curves for various frequency ranges.

Utilizing RSM, vulnerability curves are derived using both PGA and S_a as intensity measures. The spectral acceleration at the fundamental period of the structure, 0.93 sec, is used for scaling with S_a. It is an accepted fact that a set of ground motion cannot be scaled down or up too much, because both the frequency contents and duration are correlated with the intensity of ground motion. In this section, however, vulnerability curves are derived for all limit states for ground motion sets U-1, U-2, and U-3. The purpose of this attempt is to see the effect of different intensity measures on the derived vulnerability curve, not to derive a practically applicable vulnerability curve. Figure 2.18 shows the vulnerability curves derived for spectral and peak ground intensities using RSM. Vulnerability curves derived using the MCS with PGA as an intensity measure for ground motion set AV-1, AV-2, AV-3, L-1, L-2, L-3, U-1, U-2, and U-3 are also compared in Figure 2.19. The vulnerability curves derived for PGA show large differences between ground motion sets, while those derived against S_a are quite similar. The comparison yields the following conclusion.

- If PGA is used as intensity measured, the vulnerability curve significantly depends on input ground motion sets. Therefore, it is important to select ground motion sets that are most suitable in the region for which the vulnerability curves are derived.
- If S_a is used as intensity measure, any moderate number of ground motion sets can be used for the purpose of vulnerability derivation.

The second conclusion, however, may not be applicable to a structural system where higher modes dominantly govern the failure mechanism. In addition, structural periods, hence S_a, are not known for regional vulnerability analysis because the exposed stock typically includes many different structural types with varying characteristics.

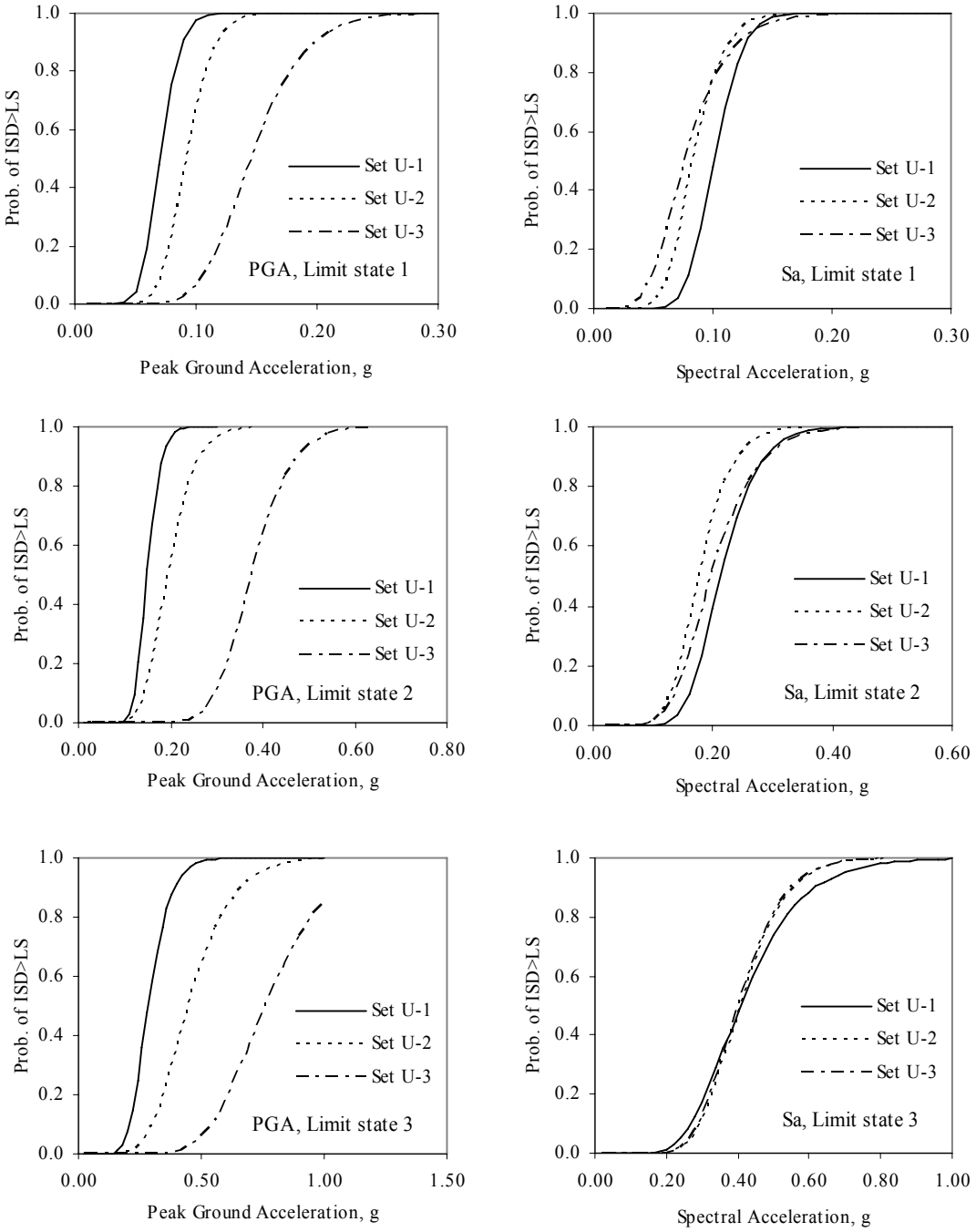

Figure 2.18 Vulnerability curves with intensity measure of PGA and S_a

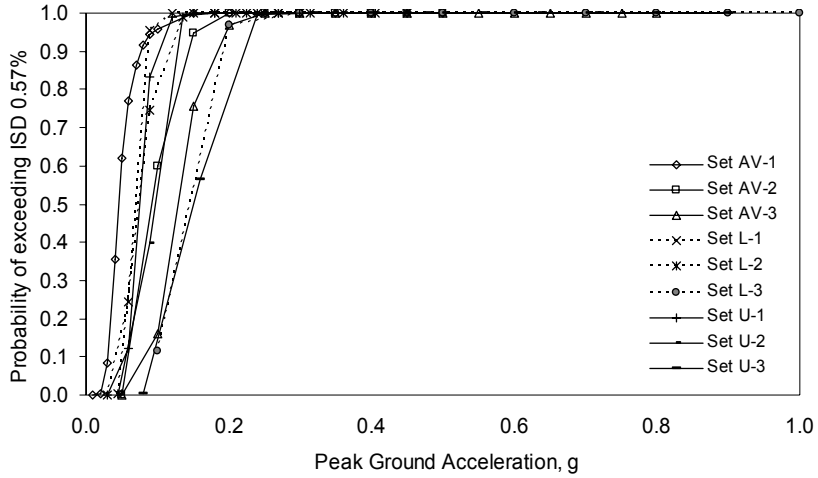

(a) Probability of exceeding ISD 0.57%, limit state 1

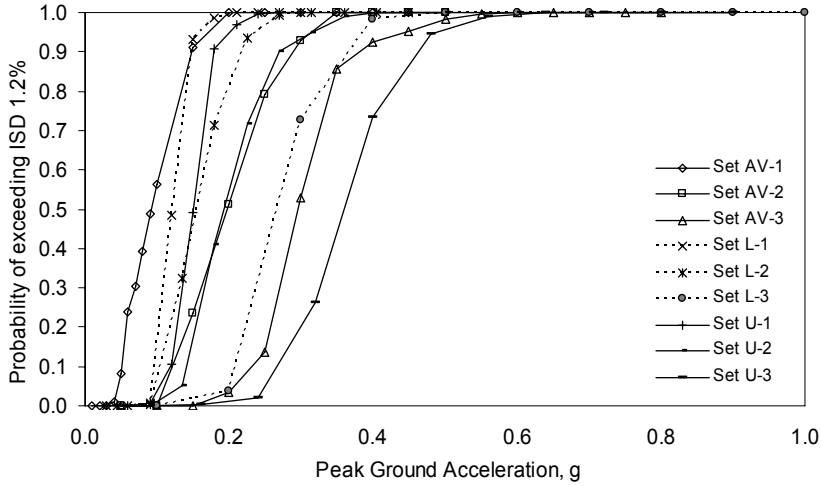

(b) Probability of exceeding ISD 1.2%, limit state 2

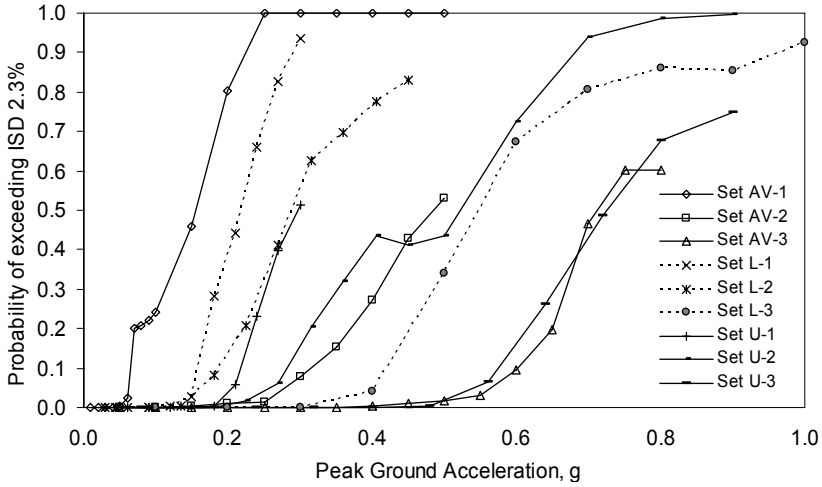

(c) Probability of exceeding ISD 2.3%, limit state 3

Figure 2.19 Vulnerability curves from MCS with intensity measure of PGA

2.4.9 Effects of Ground Motion and Material Uncertainties

The effect of material properties is investigated using analysis results from a/v ratio ground motion sets for which 10 concrete ultimate strengths and 10 steel yield strengths are combined. Also, the result of RSM is studied to examine the sensitivity of the vulnerability from each random variable.

Assuming that ISD_{max} is a function of ground motion sets, concrete ultimate strength, and steel yield strength,

$$ISD_{max} = g(X_1, X_2, X_3) \tag{2.22}$$

where X_1 : ground motion

X_2 : concrete strength

X_3 : steel strength

Mean of ISD_{max} can be evaluated by averaging the result of full simulation, thus using 100 frames, approximately, from the simulation of a single frame using mean material properties.

$$E[ISD_{max}] = E[g(X_1, X_2, X_3)] \approx g(\mu_{X_1}, \mu_{X_2}, \mu_{X_3}) \tag{2.23}$$

Figure 2.20 compares the means of ISD_{max} from the two methods, using 100 frames and using a single frame with mean material property. Up to 0.25 g, the means from the two methods are almost identical. The difference of mean values between two methods increases as the ground motion level increases. Therefore, it is speculated that ISD_{max} becomes more sensitive to material properties at a larger PGA levels than at smaller PGA levels.

Assuming all the uncertain variables, i.e., ground motion, concrete, and steel properties, are statistically independent and also assuming first order approximation, the variance of ISD can be calculated from

$$\mathrm{Var}(ISD_{max}) \approx c_1^2 \mathrm{Var}(X_1) + c_2^2 \mathrm{Var}(X_2) + c_3^2 \mathrm{Var}(X_3) \tag{2.24}$$

where $c_i = \partial(ISD_{max})/\partial X_i$ evaluated at $x_i = \mu_{Xi}$. The c_1 of the first term, which is $\partial(ISD_{max})/\partial X_1$ by definition, is not quantifiable as differentiation of ISD_{max} with ground

acceleration itself is not possible. The c_2 and c_3 values can be calculated numerically in the vicinity of mean values of concrete and steel properties. Variances, Var(X_2) and Var(X_3), are calculated from COV = 0.186, and COV = 0.107, for concrete and steel respectively. Figure 2.21 (a), (b), (d), and (e) shows ISD_{max} against f_c and F_y at small (0.05g) and large (0.35g) PGA level. From Figure 2.21 (a) and (b), it is shown that each ground motion has a different slope, $d(ISD_{max})/d f_c$. This is because the elastic modulus of concrete is affected by the ultimate strength, f_c. Therefore, the structural period is affected by f_c. As a result, the relationship between ISD_{max} and f_c cannot be represented as a general trend, i.e., it is not valid argument to say that higher concrete strength reduces structural response because ISD_{max} and f_c is correlated with spectral displacement, which is random in nature. On the contrary, the ISD_{max} at low PGA levels is rarely affected by the yield strength of steel from Figure 2.21 (d) and (e), as the elastic modulus of steel is constant regardless of yield strength. Figure 2.21 (c) and (f) shows contribution of concrete and steel strengths, which are the second and third terms of Equation (2.21), on the variance of ISD_{max}. In these figures, the first term of Equation (2.21) is zero because the plots are drawn for each ground motion, i.e., the input is deterministic. The contribution of concrete to the variance of ISD_{max} is generally larger than that of steel because the former affects stiffness, and, therefore, period and amplification characteristics.

In Section 2.2.3, RSM utilized FORM analysis to calculate the probability of reaching a certain limit state. The limit state function, Equation (2.13), can be redefined in terms of ground motion intensity at failure, Equation (2.18) as follows:

$$g\left(f_c, F_y, \bar{\varepsilon}\right) = S_{af}\left(f_c, F_y, \bar{\varepsilon}\right) - S_a \tag{2.25}$$

where three random variables are involved in the limit state function. After the FORM analysis, the sensitivity of each random variable, α, on the reliability index can be estimated. Figure 2.22 shows the sensitivity of ground motion, concrete, and steel uncertainty on the vulnerability. For serviceability limit states, i.e., ISD < 0.57%, the sensitivity of concrete is high at very low PGA levels. The sensitivity of steel is very low at low intensity, as steel does not yield. In all cases, it is observed that the sensitivity of

ground motion dominates after the probability of reaching limit ISD starts increasing from zero. This observation is verified through SDOF system analysis as shown in Figure 2.23, where the spectral displacement is plotted against period and ductility. The period range, from 0.85 to 0.95 sec, corresponds to the period of the prototype structure with concrete ultimate strength of mean ±one standard deviation. This range covers most of the possible concrete strength variation. Because steel yield has practically no effect on the structural period, the period axis represents variability in concrete only. The ultimate strength of concrete and yield strength of steel affect the ductility of structures for a given ground motion level. Because the ductility cannot be estimated without analysis, a ductility range from 1 to 2 is plotted for comparison purposes. For the three ground motion sets, U-1, U-2, and U-3, the mean spectral displacement is calculated after normalizing the ground motion to a PGA of 1g. Figure 2.23 clearly shows that the structural response parameters are significantly affected by the input motion set, while the effect of material variability is rather insignificant.

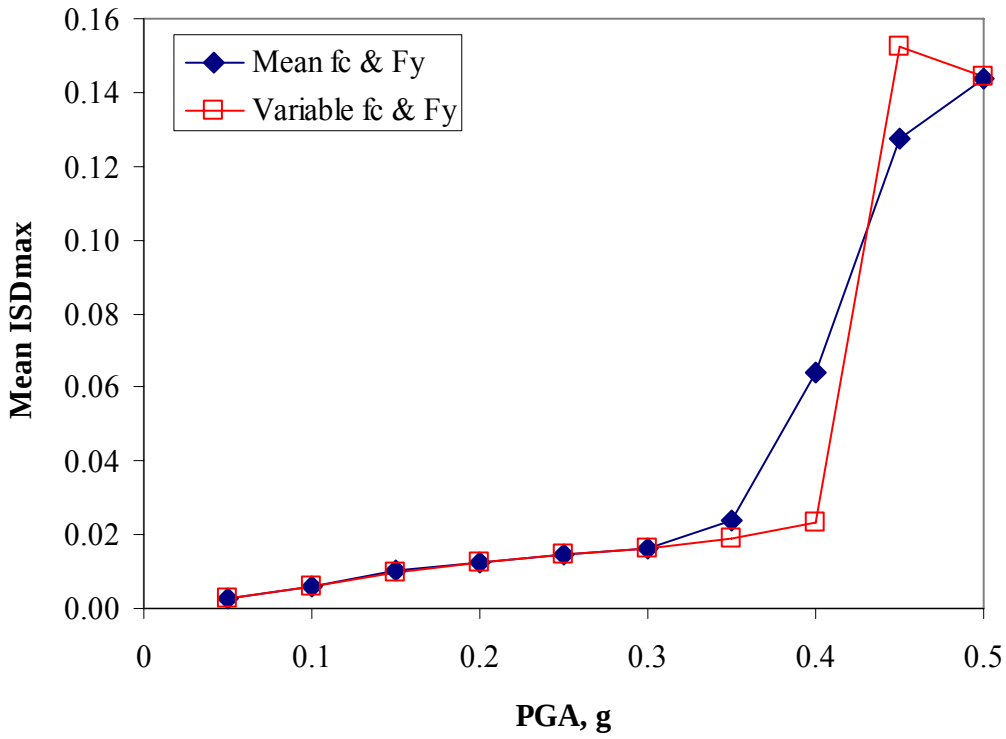

Figure 2.20 Mean ISD_{max} from mean material properties and full simulation

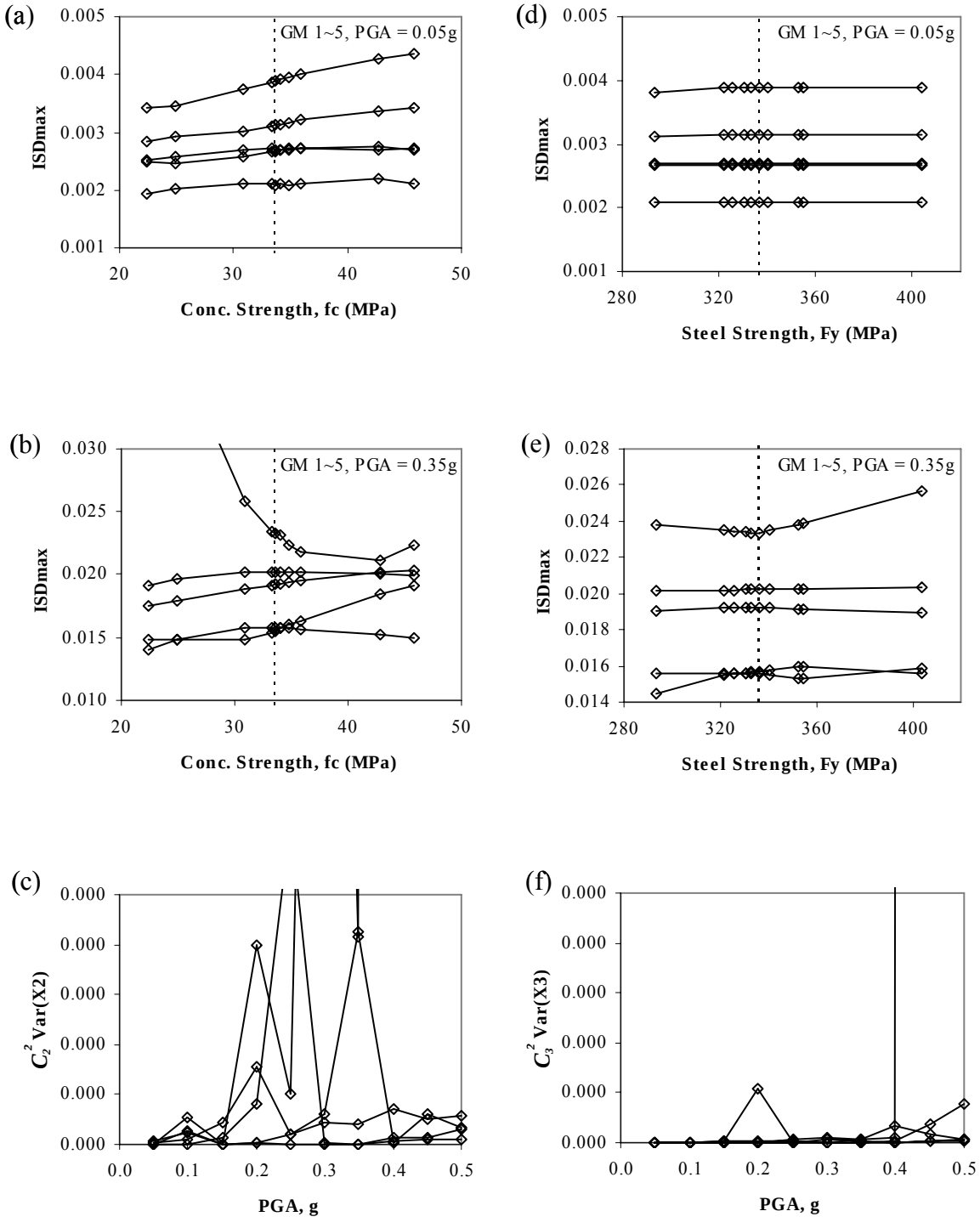

Figure 2.21 Effect of material strength on ISD_{max}

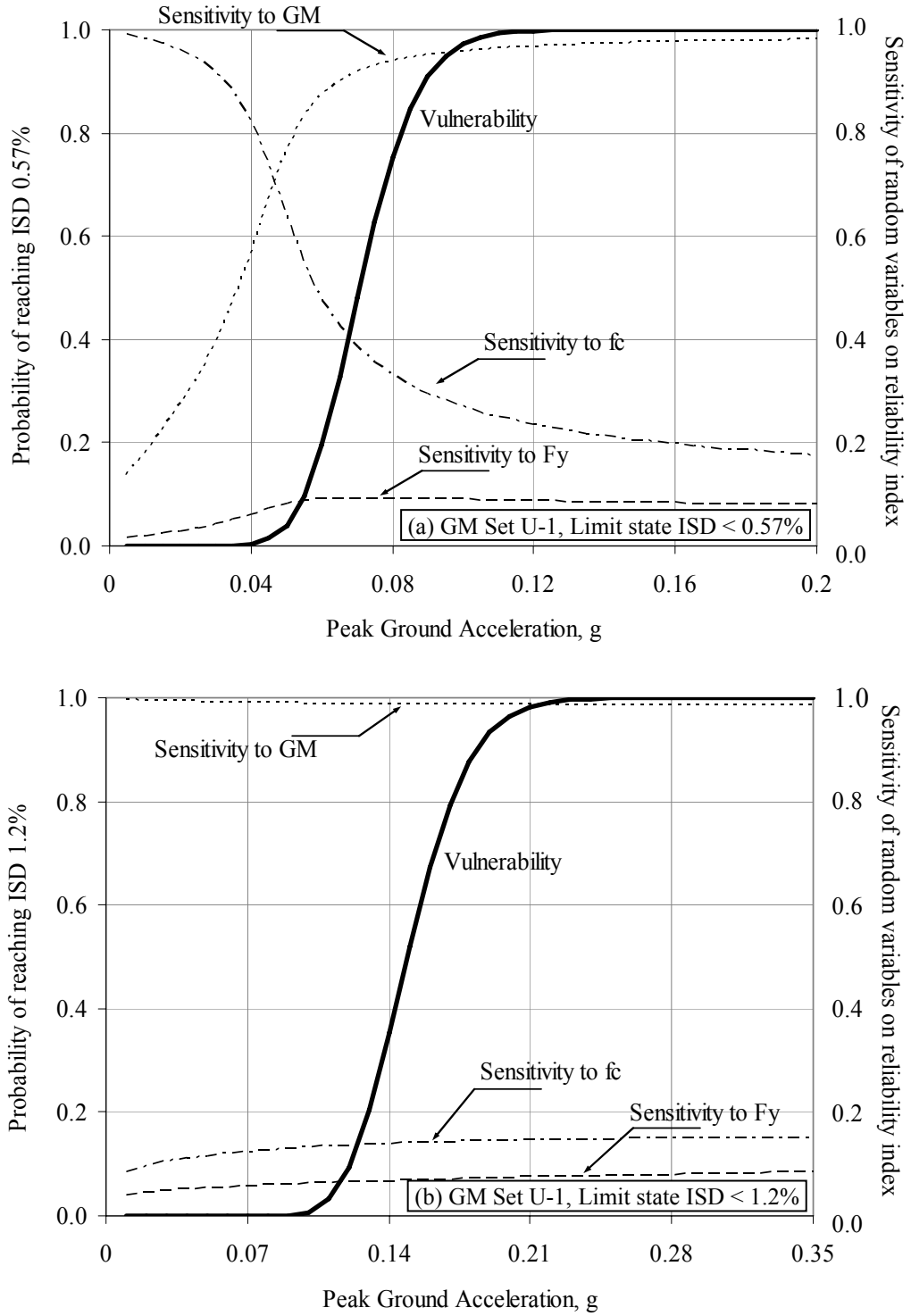

Figure 2.22 Sensitivity of random variables on vulnerability curves
(continued on next page)

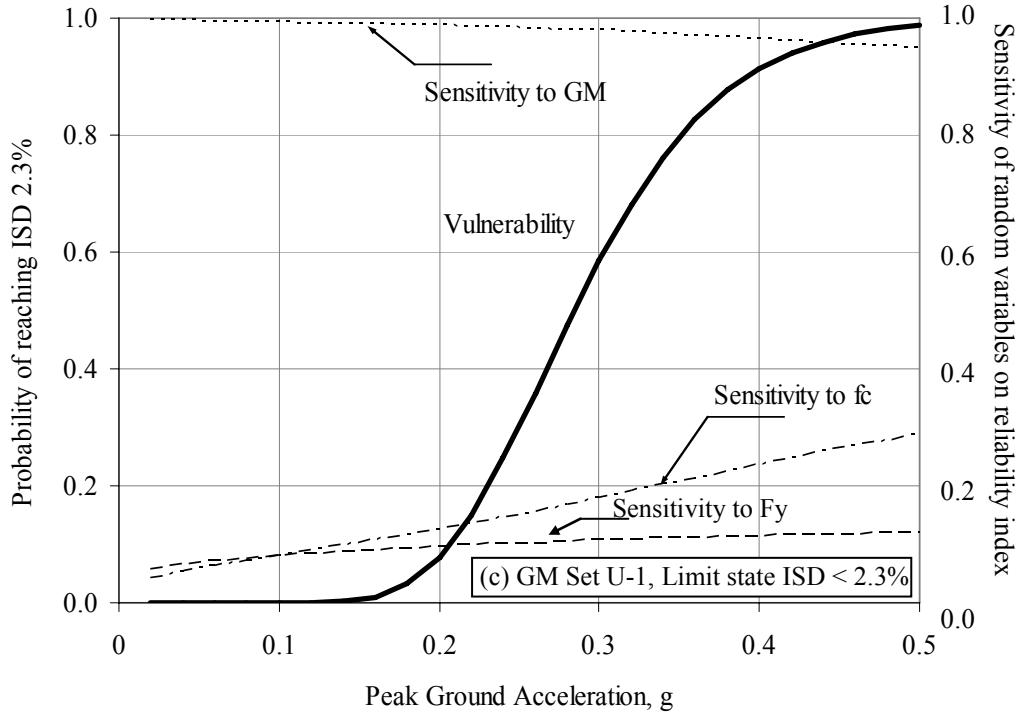

Figure 2.22 Cont. Sensitivity of random variables on vulnerability curves

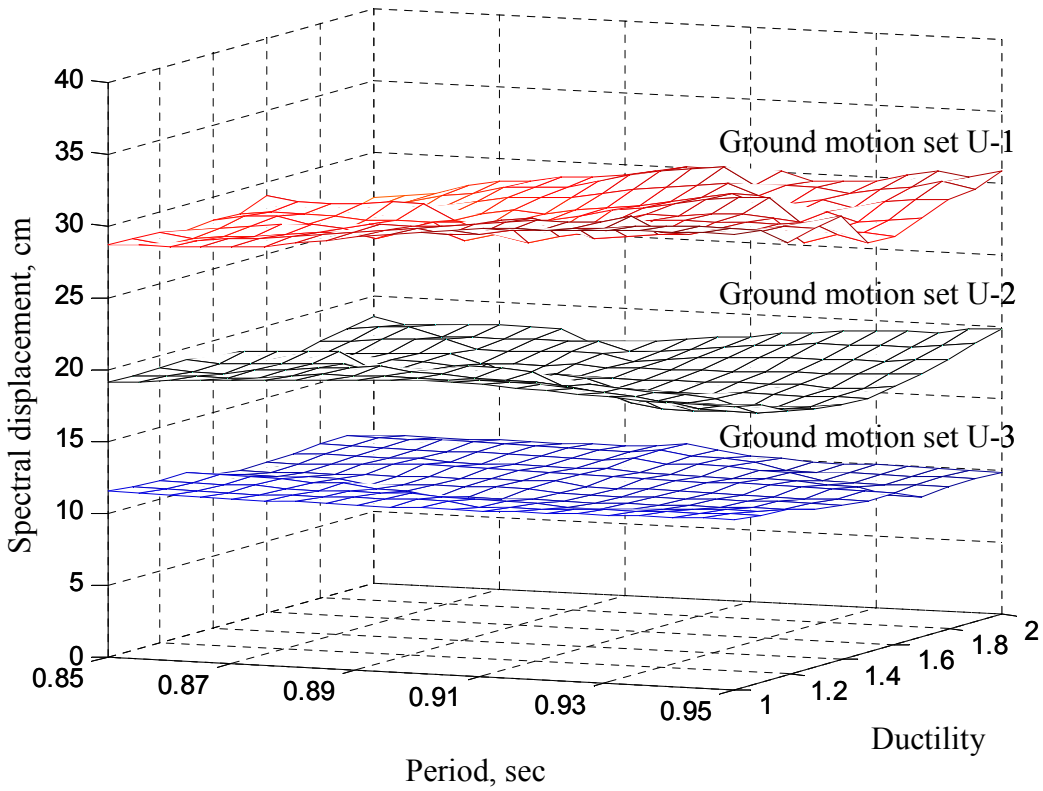

Figure 2.23 Response surface of spectral displacement against period and ductility

2.4.10 Summary and Discussions

In the course of the benchmark study of the three-story OMRCF, several aspects of vulnerability analysis are investigated. While most previous studies on vulnerability analysis were based on simplified approaches, this study is conducted with the least level of assumptions, using fiber-model inelastic dynamic analysis, and applying both MCS and RSM. The following are findings from the benchmark study of the three-story OMRCF.

- Selected ground motion sets mainly affect the derived vulnerability curves when PGA is used as an intensity measure. Thus, scrupulous consideration is required when ground motions are selected for vulnerability analysis.
- When S_a is used as an intensity measure, the variability of the derived vulnerability curves dropped dramatically. Spectral acceleration, S_a, however, is not suitable for the population of structure and structures with dominant higher modes.
- The concrete ultimate strength affects the structural response from small ground motion level because the concrete elastic modulus is related to the ultimate strength.
- At high ground motion levels, material properties contribute to the variability in structural response, but the variability is much smaller than that due to ground motion variability.
- Through the comparison of dynamic analysis with shaking-table experimental results at various ground motion levels, it is concluded that using the same level of damping for elastic and inelastic ranges may result in unconservative results.
- Rather than adopting limit states from the published literature, the limit states of the prototype structure are defined through static pushover analysis. For the selected structure, the limit states for serviceability, damage control, and collapse prevention are 0.57%, 1.2%, and 2.3% of interstory drift.

The findings as well as the application development for this study will be the basis for the vulnerability analysis of the soil-structure-interaction system.

CHAPTER 3

METHODS FOR SOIL-STRUCTURE-INTERACTION ANALYSIS

Geotechnical and structural engineering coexist as major activities in the construction of infrastructure. In conventional construction projects, geotechnical engineers investigate a construction site, and ensuing results are used by structural engineers to design structural systems, including foundations. For a structure subjected to gravity loads only, the effects of soil and foundation are considered in a superficial manner unless settlement from consolidation of soil or foundation failure is critical. The problem becomes complicated for a structure subjected to earthquake loading, where the interaction between soil-foundation and structural systems cannot be ignored. There are many empirical approaches to approximate the soil and foundations as lumped springs. These methods are the simplest for relatively approximate solution for SSI in cases of simple configurations. Extrapolations of the empirical methods to complex foundation systems with many battered piles in many layers of different soil types are fraught with problems. In addition, applications that are developed for structural analysis usually do not include functionality to model geotechnical environment. In this chapter, a brief review of conventional methods for soil-structure interaction analysis is introduced, followed by a multiplatform approach suitable for detailed soil-structure interaction simulation.

3.1 Conventional Methods for Soil-Structure-Interaction Analysis

Literature abounds with methods for practical consideration of soil and foundation systems. The approaches employed in these methods vary widely in complexity and applicability. For instance, mat foundations are often approximated with lumped springs, with the assumption that the foundation is supported on homogeneous, elastic, semiinfinite medium (Gazetas, 1991; Wolf, 1997). The application of these methods to real structure requires careful determination of equivalent elastic soil properties. Pile foundations are often approximated as beams on Winkler type springs, in which the configuration of dampers and springs varies among researchers. Hysteretic behaviors of

the springs are mostly developed from empirical data. Furthermore, behaviors of pile groups are extrapolated from a response of single pile by using group coefficients. The soil and structure interaction is an important issue not only in these typical foundation types but also embankment and abutment systems and retaining-wall structures. One of the most direct approaches is the FE method, which allows the modeling of complex structural configurations with fewer assumptions than other methods. The key influential factor for the FE approach is the soil material model, which is often complicated and whose parameters cannot be well defined. In the following sections, some of the representative approaches for soil, foundation, and structural models are introduced.

3.1.1 Direct Approach

The effects of soil structure interaction can be largely divided into kinematic and inertial interaction. Large stiff foundations impede the propagation of wave around the foundation. Therefore, the foundation input motion differs from the free field motion. In addition, the response of foundation from structural vibration deforms soil, which damp out structural response due to hysteretic energy dissipation. These interactions resulting from relatively large stiff foundations are referred as kinematic interaction. Similarly, a large mass of structures interacts with a mass of soil medium. For instance, if it is assumed that a massless structure is on top of the soil, the surface response will not be largely different from the free field motion, assuming that the foundation does not impede wave propagation. If the mass of the structure is significant, however, the surface motion of the soil column will be significantly different from the free field motion. The inertial and kinematic interactions are coupled because structures without stiffness cannot interact with soil even if the mass of the structure is significant.

The direct approach for SSI analysis accounts for inertial and kinematic interactions simultaneously, where the entire soil-structure system is modeled as a single FE model. The response of the system is solving equation of motion of the whole system:

$$[\mathbf{M}]\{\ddot{\mathbf{u}}\} + [\mathbf{K}]\{\mathbf{u}\} = -[\mathbf{M}]\{\ddot{\mathbf{u}}_{ff}\} \tag{3.1}$$

where [**M**] and [**K**] represent the mass matrix and stiffness matrix of the soil-foundation-structure system. In this approach, ground accelerations at the bottom of soil domain are applied as input motion. It is also possible to apply acceleration at one boundary with various angles and simulate wave propagation from one end of the soil domain to the other end with consideration of soil-structure interaction. This approach requires fewer approximations in terms of modeling boundaries of foundations than those required for approximate methods where only a limited volume of soil domain is modeled. The boundary of a large soil domain can be modeled with energy absorbing elements to simulate infinite soil medium beyond the soil domain. Due to the large scale of the model, however, the boundary condition of the entire system requires approximations. In addition, the FE package for this approach should be able to model structures and soil with equal rigor (Kramer, 1996). Presently, there have been few attempts of this approach, such as Humboldt Bay Bridge Project (Yang et al., 2003b), as shown in Figure 3.1, due to extremely high computational cost. The main objective for this type of analysis can be a global soil-structure interaction rather than a detailed response analysis of structures, due to expensive computational cost.

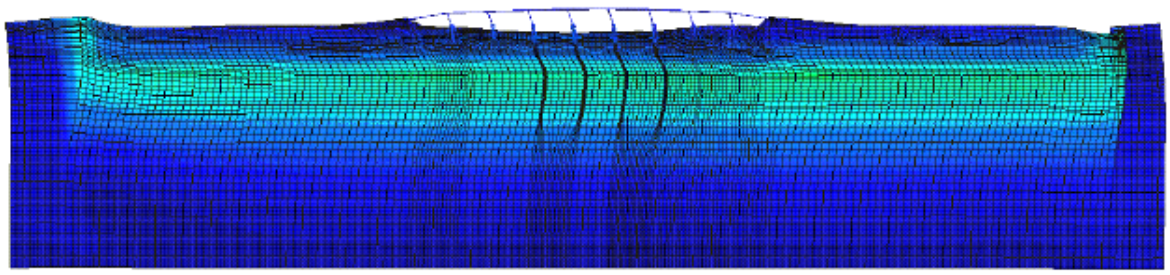

Figure 3.1 Example of direct SSI analysis approach
(Yang et al., 2003b)

3.1.2 Multistep Method

In the multistep method, the analysis of soil-structure system is undertaken in two steps: kinematic interaction and inertial interaction analysis. During kinematic interaction analysis, a structure is assumed to have stiffness without mass. The analysis of this massless structure with soil domain results in the input motion at the base of structure.

$$\left[\mathbf{M}_{\mathbf{soil}}\right]\left\{\ddot{\mathbf{u}}_{\mathbf{KI}}\right\}+\left[\mathbf{K}\right]\left\{\mathbf{u}_{\mathbf{KI}}\right\}=-\left[\mathbf{M}_{\mathbf{soil}}\right]\left\{\ddot{\mathbf{u}}_{b}\right\} \tag{3.2}$$

where $[\mathbf{M}_{\text{soil}}]$ is a mass matrix of soil domain, $[\mathbf{K}]$ is a stiffness matrix of soil and structure, $\{\ddot{\mathbf{u}}_{\mathbf{KI}}\}$ is response from kinematic interaction, and $\{\ddot{\mathbf{u}}_{b}\}$ input excitation at soil base. The inertial interaction analysis includes mass of soil and structure. The inertial forces from the acceleration of kinematic interaction and base motion are applied only to structural masses.

$$\left[\mathbf{M}\right]\left\{\ddot{\mathbf{u}}_{\mathbf{II}}\right\}+\left[\mathbf{K}\right]\left\{\mathbf{u}_{\mathbf{II}}\right\}=-\left[\mathbf{M}_{\mathbf{structure}}\right]\left\{\ddot{\mathbf{u}}_{\mathbf{KI}}+\ddot{\mathbf{u}}_{b}\right\} \tag{3.3}$$

where $[\mathbf{M}]$ is a mass matrix of soil domain and a structure, $[\mathbf{M}_{\text{structure}}]$ is mass matrix of structure, and $\{\ddot{\mathbf{u}}_{\text{II}}\}$ is response from inertial interaction. The overall response from these two-step analyses is identical to the response from direct approach.

$$\left\{\mathbf{u}\right\}=\left\{\mathbf{u}_{\mathbf{KI}}\right\}+\left\{\mathbf{u}_{\mathbf{II}}\right\} \tag{3.4}$$

For a detailed derivation, reference is made to Kramer (1996). This multistep approach is theoretically correct but has limited application. To superimpose the responses from kinematic and inertial interaction, the soil medium should be linear elastic, which is not the case in real problems. In addition, the inertial interaction analysis requires mass and stiffness of the entire soil-structure system. The modeling efforts and computational costs are almost same as those required for the direct approach in Section 3.1.1. The multistep approach is advantageous if the foundation is rigid, for which the soil system can be approximated as a set of equivalent springs (Kramer, 1996). These equivalent lumped springs will be briefly introduced in Section 3.1.4.

3.1.3 Applicability of Approximate Methods

The rigorous approach for SSI analysis requires large modeling efforts and computational power. The direct approaches which can simultaneously consider wave propagation as well as soil-structure interaction do not guarantee a better solution due to uncertainties and approximations in subsurface conditions. In the multistep approach, the kinematic interaction analysis requires at least a two-dimensional wave propagation analysis, and inertial interaction analysis requires the entire model of the soil-structure system. Due to large computational and modeling efforts, in practice, surface motions are applied to structures with flexible foundations.

$$\left[\mathbf{M}_{\text{structure}}\right]\{\ddot{\mathbf{u}}\}+\left[\mathbf{K}_{\text{soil}}+\mathbf{K}_{\text{structure}}\right]\{\mathbf{u}\}=-\left[\mathbf{M}_{\text{structure}}\right]\{\ddot{\mathbf{u}}_b\} \tag{3.5}$$

In this approach, the foundation is usually modeled as a set of lumped springs or more sophisticated FE models. The flexible foundation can account for hysteretic energy dissipation and structural period elongation. But in this approach, the inertial interaction between soil and structural systems cannot be modeled.

The effect of this approximate approach can be investigated using transfer functions, which is defined as the ratio of output motion amplitudes to input motion amplitudes in frequency domain. The transfer functions can be easily estimated as closed form solutions for one-dimensional continuum, which is only applicable to soil columns. For a soil and structure system in a three-dimension with arbitrary configuration, a discrete numerical approach can be used to estimate transfer functions. The equation of motion of soil-structure system, Equation 3.6, can be uncoupled with fundamental modes by using modal vector, Equation 3.7. The decoupling results in a series of single degree of freedom (SDOF) equations, as shown in Equation 3.8.

$$[\mathbf{M}]\{\ddot{\mathbf{u}}\}+[\mathbf{K}]\{\mathbf{u}\}=-A_g(t)[\mathbf{M}]\boldsymbol{l} \tag{3.6}$$

$$[\boldsymbol{\Phi}]^T[\mathbf{M}][\boldsymbol{\Phi}]\{\ddot{\mathbf{q}}\}+[\boldsymbol{\Phi}]^T[\mathbf{K}][\boldsymbol{\Phi}]\{\mathbf{q}\}=-A_g(t)[\boldsymbol{\Phi}]^T[\mathbf{M}]\boldsymbol{l} \tag{3.7}$$

$$m_i\ddot{q}_i+c_i\dot{q}_i+k_iq_i=-A_g(t)f_i,\quad i=1,2,\ldots,n \tag{3.8}$$

where $\mathbf{M}$: mass matrix of full soil-structure domain

$\mathbf{K}$: stiffness matrix of full soil-structure domain

$\boldsymbol{\Phi}$: Eigen matrix

q_i : modal response of i^{th} mode

i : mode number

c_i : damping coefficient of i^{th} mode

$A_g(t) = Q_0 \sin(\bar{\omega}t)$: input motion

f_i : i^{th} element of $[\mathbf{\Phi}]^T[\mathbf{M}]\boldsymbol{l}$

From fundamental structural dynamics, the closed form solution for the input to output ratio of the i^{th} mode is

$$A_i = \frac{-Q_0 f_i / k_i}{\sqrt{(1-\beta_i^2)^2 + (2\xi_i\beta_i)^2}} \tag{3.9}$$

where β_i is ratio of excitation frequency to modal frequency, $\bar{\omega}/\omega_i$. Relative displacement of i^{th} mode at Degree of Freedom (DOF) j becomes

$$u_{j,i} = \phi_{ji} A_i = \phi_{ji} \frac{-Q_0 f_i / k_i}{(1-\beta_i^2)^2 + (2\xi_i\beta_i)^2} \cdot \left[(1-\beta^2)\sin\bar{\omega}t - 2\xi\beta\cos\bar{\omega}t \right] \tag{3.10}$$

Superposing modal response at DOF j result in

$$u_{j,tot} = \max\left(u_{base} + \sum_{i=1}^{n} u_{j,i} \right) = \max\left(-Q_0/\bar{\omega}^2 \sin(\bar{\omega}t) + \sum_{i=1}^{n} \phi_{ji} A_i \right) \tag{3.11}$$

where u_{base} is the amplitude of input motion as below.

$$u_{base} = -Q_0/\bar{\omega}^2 \tag{3.12}$$

The transfer function of total displacement of DOF j becomes

$$F(\bar{\omega}) = \frac{u_{base} + u_{j,tot}}{u_{base}} \tag{3.13}$$

To investigate the effect of soil-structure interaction on the input motion of a structure, a simplified soil-structure system is modeled in Figure 3.2. Transfer function is defined as the ratio of input motion amplitude at the base of soil domain to the amplitudes at various surface points (A, B, C, and D). The following properties are assumed for soil and structures.

<u>*Soil*</u> Assume elastic soft soil deposit on rigid bedrock

Shear modulus G = 13000 kPa

Poisson's ratio v = 0.4

Density $\rho = 1.3$ ton/m^3

Depth 30 m

Fundamental period of soil domain

$$T_n = \frac{4H}{v_s(1+2n)} = 1.2,\ 0.4,\ 0.24, 0.171,\ \text{... sec}$$

Structure Assume simplified 3x3 bay, three-story building

Foundation Rigid mat foundation (15 m x15 m)

Total mass (17.8 ton × 12 × 4) × 0.8 = 680 ton

where 0.8 of 1st modal participation is assumed.

2000 and 5000 ton are also tried for parametric study

1st mode period 0.9 sec

FE model

Element: 8-node brick elements

Boundary condition:

Internal nodes: All DOFs are restrained except x-directional DOFs.

Support nodes: All DOFs are restrained.

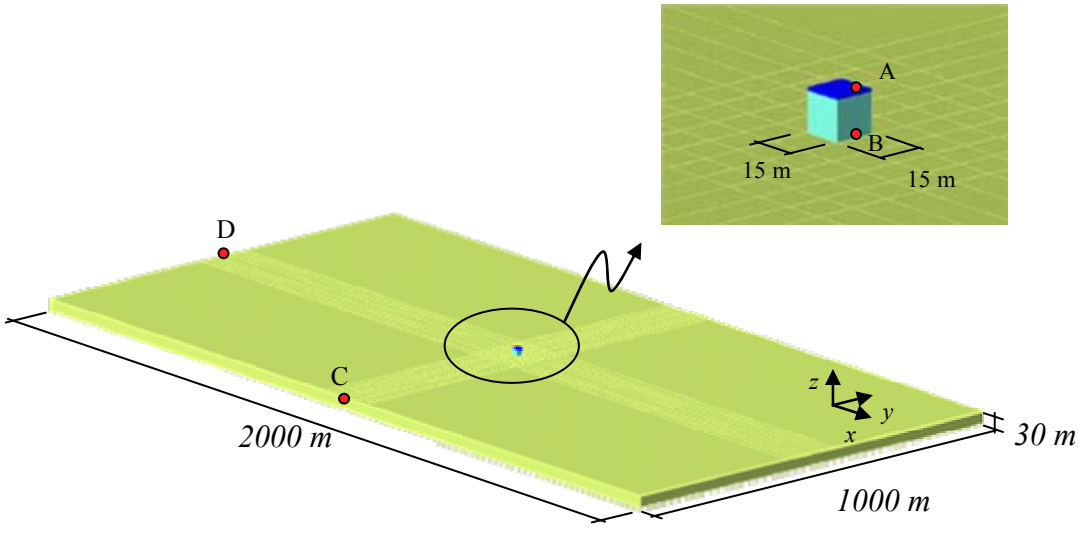

Figure 3.2 Idealized full soil-structure system

The transfer functions estimated with Equation (3.13) is presented in Figure 3.3. Figure 3.3 (1) shows the transfer functions when the structural mass is 680 tons, which is equivalent to the modal mass of the 1st mode of the 3x3-bay concrete frame structure. The transfer function at the bottom of the structure (point B in Figure 3.2) is similar to the transfer functions of the free field. For parametric study, the structural mass is increased to 2000 and 8000 tons with same structural period, as shown in Figure 3.3 (2) and (3). With increased structural mass, the transfer functions at the bottom of the structure deviate from the transfer functions of the free field, while the transfer functions at the points far from structure (points C and D) remain similar to that at the free field. This comparison qualitatively illustrates the effect of a massive structure on the foundation input ground motion.

In many practical approaches, surface motion is used as input motion and soil is accounted for only as a flexible foundation considering kinematic interaction, as shown in Figure 3.4. To estimate the effect of this approximation, the transfer function of the relative structural displacement is compared in Figure 3.5 for structural mass of 680, 2000, and 8000 tons. The full SSI in Figure 3.5 refers to the transfer function from the modeling of a full soil-structure system shown in Figure 3.2. The transfer function of kinematic SSI system refers to the system in Figure 3.4. The transfer function of fixed support is estimated by multiplying the transfer function of soil column to the transfer function of structure itself with fixed support. Figure 3.5 shows that the structural response from the approximate approach considering only the kinematic SSI is close to that of full SSI, even though the difference increases as structural mass increases.

The comparisons in this study show that using surface motion and modeling the soil and foundation as a flexible base is an approximate but reasonable approach. This analysis result shows only elastic response. In the inelastic soil domain, modeling surrounding soil with inelastic material model will be a reasonable approximation of SSI in comparison with fixed-base system, unless the structure is extremely massive in comparison to the soil. The study in Sections 4 and 5 uses this approach rather than modeling the full soil-structure domain including soil mass.

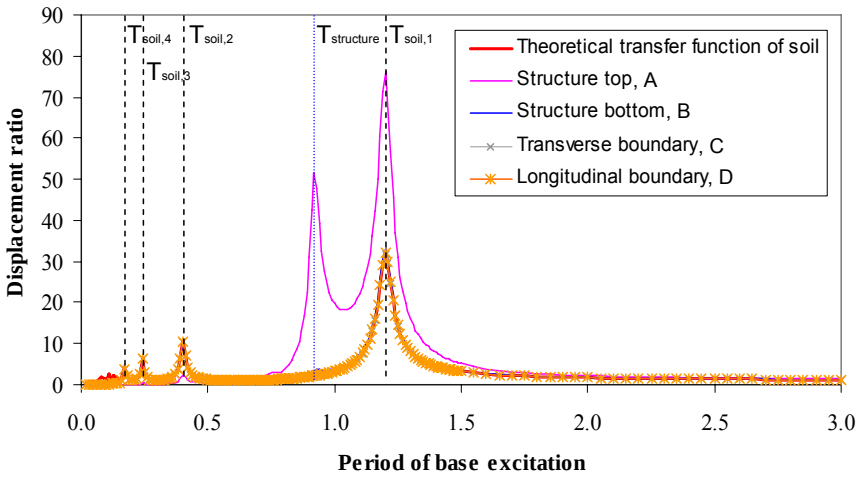

(1) Transfer function when structural mass is 680 ton

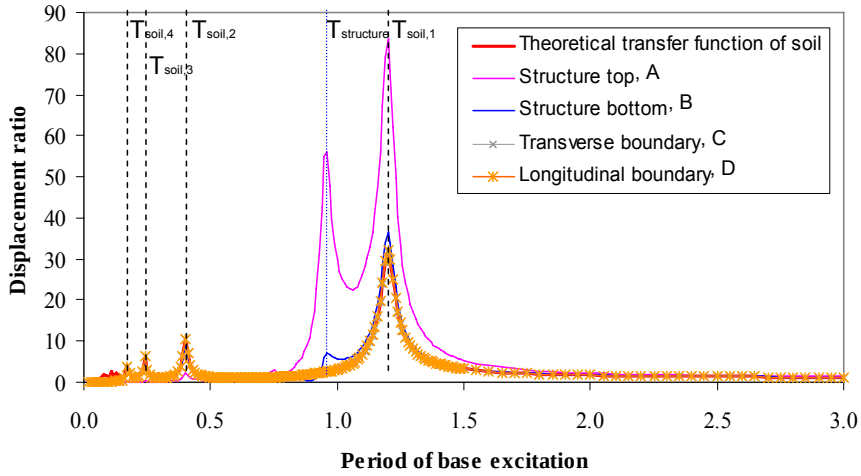

(2) Transfer function when structural mass is 2000 ton

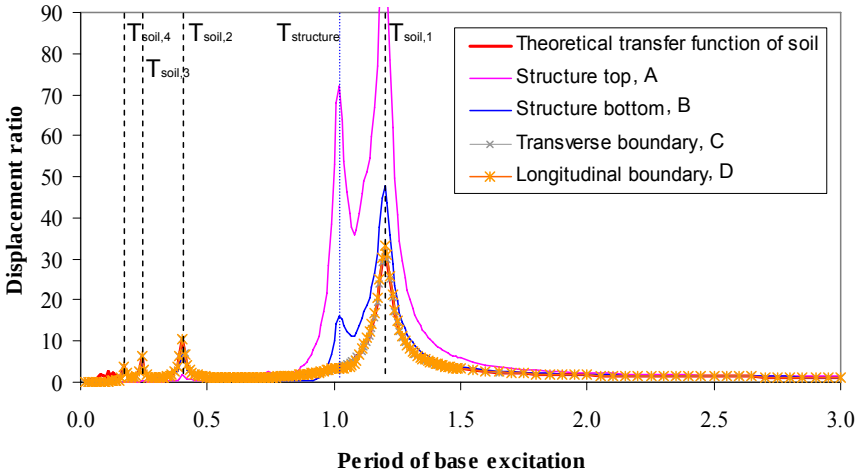

(3) Transfer function when structural mass is 8000 ton

Figure 3.3 Transfer functions of the idealized full Soil-Structure System

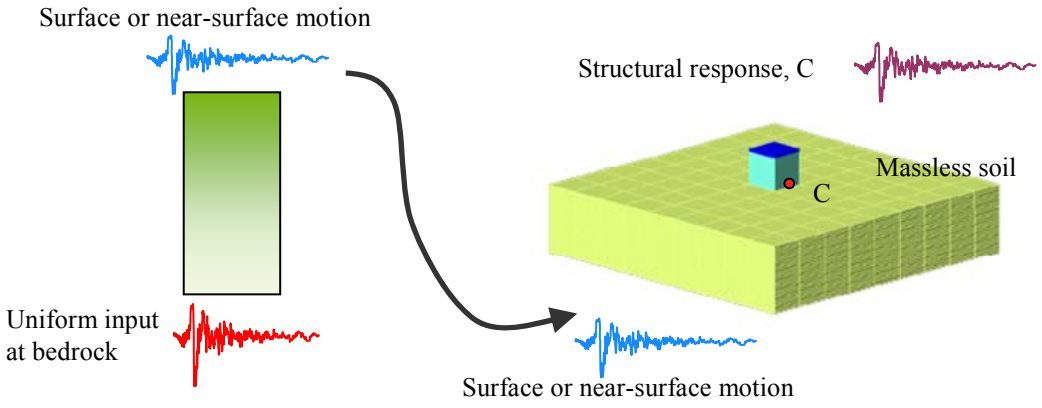

Figure 3.4 Practical SSI model with kinematic interaction

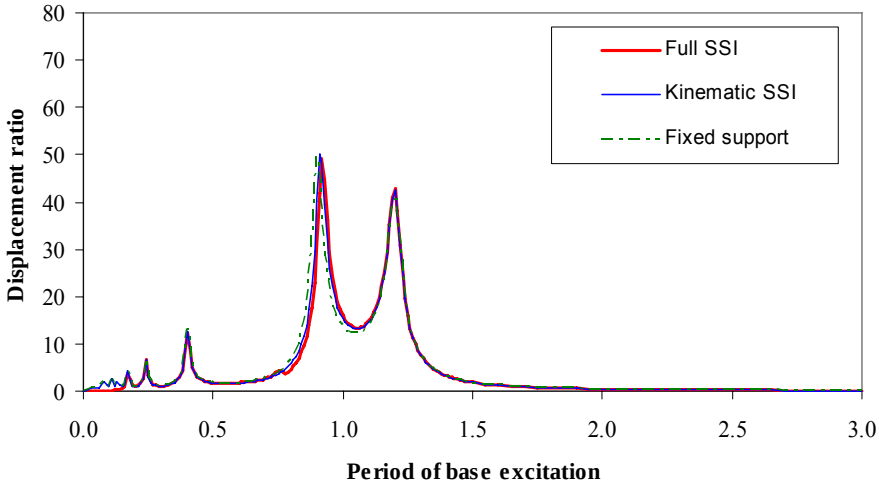

(1) Transfer function when structural mass is 680 ton

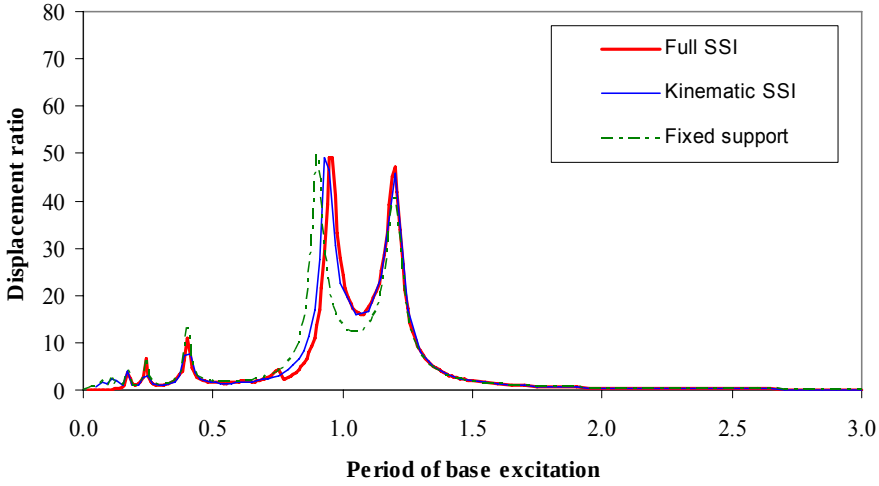

(2) Transfer function when structural mass is 2000 ton

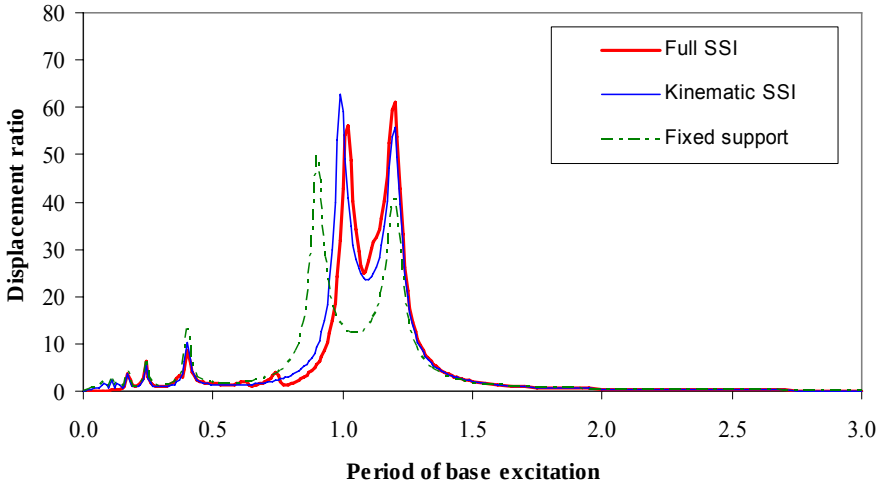

(3) Transfer function when structural mass is 8000 ton

Figure 3.5 Transfer functions of relative structural displacement

3.1.4 Lumped Spring Models for Mat Foundation

Lumped spring and dashpot models for mat foundations have been developed by many researchers. Newmark and Rosenblueth (1971) summarized the lumped spring and dashpot representation of disk on elastic medium. Wolf (1997) proposed a truncated cone model and spring-dashpot-mass model with/without internal degree of freedom. Gazetas (1991) proposed a lumped spring and dashpot damping model for irregular shaped foundations, where the damping elements consist of hysteretic and radiational damping components. All of these approaches assume that soil is an elastic semiinfinite medium, that the effect of soil is represented by lumped springs, dashpots, and effective masses, and that the foundation is rigid and massless. The spring and damping properties are represented as frequency-dependent variables, as shown in Table 3.1 and Figure 3.6. These elements can be easily modeled in structural analysis platforms, as most platforms include springs and dashpots. Unfortunately, there are many limitations in adopting these properties in structural analysis:

- Most spring and dashpot properties are proposed in frequency domain. But almost all nonlinear analyses of structures are conducted in time domain. Hence, the values of spring and dashpot at specific frequency should be selected.
- The studies on lumped spring and dashpot properties are based on the assumption that soil is a homogeneous, semiinfinite elastic medium. None of the assumptions are close to reality. The modulus of soil highly depends on the shear strain from ground shaking (far field) as well as from structural movement (near field). The selection of equivalent shear modulus and approximation of soil spring involves large uncertainties.

Recent studies by Cremer et al. (2002) allowed modeling of soil with hysteretic and radiational damping in structural analysis applications. However, the approach requires implementation of a new element within a structural analysis package, which is not readily possible unless the source code of the application is accessible. However, the soil, mat foundation, and structural system can be fully modeled in an FE analysis package as long as reliable soil material models are available. This approach is most attractive in nonlinear structural analysis.

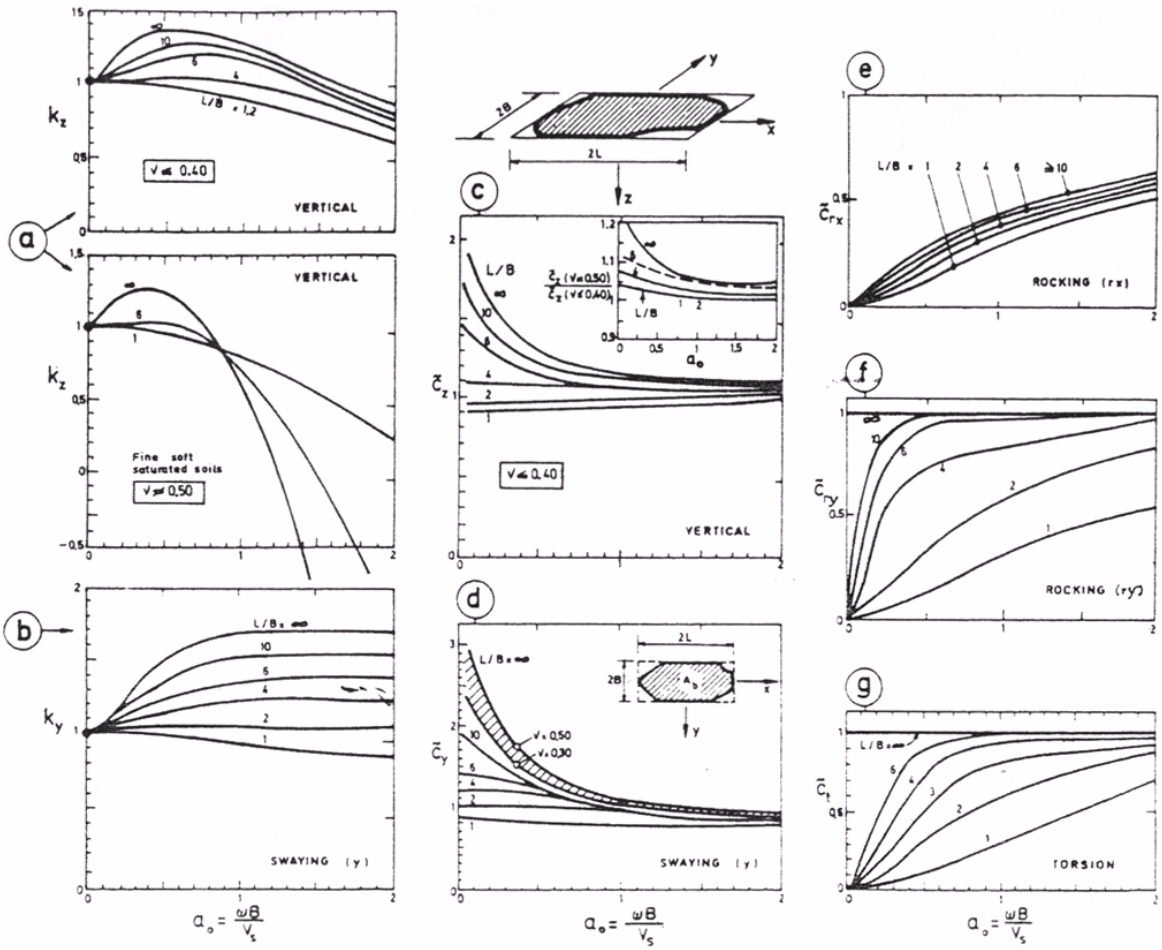

Figure 3.6 Dynamic stiffness and damping coefficients of surface foundations (after Gazetas, 1991)

Table 3.1 Surface stiffness of a rigid plate on elastic medium

	Static stiffness, K	Radiation dashpot coefficient, C
Vertical (z)	$K_z = \frac{2GL}{1-\nu}\left(0.73+1.54\left(\frac{A_b}{4L^2}\right)^{0.75}\right)$	$C_z = \left(\rho V_{La} A_b\right)\cdot \tilde{c}_z$
Horizontal (y) Lateral	$K_y = \frac{2GL}{1-\nu}\left(2.00+2.50\left(\frac{A_b}{4L^2}\right)^{0.85}\right)$	$C_y = \left(\rho V_s A_b\right)\cdot \tilde{c}_y$
Horizontal (x) longitudinal	$K_x = K_y - \frac{0.2GL}{0.75-\nu}\left(1-\frac{B}{L}\right)$	$C_x = \rho V_s A_b$
Rocking (rx) about x-axis	$K_{rx} = \frac{GI_{bx}^{0.75}}{1-\nu}\left(\frac{L}{B}\right)^{0.25}\left(2.4+0.5\frac{B}{L}\right)$	$C_{rx} = \left(\rho V_{La} I_{bx}\right)\cdot \tilde{c}_{rx}$
Rocking (ry) about y-axis	$K_{ry} = \frac{3G}{1-\nu} I_{by}^{0.75}\left(\frac{L}{B}\right)^{0.15}$	$C_{ry} = \left(\rho V_{La} I_{by}\right)\cdot \tilde{c}_{ry}$
Torsion	$K_t = 3.5GI_{bz}^{0.75}\left(\frac{B}{L}\right)^{0.4}\left(\frac{I_{bz}}{B^4}\right)^{0.2}$	$C_t = \left(\rho V_s I_{bz}\right)\cdot \tilde{c}_t$

Note: Table from Gazetas (1991)

1. Total damping $C = \text{radiation}\, C + \frac{2\tilde{K}}{\omega}\beta$, where β is the hysteretic damping parameter.
2. Dynamic stiffness can be calculated as $\tilde{K}(\omega) = K \cdot k(\omega)$ where dynamic stiffness coefficient, $k(\omega)$, as shown in Figure 3.6.
3. $\tilde{c}_z$, $\tilde{c}_y$, $\tilde{c}_{rx}$, $\tilde{c}_{ry}$, and $\tilde{c}_t$ can be found from Figure 3.6.

3.1.5 Beam on Winkler-type Foundation for Piles Foundation

Pile foundations are used to transfer gravity loads from structures to stiff soil layers by end bearing or side friction. Pile foundations also resist horizontal as well as tensile forces from overturning of a structure against earthquake loads. After failures of a number of pile-supported bridges during recent earthquakes, such as the 1994 Northridge Earthquake in California and the 1996 Hyogo-ken Nanbu earthquake in Japan, the study on soil-foundation-structure interaction gained considerable attention (Badoni and Makris, 1997). There are many numerical methods to account for the interaction between soil, pile, and structures. Among many methods, the beam on Winkler type foundation

approach is widely adopted due to its simplicity and ability to account for nonlinear behavior of soils (Kornkasem et al., 2003). The Winkler-type foundation model consists of elements for piles and soils. The hysteretic behavior of soil and the configuration of these springs vary among researchers.

In the Winkler-type pile model, the piles are usually modeled as frame elements. The pile is divided into several elements along the length of the pile, depending on the number of distinct soil layers. The behavior of a pile is more sensitive to the discretization of the top portion of piles. Typically, a 10-diameter depth of the top portions is discretized into at least 5 elements for a long pile.

Much literature exists regarding the definition of the characteristics of soils surrounding piles. The lateral soil resistance is defined with *p-y* curves, and vertical soil resistance is defined with *t-z* curves for side frictions and *q-z* curves for end bearings. Empirical curves for vertical resistances were developed by Aschenbrener and Olson (1984), Coyle and Reese (1996), Heydinger (1989), Lam and Martin (1986), Mosher (1984), Reese and O'Neill (1988, 1989), and Vijayvergiya et al. (1969). Theoretical derivations were developed by Randolph and Wroth (1979) and Kraft et al. (1981). Although there are many suggested curves, and some of them are used more frequently than others, there is no universally adopted approach because most of the methods are derived for specific soil and pile configuration. Among the previously mentioned procedures, the ones presented in *Seismic Design of Highway Bridge Foundations, Vol. II*: *Design Procedures and Guidelines* by Lam and Martin (1986) are the most frequently adopted by designers. The lateral resistances, *p-y* curves, also have been developed by several researchers. Among many methods, those proposed in API (1991) are most widely adopted for soft clay (Matlock, 1970), stiff clay over water table (Reese and Welch, 1975), and sand (O'Neill and Murchison, 1983).

Most Winkler-type foundation approaches divide the soil medium into near field and far field soil. The near field soil springs represent the hysteretic energy dissipation of soil close to pile. The far field soil springs represent elastic deformation of infinite medium as well as radiational damping. Figure 3.7 illustrates two examples of the Winkler-type foundation model: in Figure 3.7 (a), the radiational damping elements are

placed in parallel with hysteretic spring elements, while in Figure 3.7 (b), those are placed in series.

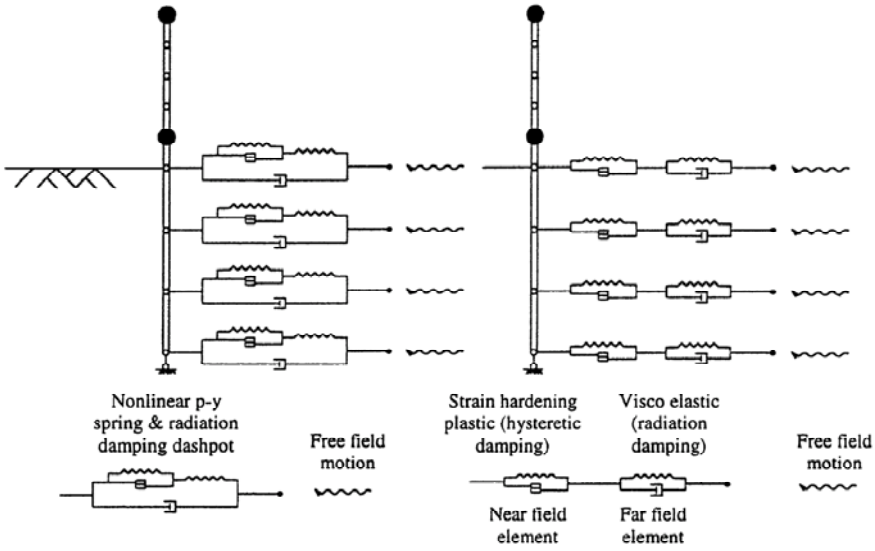

(a) Parallel radiation damping model
Kagawa and Kraft (1980a, 1980b)
Badoni and Makris (1996)

(b) Series radiation damping model
Nogami and Konagai (1987, 1988)
El-Naggar and Novak (1996)

Figure 3.7 Winkler-type pile foundation models
(after Wang et al., 1998)

The majority of pile foundations are supported on pile groups rather than on single piles. Due to the pile-soil-pile interaction, the single pile models cannot be directly applied to model the group effects. Based on empirical data, the group effects are mostly taken into account by applying interaction factors (*y*-modifier, *p*-modifier, and modulus modifier). A pile group can be easily analyzed using the p-y method. But the empirical relationship has limited applicability to a wide range of pile spacings and pile configurations.

The Winkler foundation model is most frequently used in practice due to its simplicity in modeling and low computational cost. When the subsurface condition is not well known, these empirical approaches are the most efficient way of modeling pile foundations. Nevertheless, no universally accepted Winkler-type foundation model implies that the confidence of this approach is very limited. This limitation stems largely from the empirical approach that is adopted at every step of the procedure, such as

definition of soil springs, configuration of these springs, group effects, and the effect of pile caps. This limitation lends weight to the FE approach, whose reliability depends primarily on the behavior of the material model only.

3.1.6 FE–Based Soil and Foundation Models

The FE-based soil and foundation analysis considers various configurations of pile and soil with diverse constitutive models. The computational cost for these types of analyses is much more expensive than that of empirical lumped spring approaches. But the FE approach has many advantages over the empirical methods. Fan (1996) summarized the advantage of the FE-based method as follows:

- The method can take into account various boundary conditions and pile geometry
- Various types of material constitutive models can be included in the system
- The continuity of soil mass and pile/soil interface behavior can be considered
- Effects of various pile or soil properties on the pile responses can be studied systematically

In the FE approach, the constitutive models of soils are the most basic and influential factors. The characteristics of soil vary widely, depending on soil properties such as cohesion, friction angle, existence of water, confining pressure, permeability, overconsolidation ratio, etc. Most of these properties can be obtained only from lab tests.

Soil can be categorized largely into cohesionless and cohesive soil. Soil is classified as cohesive when the shear strength is insensitive to the confining pressure, as illustrated in Figure 3.8 (a). Such materials include, for example, organic soils or clay under fast, undrained loading conditions. Yang et al. (2003a) implemented the cohesive material model in the FE package, OpenSees. In their model, the octahedral shear strength of cohesive soil is defined as

$$\tau_f = \frac{2\sqrt{2}\sin\phi}{3-\sin\phi} p_i^{'} + \frac{2\sqrt{2}}{3} c \tag{3.14}$$

where τ_f is octahedral shear strength, ϕ is friction angle, $p_i^{'}$ is initial effective confinement, and c is cohesion. For cohesive soil, the friction angle is assumed to be

zero. Nonzero friction angle can be also used for material with cohesion and friction. The stress-strain relationship is defined by a hyperbolic curve,

$$\tau = \frac{G\gamma}{1+\gamma/\gamma_r} \tag{3.15}$$

where G is shear modulus, γ is octahedral shear strain, and γ_r is reference shear strain. The typical values of the parameters for soft, medium, and stiff clay are introduced in Section 4. As opposed to the cohesive material, the shear strength of cohesionless material depends on confining pressure, as shown in Figure 3.8 (b). The dynamic behavior of this type of material is a function of friction angle, effective confining pressure, density ratio, etc. The shear strength of cohesionless material in OpenSees is in the form of Equation (3.14), with zero cohesion. The numerical models for these material types are much more complicated than those introduced in this section. For further information, reference is made to Yang et al. (2003a).

The above-referenced introduction on material behavior is based on the assumption that load is applied at a fast rate; therefore, both cohesionless and cohesive materials can be assumed as undrained conditions. In slow rate loading situations, the change in effective stress should be taken into account. For this type of problem, the FE approach is available to consider additional degrees of freedom at each node, which represent pore water pressure, and whose values are functions of time and permeability of material (Fluid-Porus Solid Model in OpenSees). In this study, it is assumed that all materials are in undrained condition because the earthquake load is applied relatively quickly.

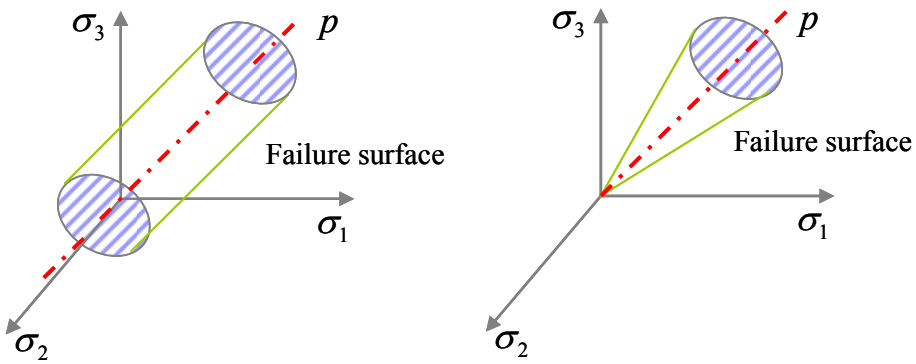

(a) Cohesionless material (b) Cohesive material

Figure 3.8 Failure surfaces of cohesionless and cohesive material

3.2 Development of Hybrid Multiplatform Simulation Framework

In this section, a framework for multicomponent hybrid simulation is proposed. The framework allows combination of various analytical platforms and geographically distributed experimental models into pseudo-dynamic hybrid simulation. The object-oriented architecture of the framework enables extremely simple integration of new analysis platforms or implementation of new analysis schemes. Four application examples are introduced: three-site, small-scale hybrid experiment; three-site, large-scale pier experiment; multiplatform analysis of a bridge with soil and structural models on different platforms; and multiplatform analysis of a complex high-rise building. These experiments and analyses serve as good examples of collaborative research among geographically distributed institutes and among distinctive analysis platforms. These examples as well as the object-oriented architecture prove the promising potential of the proposed framework.

3.2.1 Introduction

Analytically-oriented researchers have been developing applications to predict structural response based on principles of mechanics and/or observational-empirical data utilizing readily accessible computational resources. The ensuing analytical platforms are diverse in nature and have excellent problem-solving capabilities. Unfortunately, most or even all of these developments are limited to solving a specific set of relatively narrow problems of components within complex structural systems. An approach that has the minimum assumptions and provides the best available option is to model each component using the most suitable analytical model and integrating the various contributions into a fully interacting system. Whereas in theory the objective of accounting for interacting inelastic components could be achieved within one analysis platform, this possibility is not achievable with any existing package, and is unlikely to happen in the near future. It is indeed a fact that different analysis programs exhibit strengths and weaknesses and that combining programs with no restrictions placed on the selection is the obvious and only way forward.

Laboratory tests are one of the three fundamental sources of knowledge from which understanding of the behavior of structural systems can be attained; the other being field observations and analytical simulations. Due to the dimensions of civil engineering structures, such as buildings, bridges and utility networks, experiments are usually conducted on the most vulnerable components of a system and often at a reduced scale. Currently, the number of full-scale complete structure tests is very limited. Examples of full-scale system tests are Negro et al. (1996), Molina et al. (1999), Pinho and Elnashai (2000), Chen et al. (2003), and Jeong and Elnashai (2005). Even in the aforementioned cases, the foundations and soil were not modeled. A system by which a number of laboratories could combine their capabilities to undertake a set of integrated component tests of structural and geotechnical elements for example would provide an exceptionally attractive option for assessment of complex interacting systems with neither the assumptions necessary for conducting stable inelastic dynamic analysis, nor the limitations of small scale testing that would be required to fit all components into one laboratory.

The case is made above for distributed analysis, in contrast to using one analytical platform, and distributed testing, in contrast to using one experimental facility. There also exists a combination between the two, once the concept of a distributed representation is accepted. (Watanabe et al., 1999; NSF, 2000; Tsai et al., 2003; Kwon et al., 2005; Pan et al., 2005; Takahashi and Fenvas, 2006). It has hitherto remained, however, a rather arduous task that requires extensive knowledge of both experimental and analytical tools, their detailed input-output requirements, and necessitates considerable programming effort. The procedures have indeed not been sufficiently robust and had therefore remained in the advanced research domain, not in the persistent application domain.

This section addresses the above problem and proposes a simple, transparent and fully modular framework that allows the utilization of analytical platforms alongside experimental facilities for the integrated simulation of a large complex system. Whereas the framework presented is simple and intuitive, its impact on structural and geotechnical research is substantial. The approach utilizes pseudo-dynamic (PSD) simulation, distributed analysis and experimentation. It enables the combination of unique analysis applications in various fields and promotes collaboration of nationally and internationally

distributed experimental and analytical simulation sites interested in large complex systems. The framework presented in this section is an extension of the previous development by Kwon et al. (2005). The following section provides brief conceptual background on the framework followed by the architecture and data-flow of the development. Two analysis examples and two experimental examples are introduced, followed by notes on future prospects.

3.2.2 Pseudo-Dynamic Integration Scheme

The pseudo-dynamic (PSD) test methods have been a research topic for several decades. The earliest introduction of the PSD method was by Takanashi et al. (1975), which evolved toward the substructure PSD test (Dermitzakis and Mahin, 1985), and the distributed PSD test (Watanabe et al., 2001), Figure 3.9. In Europe, the first pseudo-dynamic test setup was developed and verified at Imperial College (Elnashai et al., 1990), in collaboration with Japanese researchers. In these conventional PSD tests, predicted displacements are imposed and measured restoring forces are used in the time integration scheme. These methods are in a mature state in comparison with a newly explored PSD test field such as real-time testing (Nakashima et al., 1992; Carrion and Spencer, 2006), continuous PSD testing (Takanashi and Ohi, 1983), and effective force testing (Dimig et al., 1999). The proposed framework adopted a conventional PSD testing scheme with its well established theory.

The implicit time-step integration scheme, in which initial stiffness is required, has been used for PSD testing in two main thrusts: an iterative implicit method achieving equilibrium at each time step through subcycling (Shing and Manivannan, 1990; Shing et al., 1991), or linearly implicit and nonlinearly explicit, operator splitting (OS) method (Nakashima et al., 1987). Ghaboussi et al. (2004) developed a Predictor-Corrector (PC) algorithm which yields a better result compared to the α-OS scheme, when the response ventures deeply into the inelastic range.

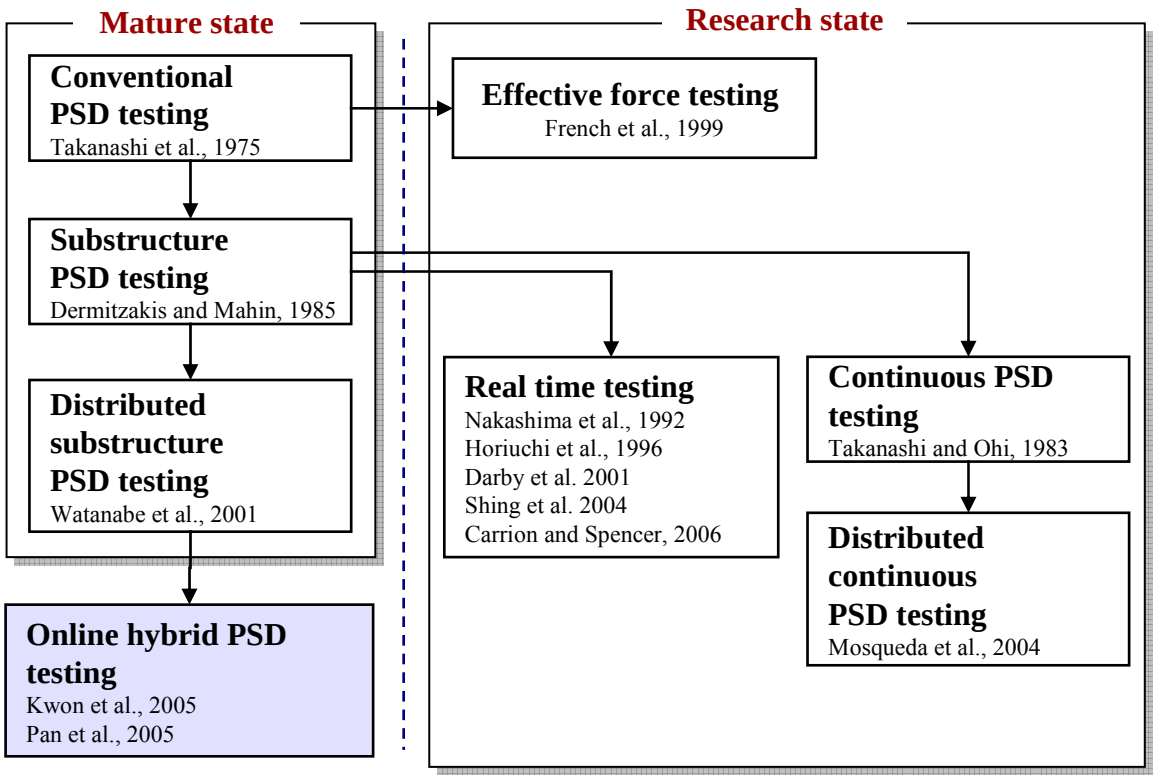

Figure 3.9 Backgrounds on PSD test

The proposed framework is independent of the integration scheme. Therefore, any feasible scheme may be appended to the developed software as long as displacements are imposed and measured quantities are used for the next step. This limitation also can be lifted if necessary. Currently, the Operator Splitting Method, in conjunction with α-modified Newmark scheme (α-OS method), is implemented. The accuracy and stability of the α-OS method was thoroughly studied by Combescure and Pegon (1997), and their main observations are summarized below.

- When the initial stiffness matrix is higher or equal to the instantaneous tangent stiffness, the scheme is unconditionally stable.
- The scheme behaves accurately for the frequency band of interest by an adequate choice of the time step.
- When the structure under consideration does not lose too large a part of its initial stiffness during the test, the non-iterative (incremental) α-OS is a good alternative to the more complex iterative schemes.

- When the structure undergoes severe stiffness degradation, the scheme is still accurate and stable for the low frequency modes of the structure, which are usually dominant.

The equation of motion of a structure may be expressed in terms of the second-order partial differential equation below.

$$\mathbf{Ma}(t) + \mathbf{Cv}(t) + \mathbf{r}(t) = \mathbf{f}(t) \tag{3.16}$$

where **M** and **C** are mass and stiffness matrices, **r**(t) is a restoring force vector, and **f**(t) is an applied force vector. A state of a structure, i.e. displacement, velocity, and acceleration, at the n + 1$^{\text{th}}$ step consists of known terms from the n^{th} step and unknown terms which need to be determined. In the PSD test using the α-OS method, the known or predicted terms are applied to a structure, and the measured restoring forces from the structure are used to evaluate the unknown terms. The PSD test procedure using α-OS scheme can be summarized as below, Combescure and Pegon (1997).

1. Choose Δt
   Evaluate $\hat{\mathbf{M}}$
   $\hat{\mathbf{M}} = \mathbf{M} + \gamma\Delta t(1+\alpha)\mathbf{C} + \beta\Delta t^2(1+\alpha)\mathbf{K}^{\mathrm{I}}$
2. Set $n = 0$
   Initialize $\tilde{\mathbf{d}}_0$, $\mathbf{d}_0 = \tilde{\mathbf{d}}_0$, $\mathbf{v}_0$, $\mathbf{a}_0$, $\tilde{\mathbf{r}}_0$, and $\mathbf{f}_0$
3. Input excitation $\mathbf{f}_{n+1}$
4. Compute $\tilde{\mathbf{d}}_{n+1}$ and $\tilde{\mathbf{v}}_{n+1}$
   $\tilde{\mathbf{d}}_{n+1} = \mathbf{d}_n + \Delta t\mathbf{v}_n + \frac{\Delta t^2}{2}(1-2\beta)\mathbf{a}_n$
   $\tilde{\mathbf{v}}_{n+1} = \mathbf{v}_n + \Delta t(1-\gamma)\mathbf{a}_n$
5. Impose $\tilde{\mathbf{d}}_{n+1}$ to the structure
6. Measure restoring force, $\tilde{\mathbf{r}}_{n+1}^m$, and displacement, $\tilde{\mathbf{d}}_{n+1}^m$
7. Compute $\tilde{\mathbf{r}}_{n+1} = \tilde{\mathbf{r}}_{n+1}^m - \mathbf{K}^{\mathrm{I}}\left(\tilde{\mathbf{d}}_{n+1}^m - \tilde{\mathbf{d}}_{n+1}\right)$
8. Compute
$$\hat{\mathbf{f}}_{n+1} = (1+\alpha)\mathbf{f}_{n+1} - \alpha\mathbf{f}_n + \alpha\tilde{\mathbf{r}}_n - (1+\alpha)\tilde{\mathbf{r}}_{n+1} + \alpha\mathbf{C}\tilde{\mathbf{v}}_n - (1+\alpha)\mathbf{C}\tilde{\mathbf{v}}_{n+1} + \alpha\left(\gamma\Delta t\mathbf{C} + \beta\Delta t^2\mathbf{K}^{\mathrm{I}}\right)\mathbf{a}_n$$
9. Solve for $\mathbf{a}_{n+1}$ from $\hat{\mathbf{M}}\mathbf{a}_{n+1} = \hat{\mathbf{f}}_{n+1}$

10. Compute $\mathbf{d}_{n+1}$ and $\mathbf{v}_{n+1}$

$$\mathbf{d}_{n+1} = \tilde{\mathbf{d}}_{n+1} + \Delta t^2 \beta \mathbf{a}_{n+1}$$

$$\mathbf{v}_{n+1} = \tilde{\mathbf{v}}_{n+1} + \Delta t \gamma \mathbf{a}_{n+1}$$

11. Set $n = n + 1$ and go to step 3

In the above procedure, the initial stiffness matrix, $\mathbf{K}^1$, is used to correct the restoring force in step 7 and to establish equivalent mass matrix in step 1, which is used to calculate the acceleration of next step, $\mathbf{a}_{n+1}$ in step 9. Thus, to use the α-OS method for PSD tests, the initial stiffness matrix should be established prior to dynamic analysis. The stiffness matrix may be formed from simple pretests or preanalysis.

In this study, the α-OS integration scheme is implemented in the main body of the software, UI-SimCor, which controls each module and performs integration. All other static analysis or experiments are conducted as separate modules. The structure enables attaching a new module, be it a test specimen or an analysis program, in a manner which is exceptionally simple.

3.2.3 Conceptual Background of Hybrid Multi-Platform Simulation

In a conventional PSD test, the structural mass, damping, and inertial forces are defined within a computational module. The predicted structural deformation at the control points is statically applied to a structure to estimate the restoring force vector. In a conventional PSD test of a whole structure, such as the three-storey frame depicted in Figure 3.10 (a), degrees of freedom (DOFs) with lumped masses are included in the equations of motion. If the three-story structure is pseudo-dynamically tested, it is assumed that the mass of each floor can be lumped at a single control point, and one actuator per story is normally used to apply inertial forces, for planar structures. Thus the computational module handles the equations of motion with three translational DOFs.

The experimental specimen for the PSD test may also be represented numerically, as shown in Figure 3.10 (c). The analytical model may use refined meshes to capture propagation of damage. Hence the model may include a larger number of DOFs than the equations of motion where only the DOFs with lumped masses are used. The predicted

displacements at the control points are applied, and the restoring forces at these points are returned to the equations of motion.

Where substructuring is required, force equilibrium and displacement compatibility should be satisfied at interfaces between substructured components. Hence, the control points for PSD simulation should include nodes at interfaces, as well as nodes with lumped masses.

When testing a critical element and analyzing the rest of the structure, sub-structured PSD simulation can be used. In the conventional approaches for sub-structured PSD simulation, a single analysis platform is combined with a time integration module, as shown in Figure 3.10 (b). This approach is adequate if the adopted analysis platform can represent the true structural responses. In most situations, however, the analytical platform is limited to dealing with a simple nonlinear model. By completely separating the restoring force modules from the time integration scheme, and by allowing an unhindered combination of restoring forces from various analytical modules, a complex structural system can be accurately modeled. In the proposed framework, the PSD test algorithm itself is identical to the conventional method. But the way it combines several restoring force modules, whether analytical or experimental, and the communications between modules are the most distinctive characteristics of the development.

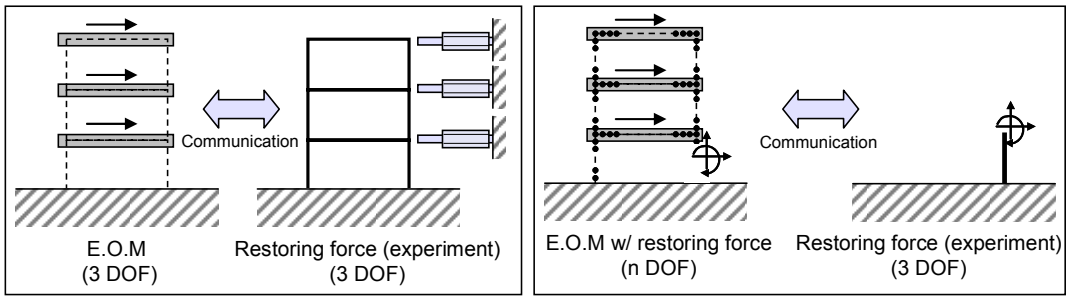

(a) Conventional PSD experiment

(b) Conventional sub-structured PSD experiment

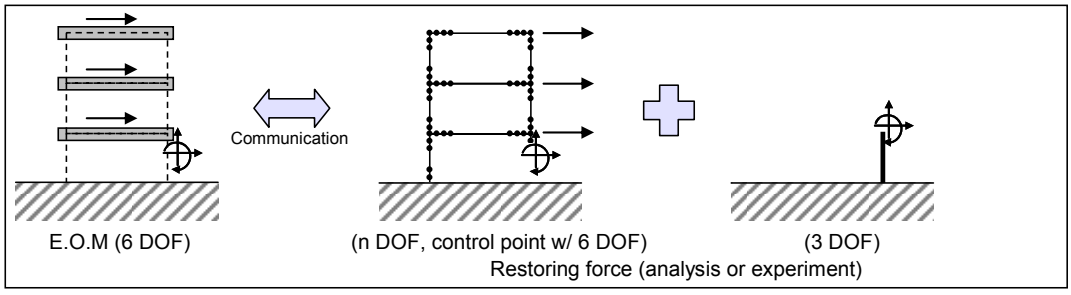

(c) Proposed Sub-structured PSD simulation

Figure 3.10 Substructuring of PSD Simulation

In the proposed framework the whole system can be substructured into several components, which can be either simulated in analytical platforms or physically tested. Then, nodes and DOFs are assigned at the location of lumped masses and at the interface of different structural components to ensure displacement compatibility and force equilibrium. The analytical substructure model can be further discretized.

The analysis of an inelastic system usually involves iteration as the stiffness of the system changes with displacement. There are diverse numerical methods to solve the inelastic problems with efficiency and accuracy. In most methods, when convergence criteria are not satisfied up to prescribed iteration steps, the analysis step is reduced (step reduction), and iteration is restarted. Even though the nonlinear element is path dependent, structural analysis applications are written in a way that the elements do not remember displacement history when step reduction is conducted, allowing many trial step reductions until convergence criteria is satisfied. Unfortunately, the step reduction cannot occur when experiments are involved or when the analytical model should be controlled only from the user interface level. In that case, small analysis steps should be used to minimize unbalanced forces, and the unbalanced forces at one step must be equilibrated at the next step rather than reducing steps and running iterations.

Pseudo-dynamic integration schemes are inherently developed to handle this type of problem, where part of a structure is assumed to be an experimental specimen, which does not allow iteration. The proposed framework in this study takes advantage of the PSD scheme to combine various analytical platforms and experimental tests where restoring forces of structural components are taken from analytical model or experimental specimen. The proposed framework includes only rate-dependent components of structural systems such as mass matrix and damping matrix. All structural models are distributed to external static analysis modules or experimental specimens. The architecture of the framework will be introduced in detail in Section 3.2.4. The advantage of the approach is that the analysis platform can be fully modular, as the developer of each analysis platform needs only to consider the hysteretic response of a structural model. The limitation of this approach at the current stage is that additional time is required to transfer data from one platform to another. The advantages and limitation will be further articulated in Section 3.2.9.

3.2.4 Architecture of Framework

The basic concept of the framework is that analytical models associated with various platforms or experimental specimens are considered as a super-element with many DOFs. Each of these elements are solved on a single computer or on multiple computers connected through the network. Figure 3.11 illustrates the overall architecture of the framework, termed UI-SimCor. The main routine shown in the figure enforces static equilibrium and conducts dynamic time integration. In this process, the structural model is fully encapsulated as objects of a class. Hence it is straightforward to add new time integration methods to enforce static equilibrium.

There are two classes in UI-SimCor: MDL_RF (restoring force module) and MDL_AUX (auxiliary module). The objects of MDL_RF class represent structural components. The main functionality of this class is abstraction of the structural components at remote sites. The main routines such as dynamic integration schemes impose displacement onto the structural components and retrieve restoring forces without consideration of communication with remote sites regardless of whether the components are experimental specimens or analytical models. This abstraction allows exceptionally easy implementation of new simulation tools and components.

Another important functionality of the MDL_RF class is communication. When the main analysis routines impose a displacement on a structural component represented by an object of MDL_RF class, the object reformats the data for the pre-specified protocol, opens connections to the remote sites, and sends the reformatted data. Six types of communication protocols are implemented in the current release. These are introduced in the following section. MDL_RF class includes other functionalities such as checking force and displacement capacities at every time step. In addition, the object of MDL_RF class shows the communication status and monitors communicated values at each time step, Figure 3.12.

MDL_AUX class is used to control experimental hardware other than actuators. The object of this class has a function to send out pre-specified commands to remote sites. Upon reception of the command, the remote sites can take actions such as taking pictures or triggering data acquisition.

At remote sites, it is necessary to have a program interface which opens communication ports for the main framework, imposes displacements on the analytical model and returns measured data. The interfaces for analytical platforms have been developed for ZEUS-NL (Elnashai et al., 2002), OpenSees (McKenna and Fenves, 2001), FedeasLab (Filippou and Constantinides, 2004), ABAQUS (Hibbit et al., 2001), and VecTor2 (Vecchio and Wong, 2003).

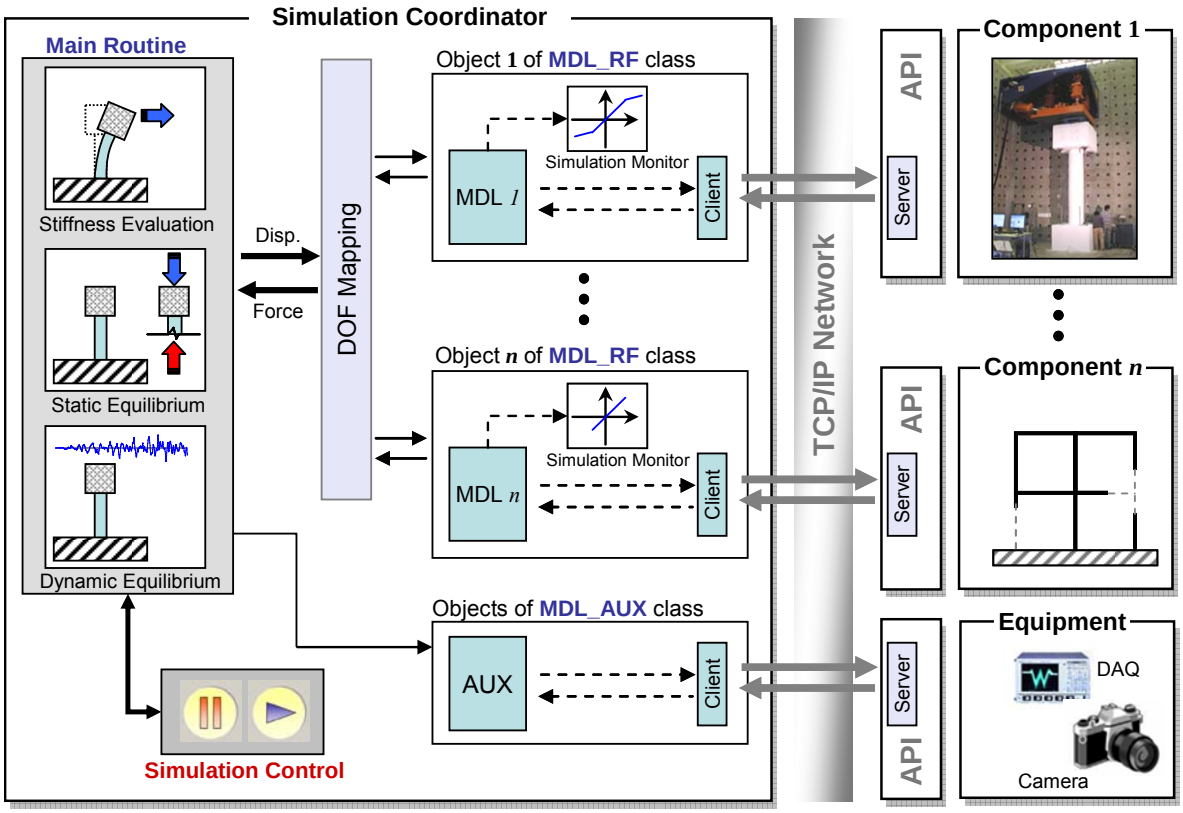

Figure 3.11 Architecture of proposed hybrid simulation framework

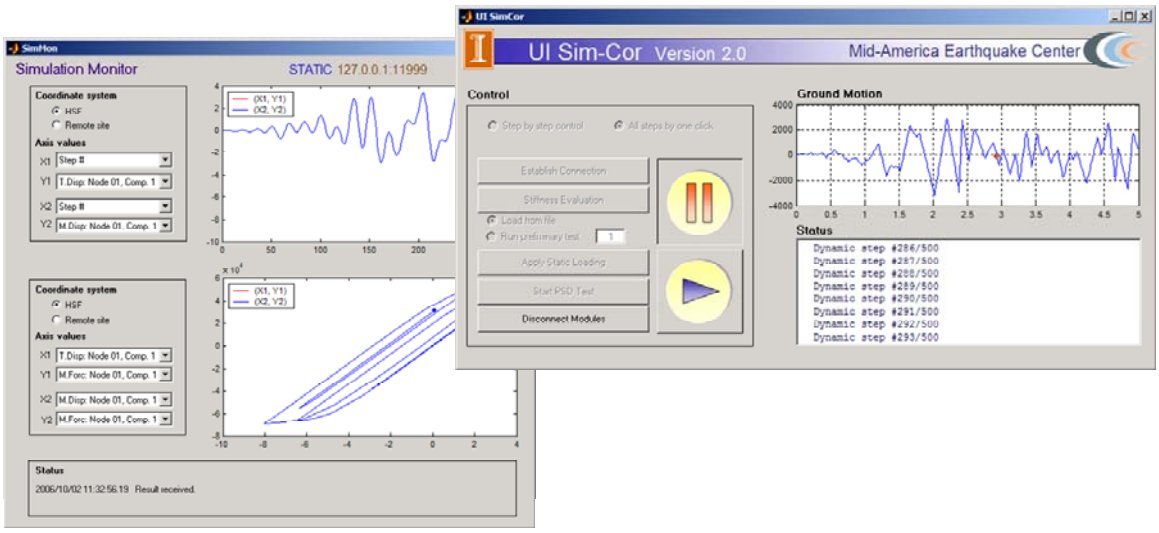

Figure 3.12 Monitoring window of MDL_RF class and GUI of UI-SimCor

3.2.5 Simulation Procedure and Data Flow

A typical simulation procedure where three communication layers are identified as 'User', 'Simulation Framework', and 'Remote Sites' is illustrated in Figure 3.13. The user of the hybrid simulation framework can start the simulation, monitor the current status, and pause the simulation based on the messages from the monitoring window. A simulation framework is responsible for initialization, stiffness estimation, response history integration, and communication with remote sites. The remote sites are responsible for running analyses or experiments for given displacements and returning measured responses. The simulation procedure shown in Figure 3.13 is for a configuration with NTCP protocol which will be introduced in Section 3.2.6. In this protocol, whenever the command is sent to remote sites, the remote sites send acknowledgement to confirm the receipt of the incoming command. The data flow shown in Figure 3.13 may vary depending on the protocols or simulation configuration.

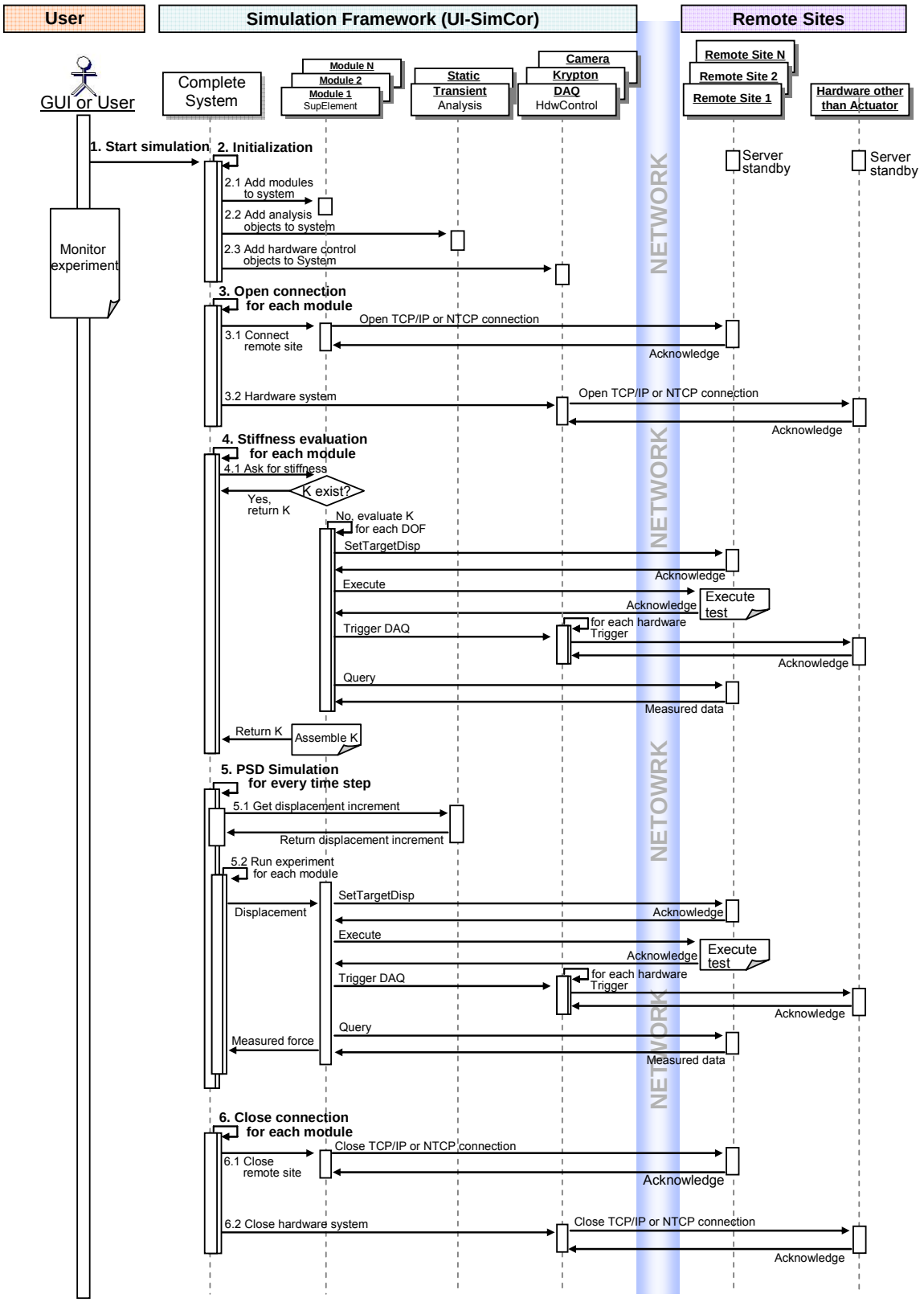

Figure 3.13 Simulation procedure and data flow

3.2.6 Communication Protocols

The communication over a network, following standard protocol, is one of the most important requirements for geographically distributed hybrid simulation. In the proposed framework, six communication protocols are implemented: NTCP, LabView1, LabView2, TCP/IP, NHCP, and a protocol for OpenFresco (Schellenberg and Mahin, 2006). To promote collaboration of equipment sites across the United States, the Network for Earthquake Engineering Simulation (NEES) consortium developed a standard communication protocol, NEESgrid Teleoperation Control Protocol (NTCP), (Pearlman, 2004). The NTCP allows secured communication between remote sites through an NTCP server. To send commands to hardware equipments, the NTCP server sends unencrypted, ASCII format data, which is often referred as LabView protocol. In the NTCP and LabView protocols (in current version, LabView1), whenever commands are sent to remote sites, the remote sites send an acknowledgement back to the main framework to confirm the receipt of the data, as shown in Figure 3.13. Between proposal and execution of the commands, the main framework checks relaxation of displacement or force. This procedure delays simulation time. Thus, a modified version of LabView protocol, referred to as LabView2, is also implemented into the framework. In LabView2, whenever target displacements are sent to remote sites, remote sites run experiments or analyses and send back the measured responses. The LabView1 and LabView2 protocols utilize ASCII format communication. The ASCII format data is efficient to interpret, as all commands and values are readable in text format, but it requires significant costs to convert from binary data to ASCII format and ASCII format to binary data. In addition, ASCII format data requires much larger communication traffic. Thus, in addition to LabView1 and LabView2 type protocol, a binary communication protocol (referred as TCP/IP in the framework) is also implemented for which a pure binary format is used for communication. Recently, NEESit has been developing a NEES Hybrid Simulation Communications Protocol (NHCP), a successor of NTCP. The earliest version of NHCP is also implemented in UI-SimCor. UI-SimCor also provides a communication to OpenFresco through the Matlab library built by developers of OpenFresco. These versatilities in communication encourage involvement of a wide range of equipment sites and analysis platforms.

3.2.7 Analysis Platforms

The proposed framework assumes that the remote sites are analyzed or tested for imposed displacement and returns the measured responses. Due to the fully modular, object-oriented architecture, this requirement is not absolutely necessary and can be easily lifted if new analysis methods require other values, such as velocity or acceleration and takes measured responses to model structural elements like dampers or control systems. In the current framework, only a conventional PSD scheme is implemented. Therefore, the analysis platforms and experimental sites should impose displacements received from UI-SimCor and make an output for force and displacement measurements.

The main challenge in integrating analysis platforms into hybrid simulation framework is the development of the program interfaces, which receives incoming data from UI-SimCor, executes commands, and sends the structural responses. If the analysis platforms are operated only by Graphical User Interface (GUI), the program interfaces cannot be easily developed unless the source code of the GUI is accessible. On the other hand, if the applications can be run in console mode, the interfaces can be relatively easily developed by writing a wrapper application. Another requirement for the analysis platform is that the platform should be able to impose displacements which are not known before the start of the analysis. Based on these requirements as well as the necessity for diverse analytical environment, interfaces for the following analysis platforms are developed: Abaqus, FedeasLab, OpenSees, Vector2, OpenFresco and ZEUS-NL. Table 3.2 summarizes the main features of these analysis platforms. The proposed framework accompanying various analysis platforms and potential experimental models constitutes an exceedingly strong foundation for structural research.

Table 3.2 Analysis applications for which interfaces are developed

Application	Reference	Features
Abaqus	Hibbit, 2001	General FE package with numerous material models and element types Weak in modeling of concrete or soil Need to restart at every time step which slows the PSD simulation Commercial code
FedeasLab	Filippou, 2004	Matlab based FE package Good for concept development Noncommerical code
OpenSees	McKenna and Fenves, 2001	Actively being updated Include soil material model and fiber-based frame element model Open source code Noncommercial code
Vector	Vecchio and Wong, 2003	Analysis of concrete continuum Modified compression field theory Commercial code (noncommercial for basic programs)
ZEUS-NL	Elnashai et al., 2002	Fiber-based frame elements Geometric and material nonlinearity Verified through various experiments Noncommercial code

3.2.8 Application Examples

The framework has been adopted for several analytical and experimental examples. This section briefly introduces major application examples, including the objective of simulation and simulation configuration.

3.2.8.1 Three-Site Hybrid Test with UI-SimCor

The UI-SimCor hybrid simulation framework is validated through conducting a three-site hybrid simulation example (NEESit Phase I Hybrid Simulation Project, Spencer, et al., 2006a). The three sites involved in this project are: University of Illinois at Urbana-Champaign (UIUC), University of California at Berkeley (UCB), and San Diego Supercomputer Center (SDSC). Each experimental site is equipped with a small testing

facility developed for the verification of hybrid simulation as follows: MiniMOST 1 (Gehrig, 2004) at UIUC and SDSC, and μ-NEES (Schellenberg et al., 2006) at UCB. The MiniMOST 1 specimens behave in the linear elastic range, while the specimen employed by the μ-NEES facility behaves in the inelastic range. It is considered that the experimental specimens from the three sites represent piers of a bridge. The remaining structural elements are modeled in ZEUS-NL, as shown in Figure 3.14. Simulation was carried out at the rate of 6.5 sec/step. The slow simulation rate is due to limitations of the load cell employed in the MiniMOST 1 experiment (Note that the MiniMOST 1 at UIUC and SDSC have recently been updated to remove this limitation). Figure 3.15 compares the responses from the three-site hybrid simulation. The experimental results are very close to the analytical simulation result. The slight difference is caused by inaccurate representation of the inelastic behavior of the μ-NEES specimen with a hysteretic spring model. This project verified that the proposed framework runs reliably and requires minimum effort to customize at remote sites.

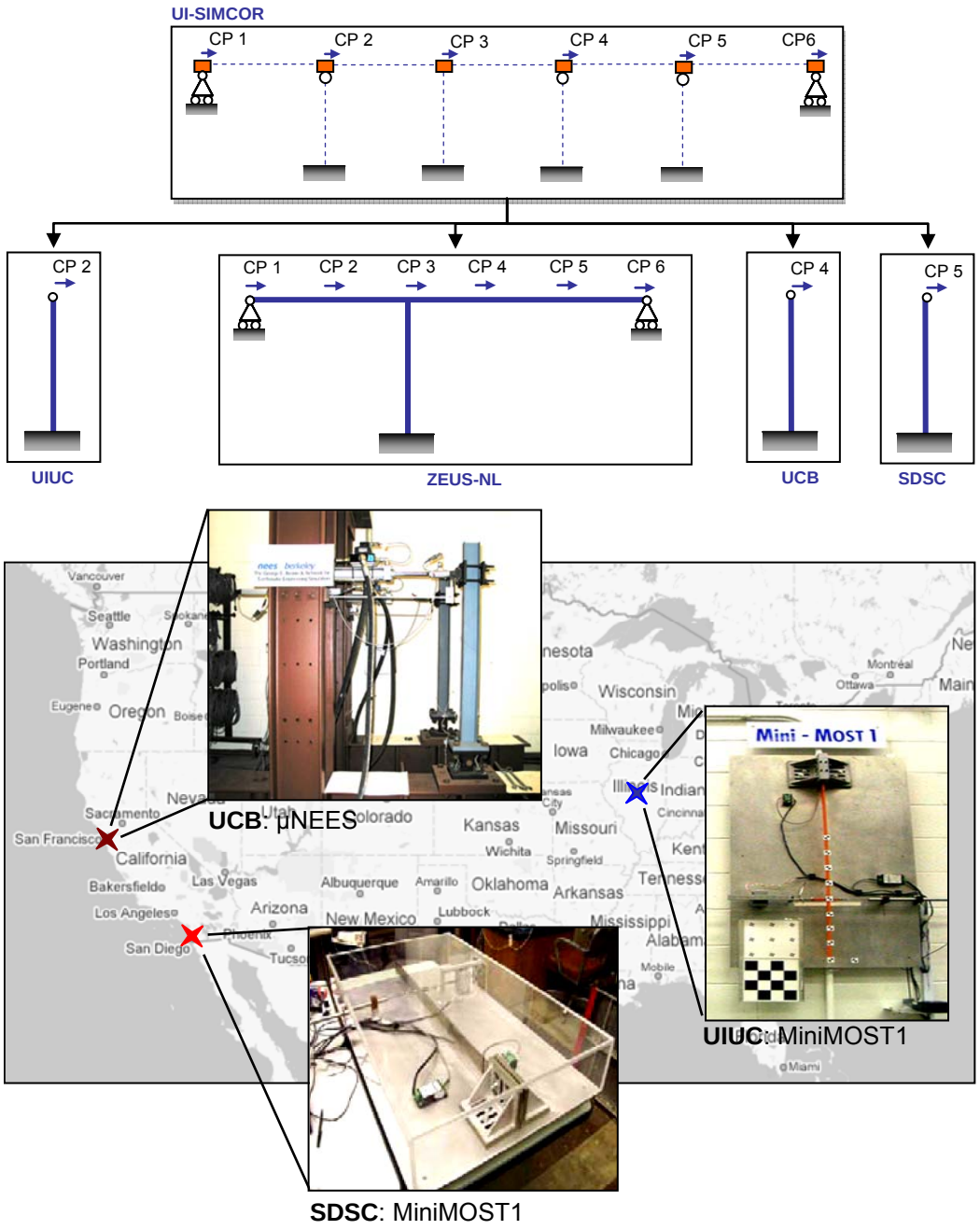

Figure 3.14 Simulation configuration of three-site experiment

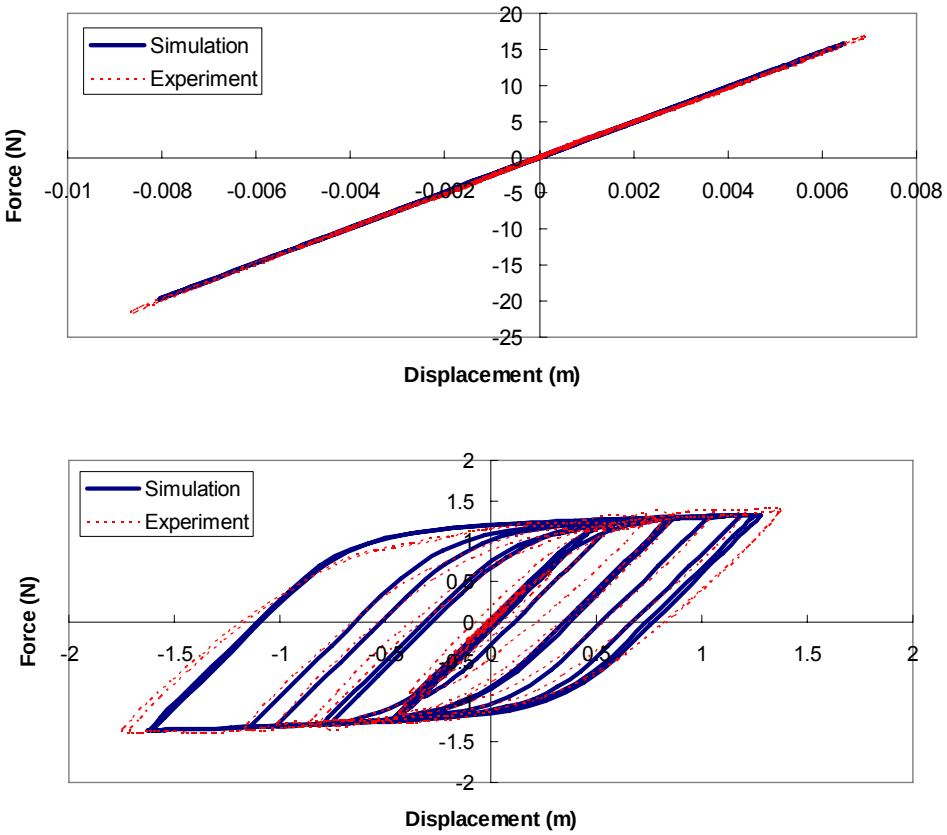

Figure 3.15 Comparison of analytical and experimental results

3.2.8.2 MRO Bridge Simulation

The Meloland Road Overcrossing (MRO) Bridge is equipped with 32 channels of accelerometers and measured several sets of earthquake ground motions. As part of a study for soil-structure interaction, the bridge was modeled with the best applications for each structural component. OpenSees is used to model geotechnical environment including embankments, piles, and foundations with state-of-the-art soil material models. ZEUS-NL is used to model super structures. Each structural component, such as central pile foundation, embankments, and combined system are thoroughly verified through literature review and measured responses. The structural model in ZEUS-NL and the geotechnical model in OpenSees is combined with UI-SimCor. This analysis is a good example of utilizing the best features of different analysis platforms. Further detailed information about this bridge analysis is introduced in Section 4.3 and Kwon and Elnashai (2006).

3.2.8.3 MISST Project

To demonstrate the efficacy of the UI-SimCor framework, the MISST (Multi-Site Soil-Structure-Foundation Interaction, Spencer et al. 2006b) project is presented. MISST also provides a demonstration of the potential of NEES to investigate classes of problems that could not be studied previously. The tested bridge is based on Collector-Distributor 36 of the I-10 Santa Monica Freeway that was severely damaged during the Northridge Earthquake in 1994, Figure 3.16 (b). In this experiment, two experimental sites (one pier in UIUC and another pier in Lehigh University, LU) and two analytical models (geotechnical model in Rensselaer Polytechnic Institute, RPI, and structural model in UIUC) are integrated using UI-SimCor, Figure 3.17. To satisfy capacity limitations of the test equipment, a 1/2 scale model of the prototype pier was constructed and tested at UIUC. The diameter of tested specimen was 24 inches with a reinforcement ratio of 3.11% and 0.176% for the longitudinal and transverse directions, respectively. Several hybrid simulations were carried out. These simulations included both small and large amplitude tests. The small amplitude test was intended to verify the functionality of all components and equipment while the large amplitude tests were intended to replicate the observed damage in the prototype structure. Two earthquake records that were captured during the Northridge earthquake of 1994 were employed during these simulations. The first record was strong motion data collected at the Santa Monica City Hall, which had a peak ground acceleration (PGA) of 0.37g. The second record was collected at the Newhall Fire Station and had a PGA of 0.58g. In both cases, the acceleration record was applied along the longitudinal direction of to the bridge structure.

The coordination and communication of the three sites, UIUC, LU, and RPI, for the five component hybrid and geographically distributed simulation worked seamlessly. Despite the brittle nature of the specimens, the simulation was able to continue on well past the initial shear failures observed at both the UIUC and LU sites. Furthermore, the redistribution of forces between the two bridge piers indicated that full interaction was taking place between the remotely distributed sites. Thus UI-SimCor proved to be quite effective and robust. Moreover, the failure modes obtained, Figure 3.16 (a) and (c), are similar to those in the prototype observed following the 1994 Northridge earthquake, Figure 3.16 (b). Thus, the observed and complex field behavior of a complicated

structural system was successfully reproduced. The MISST project not only demonstrated new opportunities to address or propose innovative design approaches for bridge structures, but also clearly demonstrates how distributed simulation can be applied to address problems which have previously been unapproachable to the earthquake engineering community.

(a) Pier 1 - UIUC (b) Santa Monica Freeway (c) Pier 3 - Lehigh

Figure 3.16 Comparison of observed behavior
(after Spencer et al. 2006b)

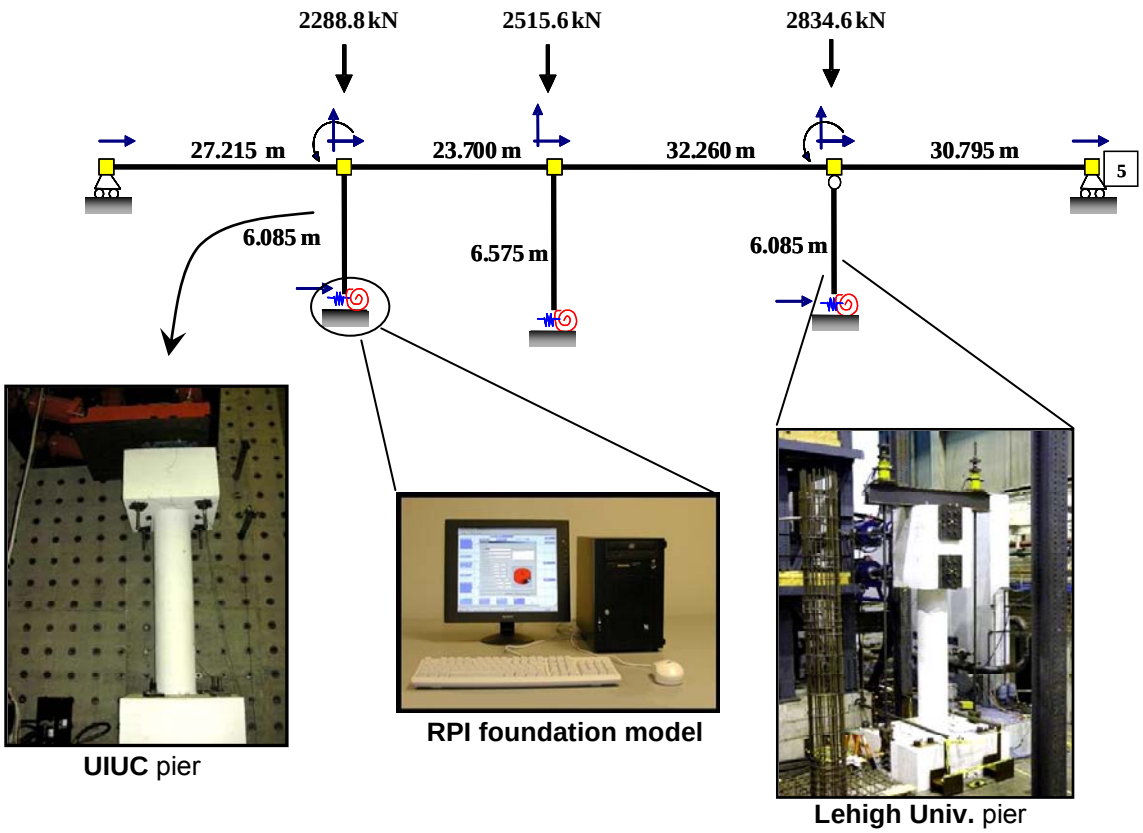

Figure 3.17 Experiment configuration of MISST project
(after Spencer et al., 2006b)

3.2.8.4 Highrise Complex Structure

The structural system of a high-rise building is not a direct extension of low-rise structures due to its more complex configurations and the needs to resist much larger external loads. In addition, the lateral displacement is an important issue for the comfort of residents. Hence, normal analytical methods for low-rise buildings do not work well for the capacity evaluation of a high-rise structure. The following example presents the application of multiplatform simulation to analyze a complex high-rise structure.

An actual RC high-rise building, Tower C03 at Dubai, United Arab Emirates, is chosen as a representative building because of its well-designed core walls and their combination with outer frames, as shown in Figure 3.18. Frame F4 in Figure 3.18, which includes dual core walls and beam-column frame, is chosen as the reference structure for the building analysis. It is analyzed using two analysis platforms: VecTor2 and ZEUS-NL. The former, VecTor2, is capable of analyzing an RC continuum based on the

Modified Compression Field Theory (MCFT) by Vecchio and Collins (1986). The latter, ZEUS-NL, utilizes fiber-based frame elements.

The shear significant lower regions of the walls, 1st - 10th stories of the building, are modeled as RC continuum elements in VecTor2, while the remaining parts of the walls and frame are simulated with fiber-based beam-column elements in ZEUS-NL. In UI-SimCor, there are control points in the substructured models, with lumped masses and DOF of interest for applied loads and response displacements. These control points are defined in order to form the global mass and stiffness matrices necessary in PSD algorithm, and to serve as the common interfaces between substructures. In each analytical module, these control nodes are associated with other nodes through finite elements. When two analytical modules with different resolutions are combined, it is essential to properly consider DOFs at the boundaries of two modules. For instance, the concrete continuum in VecTor2 is modeled with plane stress element whose nodes have two DOFs, while the 2D frame elements in ZEUS-NL include three DOFs per node. Thus, to couple these elements with different resolutions and to prevent stress concentration on a module in high resolution, multipoint constraint equations are derived and applied.

The simulation model is shown in Figure 3.19. Ground motions are selected considering various epicentral distances and soil conditions. Figure 3.20 presents two sets of displacement response histories, r, at two different floor levels (1st and roof stories), using a record from the 1999 Kobe earthquake. The analysis results from the multiplatform simulation are compared with those from the frame analysis of skeletal model in ZEUS-NL. At lower levels of the building, the drifts computed from the multiplatform simulation are much larger than those from the pure ZEUS-NL model, while at roof story they are close to each other. The large difference at the lower level results from shear deformation, as considered by concrete continuum model in VecTor2. Further detailed information about this multi-platform simulation is available at Ji et al. (2007).

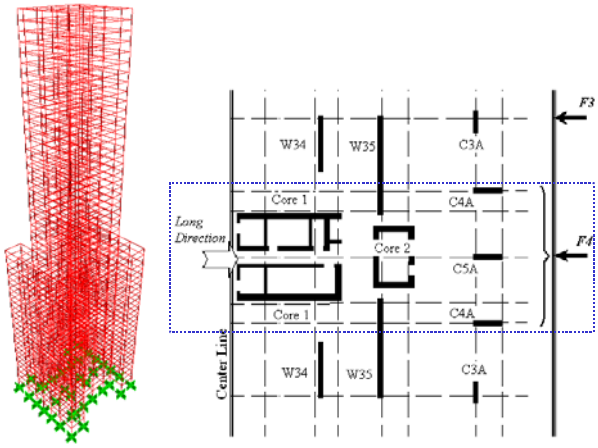

Features	Description
Height (m)	184.000
Total Stories	54
Regular Storey Height (m)	3.400
Irregular Storey Height (m)	4.488
Core Walls (Exterior and Interior Size)	9.43x3.25 (8.48x2.55) (m)
	9.33x3.15 (8.48x2.55) (m)
	9.18x3.05 (8.48x2.55) (m)
Concrete f'c (MPa)	60 (wall); 40 (slab)
Reinforcing Bars fy (MPa)	421 (Grade 60)

Figure 3.18 3D SAP2000 Model, Half plane view and main features

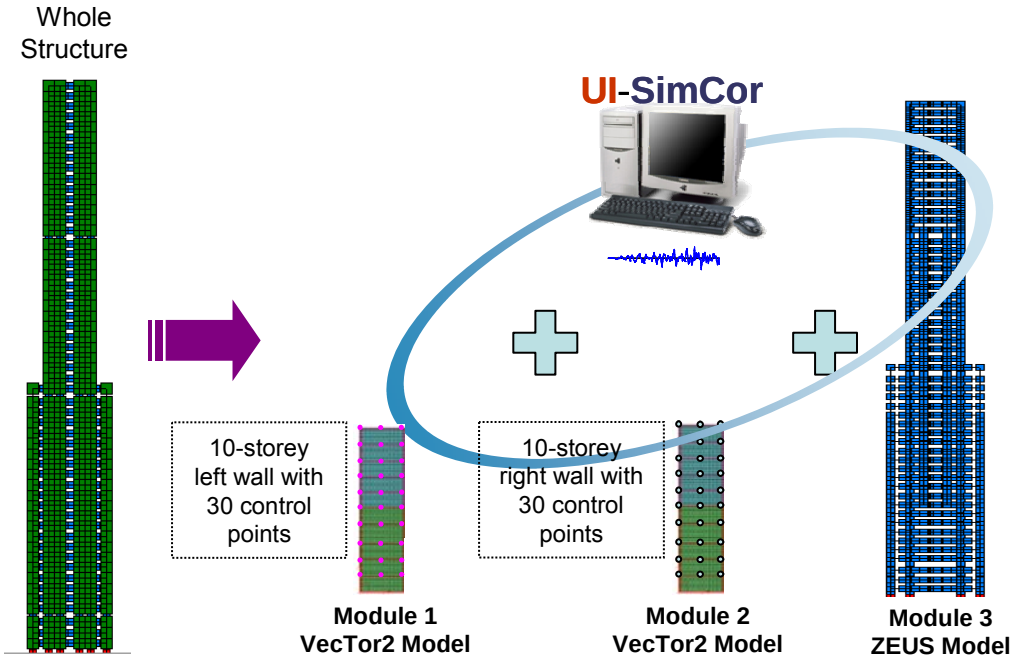

Figure 3.19 Multiplatform analysis of a high-rise complex structure

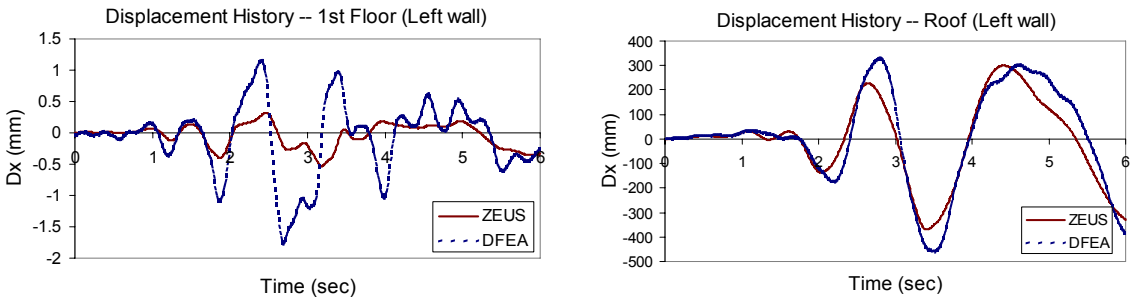

Figure 3.20 Sample lateral displacement history comparisons

3.2.9 Potential, Limitations, and Challenges

The proposed framework allows combination of various state-of-the-art analysis platforms and physical models that can best represent the structural components comprising the assessed system. These components are connected and coordinated through a TCP/IP-based online network that allows geographical distribution of the individual component, nationally and internationally. The framework allows distribution of computational resources for large and complex problems with a few coupled DOFs, such as a pile group foundation model with tens of thousands of DOFs connected to a pier at single node. In addition, the object-oriented program architecture and the simple concept of the framework allow exceedingly easy implementation of a new analysis algorithm or inclusion of a new analysis platform.

The proposed framework, however, has limitations. Because the forces and displacements at all DOFs should be communicated through a network, the network traffic demands can be expensive for a system with a large number of DOFs. But this limitation will be overcome with advances in network speed, similarly to the FE approach, which had limited application before the advancement of computational power. In addition, at the current state of practice and research, few PSD simulations involve large numbers of DOFs. One of the currently addressed challenges is conducting hybrid simulations for velocity-sensitive applications, such as frequency-dependent dampers and other rate-sensitive applications. Real-time hybrid, geographically-distributed simulations remain a major challenge.

CHAPTER 4

VERIFICATION AND APPLICATION OF SOIL-STRUCTURE INTERACTION MODEL

The SSI system can be analyzed with various methods, as discussed in Chapter 3. Lumped-spring approaches based on empirical data are the most practical methods, but they have limited applicability. The FE approach is computationally expensive, but it may be applied to general soil-foundation configurations with the least number of approximations. With the advance in computational power, computationally involved approaches are gaining the interest of researchers. In this chapter, a verification study of FE approach is conducted through several experimental studies. To understand the most basic soil-structure interaction, two lateral load tests of single pile in cohesionless soil and in cohesive soil are analyzed. Thereafter, a heavily instrumented bridge system is analyzed with multiplatform analysis framework, in which an FE geotechnical model is combined with a fiber-based structural model. The last section of this chapter introduces a bridge retrofit project, in which the foundation properties are estimated from FE models and an SSI model is assembled.

4.1 A Single Pile in Cohesionless Material

The objective of this section is to verify an FE approach of a soil-pile system before it is applied to structural system for vulnerability analysis. Mustang Island lateral load test (Rees et al., 1967) is selected as a benchmark study. The test result has been used by several researchers to validate their approach in analysis of soil-pile system. Kornkasem et al. (2003) proposed soil and pile models and verified them with results from the in-situ tests. In their approach, the pile is modeled as elastic beam-column elements, laterally supported by a Winkler-type foundation. Soil is modeled with nonlinear spring elements at near field to account for local nonlinearities around soil-pile interface. Far field was modeled with elastic springs to consider infinite soil medium. The local nonlinear springs can take into account formation of gap between pile and soil alongside nonlinearity of

soil defined by p-y curves. In the verification study, the p-y curves needed to be calibrated to obtain a good match with results from the field tests. Fan (1996) developed an FE code to analyze soil-pile system and verified it through comparison with the Mustang Island lateral load test. As nonlinear FE analyses required much more soil properties than what can be obtained from conventional laboratory tests, many model parameters were adopted from 'typical' soil properties. For instance, the horizontal earth pressure against pile, K, was selected after parametric study and the friction angle between pile and soil was assumed to be $2/3\phi'$. The analysis result matched well with experimental data. This type of approach, however, always involves approximation of model parameters based on engineering judgment mainly due to lack of data.

In this section, three-dimensional material models developed by Yang et al. (2003a) are used to verify the FE approach. Many unknown parameters are adopted from typical values suggested by Yang et al. (2005). This approximation does not necessarily mean that the approach is not correct. As the nonlinear FE approach has been developed from many theoretical as well as experimental bases from material levels, it is natural to calibrate some of the parameters unless the in-situ condition is exactly same as the condition from which the code was developed. The assumptions and numerical models are introduced in the subsequent sections.

4.1.1 Site Condition and Test Procedure

The test site consists of sandy clay seams underlain by a layer of firm gray clay and a layer of silty fine sand. Before the lateral load test, 2.44 m of clay layer were removed and backfilled with 0.76 m of sand. The sand at the test site varied from clean fine to silty fine, both exhibiting high relative density. The angle of internal friction, ϕ, was determined to be 39 degree, and the value of the submerged unit weight, γ', was 1.06 ton/m^3. The water table and ground levels were the same after backfill. Boring tests at two locations were conducted. Blow counts from a standard penetration test (SPT) ranged from 12 at around 1.0 m below ground level, to 79 at the 12 m depth. The test pile was hollow circular steel pile with a diameter of 0.61 m and a thickness of 9.5 mm. The pile

was equipped with 40-strain gauges along the length. Two reaction piles were driven at the distance of 3.3 m and 4.6 m from the center of the test pile. The test setup and soil profile are given in Figure 4.1 and 4.2, respectively. For detailed test site conditions, reference is made to Cox et al. (1974).

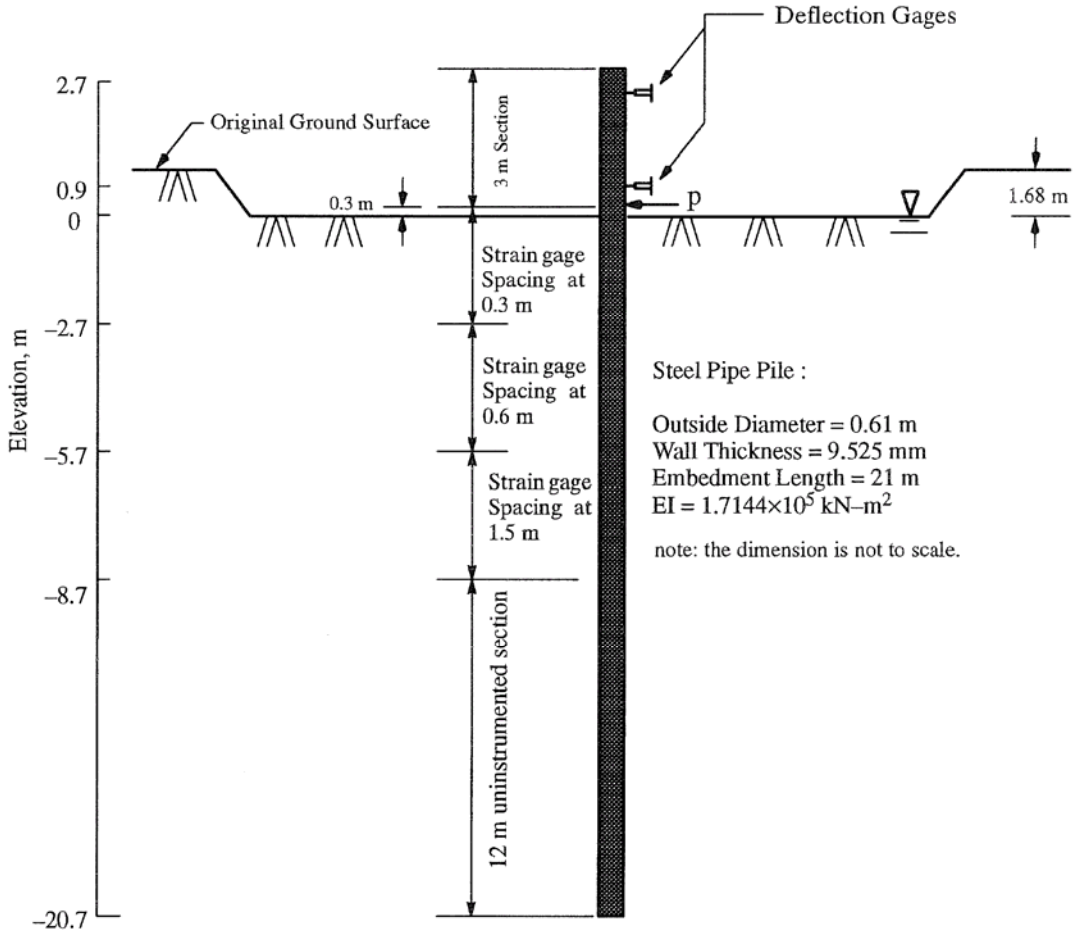

Figure 4.1 Lateral load test setup of a pile in cohesionless soil
(after Fan, 1996)

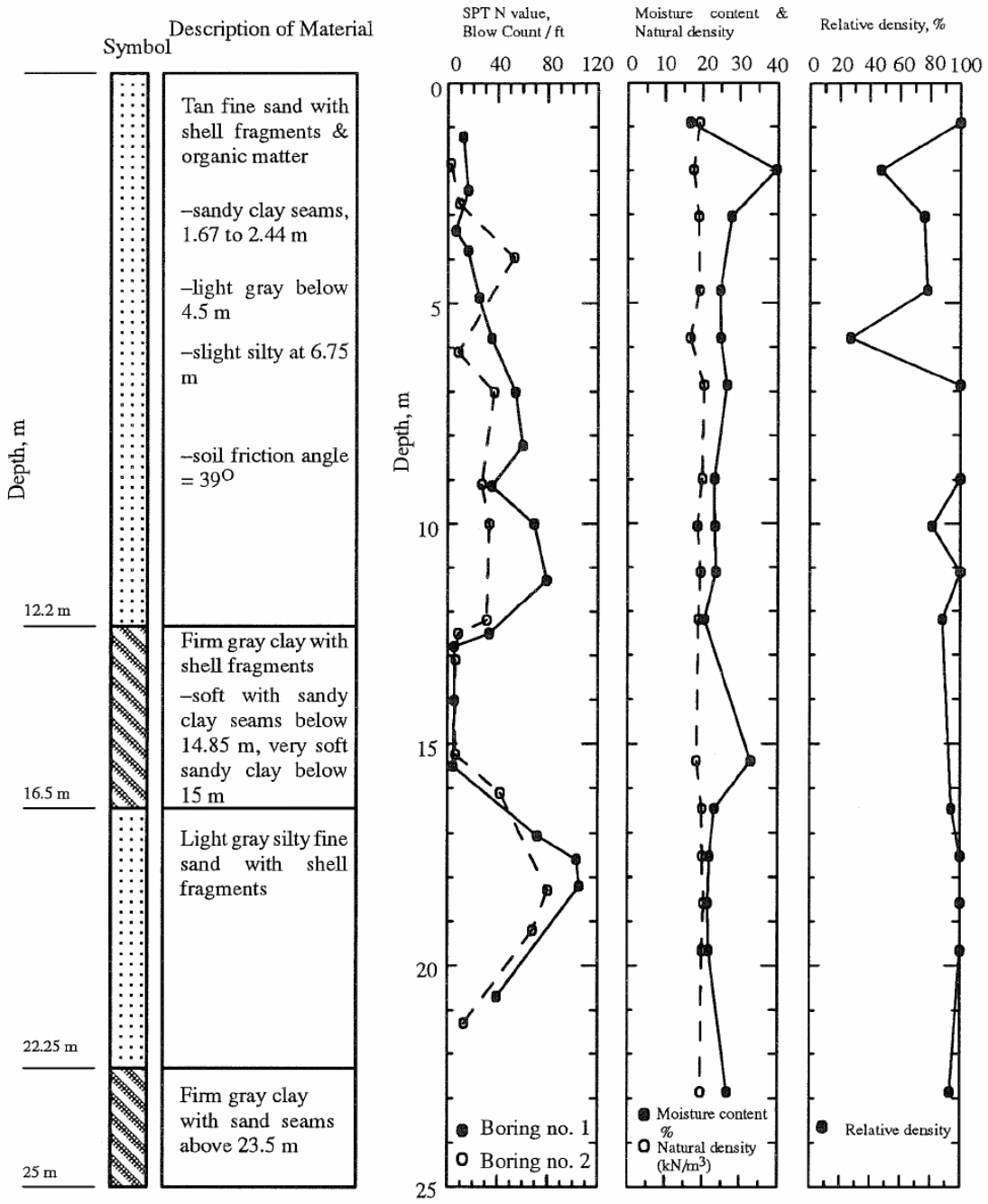

Figure 4.2 Penetration test blow counts and relative density values (after Fan, 1996)

4.1.2 Finite Element Model

4.1.2.1 Geometry

The soil surrounding the test pile is modeled as a large cylinder, (Figure 4.3). The radius of the entire soil domain is about 33 times larger than the radius of the pile. Considering the fact that most inelastic soil deformation occurs in the vicinity of the pile and elastic deformation at the far field is not significant, this size of the soil domain is large enough to be considered as a horizontally infinite medium. Both pile and soil are modeled using 8-node brick elements. The exterior dimension of the pile is the same as the tested pile, but a larger thickness is used in the FE model. Thus, the modulus of the pile was adjusted so that the pile for the FE model has similar flexural rigidity with the original. Utilizing the symmetry of soil and pile, only half of the system was modeled. The boundary surrounding soil domain is assumed to be fixed in lateral movement and free in vertical movement, to allow settlement during gravity load application.

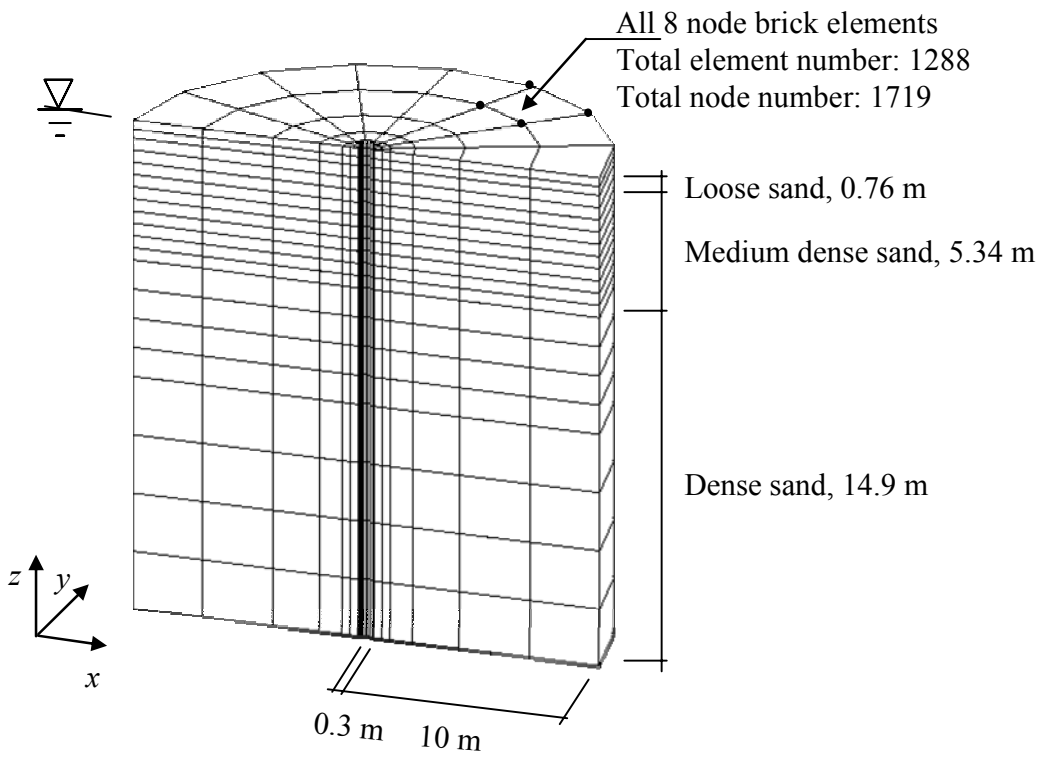

Figure 4.3 Finite element mesh of pile and surrounding soil

4.1.2.2 Soil Properties

By comparing SPT blow counts with physical properties of sand, the sand from a depth of 0.0 m to 6.1 m was classified as medium dense, 6.1 m to 12.2 m as dense, and 16.5 m to 22 m as dense sand (Reese et al., 1967). In the FE model, the backfilled sand layer, i.e., top 0.76 m, is assumed to be loose sand to account for the backfill. The layer from 0.76 m to 6.1 m is assumed to be medium-dense sand, and 6.1 m and below is assumed to be dense sand. Cox et al. (1974) reported that the friction angle of the sand in the tested site was 39 degree. As the relative densities of sand from the boring tests ranged from 45% to 100%, and blow counts varied from 12 to 79, as shown in Figure 4.2, assuming constant friction angle is not appropriate. In this verification study, the friction angle is assumed to be 29, 37, and 40 degrees for loose (0.76 m), medium-dense (0.76 m ~ 6.1 m), and dense layers (6.1 m and below), respectively. The friction angles as well as other soil properties are based on the suggestion by Yang et al. (2005) and are summarized in Table 4.1.

Table 4.1 Typical cohesionless soil properties

Property	Loose sand (Dr = 15%~35%)	Medium-dense sand (Dr = 65%~85%)	Dense sand (Dr=85%~100%)
Density, ton/m^3	1.7	2	2.1
Shear modulus, kPa at $p' = 80\,\text{kPa}$	55000	75000	130000
Bulk modulus, kPa at $p' = 80\,\text{kPa}$	150000	30000	390000
Friction angle, degree	29	37	40

4.1.2.3 Soil-Pile Interface

The soil and pile have distinctively different material properties. Thus, the boundary between the two materials should be appropriately represented in an FE model. Fan (1996) summarized that the soil-pile interface behaves in the following modes:

Stick: $\sigma_N^{'} > 0$ and $\left|\sigma_T^{'}\right| - \sigma_N^{'} \tan\delta < 0$

Slip: $\sigma_N^{'} > 0$ and $\left|\sigma_T^{'}\right| - \sigma_N^{'} \tan\delta \geq 0$

Debonding: $\sigma_N^{'} \leq 0$

where $\sigma_N^{'}$ is stress normal to pile surface, $\sigma_T^{'}$ is tangent stress, and δ is coefficient of friction between soil and pile. When normal stress is compressive and tangent stress at the contact of pile and soil is smaller than frictional resistant, soil and pile stick together (stick mode). When the tangent stress is larger than frictional resistant, the two materials slip (slip mode). When the normal stress is tensile stress, the soil debonds from the pile. This type of behavior is generic coulomb-friction material type and can be modeled with Pressure Dependent Material in OpenSees.

The frictional coefficient between soil and pile should always be equal or smaller than the internal frictional coefficient of the surrounding soil. Olson (1990) proposed a frictional coefficient as a function of blow count: based on the blow count, the frictional coefficient between soil and pile are chosen to be 15 degree for loose and medium-dense layers, and 30 degree for dense layers. These coefficients are within the range suggested by Das (2003), where friction coefficients are in the range of $0.5\phi' \sim 0.8\phi'$.

The thickness of the interface element should be close to zero in an ideal model. The zero-thickness interface elements have been developed in various ways. Elnashai (1984) developed the bond-slip element to model composite behavior of steel and concrete. Desai et al. (1984) developed an FE element to model the interface between soil and pile. When a brick element with coulomb-friction material property is utilized to model this interface element, it is not possible to use zero-thickness due to ill-conditioning of stiffness matrix. After parametric study, Desai et al. (1984) suggested that the ratio of thickness of the interface element to the dimension of the surrounding element can be in the range of 0.01 to 0.1. In the FE model of the tested pile, the thickness of the interface element is assumed to be 0.03 m.

4.1.3 Analysis Result and Comparison with Experimental Data

The FE analysis was conducted on a desktop computer with a Pentium IV 2.65 GHz and 1 GB of RAM. Before applying lateral displacement on top of pile head, gravity load was applied to impose confining pressure at soil. All layers of soil are modeled with pressure-dependent material because the property of cohesionless material strongly depends on confining pressure.

Load-deformation is compared with measured data and with analysis results based on Duncan et al. (1994), as shown in Figure 4.4. Duncan et al. proposed a characteristic load method that is simpler in the estimation of pile response than p-y approach. Figure 4.4 shows that the FE method does not exactly follow the measured data. Taking into account many unknown input parameters, however, this level of accuracy is regarded as acceptable in this study.

An exaggerated view of soil deformation around the pile head at 40 mm of lateral displacement at pile top is shown in Figure 4.5. The soil at the tail of the pile movement settles, while the soil at the direction of the pile movement bulges up. The settlement of soil is due to the force of gravity on cohesionless material.

Figure 4.6 shows x component normal stress distribution. The first two layers of elements (loose sand) have smaller resistance than the underlain medium-dense layers. Peak lateral stress occurs at the 4^{th} to 5^{th} layers (1.8 m ~ 2.3 m). It may be assumed from the stress distribution that the lateral pile response is very sensitive to the properties of top layers, approximately 5 to 10 pile diameter in depth. Soil behind the pile does not have noticeable tensile stresses, as cohesionless material cannot resist tensile force.

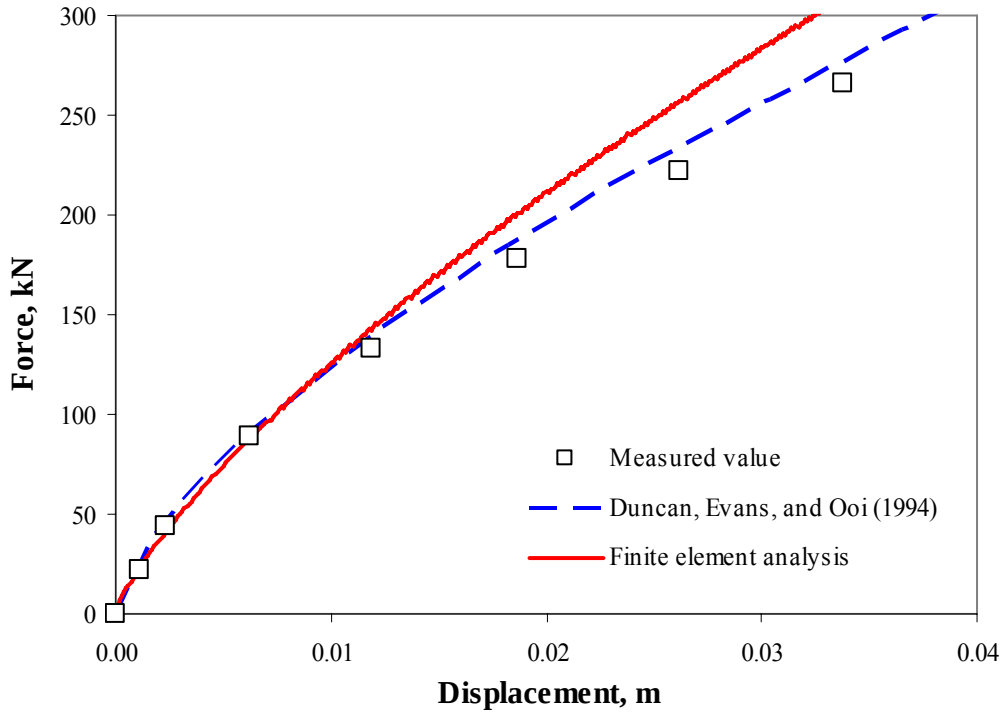

Figure 4.4 Load-displacement relationship at pile top

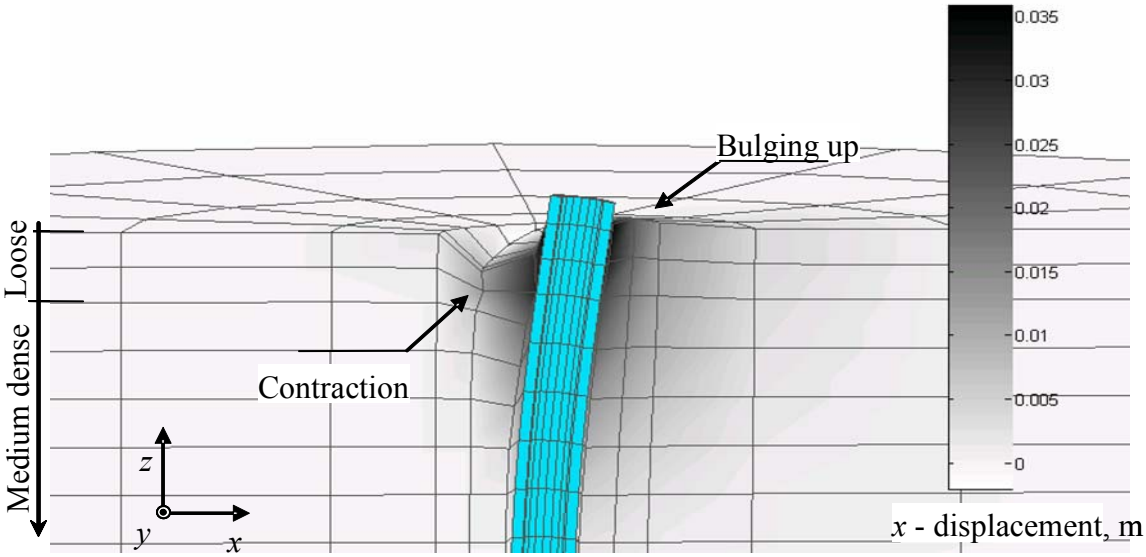

Figure 4.5 Soil deformation at pile top displacement of 40 mm

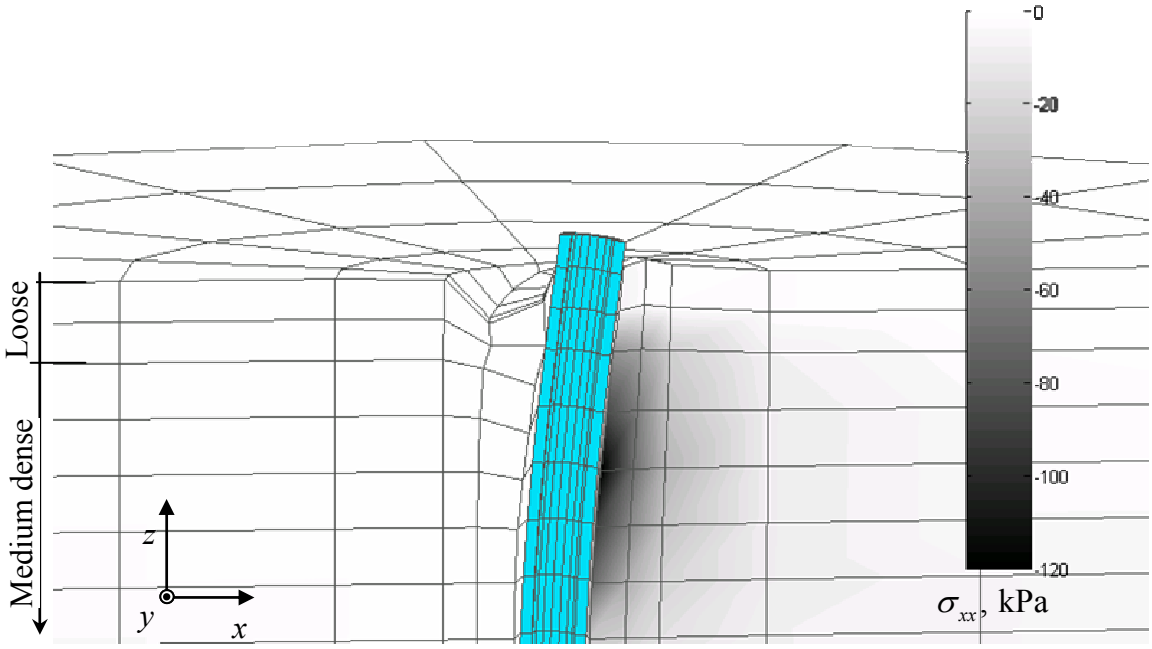

Figure 4.6 Stress distribution at pile top displacement of 40 mm

4.2 A Single Pile in Cohesive Material

In the previous section, a laterally loaded pile in cohesionless material is used to verify the FE approach with inelastic soil material model. In this section, a laterally loaded pile in stiff clay is used as a benchmark. These two case studies cover the two extreme soil conditions in the sense that one of them consists of all cohesionless layers and the other one consists of all cohesive layers. Throughout these two verification studies, it can be assumed that the FE approach with inelastic soil material can be adopted for other soil conditions that lie between these extremes.

4.2.1 Site Condition and Test Procedure

A brief summary of the site condition and test procedure is given in this section. For detailed test information, reference is made to Reese et al. (1975). A pit 13.7 m wide by 15.2 m long by 0.9 m deep was excavated at the test site and flooded with water to saturate the near surface clays to simulate conditions that would exist in an ocean floor. After the test pile was installed, a water table was maintained a few inches above the

ground level. A pile with a diameter of 0.61 and a thickness of 0.96 cm is used for the lateral load test. Before the pile was driven into the site, the thickness of the top 7 m of the pile was increased by 1.56 cm by wrapping the pile with semicircular steel sections. The total length of the pile below ground level is 14.9 m. Load is applied at 0.3 m above ground level, as shown in Figure 4.7.

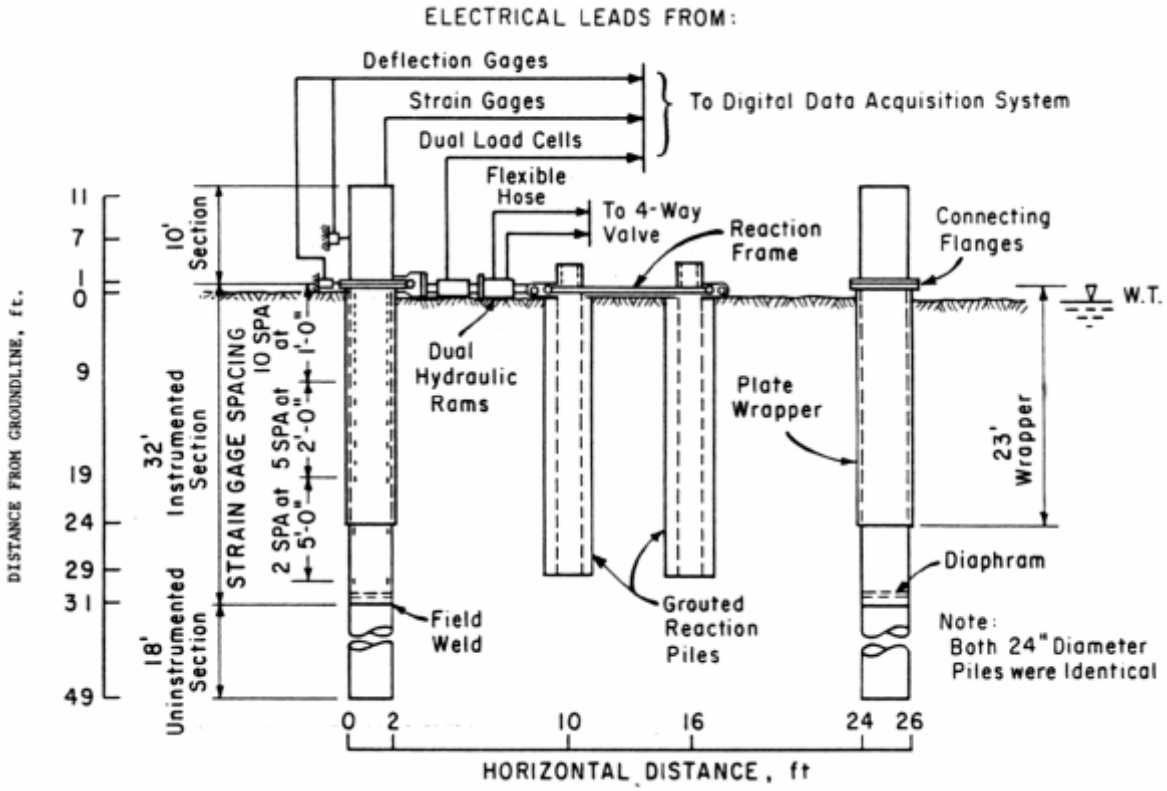

Figure 4.7 Lateral load test setup of a pile in cohesive soil
(after Reese et al., 1975)

The site consists of clay layers with increasing shear strength with depth. Three tests: unconfined, triaxial, and penetrometer were conducted to determine the undrained shear strength. The results from the tests were not consistent, however, as shown as Figure 4.8. The penetrometer tests overestimated at shallow depth and largely underestimated at 15 m depth in comparison with the other two tests. Reese et al. (1975) commented about the accuracy of the shear strength as follows:

- In the medium soft clays found in the upper 1.2 m, the in situ shear strength is accurately represented.
- In the zone from 1.2 to 3.0 m, the effect of jointing is serious and the actual shear strength is less accurately known. It is believed to be less than indicated by the penetromenter, but more than indicated by triaxial test.
- Below 3 m, jointing is still important, but the triaxial test results are probably good indicators.

The shear strength ranged from 30 kN/m^2 at the surface to 950 kN/m^2 at the 15 m depth. Figure 4.9 shows the soil profile along the depth of the test site. The boring test was made 4 months after the pit was excavated and flooded with water to represent the soil conditions at the time of the test.

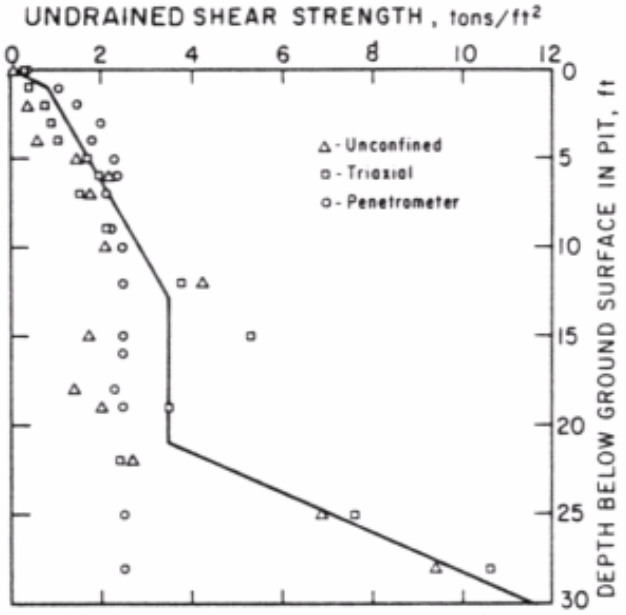

Figure 4.8 Shear strength distribution of test site
(after Reese et al., 1975)

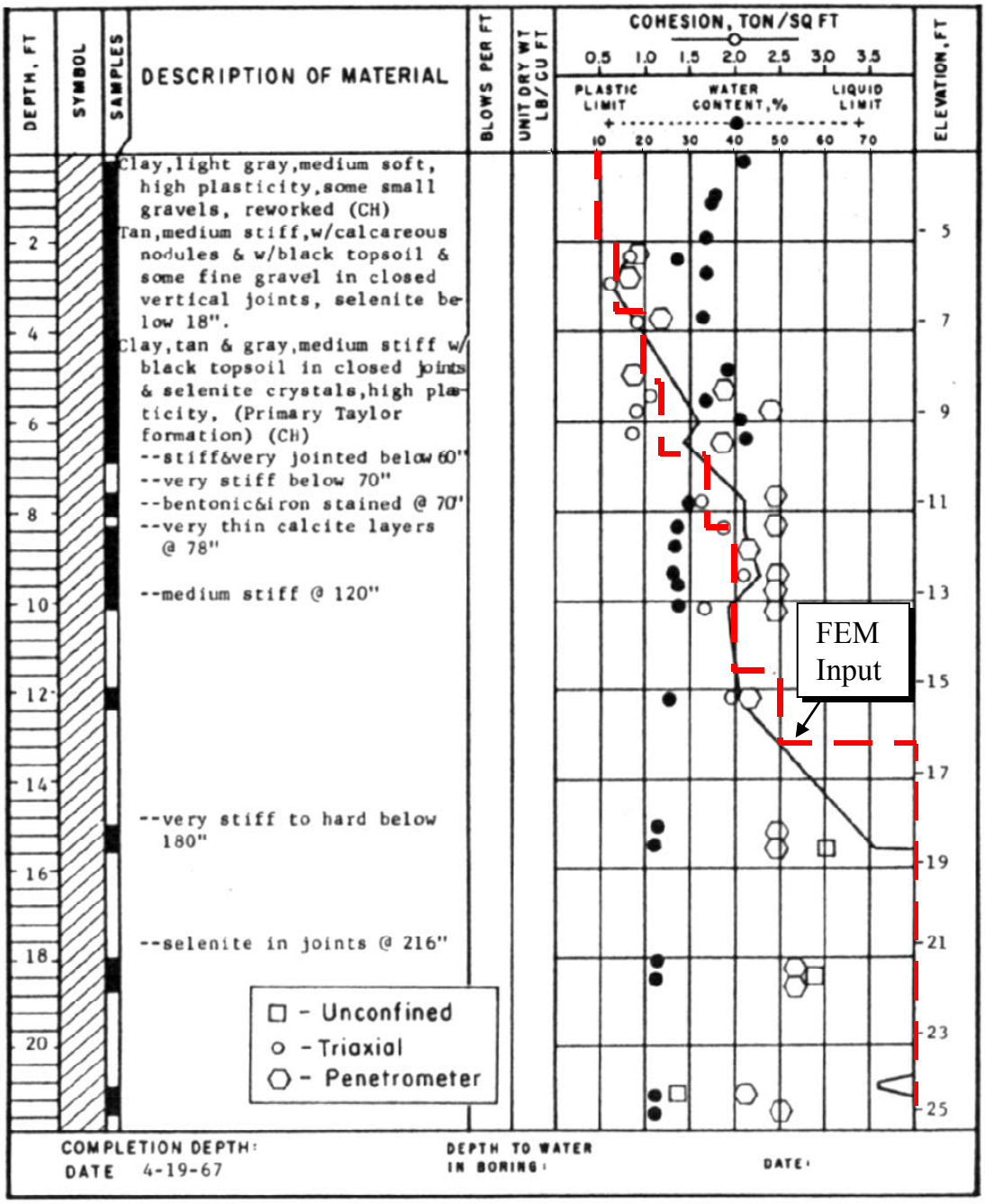

Figure 4.9 Soil profile of test site
(after Reese et al., 1975)

4.2.2 Finite Element Model

4.2.2.1 Geometry

The soil surrounding the test pile is modeled as a large cylinder, as shown in Figure 4.10. The radius of the soil domain is about 33 times larger than the radius of the pile. Both pile and soil are modeled using 8-node brick elements. The thickness of the pile is uniform in the FE model. Thus, the modulus of the pile was adjusted to account for the thickness variation along the depth of pile. Utilizing the symmetry of soil and pile, only half of the system was modeled. The boundary of the surrounding soil is assumed to be fixed in lateral direction.

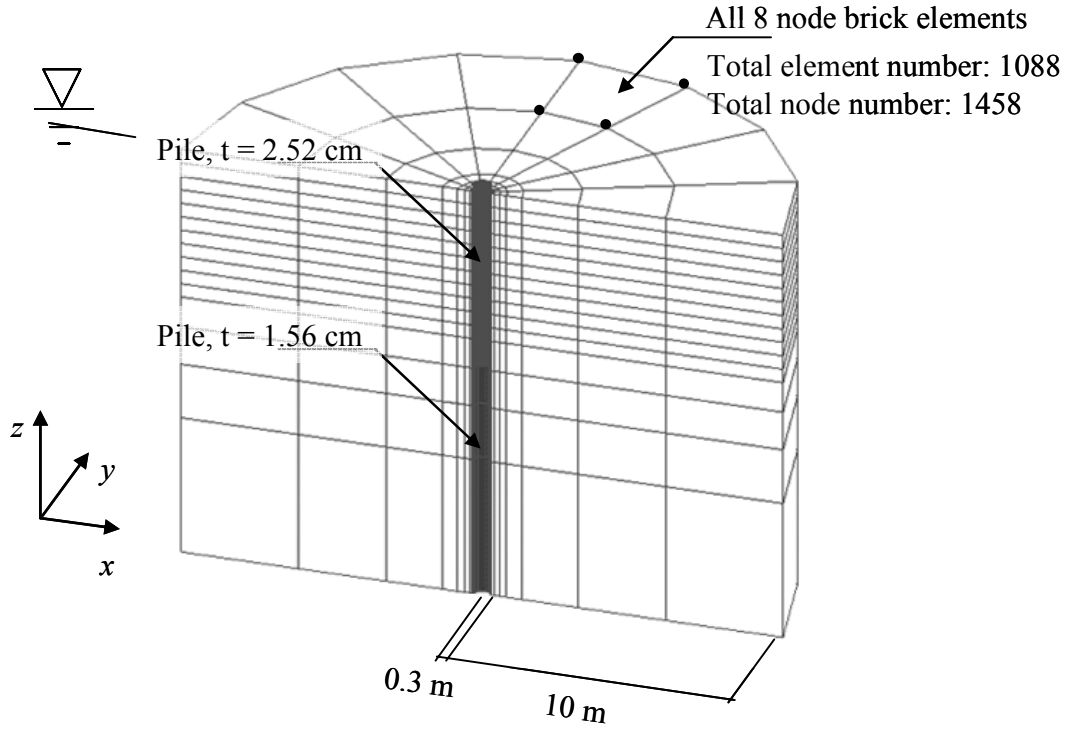

Figure 4.10 FE model of a pile in cohesive soil

4.2.2.2 Soil Properties

The soil is divided into 15 layers for the FE model, where the cohesion values from the results of the triaxial shear tests were used. In Figure 4.9, a dashed line indicates the cohesion values used in the analysis. Pressure-independent material in OpenSees, Yang et al. (2003a), is used to model clay. The material model requires shear and bulk modulus,

density, and cohesion. The test result did not provide any information other than cohesion. Thus, all other properties were assumed to follow the suggestion by Yang et. al. (2005), as summarized in Table 4.2.

4.2.2.3 Soil-Pile Interface

The interface between pile and clay should show cohesion, slip, and debonding. The pressure dependent material that was used in Case Study 1 cannot exhibit cohesive behavior. Taking into account that the load-deformation relationship is more sensitive to the formation and close of gap rather than cohesion and slippage of clay at the surface of pile, pressure dependent material is used as interface model. The friction angle of the interface element is kept very low, as it represents clay behavior at the pile surface. The thickness of the interface element is 1.3 cm.

Table 4.2 Typical cohesive soil properties

Property	Soft clay	Medium clay	Stiff clay
Density, ton/m^3	1.3	1.5	1.8
Shear modulus, kPa	13000	60000	150000
Bulk modulus, kPa	65000	300000	750000
Cohesion, kPa	18	37	75
Friction angle, degree	0	0	0

4.2.3 Analysis Results and Comparison with Experimental Data

Gravity was applied prior to applying lateral displacement on top of the pile head. All layers of soil are modeled with pressure-independent material, and it was assumed that the strength of the clay is only a function of cohesion (i.e., zero-friction angle).

Load-deformation is compared with measured data and with analysis results using the *p-y* method by Reese et al. (1975) in Figure 4.11. The *p-y* method shows an exact match with the test results, as the *p-y* curves were derived from the measured data of pile rather than from soil material properties. The FE approach used in this study overestimated the stiffness at small displacement, which may result from approximation of elastic soil properties, such as shear and bulk modulus, which are not measured with soil specimens. Bowles (1996) suggested that hard clay has a shear modulus in the range of 17 to 36 MPa, which is less than 25% of what Yang et al. (2005) suggested. When the values suggested by Bowles were used, the FE analysis result was closer to experimental value than the result using shear modulus from Yang et al.

Figure 4.12 shows the deformed shape of the pile when the pile top displacement is 20 mm. The volume of the interface element using a pressure-dependent element increased significantly at the tail of pile movement. This volume increase without stress represents gap formation. Unlike the cohesionless material in Case Study 1, the soil behind pile does not settle down due to the cohesion of the clay. Figure 4.13 shows x-directional stress distribution where compression zone of the soil is clearly shown as a darkened area.

Figure 4.14 compares the hysteresis loop of a single pile in sand (Section 4.1) and in clay (this section). The effect of soil medium is distinctively shown in the figure. Note that the pile in the clay shows pinching behavior due to the formation and closing of the gap, while pile in sand does not. This subtle difference cannot be easily understood and modeled using a more simplified approach such as lumped spring or *p-y* method.

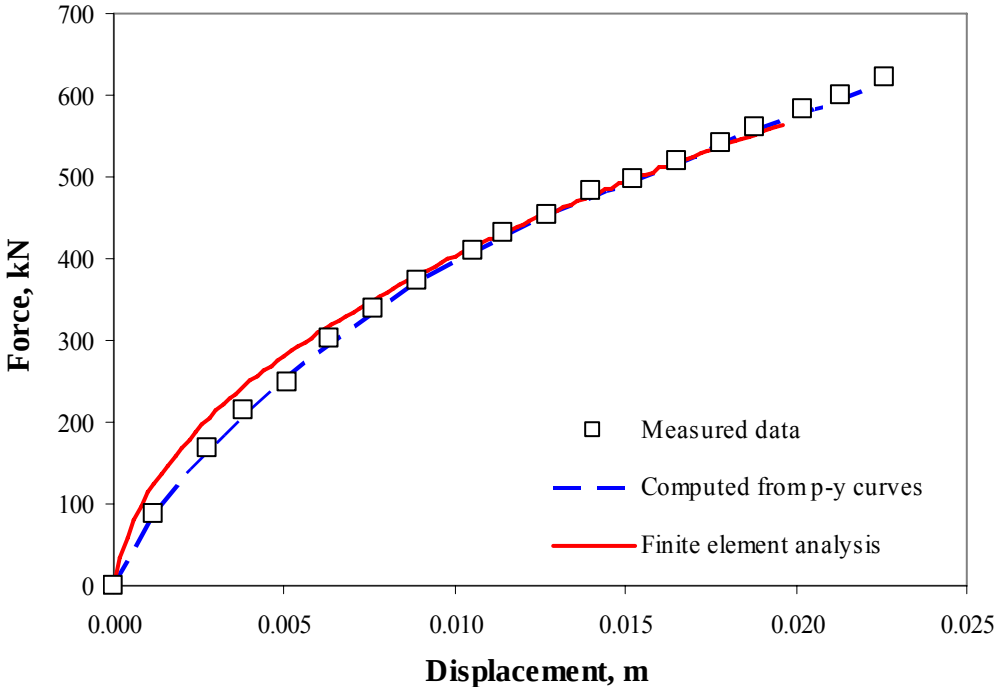

Figure 4.11 Load-displacement curves of a pile in cohesionless soil

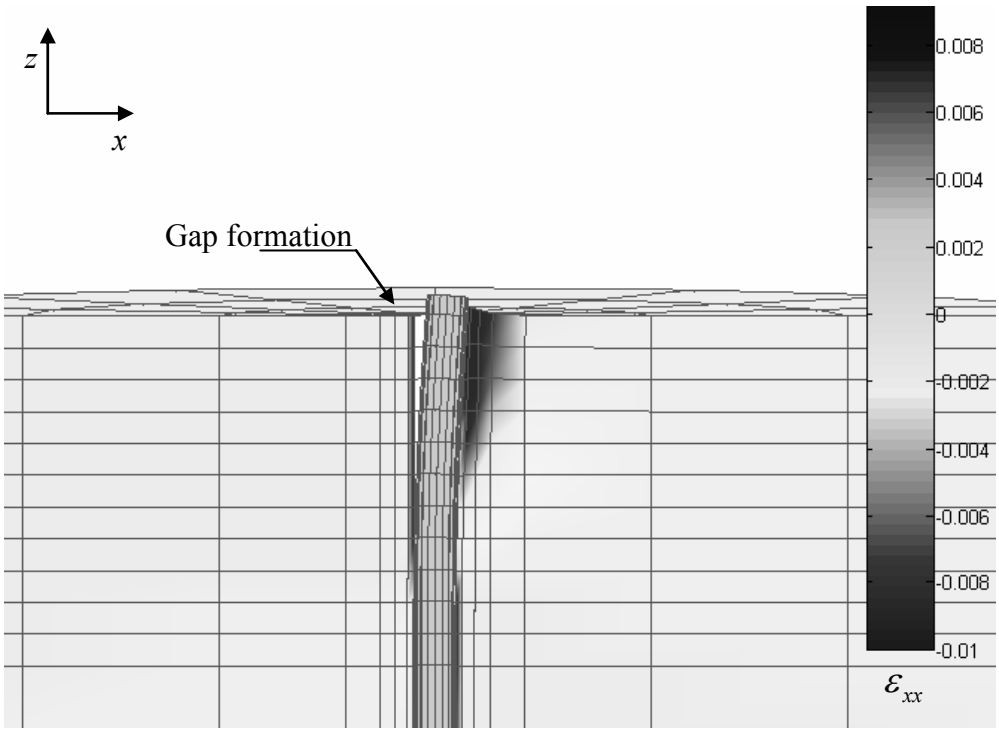

Figure 4.12 Soil deformation at pile top displacement of 20 mm

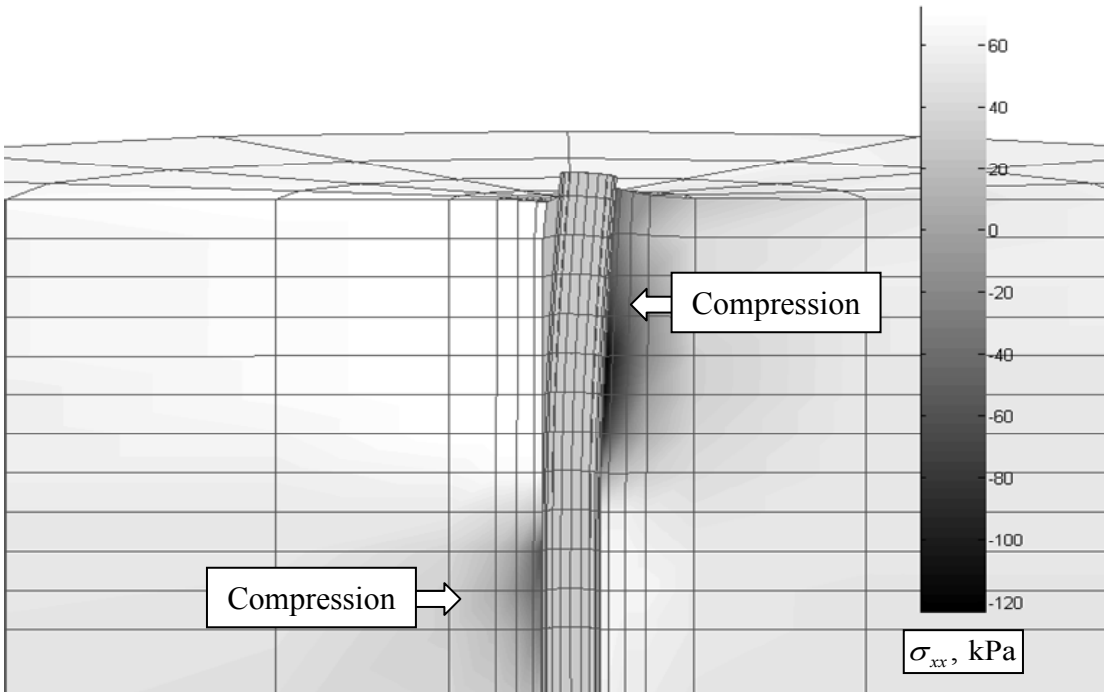

Figure 4.13 Stress distribution at pile top displacement of 40 mm

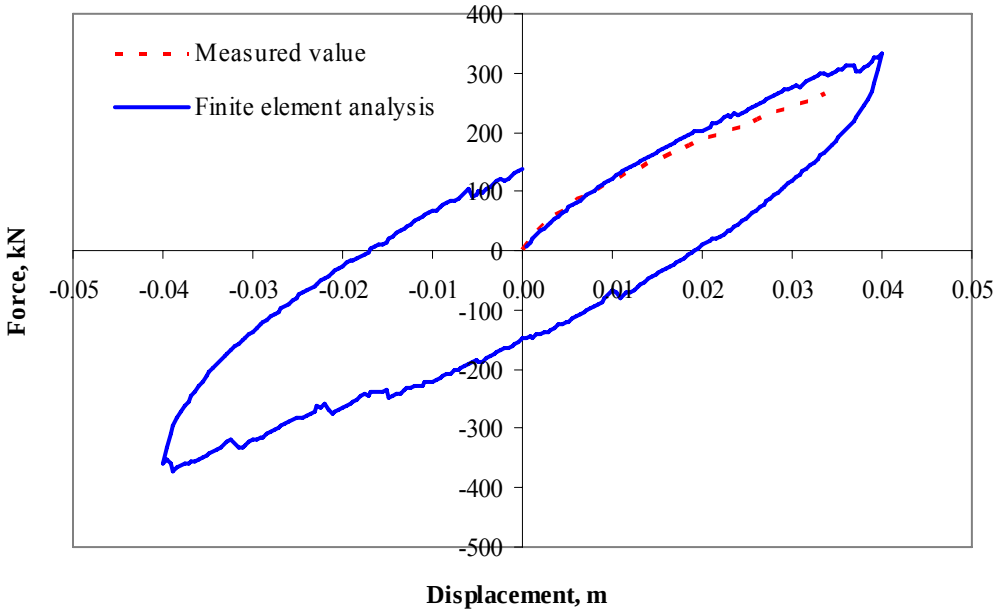

(a) Hysteresis loop of a laterally loaded pile in cohesionless material

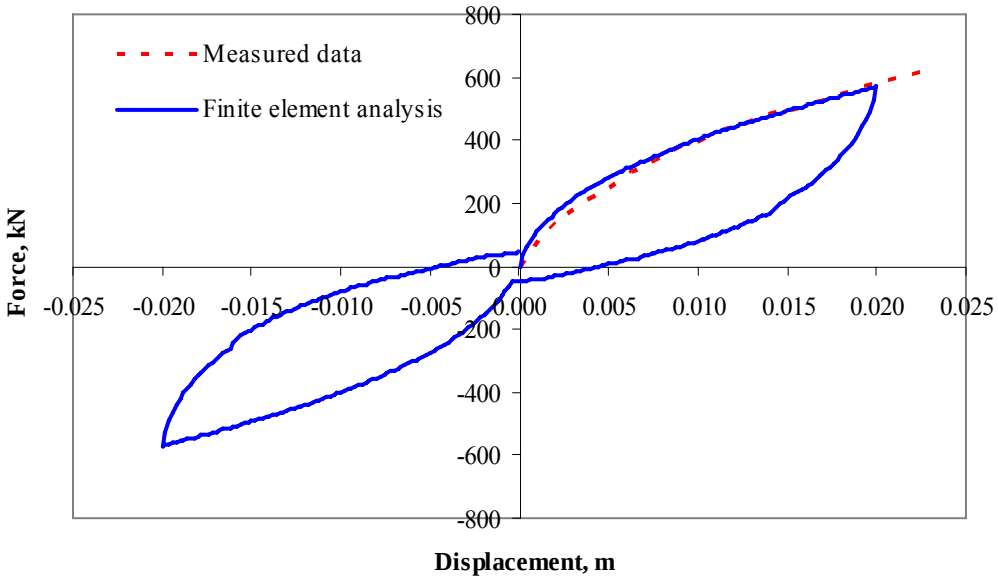

(b) Hysteresis loop of a laterally loaded pile in cohesive material

Figure 4.14 Comparison of hysteresis loops of single pile

4.3 Application I: Meloland Road Overcrossing Bridge

4.3.1 Introduction

The Meloland Road Overcrossing (MRO) Bridge is chosen as a benchmark for a soil-structure-interaction study. In 1992, the bridge was instrumented with 26 channels of accelerometers in 1978 and augmented by 6 channels. Twelve channels in a downhole array configuration were also installed to monitor propagation of waves from deep soil layers to the surface. The 1979 Imperial Valley Earthquake (M_L = 6.6) was the largest recorded event at the site, with peak ground acceleration of 0.32 g. The recorded ground motion from this earthquake has been studied extensively during the 1980s and 1990s (Norris and Sack, 1986; Werner et al., 1987; Zhang and Makris, 2002, among many others). To investigate the dynamic soil properties, suspension logging tests and lab tests of soil specimens were conducted. These studies, as well as recorded ground motions from five earthquakes, are used to validate the analytical approach presented in this study.

The main objective of this section is to verify the inelastic FE approach for running soil structure interaction analysis. The MRO Bridge is decomposed into three components: bridge, pile group foundation, and embankments. Each component is verified through comparison with previous studies and then combined for full soil-structure system analysis. The analysis is conducted with the UI-SimCor introduced in Section 3.3. The mass of embankments of the combined system is determined from modal properties of embankment. Then, the soil-structure system is analyzed for five sets of ground motions and compared with measured responses to verify this approach.

4.3.2 Bridge and Site Properties

The MRO Bridge is located over Interstate 8, approximately 0.5 km from the fault rupture of the 1979 Imperial Valley Earthquake. The bridge consists of two spans of prestressed box-girder decks monolithically connected to the center pier. The deck has three types of sections. In the vicinity of the center, the deck is fully filled with concrete. Near the pier connection and abutments, the deck consists with four webs, and top and bottom flanges. Most other portions are hollow box sections. The abutments are placed

on filled embankments. Seven piles are driven at each abutment. Each side of abutment has 5.9 m wing-wall. The dimensions of embankments are 7.9 m in height, 42 m in bottom width, and 10.4 m in top width. The side slope of the embankment side is 0.5. The pier at the center of the bridge is 7.9 m in height from the top of piles, with a diameter of 1.5 m. A total of 18 longitudinal reinforcement bars are used in the pier. The pier and its foundations are supported on 25 timber piles, spaced at 0.91 m. Figure 4.15 depicts the configuration of MRO Bridge with the location of accelerometers in the transverse direction. Reference is made to Zhang and Makris (2001) for detailed dimensions of the bridge.

The MRO Bridge site has a deep soft alluvium profile. The dynamic properties of the site were investigated as part of the ResOlution of Site Response Issues from the Northridge Earthquake (ROSRINE) test program (Anderson, 2003). The shear wave velocity ranges from 140 m/sec near the surface to 730 m/sec at the depth of 150 m. Figure 4.16 shows shear wave velocity profile from the suspension logging test and lab tests with soil lithology along the depth of the site.

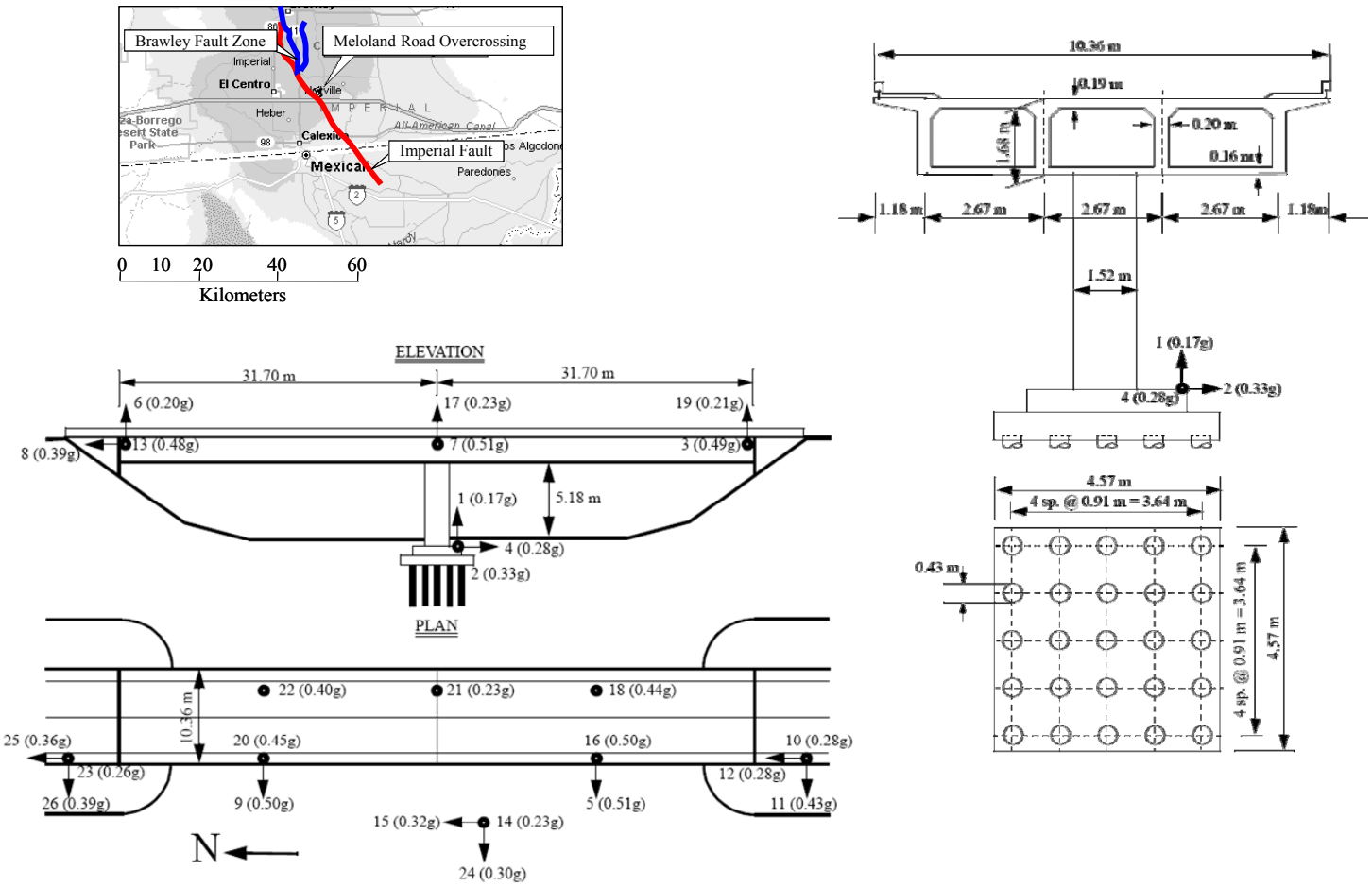

Figure 4.15 Location and configuration of MRO Bridge
(after Zhang and Makris, 2001)

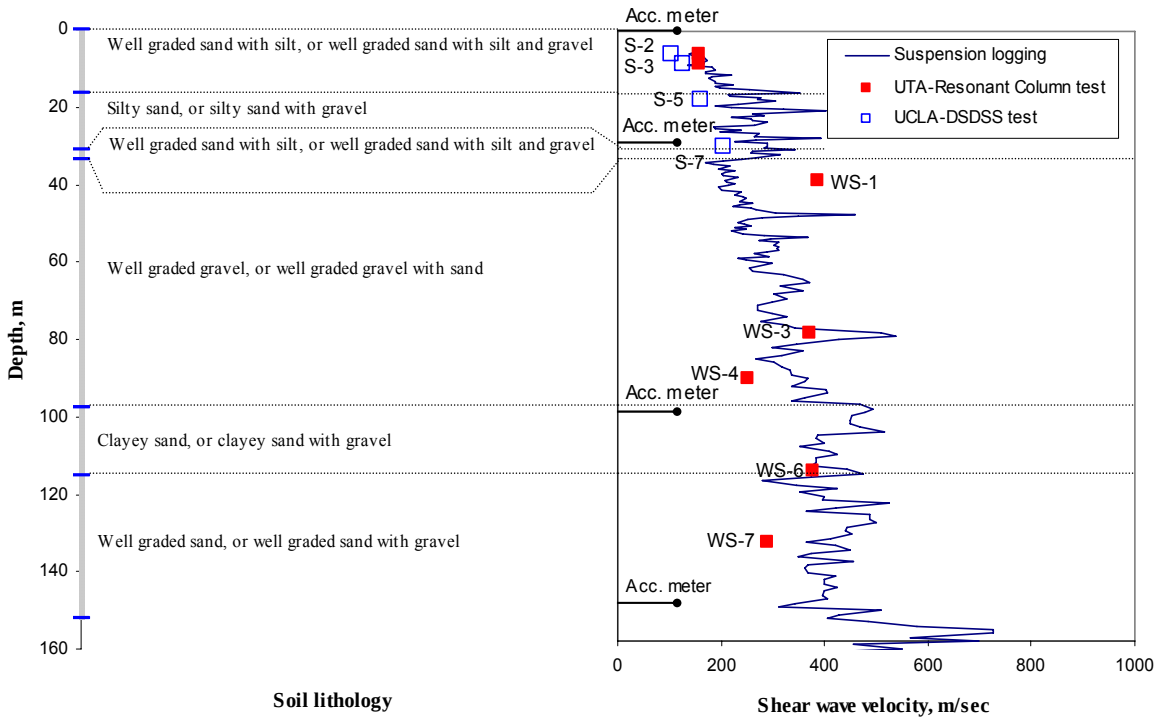

Figure 4.16 Shear wave velocity profile of the MRO Bridge site

4.3.3 Pile Group Analysis

The stiffness of this pile group has been investigated by several researchers (Zhang and Makris, 2002; Douglas et al., 1991; Wilson and Tan, 1990a, 1990b; Maragakis et al., 1994). The latter researchers ran a 3D FE analysis using an equivalent linear approach. In their analysis, the modulus of elasticity was initially assumed to be equal to the widely accepted standard values corresponding to the soil type of each layer. Poisson's ratio was 0.5 for saturated layers. For unsaturated layers, the Poisson's ratio was estimated based on the values provided by Bowles (1996). After running elastic analysis, the deformation of each layer was used to adjust the shear moduli for the next iteration based on standard shear modulus reduction versus shear strain curves. The iteration was continued until the modulus of elasticity converged. The results were provided in the form of stiffness as a function of displacements and rotations. As this approach used the equivalent linear method, it could not accurately estimate the inelastic constitutive behavior of soil especially at large strain levels. At very low strain levels, the result of this approach can

be considered close to in-situ values. In their analysis, a coarse mesh was used with 310 solid elements and 75 beam elements to define 25 piles and 7 layers of soil. Advances in computational power and inelastic soil material models allow more involved and representative analysis of the same pile group. In this study, an inelastic analysis using realistic soil material models is conducted to estimate the stiffness of the pile group.

4.3.3.1 Finite Element Model

Pile properties

The timber piles used in this study have diameters of 32 cm at the top and 20 cm at the bottom. The modulus of elasticity of the timber pile is assumed as 1.24×10^7 kPa following Maragakis et al. (1994). In the FE model, the piles are assumed to be prismatic with rectangular cross sections. Thus, the modulus of elasticity is adjusted so that the flexural rigidities are similar to the original piles.

Soil properties

Strength parameters such as friction angles and cohesion are important for large strain response, while the elastic shear modulus and bulk modulus have a dominant role in small strain response. Norris (1986) reported friction angles and cohesion of the studied site. Recently, as part of the ROSRINE project (Anderson, 2003), field and laboratory tests of the MRO Bridge site were conducted. A suspension logging test was used to estimate in-situ shear wave velocity. For laboratory tests, combined Resonant Column/Cyclic Torsional shear (RC/CT) tests and Dual Specimen Direct Simple Shear (DSDSS) tests were conducted. Figure 4.17 compares the low-strain shear modulus used in the study of Maragakis et al. (1994), the RC/CT test, the DSDSS test, and from in-situ suspension logging test. The results of these tests showed a similar trend; shear wave velocities generally increase with the depth of soil. However, the shear wave velocity estimated from each test varied significantly, in the order of several hundred percent. The lab tests provided more detailed dynamic properties than the in-situ tests. Those values, however, were not enough for utilizing three-dimensional nonlinear material models. Therefore, in the current study, standard values suggested by Yang et al. (2005) are

adopted. The unknown material properties are inferred from cohesion for clay and friction angle for sand. In Maragakis et al. (1994), the clay layers are located between 0~2.7 m, 6 m~10.7 m, and 15 m and below. Each clay layer has a cohesion of 35.9 kPa, 76.6 kPa, and 86.2 kPa, respectively. Based on the latter values, shear moduli are chosen as 60,000; 150,000; and 150,000 kPa, for each clay layer, respectively. Seed and Idriss (1970) reported the relationship between cohesion and shear modulus as a function of shear strain. At very low strain levels (shear strain smaller than 10^{-5}), the ratio of shear modulus to cohesion ranges from 1000 to 3000. For the above shear modulus values, the ratios are 1671, 1960, and 1740, all of which are within the range established by Seed and Idriss. Poisson's ratio of the clay layer is assumed to be 0.4. The other in-between layers are silty sand with friction angle of 32 to 33 degree and relative density of 45 ~ 52%. All layers with cohesionless soil are in the range of medium sand by Yang et al. (2005). Figure 4.18 shows summary of material properties used in this study.

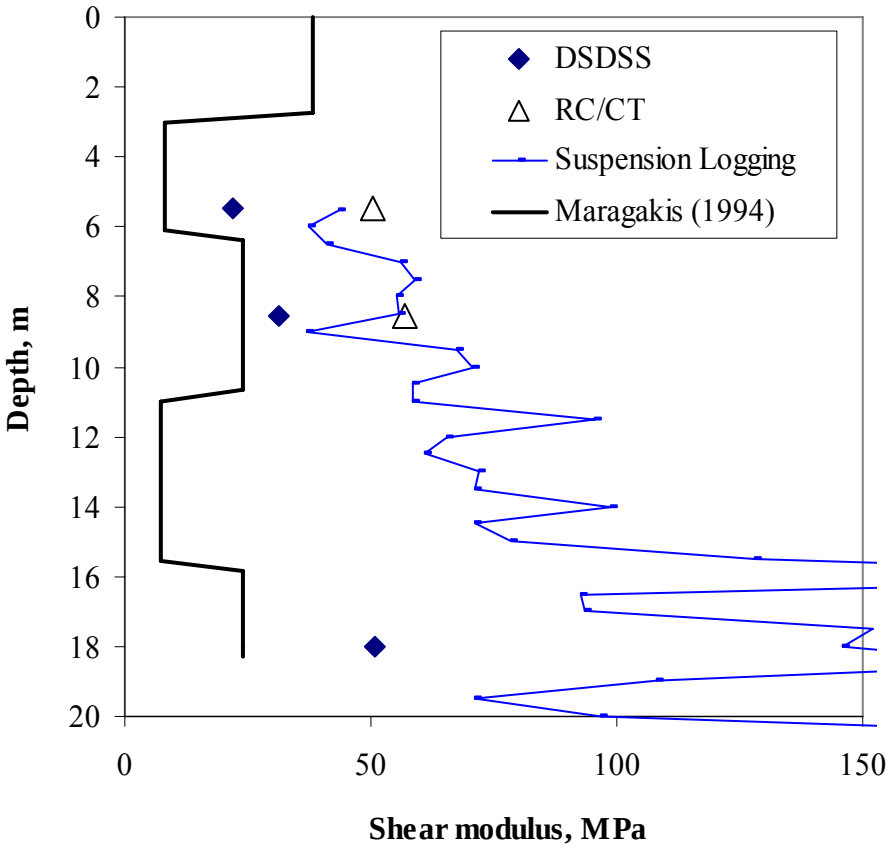

Figure 4.17 Shear wave velocity profiles from various sources

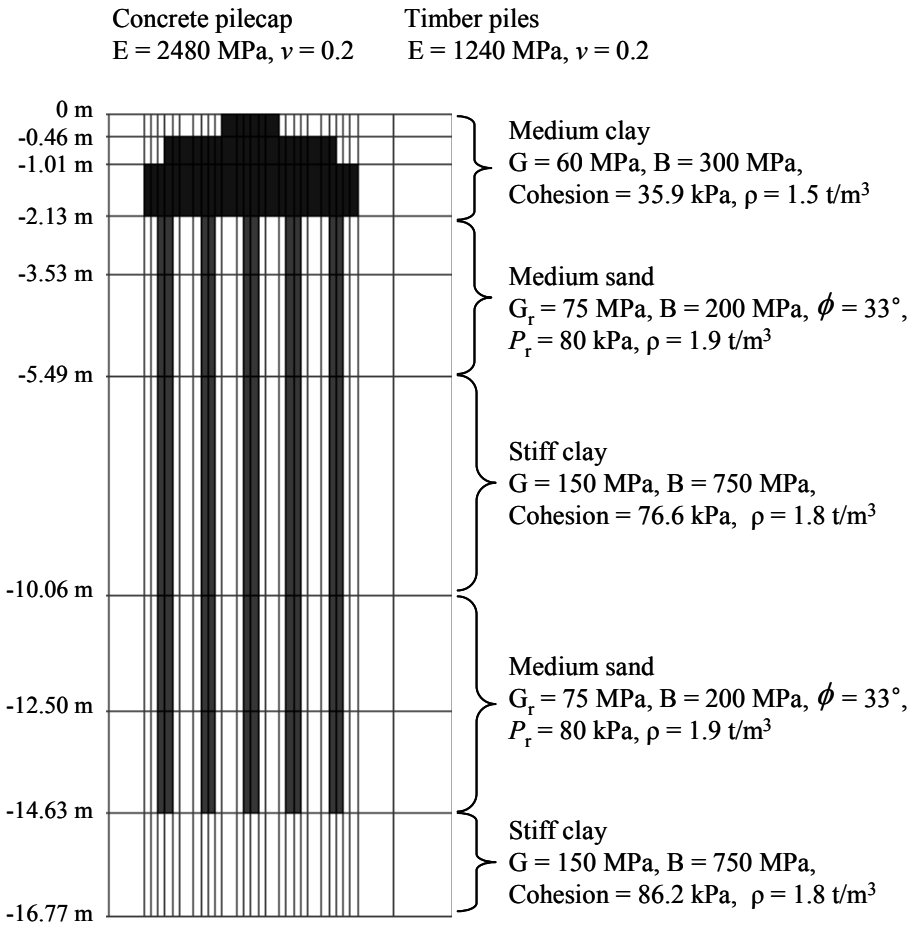

Figure 4.18 Material properties used for pile-group analysis

Finite element mesh

Two models with different levels of refinements are used. It is expected that the behavior of a pile group is more governed by global soil–pile group interaction rather than soil–pile interaction of individual shafts. Therefore, interface elements between pile and soil are not included in this analysis. A cylindrical soil medium with a diameter of 48 m is modeled, which is 10.5 times larger than the pile cap dimension. The depth of the soil medium is 17 m, as shown in Figure 4.19. This dimension of soil medium is considered to be large enough to capture the inelastic soil behaviors in the vicinity of pile group and elastic soil deformation far from the pile group. Two levels of mesh refinements are investigated; one with 1818 and the other with 2916 elements, as shown in Figure 4.20 (a) and (b), respectively. In both models, symmetry is utilized to reduce the number of

elements. Circular piles are replaced with an equivalent rectangular cross section to reduce the number of elements. All elements are 8-node brick. The top of the pile cap is restrained by a control node, which connects the top nodes of the pier with rigid frame elements.

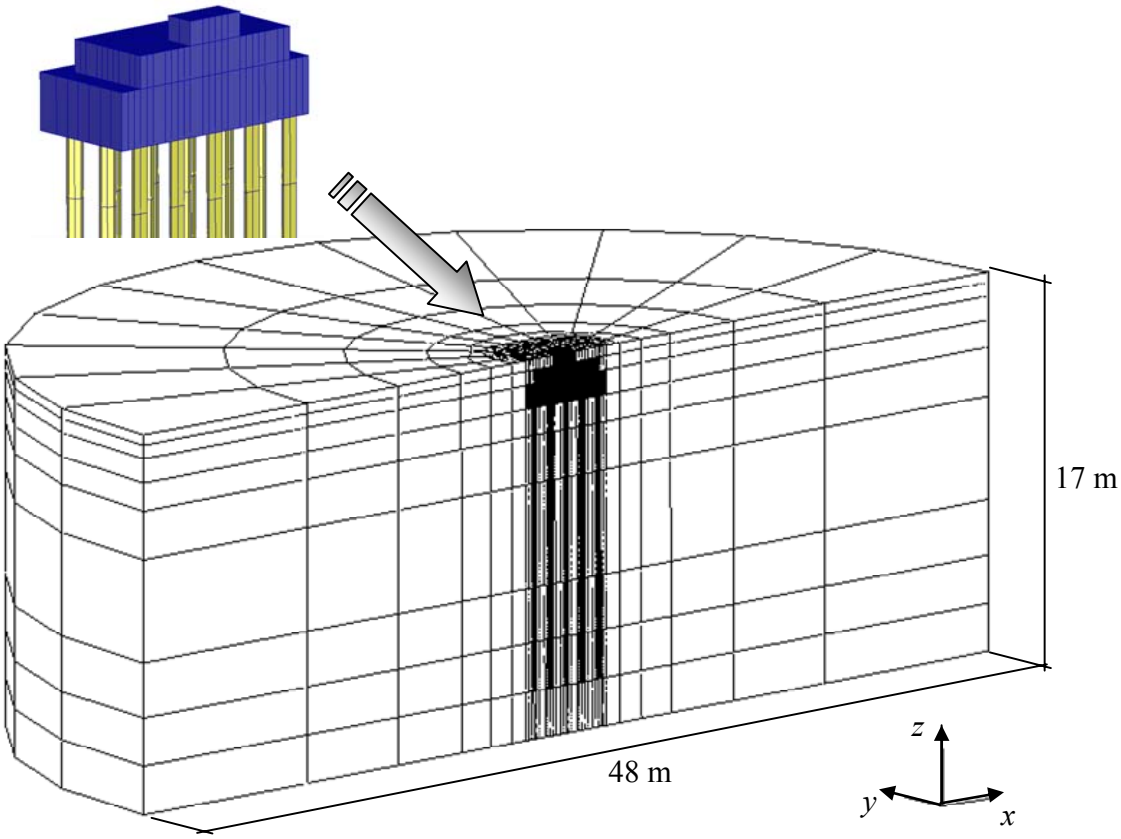

Figure 4.19 Three-dimensional FE model of pile group

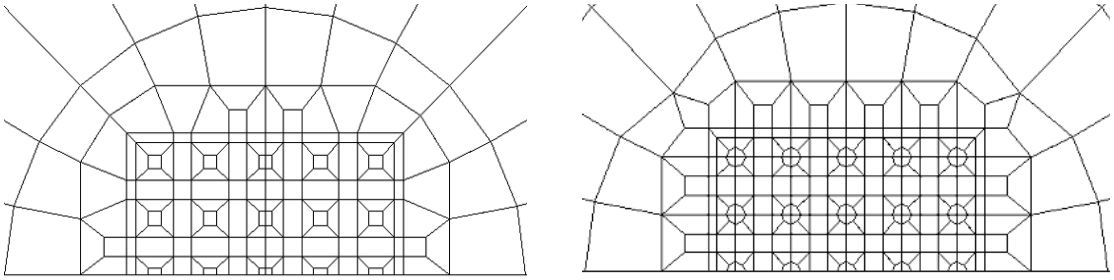

(a) FE mesh with 1818 elements (b) FE mesh with 2916 elements

Figure 4.20 Two level of mesh refinements

4.3.3.2 Analysis Result

The horizontal, rotational, and vertical stiffness values are estimated by applying displacements and measuring reaction forces. Figure 4.21 shows the evaluated horizontal stiffness and compares it with previous studies. Note that some previous work is based on equivalent linear methods corresponding to a certain level of ground excitation, which partially explains the difference of estimated stiffness. The following is observed from the stiffness comparison:

- The estimated stiffness values from previous researchers vary significantly due to largely different approaches employed.
- The stiffness from inelastic FE approach is within the range of the previously proposed values.
- Two level of mesh refinements result in very similar stiffness values, which shows that for pile group behavior, global soil deformation is more important factor than that of a single pile analysis.

The estimated stiffness properties are for a low displacement amplitude of 0.6 mm. Therefore, the similarity between two levels of refinement is expected. To compare the effect of mesh refinement deep into the inelastic range, pushover analyses are conducted. Figure 4.22 shows the displacement–load curve for the two models. It is confirmed from that the coarse mesh with 1818 elements is acceptable. Figure 4.23 shows the distribution of x-directional normal stress, σ_{xx}. The stress distribution shows that a compressive zone is formed at diagonal direction from the pile cap. It is important to take into account the influence of pile cap on the behavior of pile group, which is mostly neglected in simplified approaches, such as *p-y* springs with beam on Winkler-type foundation, for calculating pile-group stiffness. Figure 4.24 and 4.25 compare vertical and rotational stiffness from inelastic FE approaches with the stiffness values from previous researches.

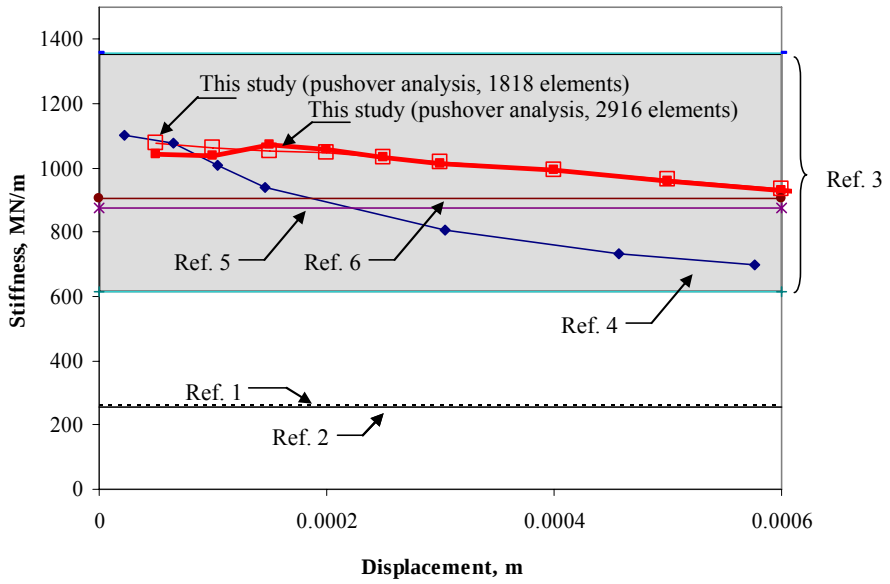

Ref 1. Zhang and Makris [2001]: Equivalent linear method with lumped spring representation

Ref 2. Douglas, Maragakis, and Vrontinos [1991]: System identification

Ref 3. Crouse [1992]: Estimation from experimental data

Ref 4. Maragakis, Douglas, and Abdel-Ghaffa [1994]: Equivalent linear FE analysis

Ref 5. Maragakis, Douglas, and Abdel-Ghaffa [1994]: Optimal values identified from dynamic field test

Ref 6. Norris and Sack [1986]: Equivalent linear method with beam on Winkler foundation method (*p-y* type approach)

Figure 4.21 Comparison of *x*-directional stiffness

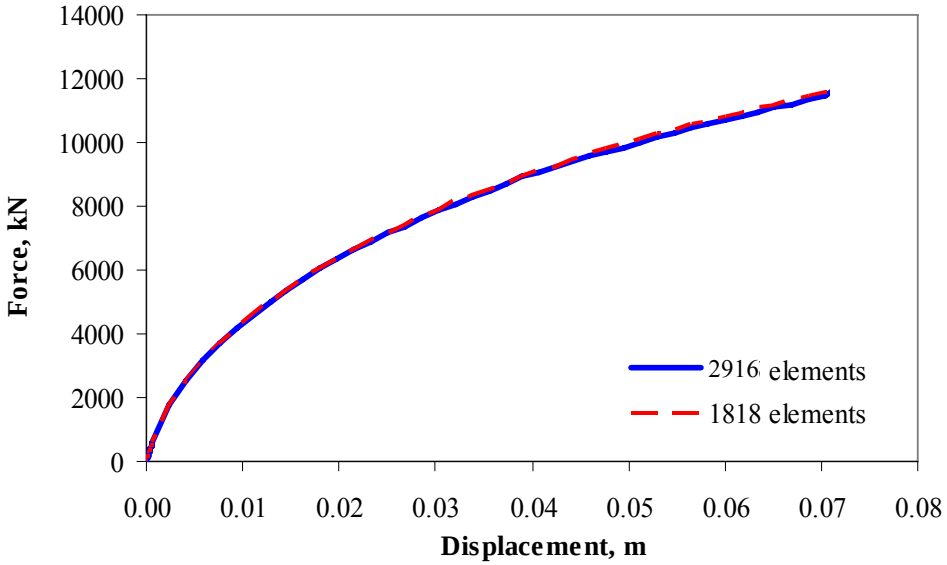

Figure 4.22 Load-deformation characteristics of two levels of mesh refinement

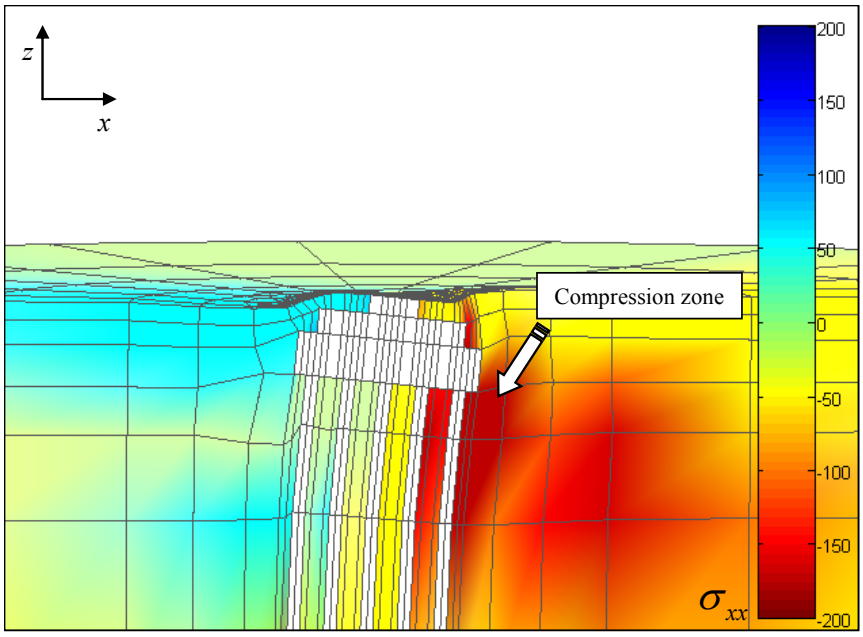

Figure 4.23 Normal stress (σ_{xx}) distribution

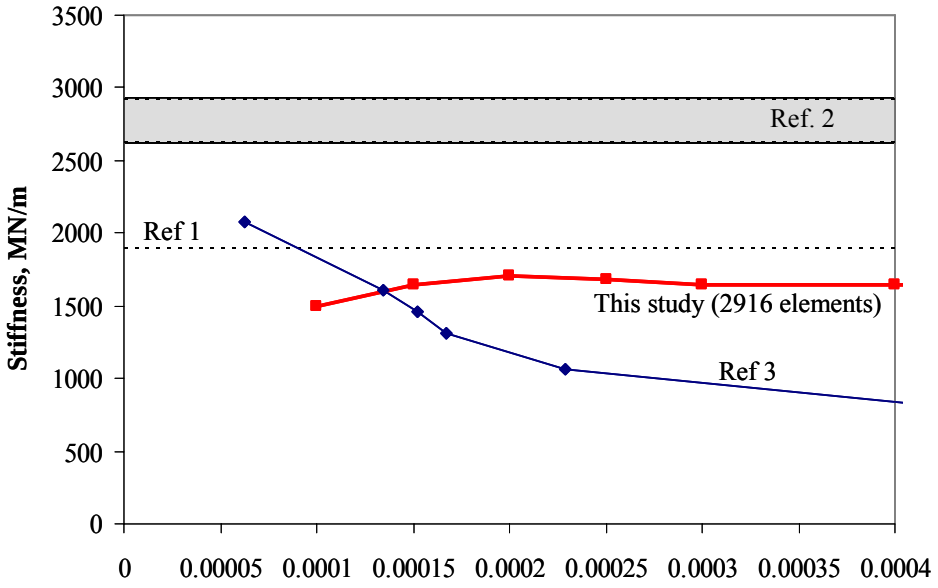

Ref 1. Douglas, Maragakis, and Vrontinos [1991]: System identification

Ref 2. Crouse [1992]: Estimation from experimental data

Ref 3. Maragakis, Douglas, and Abdel-Ghaffa [1994]: Equivalent linear FE analysis

Figure 4.24 Comparison of vertical stiffness

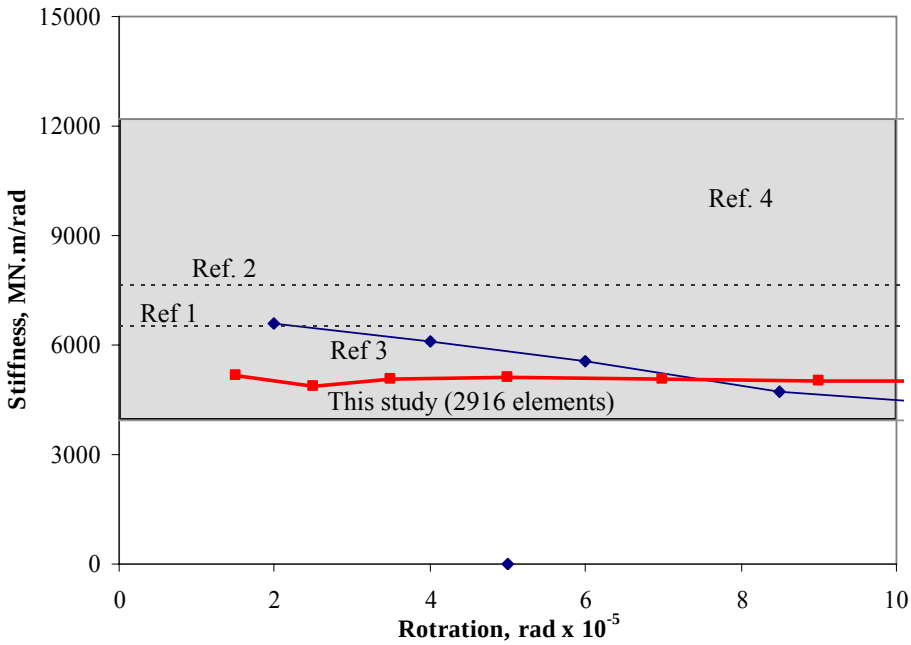

Ref 1. Douglas, Maragakis, and Vrontinos [1991]: System identification

Ref 2. Zhang and Makris [2001]: Equivalent linear method with lumped spring representation

Ref 3. Maragakis, Douglas, and Abdel-Ghaffa [1994]: Equivalent linear FE analysis

Ref 4. Crouse [1992]: Estimation from experimental data

Figure 4.25 Comparison of rotational stiffness

4.3.4 Embankment Analysis

The MRO Bridge is monolithic with abutments that are supported by seven timber piles of 18 m length. The embankment and abutments system has been studied by several researchers using widely different approaches. Wilson and Tan (1990a, 1990b) proposed a simplified method to calculate equivalent stiffness of abutments. This approach is useful to obtain an approximate estimate of the embankment stiffness in the early design process. However, it does not account for the existence of piles, abutments, nonlinearity and mass of soil. Moreover, the selection of effective length of embankment is somewhat arbitrary, and can critically affect the calculated stiffness. Werner et al. (1993) proposed

guidelines for modeling the dynamic properties of the approach embankment in which the embankment may be modeled as a lumped mass supported on a transverse embankment spring. The transverse stiffness of embankment is equivalent to Wilson and Tan's unit transverse stiffness applied to an embankment length equal to about one-sixth of the total length of the bridge. The solution of Werner et al. is not general as it is calibrated to MRO empirically and relies on approximations which may or may not be applicable to other bridges. Price (1997) proposed an equivalent linear method to model embankments. Energy dissipation at the abutment was accounted for by increasing effective viscous damping as a function of the maximum shear strains. There have been attempts to analyze short span bridges using nonlinear 3D FE models. Sweet and Morrill (1993) and McCallen and Romstad (1994) analyzed the Painter Street Overcrossing Bridge with nonlinear FE. Sweet and Morrill recommended using direct model of soil and pile systems. In the current study, a nonlinear 3D FE approach is adopted.

4.3.4.1 Finite Element Model

Material Properties

The material properties of embankment fills are based on Zhang and Makris (2002), in which density of $\rho_s = 1600\ kg/m^3$ and shear wave velocity of $V_s = 110\ m/\sec$ are used. These values correspond to shear modulus of 19.4 MPa, which belongs to the category of soft clay by Yang et al. (2005). In Zhang and Makris (2002), soil nonlinearity and damping is accounted for by using average modulus reduction and damping curves proposed by several other researchers. Inel and Aschheim (2004) surveyed properties of typical embankment fills from the California Department of Transportation. In their work, the plasticity index of embankment fill ranging from 5 to 40 is used. In the current study, pressure-independent material is used with material properties shown in Figure 4.26. The pressure-independent soil model implemented in OpenSees uses the following equation to define peak octahedral shear strength:

$$\tau_f = \frac{2\sqrt{2}\sin\phi}{3-\sin\phi} p_i^{'} + \frac{2\sqrt{2}}{3} c = \frac{G_r \gamma_{\max}}{1+\gamma_{\max}/\gamma_r} \tag{4.1}$$

where ϕ : friction angle, 0 is used for clay

c : cohesion

$p_i^{'}$: initial effective confining pressure

G_r : reference shear modulus

$\gamma_{\max}$: maximum shear strain

γ_r : reference shear strain

The octahedral shear stress and strain is defined as a type of hyperbolic function:

$$\tau = \frac{G\gamma}{1+\frac{\gamma}{\gamma_r}\left(\frac{p_r^{'}}{p^{'}}\right)^d} = \frac{G\gamma}{1+\frac{\gamma}{\gamma_r}} \tag{4.2}$$

where G : shear modulus, $G = G_r$ for clay with $d = 0$

d : pressure dependence coefficient

The above-referenced relationship is converted to modulus reduction curves and compared with previous research by Vucetic and Dobry (1991), in Figure 4.27. The pressure-independent material model is similar to the modulus reduction curve of plasticity index 30, which is within the range used by Inel and Aschheim (2004). Soil properties of supporting ground are approximated from the properties used in the pile group analysis in Section 4.3.3. As the supporting ground will remain mostly in the elastic range, the soil domain is divided into three layers along the depth. Top layer with 7.5 m of thickness is modeled with medium clay and layers below 7.5 m depth are modeled with stiff clay. The properties of timber piles are taken from the study by Maragakis et al. (1994).

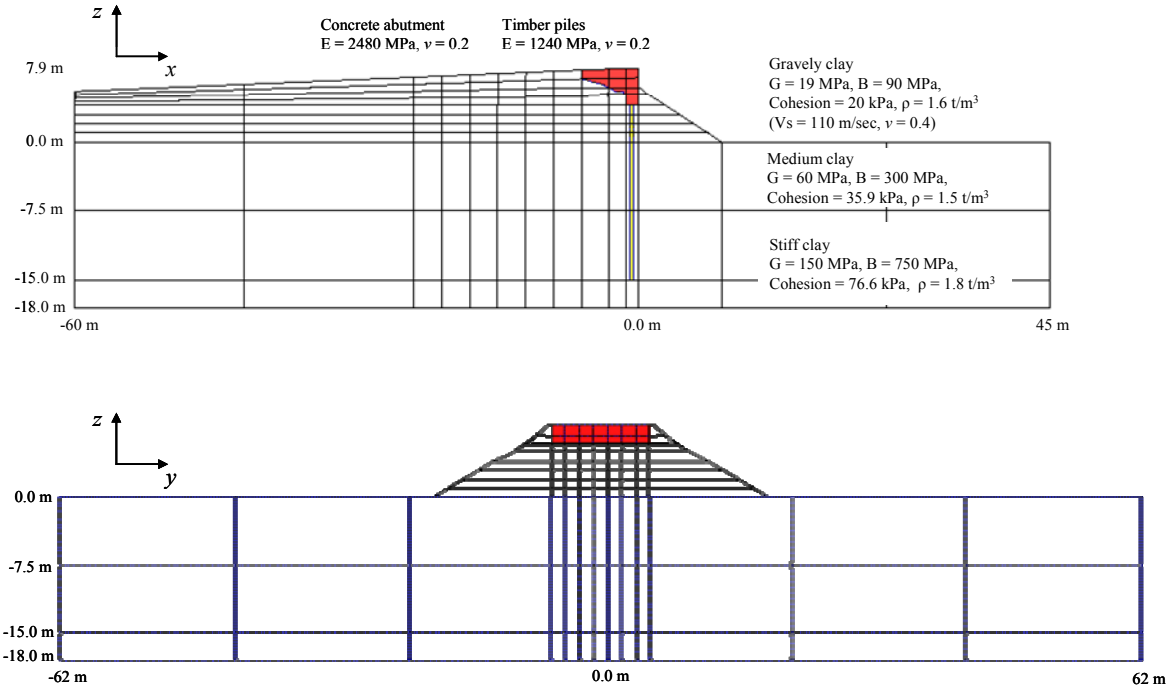

Figure 4.26 Configuration of pile-embankment-abutment system

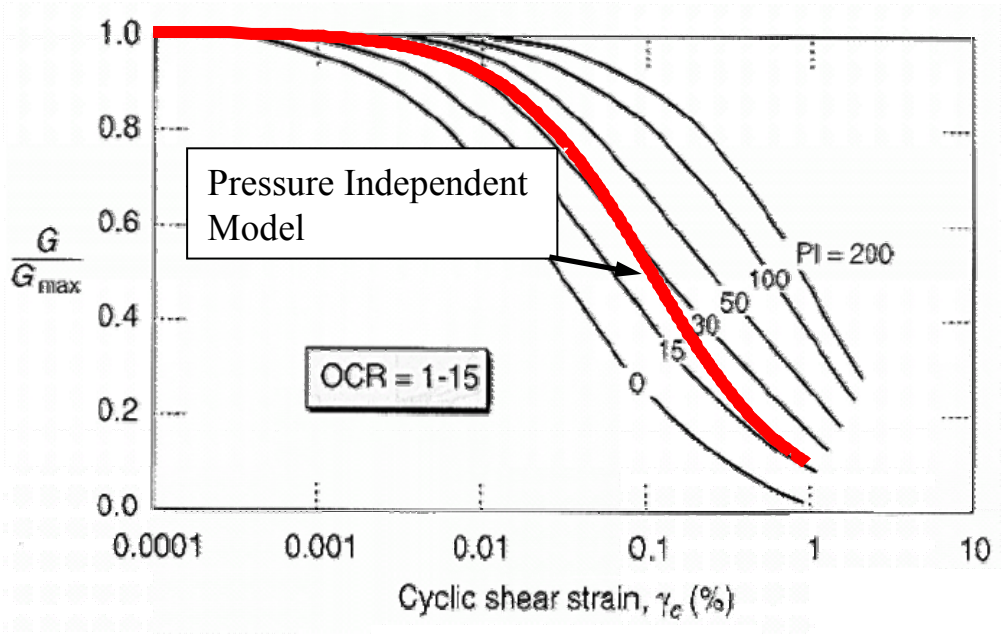

Figure 4.27 Comparison of shear modulus reduction curves

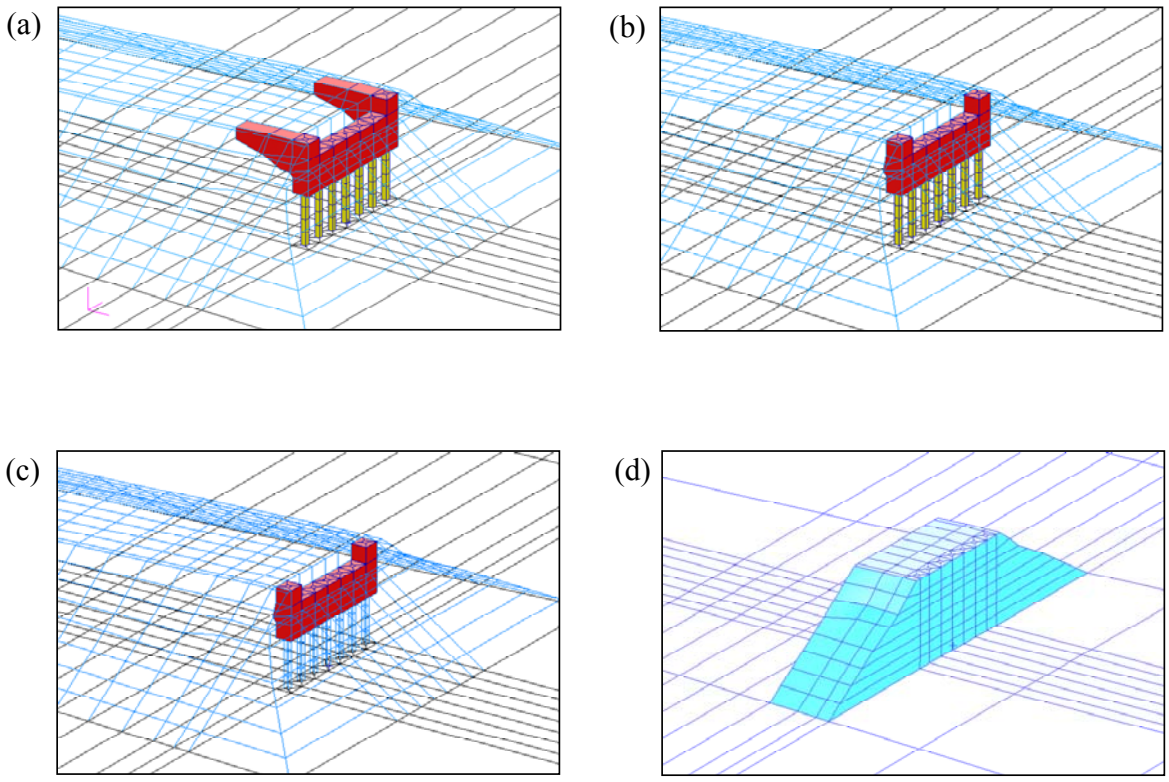

Figure 4.28 Four different FE models of embankment

Finite Element Model

All components are modeled with 8-node brick elements. The dimension of the supporting ground is 124 m by 105 m in plan with 18 m of depth, Figure 4.26. Four different abutment and embankment models are tested, as shown in Figure 4.28.

- Full embankment, wing wall, abutment and pile model
- Full embankment, abutment, and pile model (without wing wall)
- Full embankment and abutment model (without wing wall and piles)
- Embankment with effective length in Wilson and Tan (1990a); in the figure, the top of the embankments are constrained with concrete.

Timber piles in models (a) and (b) are modeled with rectangular brick elements. Assuming that the behavior of abutment and embankment is governed by global soil deformation rather than opening and closing of the gap between pile and soil, interface elements are not used for this analysis. The overall dimension of abutment in model (a) is similar to the dimensions described in previous studies. In model (a), a total of 1675 elements are used to model supporting ground, embankment, abutment, and pile groups.

A control node is placed at the top of abutment and connected to the top nodes on the abutment with a rigid frame element.

4.3.4.2 Analysis Result

Stiffness Evaluation

The evaluated stiffnesses are compared in Figure 4.29. In this figure, the analysis result from this study is identified as models (a), (b), (c), and (d) for the different embankment models in Figure 4.28. The followings are observed from the comparison.

- Comparison between model (a) with model (b) and (c) shows that the effects of wing wall and piles are non-negligible. Without piles and wing walls, the initial stiffness can be reduced by 22 %.
- Comparison of models (a) and (d) shows that representing the embankment for the length of wing wall significantly underestimates the stiffness.
- The elastic stiffness (stiffness at very small displacement) of model (d) is identical to the stiffness calculated by Wilson and Tan (1990a). However, local yielding of the embankment top reduced stiffness at a small displacement. The method by Wilson and Tan (1990a) should be applied with great caution in determining shear modulus and effective length of embankment.
- Comparison of model (a) with Ref. 3, 4, 5, and 6 in Figure 4.29 shows that the previous studies seem to underestimate embankment stiffness.

The above-referenced observations show that the bridge embankment system should be modeled including abutment, piles, and a sufficient length of embankments. Defining effective length for the embankment needs further parametric scrutiny, which is beyond the scope of this study. Using a simplified approach such as equivalent linear method or simplified embankment (shear beam model or simple formulae) may be appropriate only with careful consideration in choosing equivalent strain and effect of pile and abutments.

Figure 4.30 shows the stress ratio at the section of embankment at the abutment displacement of 100 mm. The stress ratio in the figure is defined as the ratio of deviatoric stress at Gauss point to yield stress of the material. As may be seen in Figure 4.30 (b), the embankment behind the wingwall contributes severe resistance against the transverse

movement of the abutment. Consequently, using only the wingwall length as an effective embankment length may underestimate the embankment stiffness, which partially explains the difference in stiffness between models (d) and (a) in Figure 4.29.

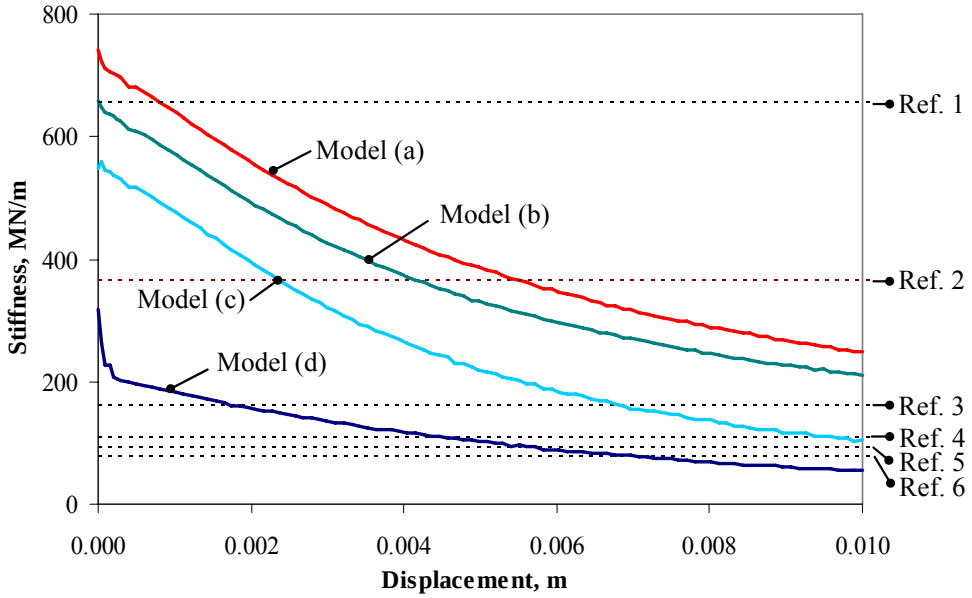

Ref 1. Caltran: Method A [from Zhang and Makris 2002]

Ref 2. Douglas, Maragakis and Vrontinos [1991] (values identified from dynamic test)

Ref 3. Wilson and Tan [1990]

Ref 4. Werner [1994]

Ref 5. Douglas, Maragakis and Vrontinos [1991]

Ref 6. Zhang and Makris [2002]

Figure 4.29 Comparison of transverse stiffness of embankment

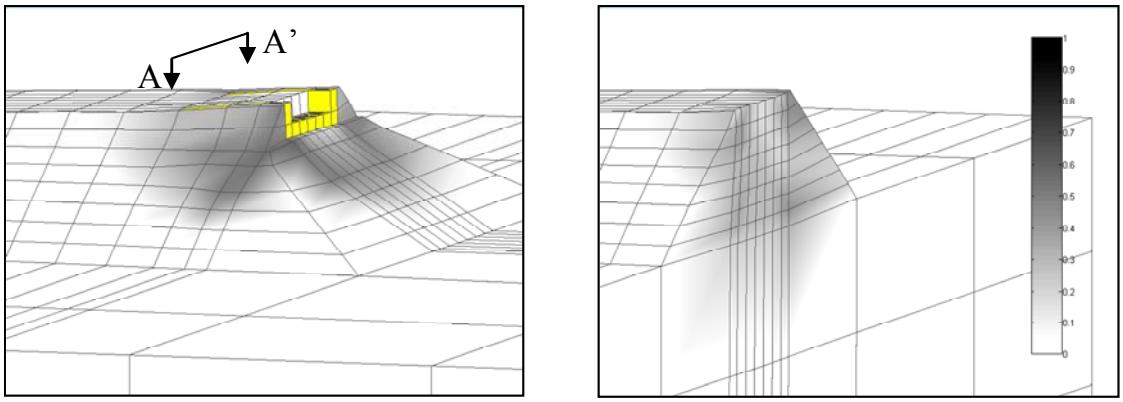

(a) Stress ratio - full embankment view (b) Stress ratio - section A-A' view

Figure 4.30 Yield stress ratio at a section of embankment

Period Evaluation

Eigen value analysis is conducted for model (a), in Figure 4.28. The first transverse and longitudinal modes are shown in Figure 4.31. The first mode is in the longitudinal direction with a fundamental period of 0.319 sec. The second mode is in the transverse direction with a fundamental period of 0.314 sec. These modal properties will be used in the following section to define the lumped mass of embankment for hybrid simulation.

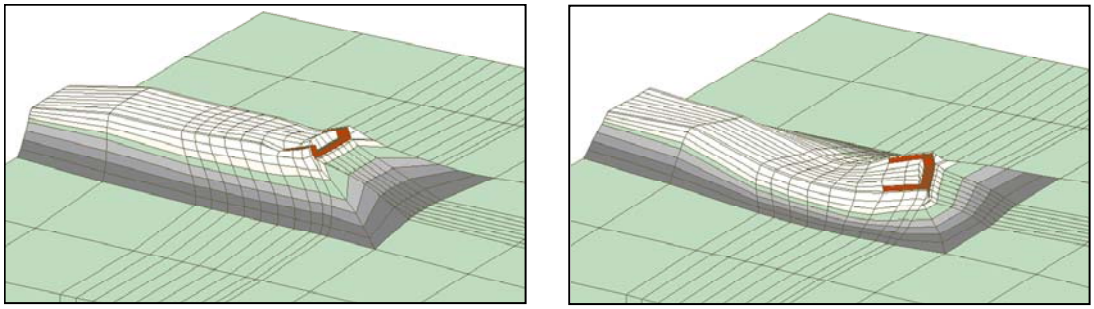

(a) 1st mode: 0.319 sec (b) 2nd mode: 0.314 sec

Figure 4.31 Fundamental periods and mode shapes of embankment

4.3.5 Soil-Structure-Interaction Analysis

4.3.5.1 Simulation Configuration

There have been various attempts to analyze highway overcrossing bridges, including embankment-bridge interaction. Many approaches used lumped springs and viscous dampers to model embankment, while others modeled bridge and embankment as a whole FE model. Based on the recorded Imperial Valley Earthquake in 1979, Werner et al. (1987) used the system identification method to assess seismic response characteristics of the bridge. In their research, they found that the transverse response of the structure is controlled by its abutment motions, with no significant dynamic amplification in the deck. For their conclusion to be reflected in the analytical model, the embankment mass and stiffness should be considerably larger than those of bridges. The previous simplified approaches, where lumped springs and dampers were used, do not fully consider the inertial effect of embankment, and the mass of the embankment is often neglected. The simplified approaches, as long as the overall system period is similar to the full model,

may result in reasonable agreement with measured data when ground motion levels are low, a problem of limited earthquake engineering significance. If the ground intensity is large and there is inelastic deformation of the embankments, the simplified approach cannot capture the effect of embankments on structural response and, therefore, the assessment results are unreliable.

In this section, the FE models in previous sections are utilized to represent the inelastic stiffness of supporting ground and embankments. The individual models are analyzed on different processors coordinated by the hybrid simulation framework UI-SimCor (Kwon et al., 2005). This approach is versatile because it combines any number of different analysis platforms or, if necessary, experiments. For models with a few coupled degrees of freedoms (DOFs), this approach is also efficient to reduce total time of analysis through distribution of computational time to several processors. The configuration of the analytical model is shown in Figure 4.32. The embankment and the bridge are coupled with one transverse DOF. The supporting pile groups and bridge are coupled with two DOFs: one transverse and one rotation. Inertial forces are represented by lumped masses placed on bridges and at the connection of abutment-bridge. The most realistic model may be modeling lumped masses at all nodal points, for which the distributed simulation framework requires large amounts of data communication. Therefore, the embankment mass is lumped at the abutment-bridge connection. The effective mass of the embankment is determined from natural frequency and stiffness considerations. From model (a) in Figure 4.28, the initial transverse stiffness of embankment is 741 MN/m. Assuming that the mass is lumped at the bridge-embankment connection, the mass can be calculated from the transverse period of embankment as $M = kT^2/(4\pi^2) = 1848\,ton$. The latter lumped mass approximately corresponds to the top half of embankment with 16 m of length, as shown in Figure 4.33.

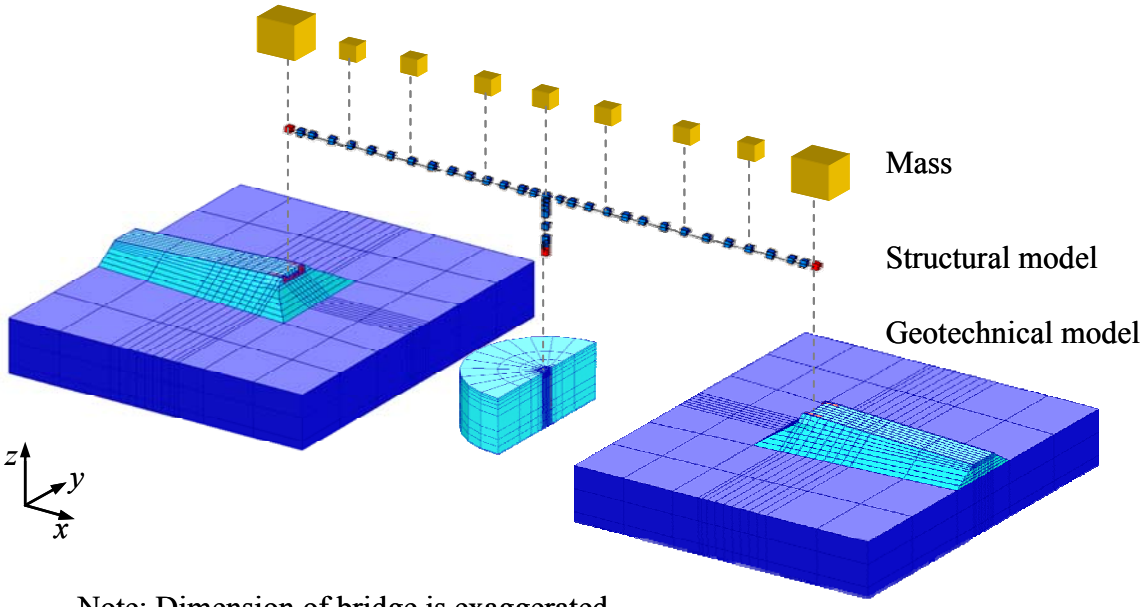

Note: Dimension of bridge is exaggerated.

Figure 4.32 Configuration of MRO bridge for multiplatform analysis

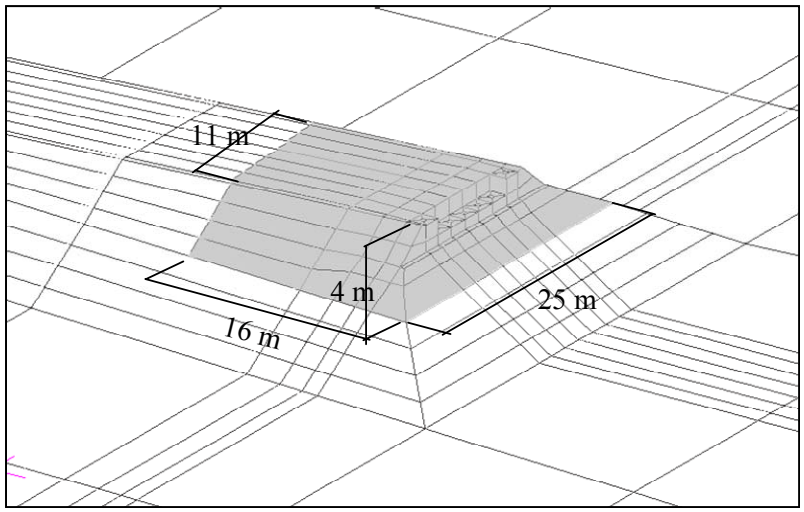

Figure 4.33 Dimension of embankment corresponding to equivalent mass

4.3.5.2 Recorded Ground Motion

The accelerometers deployed on the MRO Bridge and in its vicinity have recorded several perceptible earthquakes. At the time this research, six sets of ground motions were available, as illustrated in Table 4.3 and Figure 4.34. Among those records, five sets

of motions were recorded by accelerometers on the bridge. The largest motion was recorded from the event of 1979 Imperial Valley Earthquake with free field PGA of 0.3 g. Among the recorded events, the earthquake, GM03, has peculiar characteristics; it shows a single cycle of acceleration impulse and then the acceleration oscillates with small amplitude. A structure subjected to this type of base acceleration vibrates freely in its natural frequency after the first impact, with gradually decreasing amplitude due to energy dissipation. The damping properties of the bridge are estimated from this ground motion that represents a snap-back test.

Table 4.3 Recorded ground motions at MRO Bridge

ID	Date yr/mo/dy	ML	Lat	Long	Depth (km)	Epic. Dist. (km)	PGA (g)	Available record[1]
GM01	79/10/15	6.6	32.614	115.318	12.1	21.5	0.3	B
GM02	99/10/16	7.1	34.594	116.271	6.0	216.0	0.016	D
GM03	00/04/09	4.3	32.692	115.392	10.0	10.4	0.043	B, D
GM04	00/06/14	4.2	32.896	115.502	5.1	14.6	0.015	B, D
GM05	00/06/14	4.5	32.884	115.505	4.9	13.5	0.009	B, D
GM06	02/02/22	N/A	N/A	N/A	N/A	N/A	0.039	B, D

Note 1. B: Bridge array records, D: Downhole array records

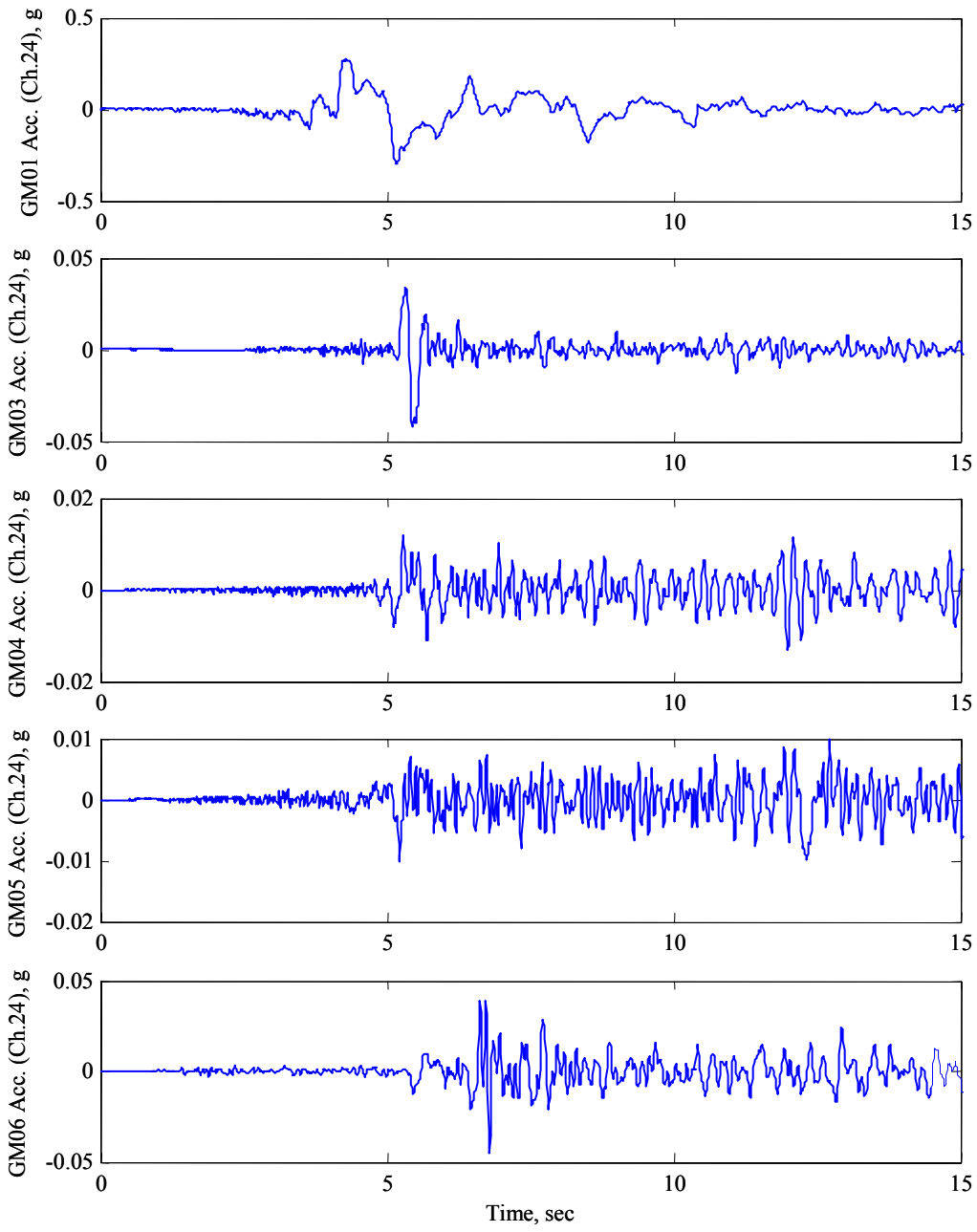

Figure 4.34 Recorded ground motions at MRO bridge site

4.3.5.3 Dynamic Properties of MRO Bridge from Measured Data

The fundamental periods and mode shapes of the embankment and bridge system are identified from recorded ground accelerations and compared with those from the analytical model. The free field ground acceleration (Channel 24 in Figure 4.15) is used as an input to the system. The accelerations measured on the bridge and embankments

(Channels 11, 3, 5, 7, 9, 13, and 26) are used as an output. Based on the input and output values, transfer functions are identified at each channel. For the calculation of the transfer functions, earthquake records are used from the beginning of each event until the bridge vibrates with certain amplitude. Figure 4.35 shows the amplitude of transfer functions at each channel for ground motion, GM03. Based on the peak amplitude of transfer function, fundamental periods and transverse mode shapes are identified. Figure 4.36 compares identified mode shapes from five sets of ground motions together with mode shape from the analytical model. From this comparison the following is concluded:

- Measured ground motions GM03 through GM06 have similar mode shapes. Considering the small amplitude of peak ground acceleration together with consistent mode shape, the structure and embankment system is expected to be within the elastic range.
- The mode shape from GM01 is distinctively different from others. It is speculated that the comparably large intensity of GM01 with PGA of 0.30g caused inelastic deformation of the embankment system.
- Identified periods are all similar, ranging from 0.31 to 0.34 sec.
- Mode shape, and fundamental period of analytical model are also similar to those identified from recorded ground motion. A comparison of the dynamic properties from analytical models with those identified from measured ground motion result in confidence regarding this analytical approach.

The damping ratio was identified using logarithmic decrement in the time domain. For an impact-like earthquake such as GM03, a simplified approach is sufficient to retrieve fundamental period and damping ratio of the system. Figure 4.37 shows acceleration response history of GM03 together with the measured acceleration at the middle of the deck (Channel 07). The superstructure was clearly vibrating with an exponential decay until the transient response damped out. The damping ratio of the system is found to be 4 %.

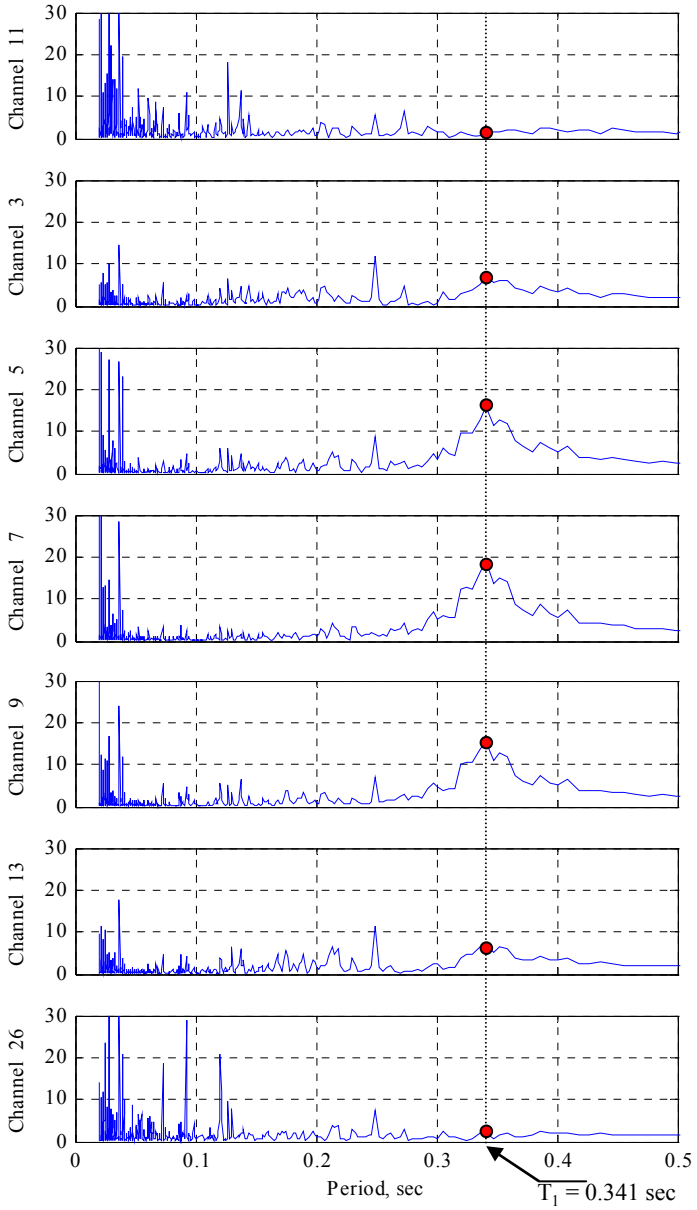

Figure 4.35 Transfer functions at each sensor location from ground motion, GM03

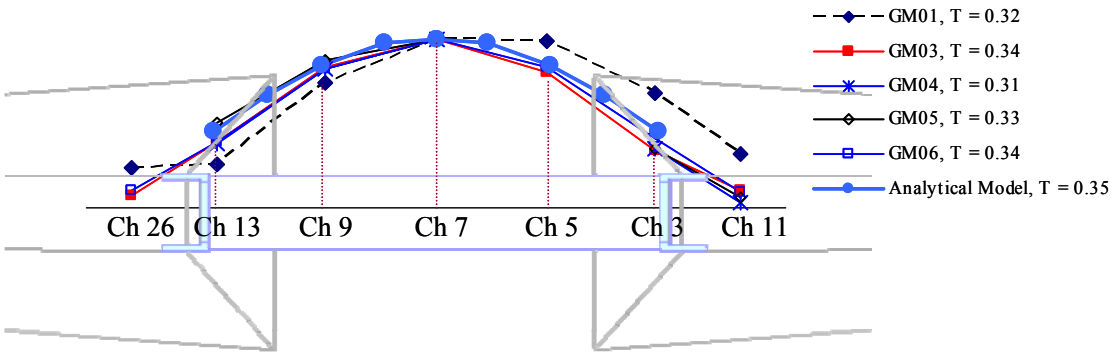

Figure 4.36 Mode shapes identified from recorded motions and analytical model

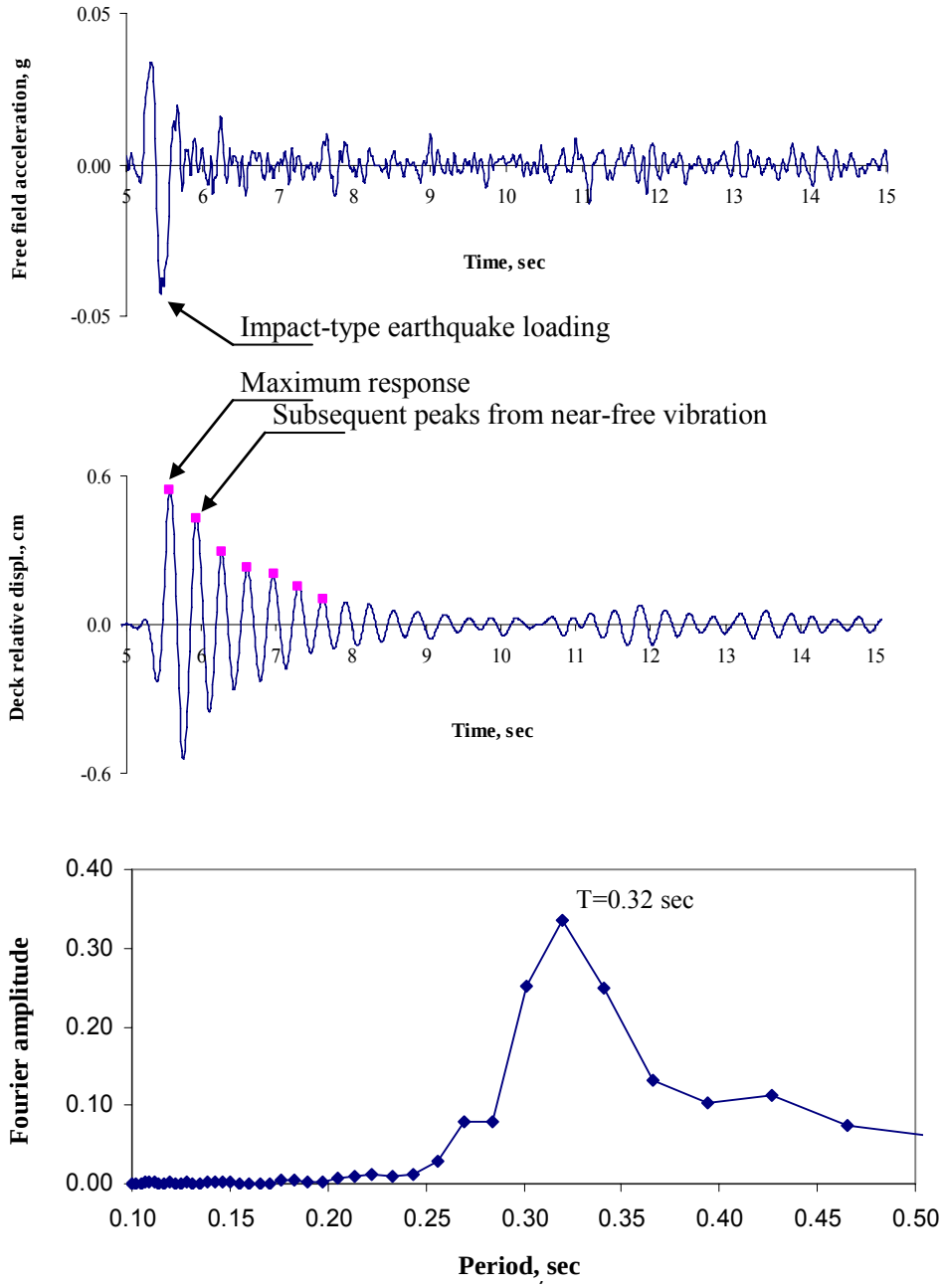

Figure 4.37 Estimation of damping ratio from logarithmic decay of bridge vibration

4.3.5.4 Analysis Result

Response history analyses are conducted for five ground motions. Free-field measurements (Channel 24) are used as an input motion. Figure 4.38 compares analysis results with recorded ground motion at the top of pier (Channel 07). The response history result shows very good matches in terms of frequency content and peak values. Figure

4.39 shows displacement and reaction forces of embankment and pile group for ground motion GM01. Note that for the ground motion with PGA of 0.3g, the embankment behaves in inelastic range while pile groups remain almost linear. The large displacement and corresponding force of embankment is mainly due to large amount of effective embankment mass lumped at the abutment-bridge connection.

4.3.6 Summary and Discussions

This section introduced an application of framework for multiplatform simulation to complex soil and structure interacting systems. The framework is presented through a reference application to an instrumented bridge subjected to real earthquake ground motion. The two-span concrete bridge and its foundations and embankments are modeled using two finite element packages interacting through a simulation coordinator. The supporting pile group of the central pier, embankments and abutments are modeled with three-dimensional finite element model using inelastic soil material in OpenSees. The superstructure is modeled using a detailed fiber approach in ZEUS-NL. The two programs are linked through UI-SimCor, a multiplatform simulation coordinator. The components and the whole system are verified through comparison with previous studies. The combined soil-structure system is verified through mode shapes, fundamental periods, and response history analyses from recorded ground motions. The main conclusions from this study are summarized below:

- Multiplatform analytical simulation is applied to analyze the MRO Bridge. The analysis result showed very good agreement with recorded data, thus confirming the potential of the multiplatform approach.
- The analytical mode shapes and fundamental periods of the whole system was very close to those identified from recorded ground motion using transfer functions. The good agreement of mode shape proves that the stiffness and effective mass of the embankment is correctly estimated and that the transverse response of bridge is mainly controlled by the response of the embankment.
- The stiffness of the inelastic model of the central pier pile group was within the range of the stiffness from previous studies. Owing to the different approaches

adopted, however, the range of the stiffness was very wide, which cannot be easily narrowed.

The newly introduced analytical approach opens up considerable application potential. The benchmark study introduced in this research utilizes two analytical platforms. Further refinements are underway in this multiplatform simulation such as a simulation of high-rise building where frame elements and shear wall are modeled on two finite element packages with unique features, at different scales, and hybrid experiment of bridges where piers are tested while the remaining structural members are simulated analytically.

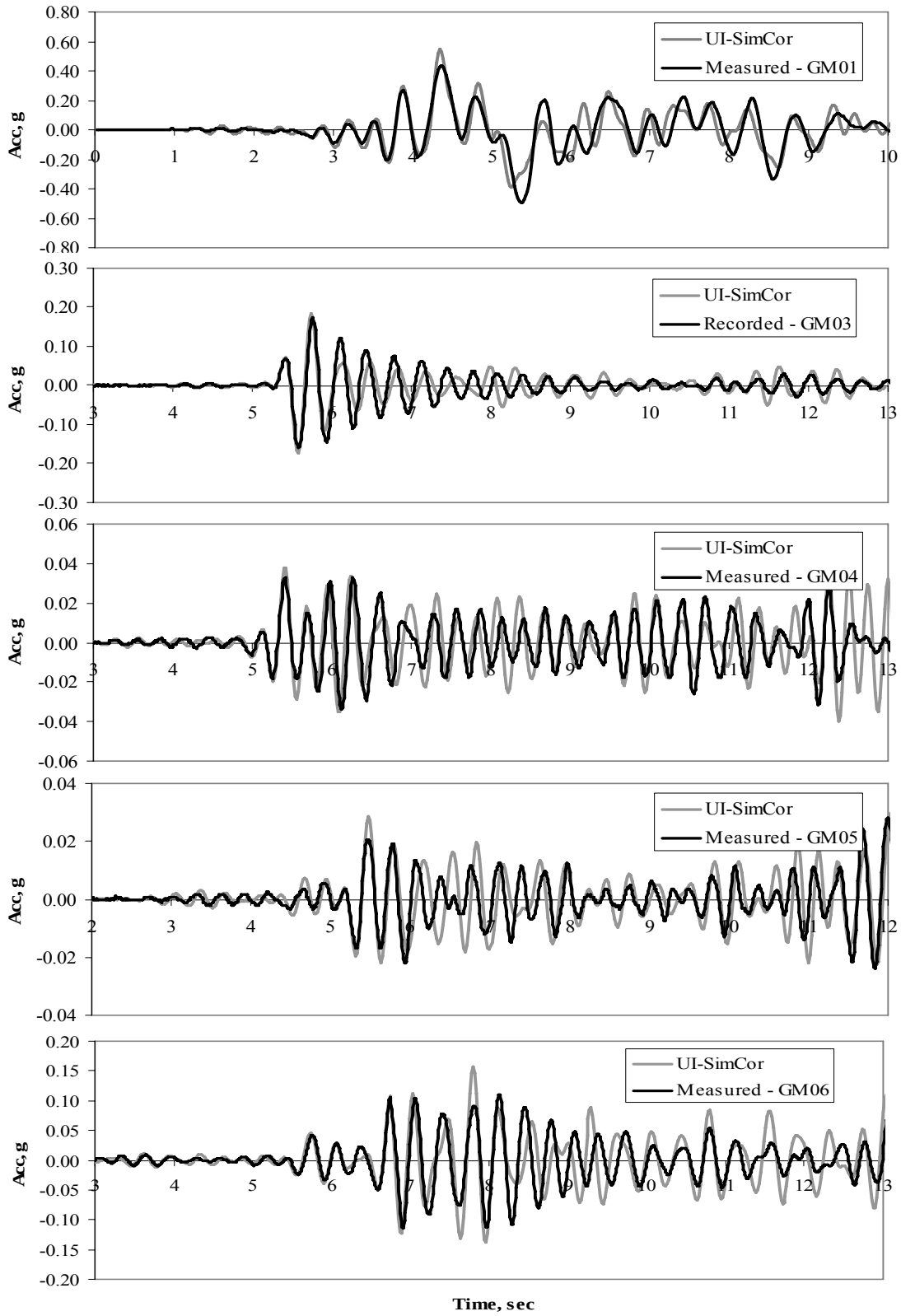

Figure 4.38 Comparison of measured bridge response with analytical result

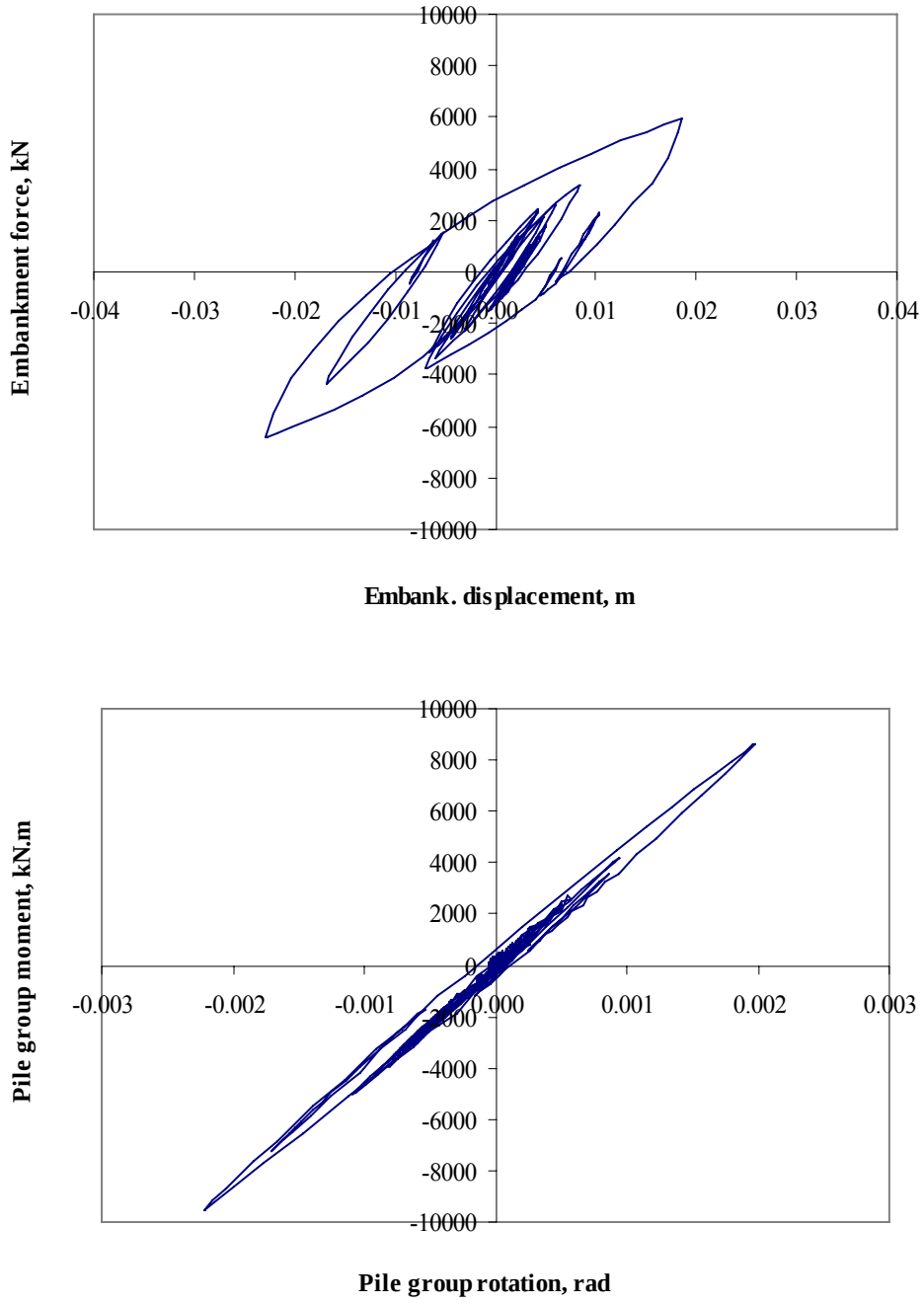

Figure 4.39 Response of abutments and pile foundations from analysis, GM01

4.4 Application II: Caruthersville Bridge

4.4.1 Overview

The Caruthersville Bridge carries route I-155 over the Mississippi River between Pemiscot County, Missouri and Dyer County, Tennessee. The 59-span, 7,100-foot bridge is about 6 miles southeast of Caruthersville and is in the vicinity of the New Madrid central fault. Construction of this bridge was completed in 1974. The superstructure consists of 11 units separated by expansion joints and supported on a variety of elastomeric and steel bearings. The main channel crossing is composed of a two-span asymmetrical cantilever steel truss and ten-span steel girders. Two approach spans are precast, prestressed concrete girders. The substructure includes piers on deep caissons and bents on steel friction piles driven into the near surface silty sands and clayey materials. Bedrock is located 2,700 feet below the sand, gravel, and hard clay strata. Figure 4.40 depicts a three-dimensional view of the bridge with a background image for the site, while Figure 4.41 shows its location.

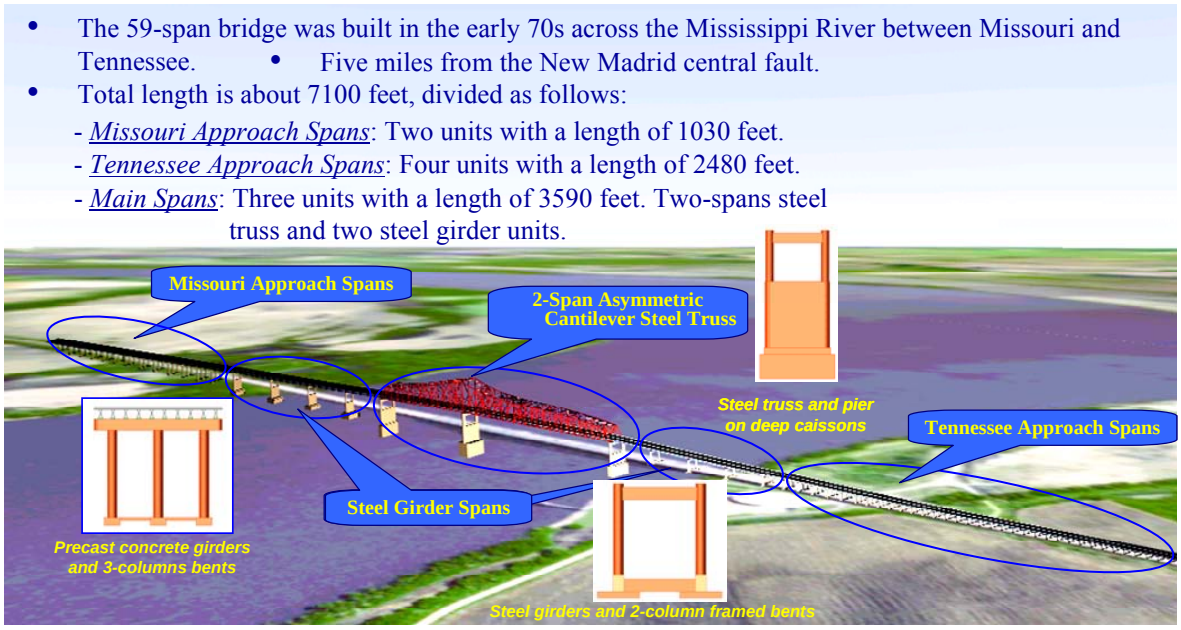

Figure 4.40 Three-dimensional view of the bridge

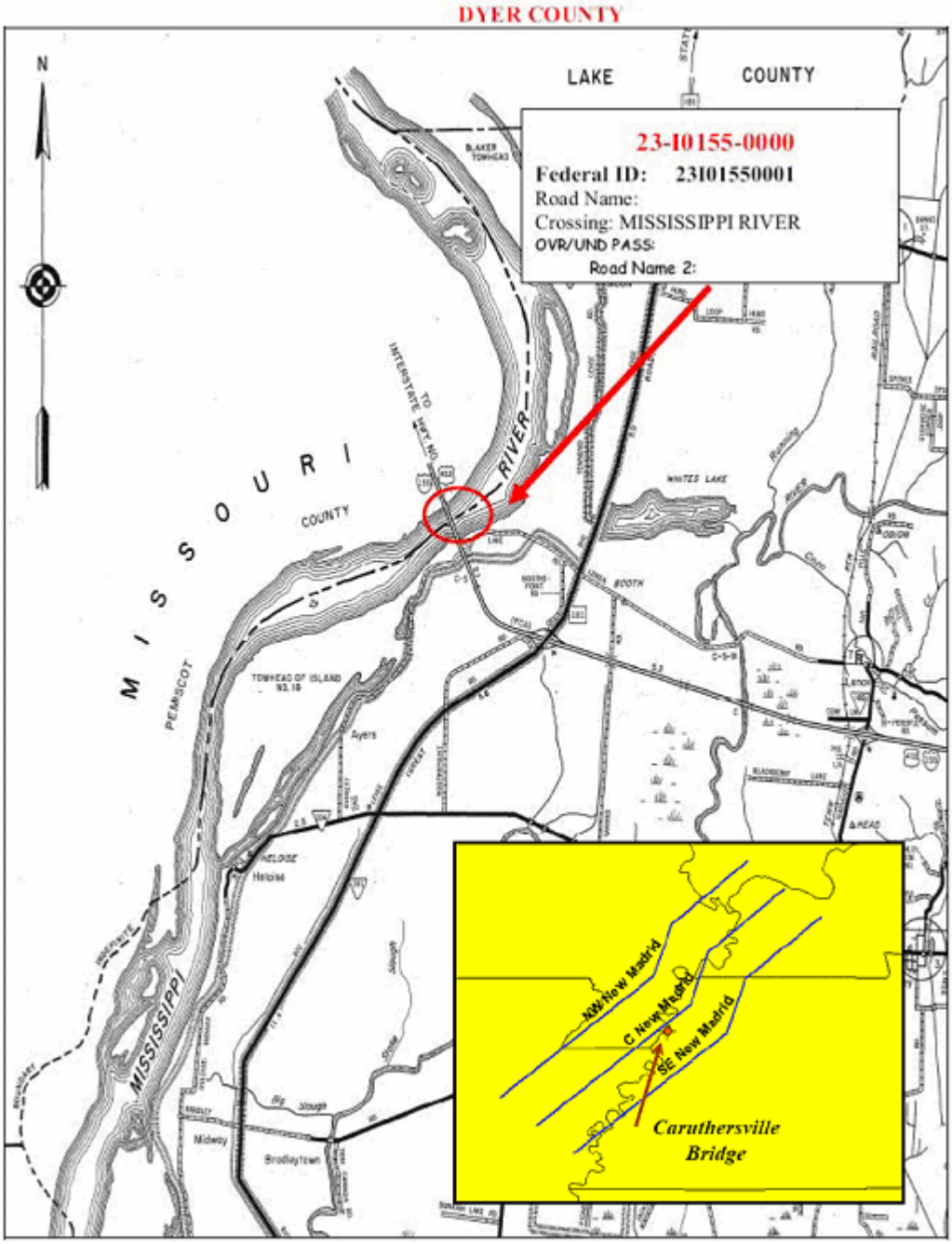

Figure 4.41 Location of the I-155 bridge with respect to the New Madrid Faults (TDOT, 2004; Fernández and Rix, 2006b)

4.4.2 Analytical Model of the Caruthersville Bridge

Detailed dynamic response simulations of the entire bridge including SSI effects are undertaken using several analytical platforms. Elastic procedures are insufficient to perform seismic assessment and retrofitting evaluation because they cannot account for redistribution of forces during progressive yielding and predict failure mechanisms. Because the investigated bridge is anticipated to respond beyond this range, inelastic (static and dynamic) analysis procedures are required to assess the seismic response under different seismic scenarios. Extensive verifications of the Caruthersville Bridge modeled in SAP2000 (CSI Inc, 2005) is carried out to enable comparisons between its results with the refined fiber modeling of the MAE Center analysis platform ZEUS-NL. The latter program is subsequently employed to predict the inelastic demand and supply. Figure 4.42 depicts the SAP2000 three-dimensional model. Based on the information obtained from the drawings and previous report (TDOT, 2004), the modeling assumptions discussed below are adopted to idealize the bridge for elastic and inelastic analysis.

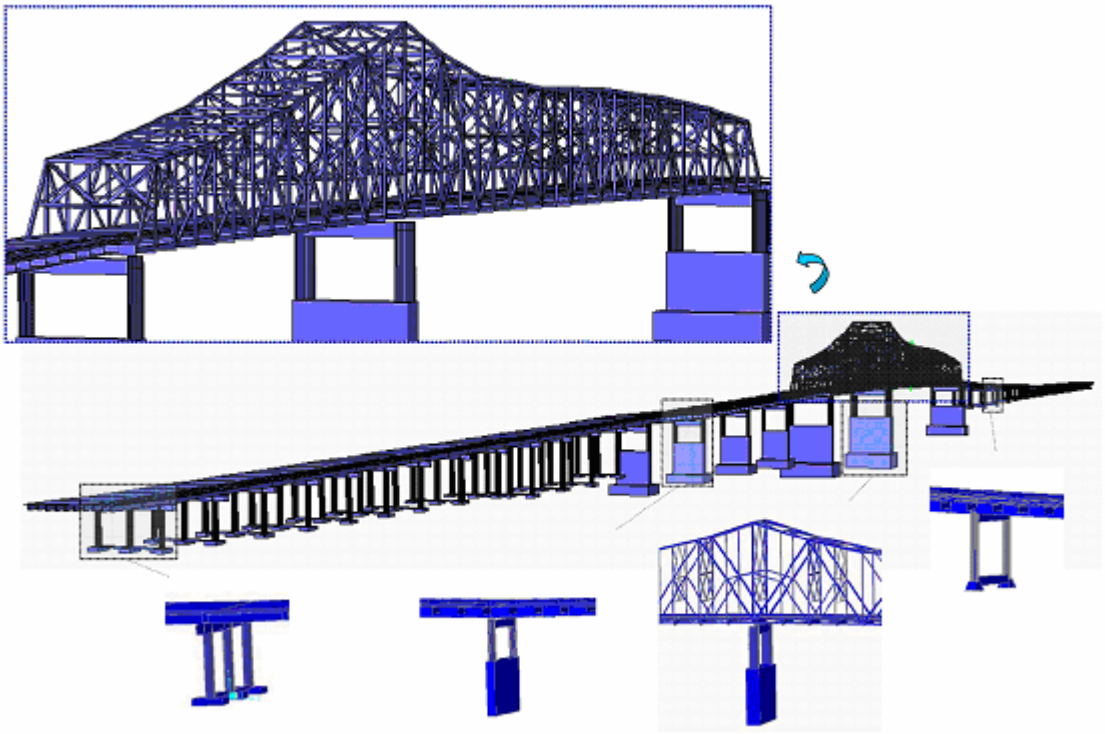

Figure 4.42 SAP2000 model of Caruthersville Bridge

4.4.2.1 Superstructure Modeling

Different steel and concrete cross-sections from the SAP2000 library are employed to realistically model the superstructure for elastic analysis, as shown in Figure 4.43. A number of features of the steel truss modeling approach are explained below.

a) At the intermediate hinge of the truss (Span 20, Bay 6), the following Degrees of Freedom (DOF) are released for the longitudinal members (refer to Figure 4.43 to 4.45)

   J1, J3, J4 and J6: Δ_X, r_X, r_Y, r_Z

   J2: Δ_X, r_Z

   J5: r_Z

   where: X, Y and Z are the longitudinal, transverse and vertical axis, respectively, and Δ is the translational DOF and r is the rotational DOF.

b) The end rotations of the vertical members (refer to Figure 4.43 and 4.44) are also released as follows:

   J1, J3, J4 and J6: r_X, r_Y

c) For inelastic analysis, joint elements are employed to control the longitudinal displacement (Δ_X) at the above-mentioned ends (refer to Figure 4.43 and 4.45). The modeling approach of this gap is depicted in Figure 4.46.

d) The six DOFs at both ends of truss members are restrained as suggested from the drawings (i.e., Figure 4.47).

e) Based on available cross-sections in the library of the employed analytical tool, equivalent cross-sections are adopted for modeling of the truss members

The abovementioned modeling approach of the superstructure is computationally demanding for inelastic analysis. It is, therefore, necessary to simplify the analytical model of the superstructure for the extensive inelastic response history analysis. It is worth noting that seismic design philosophy of bridges relies on piers to dissipate energy rather than the superstructure, which should remain elastic under the design earthquake. Therefore, the superstructure is modeled for inelastic analysis based on the conventional elastic theory using a number of equivalent cross sections connected together using rigid

arms. This modeling conforms to the following two criteria: equal sectional areas and equivalent sectional moments of inertia.

Figure 4.43 Truss intermediate hinges

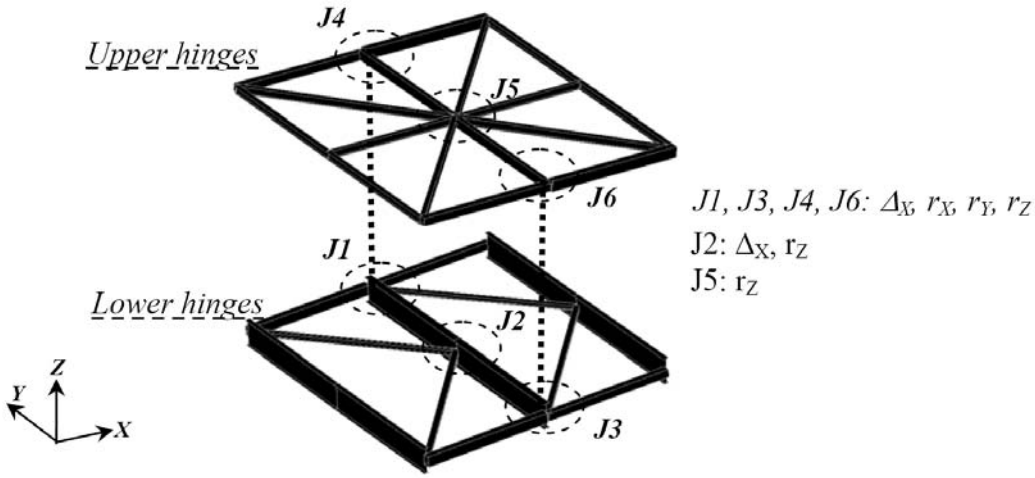

Figure 4.44 Released DOFs at the truss intermediate hinge

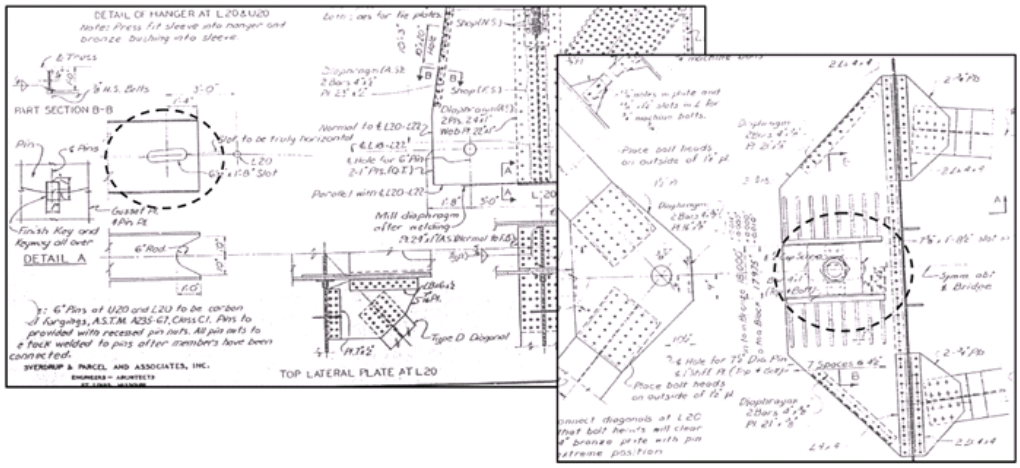

Figure 4.45 Structural gaps controlling the displacement at the intermediate hinge

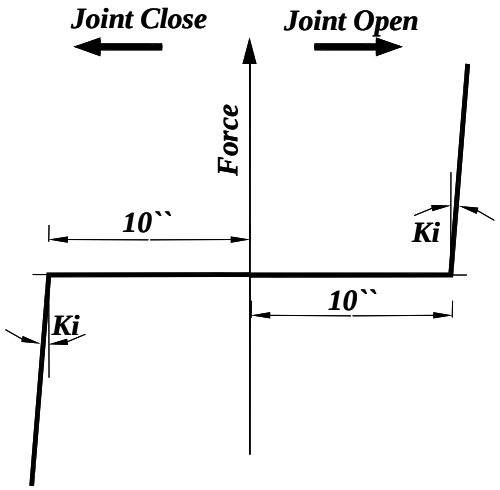

Figure 4.46 Modeling of structural gaps to control displacement

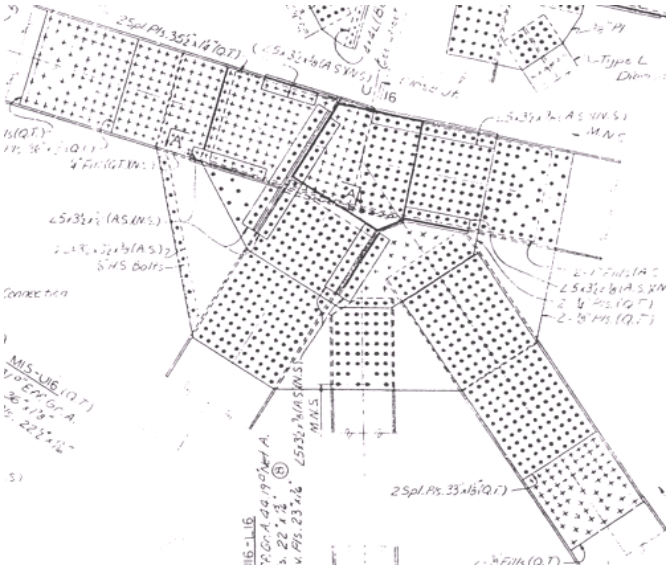

Figure 4.47 Typical truss joint details

4.4.2.2 Substructure Modeling

Gross cross-sections are employed to model the substructure and superstructure members for SAP2000 elastic analysis. The degradation in stiffness with increasing loading is only accounted for in the ZEUS-NL inelastic analysis. Based on available cross-sections in the library of SAP2000 and ZEUS-NL, equivalent RC hollow rectangular cross-sections are selected for modeling of piers 15 – 21. The selected cross-sections have equivalent area and moment of inertia of the original cross-sections (refer to Figure 4.48).

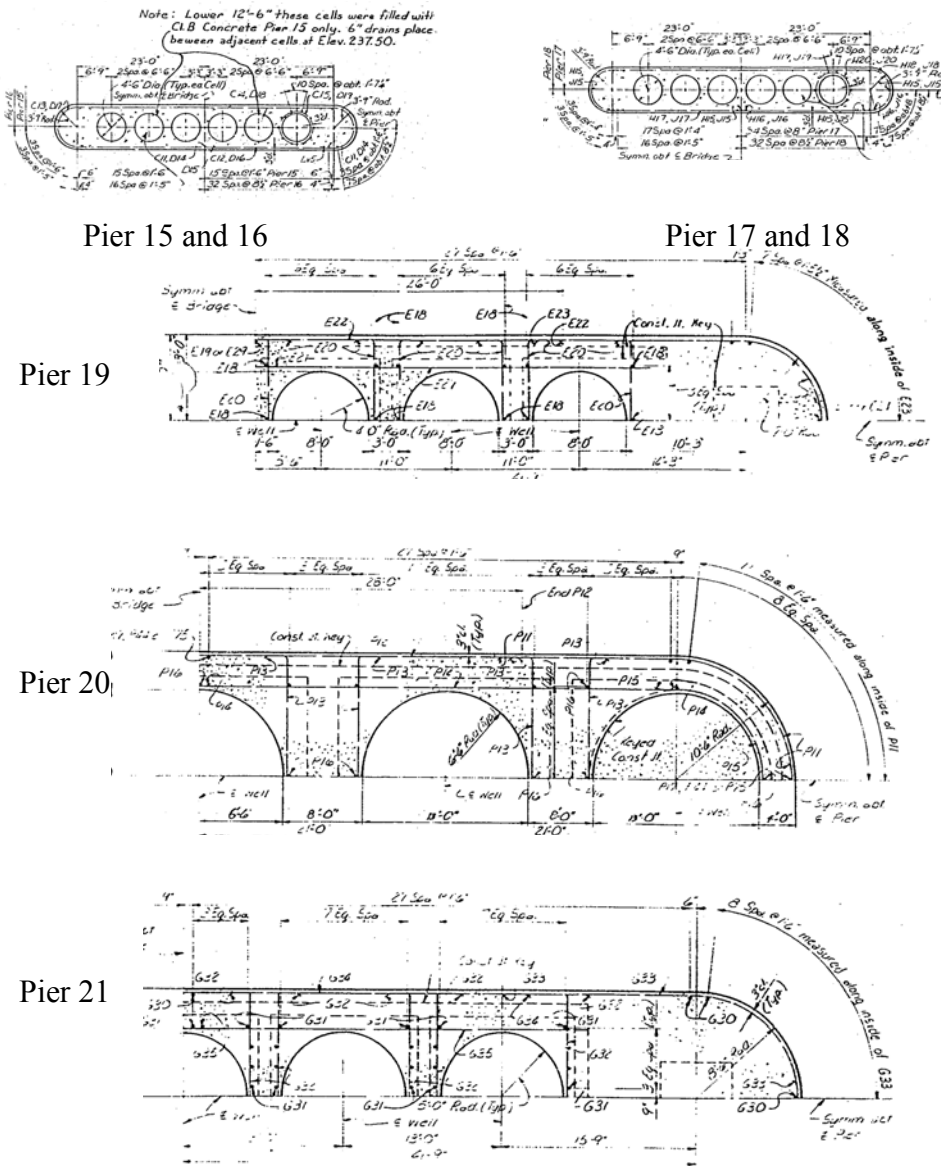

Figure 4.48 Cross-sections of Pier 15 to Pier 21

4.4.2.3 Mass Modeling

The mass of the wearing surface and roadway barriers is accounted for by using an equivalent density for the concrete deck. The mass of the concrete and steel girder stiffeners are neglected; their stiffness is accounted for by constraining the girders at these locations. Dead loads are only considered in estimation of mass. It is important to note that the open cells of the caissons are assumed to be filled with water. The total weigh of the bridge calculated from the SAP2000 model is, therefore, 1,563 MN

(351,275 kip). This includes the superstructure, substructure, nonstructural members, pile caps, and caissons. The corresponding mass is 1,912 $MN \cdot sec^2/m$ (10,918 $kip \cdot sec^2/in$). The weight of the superstructure is significant compared with the substructure in the approach spans. This is not the case for the steel girders and truss spans. This is due to the lower weight of steel members compared with the concrete counterparts and because lightweight concrete was used for the deck of the steel girders and the truss spans. Also, the massive weight of the caissons significantly increases the weight of the substructure of the latter spans.

4.4.2.4 Material and Damping

Several deficiencies in structural members are observed in the latest inspection report (TDOT, 2004). As a result of these deficiencies, the age of the bridge, and the lack of reliable information confirming the actual material characteristics, the following conservative properties are assumed:

Normal and light weight concrete: f_c' = 20.7 MPa (3,000 psi)

Prestressed concrete: f_c' = 27.6 MPa (4,000 psi)

Reinforcing steel: F_y = 276 MPa (40,000 psi)

Structural carbon steel ASTM A36-69 (F_y = 248 MPa (36,000 psi)) is used for truss members and steel beams.

The modulus of elasticity of steel (E_s) is 199,948 MPa (29,000,000 psi), while the modulus of elasticity of concrete (E_c) is estimated based on the following expression:

$$E_c = 57000\sqrt{f_c'} \text{ psi (ACI, 2002)}$$

It is important to note that underestimating the concrete strength causes reduction in stiffness and elongation in period. This has its impact on the demand predictions. It is, therefore, recommended that the necessary structural tests be performed to identify the existing material properties. This is particularly important for the bridge piers due to the significant energy dissipation anticipated in these members.

The density of normal concrete (γ_c) is 23.6 kN/m^3 (150 lb/ft^3), while it is 17.3 (kN/m^3) 110 lb/ft^3 for lightweight concrete. The former concrete density is employed to estimate the weight and mass of different RC members with the exception of the concrete deck from Pier 14 to 26, which was constructed using lightweight concrete. Weight of steel members is calculated using a steel density (γ_s) of 77.0 kN/m^3 (490 lb/ft^3).

The modes of vibration obtained from the modal analysis reflect the contribution of the steel truss to the response, as subsequently presented. Accordingly, 2% and 5% damping ratios, corresponding to steel and concrete, are considered to investigate their effect on the bridge response. The mass-proportional and stiffness-proportional parameters are calculated for Response History Analysis (RHA) based on the predominant periods of the structure in the two principle directions (Chopra, 2000). On the other hand, damping is modeled in ZEUS-NL for inelastic analysis using Rayleigh damping elements, whereby damping is defined in proportion to the mass and stiffness of the structural member. Because the hysteretic damping (damping due to inelastic energy absorption) is already accounted for in the inelastic analysis, 0.5 to 2.0% Rayleigh damping levels are investigated.

4.4.2.5 Bridge Bearings and Structural Gaps

The vertical and transverse translations as well the rotations about the longitudinal axis are fully restrained at the abutment-superstructure connection. The rotation about the transverse axis (rY) is allowed only at the hinged bearings (fixed shoes). Based on the drawings, these bearings are located at the substructure-superstructure connection of piers 2-7, 9-13, 14(right), 16-18, 20, 21(left), 22-24, 26(left), 27-30, 32-40, 42-50, and 52-59. A zero frictional resistance is initially assumed at all sliding bearings (expansion shoes). Therefore, the translational DOF (DX) and the rotational DOFs (rY and rZ) are released. Based on the drawings, these bearings are located at the two abutments and at the substructure-superstructure connection of piers 8, 14(left), 15, 19, 21(right), 25, 26(right), and 31, 41, and 51.

Although the assumption of zero friction is rather unrealistic, it was initially employed to follow the simplified assumptions typically made in design. Recent studies on behavior of complex bridges (e.g., Mwafy et al., 2006a and 2006b) have indicated that modeling of bridge bearings has a significant impact on the dynamic characteristics, capacity estimation, and demand prediction of multispan bridges. A realistic estimation of the bearing friction of the Bronze self-lubricating bearings and the steel rockers was required. Movable bearings, which have a small friction coefficient at low-velocity rates, may have higher friction under high seismic deformation. For unlubricated elastomeric bearings, this coefficient at high velocities ranges from 5 to 15%, or even higher at low temperatures (e.g., Constantinou et al., 1990; Priestley et al., 1996; Bondonet and Filiatrault, 1997). It was also concluded in previous experimental studies that the coefficient of friction slightly decreases again under the high velocities due to frictional heating.

As a result of the poor condition of a number of bridge bearings, as confirmed from available photos and inspection reports, and because the bridge is assessed under increasing levels of input ground motion; it is highly recommended that the appropriate tests be performed to estimate the behavior of the bearings.

Because no reliable information is available about the actual bearing behavior, a 5% friction coefficient is initially assumed in the ZEUS-NL inelastic analytical model. This modeling approach of the movable bearings is depicted in Figure 4.49. It is clear that slippage takes place when the applied force reaches the maximum friction developed on the contact plane of the bearing.

The structural gaps at the abutments and expansion joints are not accounted for in the SAP2000 elastic analysis. The behavior of these gaps is considered in the inelastic modeling and analysis performed using ZEUS-NL. In the latter modeling approach, joint elements with tri-linear asymmetric elasto-plastic idealization capable of representing the slippage and collision are employed. Figure 4.49 (right) shows the force versus relative displacement relationships employed to model the movable bearing at abutment with the structural gaps. In this modeling, a positive relative displacement corresponds to an opening of the joint gap and a negative displacement corresponds to a closing of the gap.

When the gap at the abutment and at the expansion joint undergoes a relative movement in the negative direction (joint close) exceeding the gap width, the joint element resists further opening (collisions).

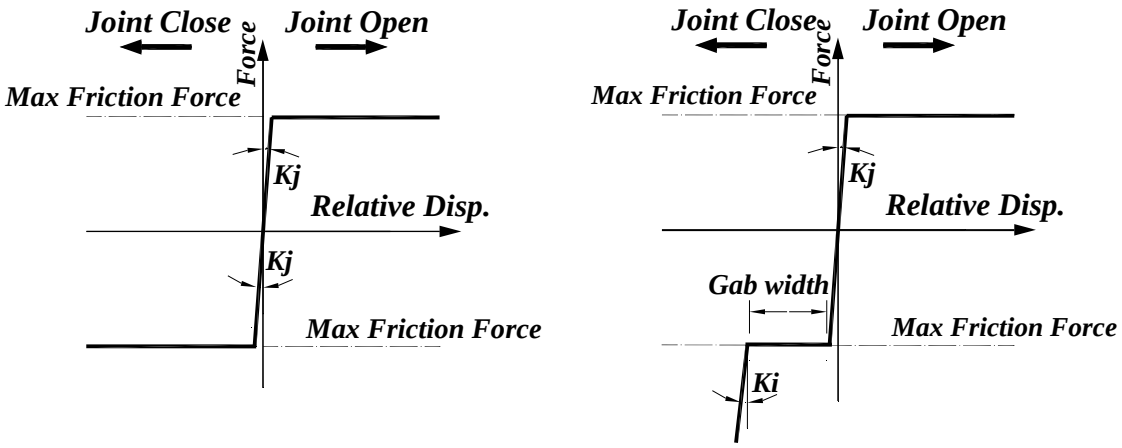

(a) with friction (b) with friction and structural gaps

Figure 4.49 Modeling of movable bearings with friction

4.4.3 Analytical Model of Soil and Foundation

Refined inelastic simulations of the foundation and the underlying substrata are undertaken using the OpenSees. The objective is to realistically estimate the soil properties required for SAP2000 and ZEUS-NL soil and foundation modeling.

4.4.3.1 Soil Properties

Figure 4.50 depicts a vertically exaggerated view of soil profile along the length of the bridge, while Table 4.4 shows characteristics of various soil classes. The site consists of 8 types of soil materials. Strata 1 and 2 are cohesive material with an unconfined compressive strength of 67 and 48 kPa, respectively. This range of strength is for medium to stiff clay. The upper layers of approach spans are covered by either strata 1 or 2. These strata are modeled with pressure-independent soil material model.

Table 4.4 Soil characteristics of the bridge site

Stratum	Soil type	N	Vs (m/sec)	G_{max} (kN/m^2)	Su (kN/m^2)	Phi (deg)	Dr (%)	Density (kg/m^3)
1	CL, ML	5-10	176.78	55541	67	0	-	1777
2	CL, CH	<5	137.16	33516	48	0	-	1782
3	SM-ML	5-10	158.50	46923	-	30	40	1868
4	SP	5-10	167.64	51711	-	32	50	1840
5	SP, SM	10-30	182.88	62244	-	35	70	1861
6	SP	30-50	213.36	88100	-	37	80	1935
7	SP	50-100	274.32	158005	-	40	100	2100
8	SP	>100	320.04	220249	-	42	100+	2150

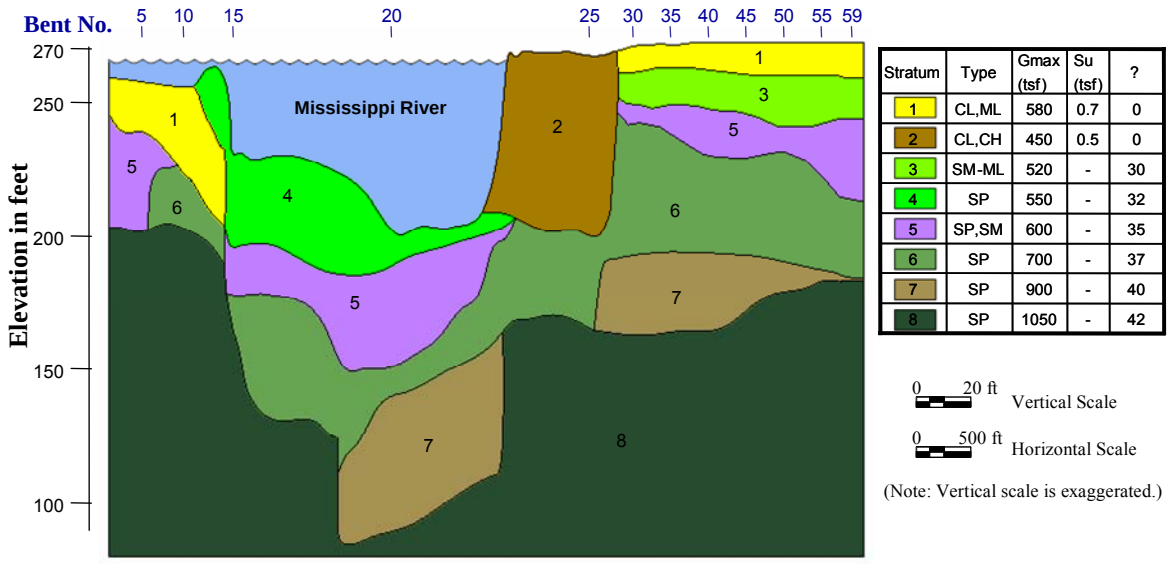

Figure 4.50 Soil profile along the length of the bridge

Strata 3 to 8 are cohesionless materials. The friction angle of the materials ranges from 30 to 42 degrees. The in-situ properties of the cohesionless material at deeper layers are expected to have higher stiffness due to the large confinement. Because the shear modulus of each stratum is provided as a constant value regardless of the depth of the stratum, it is assumed that the shear modulus is calculated at the mid-depth of each stratum. The effective reference pressure at the mid-depth is approximately calculated and used as the input parameters for soil and foundation models. Strata 3 to 8 are thus modeled with pressure-dependent material, which can dilate or contract with shear deformation depending on the initial density ratio. Based on the density ratio of various

soil profiles, strata 3 and 4 are assumed to be medium sand, strata 5 and 6 as medium-dense sand and strata 7 and 8 as dense sand. The dilatation and contraction parameters of the pressure-dependent material models are chosen from the suggested values by Yang et al. (2005). Table 4.5 shows the soil properties used in the foundation analysis using OpenSees.

Table 4.5 Soil properties for bridge foundation analysis

Stratum	**1**	**2**	**3**	**4**	**5**	**6**	**7**	**8**
Material type (Relative density)	Clay	Clay	Medium Sand (35-65%)	Medium Sand (35-65%)	Medium-dense Sand (65-85%)	Medium-dense Sand (65-85%)	Dense Sand (85-100%)	Dense Sand (85-100%)
rho (ton/m3)	1.78	1.78	1.87	1.84	1.86	1.94	2.10	2.15
refShearModul (kPa)	55541	33516	46923	51711	62244	88100	158005	220249
refBulkModu (kPa)	259192	156409	140768	155132	186733	264299	474014	660747
cohesi (kPa)	67	48	-	-	-	-	-	-
peakShearStra	0.1	0.1	0.1	0.1	0.1	0.1	0.1	0.1
frictionAng	0	0	30	32	35	37	40	42
overburden soil (kPa)			109	215	165	336	548	836
pore water pres. (kPa)			45	150	75	164	269	404
Effective pres. (p'r, kPa)	-	-	64	65	90	172	279	432
Confining pres. (p'r, kPa)	-	-	43	42	56	103	160	239
pressDependCoe	-	-	0.5	0.5	0.5	0.5	0.5	0.5
PTAng	-	-	27	27	27	27	27	27
Contrac	-	-	0.07	0.07	0.05	0.05	0.03	0.03
dilat1	-	-	0.4	0.4	0.6	0.6	0.8	0.8
dilat2	-	-	2	2	3	3	5	5
liquefac1	-	-	10	10	5	5	0	0
liquefac2	-	-	0.01	0.01	0.003	0.003	0	0
liquefac3	-	-	1	1	1	1	0	0
E	-	-	0.7	0.7	0.55	0.55	0.45	0.45

4.4.3.2 Concrete and Steel Properties

For foundation analysis, it is assumed that the pile cap and caisson behave as rigid bodies. The Young's modulus of concrete is assumed to be 10^9 kPa, which is about 40 times larger than the actual concrete modulus. This assumption is made as it is necessary to control a few nodes within the pile cap and foundation meshes, where it is likely to have locally concentrated deformation when actual concrete properties are used.

The resistance of soil medium surrounding the pile largely depends on the contact surface area normal to the direction of the pile movement. Due to the large number of piles and the amount of analyses required, it is computationally demanding to model each pile using several finite elements. A single brick element with an equivalent projected area is, therefore, used to idealize the pile section to reduce the computational demands. The equivalent element used in analysis has the similar properties of the actual piles in terms of flexural and axial rigidity. Different Young's modulus of pile is assumed for the foundation analyses ix x and r_y direction, y and r_x direction, and z direction, as shown below.

Analysis of x and ry direction: Equivalent flexural rigidity about y axis

$$E_{equiv} = (EI_{ry}) / I_{ry,equiv} = 45474 \text{ MPa}$$

Analysis of y and rx direction: Equivalent flexural rigidity about x axis

$$E_{equiv} = (EI_{rx}) / I_{rx,equiv} = 14695 \text{ MPa}$$

Analysis of z direction: Equivalent axial rigidity

$$E_{equiv} = (EA) / A_{equiv} = 21522 \text{ MPa}$$

4.4.3.3 Foundation Classes

Based on the soil profile, the number of piles, and the batter angle, 13 soil-foundation profiles were idealized using OpenSees. Unlike the pile caps of bents at expansion joint, those at other locations have battered piles. The number of piles varies from 9 to 112, depending on the supporting loads. Bent 19, 20, and 21 are supported on massive caisson. Table 4.6 shows different bent numbers and their foundation classes, while Figure 4.51

depicts a view of various foundation classes. Some of these profiles are identical in their shape and geometry, but their soil properties are different.

Table 4.6 Foundations classes of Caruthersville Bridge

Bent #	Class	Bent #	Class	Bent #	Class	Bent #	Class	Bent #	Class	Bent #	Class
2	2	12	5	22	10	32	13	42	13	52	13
3	2	13	5	23	10	33	13	43	13	53	13
4	3	14	5	24	10	34	13	44	13	54	13
5	3	15	6	25	10	35	13	45	13	55	13
6	3	16	6	26	11	36	13	46	13	56	13
7	3	17	6	27	11	37	13	47	13	57	13
8	4	18	6	28	14	38	13	48	13	58	13
9	5	19	7	29	14	39	13	49	13	59	13
10	5	20	8	30	14	40	13	50	13		
11	5	21	9	31	12	41	12	51	12		

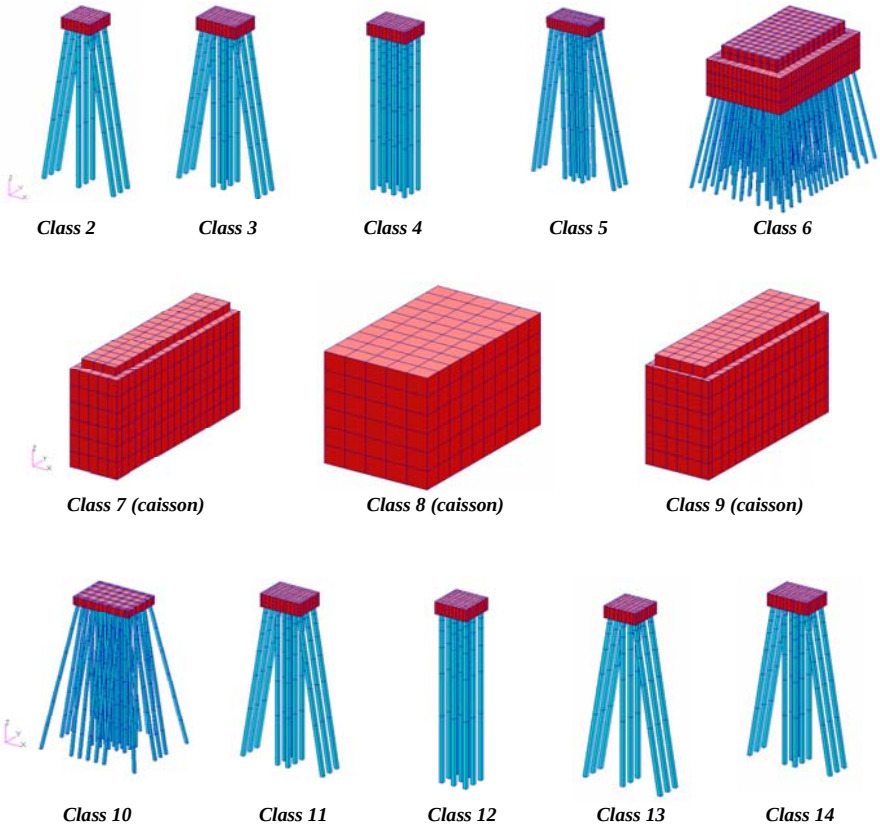

Figure 4.51 Foundation types in Caruthersville Bridge

4.4.3.4 OpenSees Finite Element Model

The foundation and soil medium are all modeled with 8 node brick elements. The side boundary of the soil medium is restrained in the horizontal translation. Vertical DOFs of the side boundary are released to allow settlement due to gravity loads. All DOFs of the bottom nodes of the soil medium are restrained. Figure 4.52 depicts the OpenSees FE model of the foundation class 2 and the surrounding soil.

To prevent unrealistic concentrated stress, it is assumed that the pile caps and caissons behave as rigid bodies. All foundation profiles, except caissons (Class 7, 8 and 9), are thus controlled using a single node connected to 8 boundary nodes, as shown in Figure 4.53. Symmetry is utilized to reduce the number of elements in the FE model and computational demands for certain types of foundation profiles (e.g., Class 6). On the other hand, it was difficult to control the response of the caissons using a single node due to their extreme stiffness. Therefore, a number of nodes are used to control their response, as shown in Figure 4.54.

Displacement-controlled pushover analyses are carried out using the above-mentioned refined FE models to evaluate the load-deformation relationship. Table 4.7 shows the DOFs controlled in the analysis. The load-deformation relationships of various foundation profiles are derived from the reactions at the control nodes.

Table 4.7 DOFs controlled in foundation analysis

Analyzed DOF	Controlled DOFs				
	x	y	z	Rx	Ry
X	1	free	free	Free	0
Y	0	1	free	0	free
Z	0	0	1	Free	free
r_x	free	1	free	1	0
r_y	0	free	free	Free	1

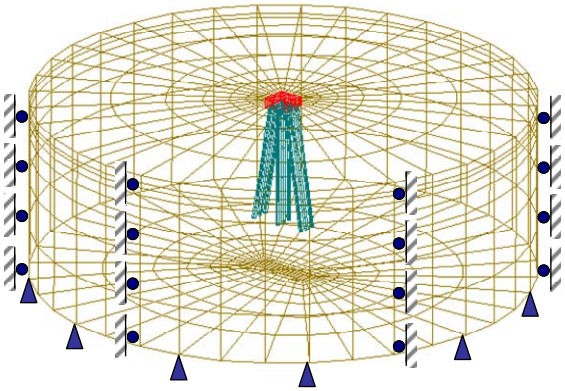

Figure 4.52 FE model of the foundation and soil

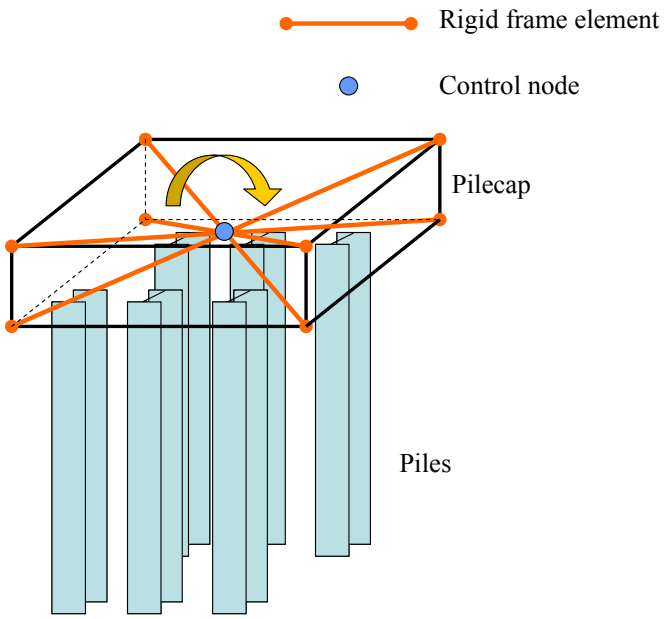

Figure 4.53 Modeling of the pile cap for FE analysis

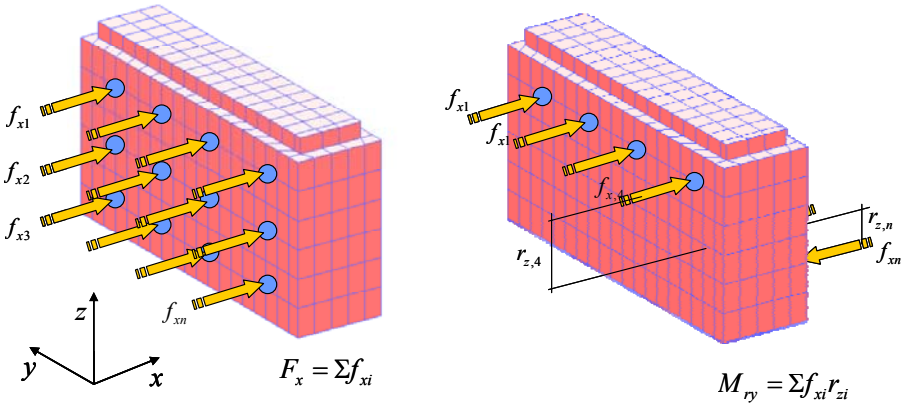

Figure 4.54 Modeling of the caissons for FE analysis

4.4.4 Soil and Foundation Response Under Lateral Loading

Results of the extensive foundation-soil analyses are presented below. The load-deformation relationship of foundation Class 2 is shown in Figure 4.55. The thin solid line is from cyclic loading, while the thick solid line is from monotonic loading. This comparison shows that the backbone of the hysteretic curve follows the monotonic pushover curve. It was decided based on this comparison to analyze other foundation profiles under monotonic loading to estimate their load-deformation relationships.

For linearization of the nonlinear stiffness of translational DOFs, maximum force is assumed to be twice the reaction of dead loads. The idealized trilinear relationships are subsequently used as soil springs for inelastic analysis. Figure 4.56 shows the deformation shapes and the corresponding load-deformation curves obtained from OpenSees pushover analysis of foundation Class 5. Trilinear idealizations are adopted to simplify the monotonic pushover curves of different foundation classes. The yield displacement and postyield stiffness values are chosen so that the trilinear model closely represents the load-deformation curve obtained from the OpenSees pushover analysis. The idealized load-deformation relationships are, therefore, used to model the foundation system in SAP2000 and ZEUS-NL models. A summary of the foundation stiffness obtained from the analysis is given in Table 4.8.

Table 4.8 Summary of foundation stiffness properties

Foundaiton	DOF	k0	d0	k1	d1	k2
Class02	X	1.0190E+06	9.0620E-04	6.6800E+05	4.5310E-03	3.9710E+05
	Y	8.8900E+05	1.3240E-03	4.7530E+05	6.6210E-03	2.1890E+05
	Z	1.5880E+06	3.4810E-04	1.5310E+06	1.7400E-03	1.4130E+06
	rx	3.8420E+06	1.0000E-03	1.7650E+06	6.0000E-03	1.0750E+06
	ry	5.6010E+06	1.0000E-03	3.0330E+06	6.0000E-03	1.3120E+06
Class03	X	1.0590E+06	9.3910E-04	6.9970E+05	4.6960E-03	4.0440E+05
	Y	1.0480E+06	1.0630E-03	6.3100E+05	5.3140E-03	3.2470E+05
	Z	1.7640E+06	3.4640E-04	1.7010E+06	1.7320E-03	1.4750E+06
	rx	4.9160E+06	1.0000E-03	2.1770E+06	6.0000E-03	1.2640E+06
	ry	8.9600E+06	1.0000E-03	5.0540E+06	6.0000E-03	1.6600E+06
Class04	X	1.2460E+06	1.4530E-03	7.3990E+05	7.2640E-03	3.7110E+05
	Y	1.1720E+06	1.7910E-03	6.0320E+05	8.9570E-03	2.6620E+05
	Z	2.3180E+06	4.3630E-04	2.1950E+06	2.1820E-03	1.8170E+06
	rx	5.8250E+06	1.0000E-03	2.7070E+06	6.0000E-03	1.2540E+06
	ry	1.2630E+07	1.0000E-03	5.6610E+06	6.0000E-03	1.5270E+06
Class05	X	1.4600E+06	9.6050E-04	1.0180E+06	4.8030E-03	6.0370E+05
	Y	1.3990E+06	1.0670E-03	9.3220E+05	5.3330E-03	5.1470E+05
	Z	2.3980E+06	3.6600E-04	2.3120E+06	1.8300E-03	2.1600E+06
	rx	5.5420E+06	1.0000E-03	3.0980E+06	6.0000E-03	1.6860E+06
	ry	1.3330E+07	3.5200E-03	7.0020E+06	8.8000E-03	3.0680E+06
Class06	X	4.5970E+06	5.0000E-03	2.3350E+06	2.5000E-02	1.5070E+06
	Y	4.0710E+06	5.0000E-03	1.6960E+06	2.5000E-02	1.0480E+06
	Z	1.0070E+07	2.7800E-03	8.4600E+06	1.3900E-02	2.4140E+06
	rx	1.8470E+08	2.0000E-03	8.0370E+07	8.0000E-03	3.9390E+07
	ry	1.6350E+08	2.0000E-03	6.7970E+07	1.0000E-02	4.8650E+07
Class07	X	1.3870E+07	5.0000E-03	6.3950E+06	2.5000E-02	3.5870E+06
	Y	1.2750E+07	5.0000E-03	5.7650E+06	2.0000E-02	2.4440E+06
	Z	1.4590E+07	2.9200E-03	8.1440E+06	1.4600E-02	1.5810E+06
	rx	1.0370E+09	8.8140E-04	5.3190E+08	5.2890E-03	4.2390E+08
	ry	9.9430E+08	8.9480E-04	2.8610E+08	4.4740E-03	1.6510E+08
Class08	X	2.3610E+07	8.0000E-03	9.1250E+06	4.0000E-02	3.8890E+06
	Y	2.2670E+07	8.0000E-03	8.4070E+06	4.0000E-02	2.6990E+06
	Z	3.3840E+07	2.5200E-03	2.3350E+07	1.2600E-02	1.7960E+06
	rx	2.6840E+09	5.0000E-04	1.7570E+09	3.0000E-03	1.3810E+09
	ry	3.3160E+09	1.0000E-03	8.6050E+08	5.0000E-03	3.7480E+08

Unit: force (kN), moment (kN.m), length (m), rotation (rad)

(continued on next page)

Table 4.8 Summary of foundation stiffness properties – *continued*.

Foundaiton	DOF	k0	d0	k1	d1	k2
Class09	X	1.5830E+07	8.0500E-03	5.0920E+06	4.8300E-02	1.6560E+06
	Y	1.6250E+07	5.9000E-03	6.4540E+06	2.3600E-02	2.5670E+06
	Z	2.3900E+07	4.8650E-04	2.1390E+07	2.4320E-03	1.8410E+07
	rx	1.9730E+09	4.0530E-04	1.0300E+09	2.4320E-03	8.2870E+08
	ry	1.5450E+09	7.1090E-04	4.7120E+08	3.5540E-03	2.4890E+08
Class10	X	1.7000E+06	1.4190E-03	1.3630E+06	7.0970E-03	9.5200E+05
	Y	1.5170E+06	1.7630E-03	1.1250E+06	8.8160E-03	7.1490E+05
	Z	3.7330E+06	4.8170E-04	3.6460E+06	2.4090E-03	3.3580E+06
	rx	3.2170E+07	1.0000E-03	2.1060E+07	6.0000E-03	1.3060E+07
	ry	8.3320E+07	9.0000E-04	5.6540E+07	5.4000E-03	3.0010E+07
Class11	X	8.3070E+05	1.3590E-03	5.6990E+05	6.7950E-03	3.3190E+05
	Y	7.5030E+05	1.8240E-03	4.3400E+05	9.1190E-03	2.1360E+05
	Z	1.8430E+06	3.9880E-04	1.7210E+06	1.9940E-03	1.5060E+06
	rx	4.3580E+06	1.0000E-03	2.3920E+06	6.0000E-03	1.3660E+06
	ry	8.9130E+06	9.0000E-04	5.3350E+06	5.4000E-03	2.0380E+06
Class12	X	2.3130E+05	3.8480E-03	1.3690E+05	1.9240E-02	1.0030E+05
	Y	1.4770E+05	5.0000E-03	8.4150E+04	2.5000E-02	5.7360E+04
	Z	1.1510E+06	5.4210E-04	9.6830E+05	2.7100E-03	8.1270E+05
	rx	1.9060E+06	1.0000E-03	1.2450E+06	6.0000E-03	7.1500E+05
	ry	4.0240E+06	1.0000E-03	2.3960E+06	6.0000E-03	9.8770E+05
Class13	X	2.8830E+05	2.5950E-03	1.8790E+05	1.2980E-02	1.4070E+05
	Y	1.5760E+05	5.0000E-03	8.9270E+04	2.5000E-02	6.3230E+04
	Z	1.2680E+06	4.0650E-04	1.1550E+06	2.0330E-03	1.0480E+06
	rx	1.9950E+06	1.0000E-03	1.3560E+06	6.0000E-03	8.7190E+05
	ry	3.5400E+06	1.0000E-03	2.4190E+06	6.0000E-03	1.1500E+06
Class14	X	2.7990E+05	5.0000E-03	1.6750E+05	2.5000E-02	1.1280E+05
	Y	1.9440E+05	5.0000E-03	1.0400E+05	2.5000E-02	7.7040E+04
	Z	1.6820E+06	5.9580E-04	1.3730E+06	2.9790E-03	1.1850E+06
	rx	2.6760E+06	1.0000E-03	1.7410E+06	6.0000E-03	1.1210E+06
	ry	6.9100E+06	1.0000E-03	4.2650E+06	6.0000E-03	1.4970E+06

Unit: force (kN), moment (kN.m), length (m), rotation (rad)

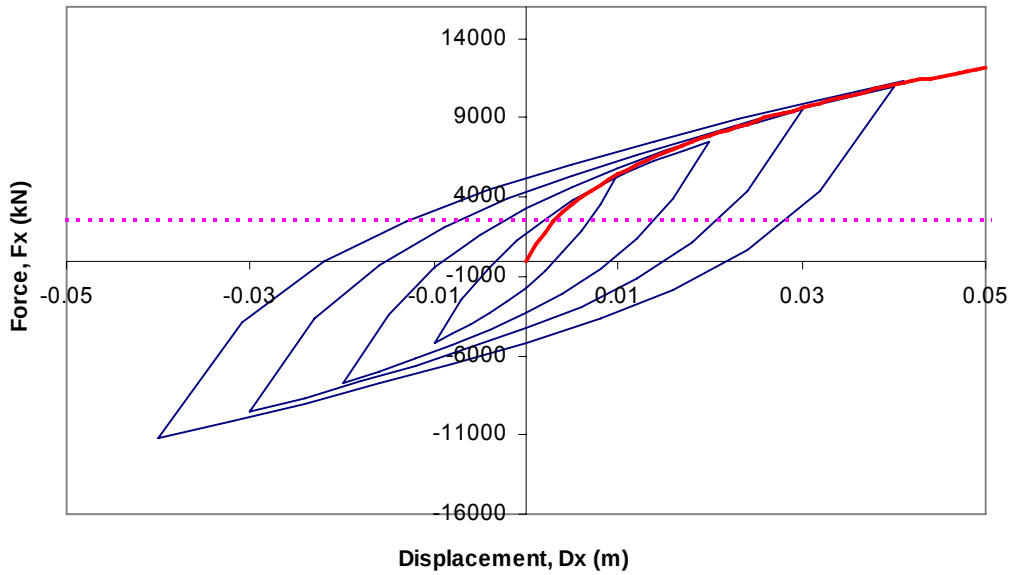

Figure 4.55 Load-deformation curve of foundation Class 2

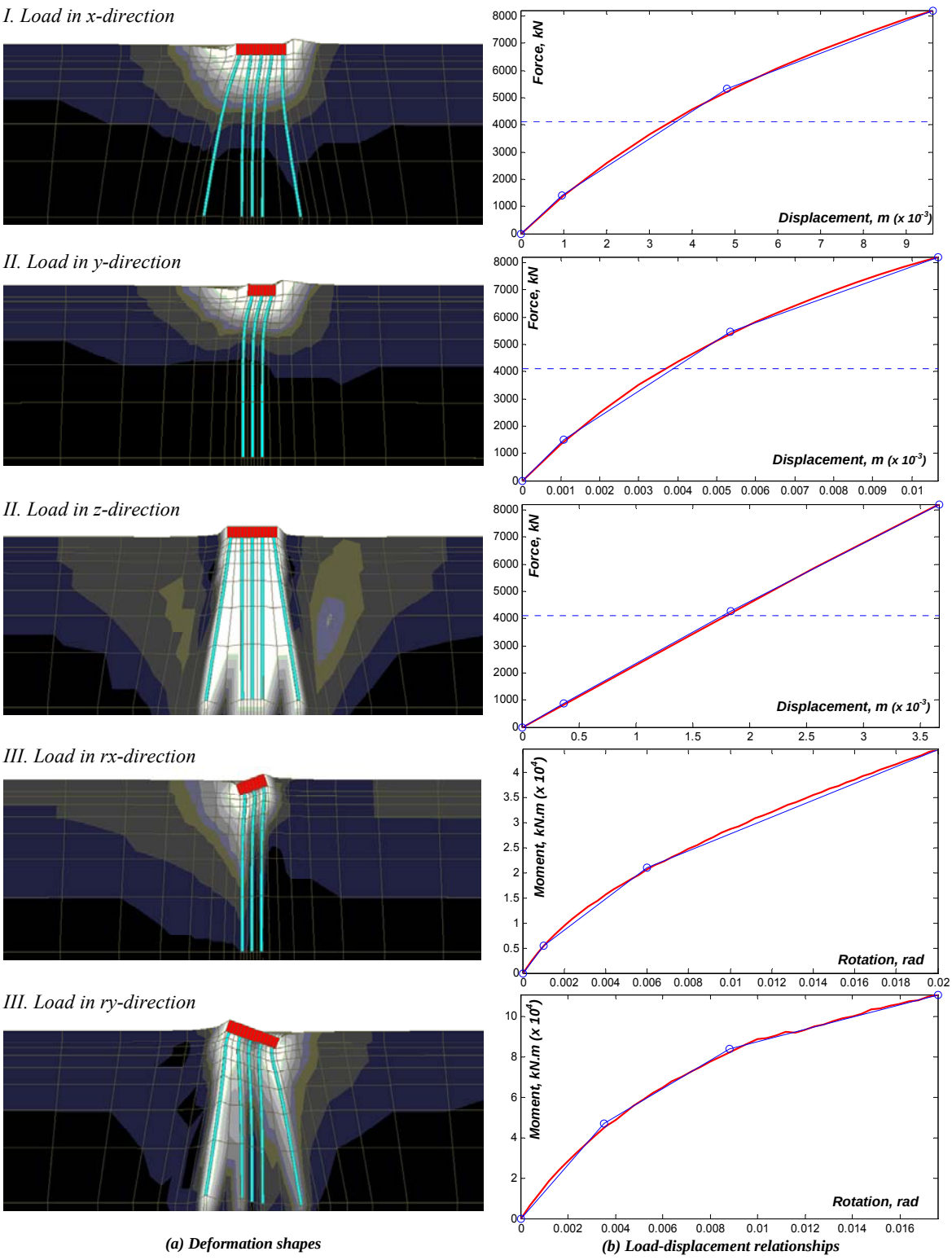

Figure 4.56 Inelastic pushover analyses of foundation Class 5

4.4.5 Dynamic Characteristics of the Bridge

Sample results from SAP2000 analyses are presented in Figure 4.57 and Table 4.9 and 4.10. The mode shapes and the corresponding periods of vibration are presented in Figure 4.57. Due to the significance of bearing friction on the dynamic characteristics of highway bridges (Mwafy et al., 2006a and b), the presented results are for two modeling approaches. The first simulation disregards the frictional resistance (Figure 4.57-a), while the second approach accounts for bearing friction using a simplified approach (Figure 4.57-b). Multilinear elasto-plastic joint elements are employed to idealize the movable bearings for the more refined inelastic analysis. The soil-structure interaction is accounted for in both modeling approaches by restraining the pile caps and the caissons at their center of gravity with grounded springs representing the foundation stiffness estimated from OpenSees inelastic analyses.

Comparison of the dynamic characteristics with and without considering bearing friction confirms the significance of the bearing frictional resistance. It is clear that the longitudinal modes of vibration of individual segments (Modes 1, 2, 4, 6, 8, 9, and 10 in Figure 4.57-a) are triggered when the bearing frictional resistance is disregarded. Unlike the latter simplified modeling, the first two modes when bearing friction is considered are transverse and vertical modes in the steel truss, while the longitudinal modes are activated at a period significantly lower than that observed in the first modeling approach. The presented sample results reflect the pressing need to account for various structural and nonstructural members as well as soil and foundation in the vulnerability assessment of major highway bridges.

It is also clear from Table 4.9 and 4.10 that about 350 modes of vibration are required to reach a 90% mass participation in the two principle directions. Higher modes of vibrations notably contribute to seismic response due to the length of the 1,700-foot bridge and the nonuniform distribution of stiffness and mass of this complex structure. Therefore, the Complete Quadratic Combination (CQC) method, which accounts for the coupling between modes, should be employed to combine the modal forces and displacement for response spectrum analysis.

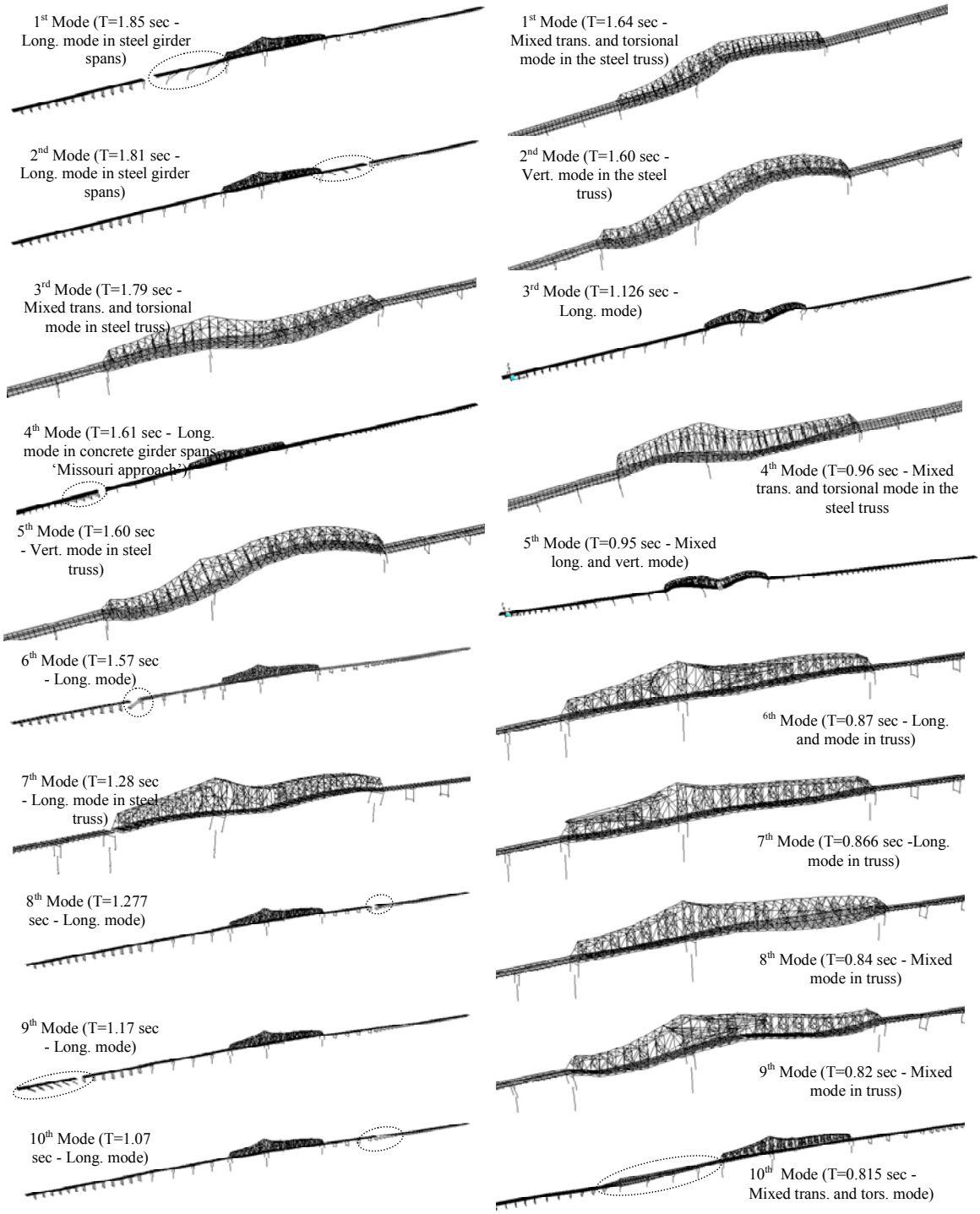

(a) Without bearing friction ***(b) With bearing friction***

Figure 4.57 Dynamic characteristics of the bridge with and without bearing friction

Table 4.9 Modal participation ratios without bearing friction

Mode No.	Period	SumUX	SumUY	SumUZ	SumRX	SumRY	SumRZ
1	1.853257	0.0385	8.446E-13	2.96E-08	9.965E-13	0.00001894	1.417E-12
2	1.806573	0.0706	8.683E-13	5.623E-08	1.02E-12	0.00003474	1.488E-12
3	1.790278	0.0706	0.0386	5.623E-08	0.1005	0.00003474	0.0331
4	1.610362	0.1069	0.0386	5.867E-08	0.1005	0.00004654	0.0331
5	1.606619	0.107	0.0386	0.0178	0.1005	0.0176	0.0331
6	1.568927	0.1123	0.0386	0.0178	0.1005	0.0176	0.0331
7	1.282327	0.2202	0.0386	0.0183	0.1005	0.0177	0.0331
8	1.276842	0.2249	0.0386	0.0183	0.1005	0.0177	0.0331
9	1.174378	0.2525	0.0386	0.0183	0.1005	0.0177	0.0331
10	1.074801	0.2802	0.0386	0.0183	0.1005	0.0177	0.0331
11	1.008221	0.3177	0.0386	0.0183	0.1005	0.0177	0.0331
12	1.007135	0.3177	0.0956	0.0183	0.2054	0.0177	0.0612
13	0.994812	0.3255	0.0956	0.0231	0.2054	0.0215	0.0612
14	0.927892	0.3255	0.1271	0.0231	0.2302	0.0215	0.0634
15	0.866217	0.3255	0.1271	0.0231	0.2302	0.0215	0.0634
16	0.864753	0.3255	0.1313	0.0231	0.238	0.0215	0.0686
17	0.860559	0.3281	0.1313	0.0241	0.238	0.0223	0.0686
18	0.825046	0.3552	0.1313	0.0241	0.238	0.0223	0.0686
19	0.812732	0.3552	0.1685	0.0241	0.255	0.0223	0.0756
20	0.802806	0.3922	0.1685	0.0241	0.255	0.0223	0.0756
21	0.799902	0.4249	0.1685	0.0241	0.255	0.0223	0.0756
22	0.797405	0.4249	0.202	0.0241	0.2888	0.0223	0.1206
23	0.768139	0.4263	0.202	0.0337	0.2888	0.0288	0.1206
24	0.728107	0.4263	0.2114	0.0337	0.2889	0.0288	0.1272
25	0.717234	0.4264	0.2114	0.0338	0.2889	0.0289	0.1272
26	0.698216	0.4264	0.2358	0.0338	0.3031	0.0289	0.1274
27	0.673665	0.4264	0.2358	0.0338	0.3031	0.0289	0.1274
28	0.665971	0.4266	0.2358	0.034	0.3031	0.0291	0.1274
29	0.662528	0.4266	0.246	0.034	0.3124	0.0291	0.1474
30	0.654134	0.4266	0.2551	0.034	0.3164	0.0291	0.1489
31	0.653544	0.4281	0.2551	0.034	0.3164	0.0291	0.1489
32	0.638066	0.4281	0.2551	0.0341	0.3164	0.0291	0.1489
33	0.634684	0.4281	0.2995	0.0341	0.3442	0.0291	0.2552
34	0.608947	0.4281	0.2995	0.035	0.3442	0.0297	0.2552
35	0.599013	0.4286	0.2995	0.05	0.3442	0.0364	0.2552
36	0.588377	0.4341	0.2995	0.05	0.3442	0.0364	0.2552
37	0.586806	0.4341	0.2995	0.0548	0.3442	0.0374	0.2552
38	0.582791	0.4341	0.3042	0.0548	0.3451	0.0374	0.2552
39	0.545687	0.4341	0.3055	0.0548	0.3451	0.0374	0.2552
40	0.534981	0.4341	0.3056	0.0548	0.3451	0.0374	0.2553
41	0.533998	0.4341	0.3057	0.0548	0.3451	0.0374	0.2556
42	0.53346	0.4341	0.3182	0.0548	0.3451	0.0374	0.2654
43	0.532535	0.4341	0.3354	0.0548	0.3528	0.0374	0.3151
44	0.521512	0.4341	0.3428	0.0548	0.3555	0.0374	0.3152
45	0.519931	0.4342	0.3428	0.0548	0.3555	0.0374	0.3152
46	0.513358	0.4342	0.3428	0.0548	0.3555	0.0374	0.3152
47	0.506246	0.4342	0.3428	0.0548	0.3555	0.0374	0.3152
48	0.502996	0.4342	0.3435	0.0548	0.3556	0.0374	0.3157
49	0.501219	0.4342	0.3435	0.0549	0.3556	0.0375	0.3157
50	0.494414	0.4342	0.3435	0.0576	0.3556	0.0378	0.3157
51	0.492455	0.4353	0.3435	0.0576	0.3556	0.0378	0.3157
52	0.492172	0.4353	0.3435	0.0576	0.3556	0.0378	0.3157
53	0.491344	0.4353	0.3435	0.0576	0.3556	0.0378	0.3157
54	0.488861	0.4353	0.3435	0.0576	0.3556	0.0378	0.3157
55	0.484422	0.4353	0.3544	0.0576	0.3572	0.0378	0.3237
56	0.479291	0.4353	0.3544	0.0576	0.3572	0.0378	0.3237
57	0.478027	0.4353	0.4156	0.0576	0.3797	0.0378	0.5585
58	0.47776	0.4354	0.4156	0.0576	0.3797	0.0378	0.5585
59	0.476116	0.4354	0.4214	0.0576	0.3822	0.0378	0.5738
60	0.474591	0.4354	0.4214	0.0576	0.3822	0.0378	0.5738
350	**0.176624**	**0.9067**	**0.9209**	**0.6999**	**0.8879**	**0.6511**	**0.9189**

Table 4.10 Modal participation ratios with bearing friction

Mode No.	Period	SumUX	SumUY	SumUZ	SumRX	SumRY	SumRZ
1	1.641388	4.114E-13	0.0403	6.4E-11	0.1027	6.649E-11	0.0344
2	1.599591	0.0005725	0.0403	0.0181	0.1027	0.0176	0.0344
3	1.125495	0.212	0.0403	0.0187	0.1027	0.0177	0.0344
4	0.961739	0.212	0.1049	0.0187	0.2108	0.0177	0.0641
5	0.954852	0.2888	0.1049	0.0239	0.2108	0.0223	0.0641
6	0.866369	0.2932	0.1049	0.0247	0.2108	0.0229	0.0641
7	0.865827	0.3011	0.1049	0.0266	0.2108	0.0243	0.0641
8	0.835024	0.3011	0.1125	0.0266	0.2246	0.0243	0.0723
9	0.823511	0.3026	0.1125	0.0302	0.2246	0.0267	0.0723
10	0.815069	0.3026	0.1896	0.0302	0.2724	0.0267	0.0786
11	0.748247	0.3026	0.2095	0.0302	0.2734	0.0267	0.0909
12	0.718237	0.3029	0.2095	0.0302	0.2734	0.0267	0.0909
13	0.706457	0.3029	0.2534	0.0302	0.3112	0.0267	0.1561
14	0.685919	0.3029	0.2546	0.0302	0.3113	0.0267	0.1562
15	0.673663	0.3029	0.2546	0.0302	0.3113	0.0267	0.1562
16	0.671697	0.309	0.2546	0.0307	0.3113	0.0269	0.1562
17	0.638975	0.3125	0.2546	0.0312	0.3113	0.0272	0.1562
18	0.632133	0.3497	0.2546	0.041	0.3113	0.0321	0.1562
19	0.631649	0.3497	0.2671	0.041	0.3181	0.0321	0.1563
20	0.616117	0.3497	0.3127	0.041	0.3473	0.0321	0.2757
21	0.587909	0.3646	0.3127	0.0463	0.3473	0.0344	0.2757
22	0.574941	0.3646	0.3168	0.0463	0.3506	0.0344	0.278
23	0.561989	0.3646	0.3168	0.0463	0.3506	0.0344	0.278
24	0.548374	0.3646	0.3189	0.0463	0.3507	0.0344	0.2835
25	0.535021	0.3646	0.319	0.0464	0.3507	0.0344	0.2835
26	0.53399	0.3646	0.319	0.0464	0.3507	0.0344	0.2835
27	0.528582	0.3646	0.3395	0.0464	0.3509	0.0344	0.2956
28	0.524452	0.3693	0.3395	0.0477	0.3509	0.0351	0.2956
29	0.521461	0.3693	0.3395	0.05	0.3509	0.0357	0.2956
30	0.516463	0.3709	0.3395	0.0504	0.3509	0.0359	0.2956
31	0.50866	0.3739	0.3395	0.0515	0.3509	0.0364	0.2956
32	0.505691	0.3746	0.3395	0.0518	0.3509	0.0366	0.2956
33	0.503368	0.3746	0.3395	0.0518	0.3511	0.0366	0.2969
34	0.499323	0.3746	0.3675	0.0518	0.3632	0.0366	0.3954
35	0.492045	0.3747	0.3675	0.0518	0.3632	0.0366	0.3954
36	0.490675	0.3748	0.3675	0.0519	0.3632	0.0366	0.3954
37	0.487804	0.3749	0.3675	0.0521	0.3632	0.0368	0.3954
38	0.482429	0.3749	0.3929	0.0521	0.3699	0.0368	0.4711
39	0.479967	0.3751	0.3929	0.0521	0.3699	0.0368	0.4711
40	0.478638	0.3751	0.4123	0.0521	0.3775	0.0368	0.5436
41	0.477763	0.3751	0.4123	0.0521	0.3775	0.0368	0.5436
42	0.475208	0.3753	0.4123	0.0521	0.3775	0.0368	0.5436
43	0.474447	0.3753	0.4123	0.0521	0.3775	0.0368	0.5436
44	0.470659	0.3753	0.4123	0.0522	0.3775	0.0371	0.5436
45	0.469851	0.3753	0.4123	0.0522	0.3775	0.0371	0.5436
46	0.469714	0.3753	0.417	0.0522	0.3777	0.0371	0.5473
47	0.468018	0.3753	0.417	0.0522	0.3777	0.0371	0.5473
48	0.467101	0.3753	0.417	0.0522	0.3777	0.0371	0.5473
49	0.464407	0.3754	0.417	0.0522	0.3777	0.0371	0.5473
50	0.463343	0.3754	0.434	0.0522	0.3837	0.0371	0.5621
51	0.462	0.3754	0.4342	0.0522	0.3837	0.0371	0.5623
52	0.460525	0.3754	0.4342	0.0522	0.3837	0.0371	0.5623
53	0.460049	0.3754	0.4342	0.0527	0.3837	0.0382	0.5623
54	0.455817	0.3755	0.4342	0.0527	0.3837	0.0382	0.5623
55	0.455049	0.3755	0.4402	0.0527	0.3847	0.0382	0.5629
56	0.450775	0.3757	0.4402	0.0527	0.3847	0.0382	0.5629
57	0.4476	0.3758	0.4402	0.0528	0.3847	0.0383	0.5629
58	0.446628	0.3758	0.4402	0.0528	0.3847	0.0383	0.5629
59	0.442867	0.3758	0.4402	0.0528	0.3847	0.0383	0.5629
60	0.438993	0.3828	0.4402	0.0529	0.3847	0.0383	0.5629
350	**0.164268**	**0.9271**	**0.9465**	**0.7349**	**0.9612**	**0.6516**	**0.9279**

4.4.6 Summary and Discussions

This section introduces the investigation to assess the seismic response of the Caruthersville Bridge on the I-155, considering Soil-Structure Interaction (SSI). The 59-span bridge was built in the early seventies across the Mississippi River between Missouri and Tennessee. It includes typical deficiencies of bridges constructed during this era. Location of the project site in the vicinity of the New Madrid central fault confirms the significance of this comprehensive study. The three-dimensional simulations of the bridge and its foundation system using state-of-the-art analytical tools and methodologies were presented. The SSI analysis is a key element in this study due to the massive and stiff foundation and the relatively soft deep soil of the site. The length of the bridge and the diversity of its structural system emphasize the importance of rigorous SSI analysis, as considered above. Several analytical platforms are employed in this study, including ZEUS-NL and OpenSees. The dynamic characteristics are significantly influenced when the bearing frictional resistance is accounted for. Without the bearing friction, the 11 segments of the bridge vibrated independently in the longitudinal direction, while friction linked them together at the expansion joint. Due to the length of the bridge and the nonuniform distribution of stiffness and mass, higher modes of vibrations notably contributed to seismic response. The refined modeling approach described in this report enables the identification of areas of vulnerability of the investigated bridge and the assessment of its complex response.

CHAPTER 5

SEISMIC VULNERABILITY OF A HIGHWAY OVER-CROSSING BRIDGE IN CENTRAL AND EASTERN U. S.

5.1 Introduction

Seismic vulnerability relationships of a commonly-used highway overcrossing bridge in the Central and Eastern U.S. (CEUS) are derived in this section using different idealizations. Soil-structure-interaction (SSI) of the bridge is accounted for by using approaches introduced in Chapter 3, using the analysis tools and procedures verified in Chapter 2, and following the research presented in Chapter 4. Four different modeling methods are adopted to represent embankment, abutments, and foundations of the bridge: (a) assuming that the abutments and foundations of the bridge are fixed, (b) using lumped springs developed from conventional pile analysis application, LPile (Ensoft Inc. 2005), (c) using lumped springs developed from three-dimensional FE application, OpenSees (McKenna et al., 2001), and (d) utilizing multiplatform analysis introduced in Section 3.3 to combine a three-dimensional FE model in OpenSees with structural model in ZEUS-NL. The components of the bridge, such as piers, fixed bearings, expansion bearings, gaps, embankments, and abutments are modeled with nonlinear elements. Limit states of these components are carefully defined. A total of 60 ground motions, 30 artificial ground motions and 30 recorded ground motions, are applied to the structure. Vulnerability curves of the bridge are derived for the four SSI approaches.

The primary objective of this study is to derive vulnerability curves of a bridge in the Central and Eastern U.S. with advanced SSI considerations. Therefore, rather than deriving a complete set of vulnerability curves covering a wide range of bridge types, vulnerability curves of a bridge representing the most typical bridge type are derived. The vulnerability curves derived for the reference bridge can be applied to a subclass of bridges with similar configurations.

5.2 Selection of the Reference Bridge

A highway overcrossing bridge at Southern Illinois is selected. The bridge has four continuous steel girders. Nielson (2005) surveyed the bridge inventory of 11 states within the Central and Southern U.S. and presented statistics on bridge configurations. The reference bridge selected in this study belongs to a category of MultiSpan Continuous Steel (MSC) Girder Bridges, which occupy the third largest portion of the entire bridge population. Mean span numbers of the MSC Bridge is 3.72, with a standard deviation of 2.53. The reference bridge has four spans, which is close to the mean span numbers of the same category. The maximum span length of the MSC Bridge is 26.38 m, with a standard deviation of 15.25 m. The maximum span length of the reference bridge is 18 m, which is a little off from the mean value. But considering the large standard deviation of the maximum span length, the length of the selected bridge represents a typical bridge configuration of the same type. Deck width is also close to the mean deck width of the MSC Bridge. Table 5.1 presents the statistics from Nielson (2005) and the corresponding values of the reference bridge in each statistic category.

Table 5.1 Bridge inventory statistics of Central and Southern U.S.

Category	Statistics (Nielson, 2005)	Reference bridge
Bridge classes	1. Multispan Simply Supported Concrete Girder (MSSS Concrete, 18.9%) 2. Single-span concrete girder (SS Concrete, 13.9%) 3. Multispan continuous steel girder (MSC Steel, 13.2%) 4. Multispan Simply Supported Steel Girder (MSSS Steel, 11.3 %) . . 10. Multispan Continuous Concrete Box Girder (MSC Concrete-Box, 0.6%) 11. Other (11.7%)	Belongs to category #3 (MSC Steel)
Span number	Statistics of MSC Steel Bridge Mean : 3.72 Standard deviation : 2.53	4
Maximum span length, m	Statistics of MSC Steel Bridge Mean : 26.38 Standard deviation : 15.25	18
Deck with, m	Statistics of MSC Steel Bridge Mean : 12.16 Standard deviation : 6.37	10.26

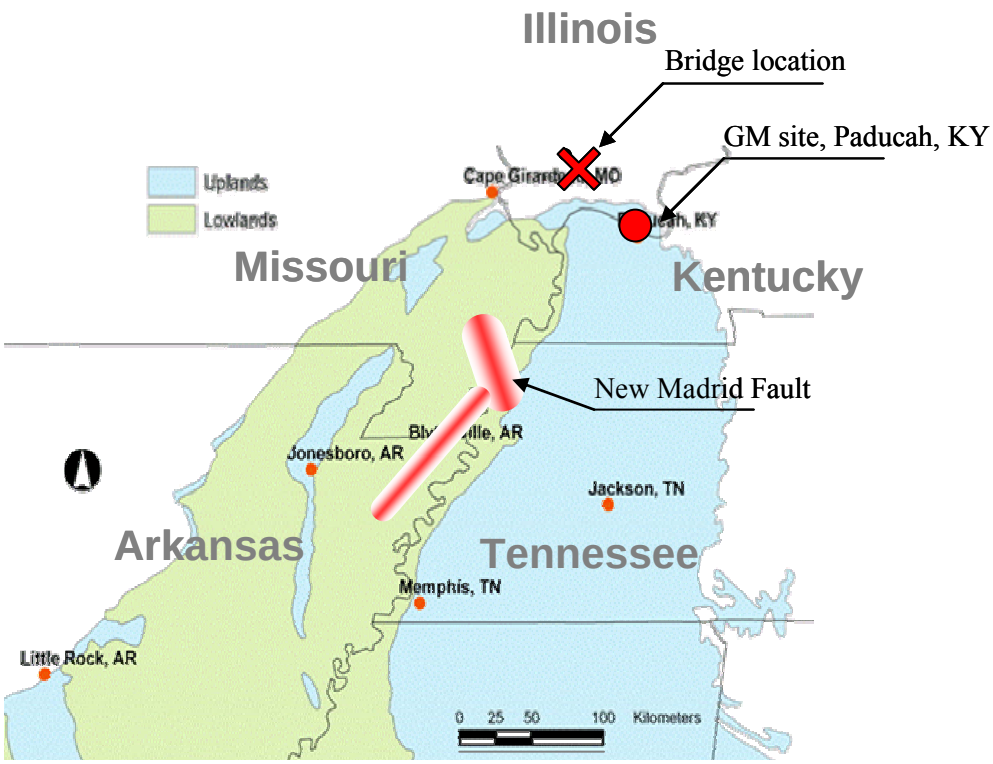

Figure 5.1 Location of the reference bridge

Figure 5.1 depicts the location of the bridge alongside the geographical distribution of two distinct soil profiles surrounding New Madrid Fault, Upland profile and Lowland profile. The bridge is located about 110 km from the New Madrid Fault. Ground motions generated for a site close to the bridge, Paducah, KY, are adopted for vulnerability analysis.

5.3 Seismic Hazard at the Bridge Site

The seismic hazard in the Central and Eastern U.S. is characterized by infrequent but damaging earthquakes. The moment magnitudes of New Madrid Earthquakes from 1811-1812 were estimated to be from 7.8 to 8.1, which ranks as some of the largest earthquakes in the U.S. since its settlement by Europeans (USGS, 2006). The damaged area by the earthquake reached 600,000, square kilometers and the earthquakes were perceived within the region of 5,000,000 square kilometers. Even though those

earthquakes occur infrequently, paleoseismic studies using liquefaction effects show that there is evidence of large, prehistoric earthquakes (Green et al., 2005) in Mid-America.

Due to the infrequent nature of earthquakes within the Central and Eastern U.S., the recorded ground motions, especially from large earthquakes, which is essential for the derivation of vulnerability curves, do not exist. Therefore, artificial ground motions as well as carefully selected ground motions from sites with similar soil profile and source mechanisms should be used for seismic vulnerability estimation. In this study, a total of 60 ground motions, 30 artificial ground motions and 30 recorded ground motions, are used for a vulnerability analysis. The selected bridge is located about 110 km from the New Madrid Fault Zone, as shown in Figure 5.1. The synthetic ground motions generated for Paducah, Kentucky (Fernández and Rix, 2006a), which is about 60 km from the studied region, is used for this study. The synthetic ground motions are generated for three return periods, 475, 975, and 2,475 years. Recorded ground motions from other regions are carefully selected. The selection criteria of the recorded motions include magnitude (6.5~10), distance (20~120 km), and site condition (B). The list of selected ground motions are presented in Table 5.2.

The response of bridges, unlike many buildings, is distinctively different along and perpendicular to its axis, due to the large aspect ratio of bridge structures and the different properties of bridge components in each direction. Bearings have distinctively different resistance in longitudinal and in transverse direction. Accordingly, it is essential to run analysis in both directions when evaluating seismic fragility of a bridge.

Most straight and symmetric bridges have an uncoupled mode of vibration in longitudinal and transverse directions. Numerical models of structural elements such as gaps and bearings also do not include coupled components in longitudinal and transverse directions. These bridge configurations and limitation in modeling allow analyzing a bridge in each direction independently. If the bridge under consideration is skewed and has highly coupled components in longitudinal and in transverse directions, it should be analyzed under biaxial or even triaxial ground motions.

When artificial ground motions are generated for a site far from an epicenter, directivities of ground motions are not considered. Therefore, the generated ground

motions represent neither fault normal nor fault parallel motion. This implies that the ground motions at a site far from an epicenter can be imposed to structures in any direction. Even though the directivity of the ground motions is not important for a site far from an epicenter, a ground motion record is related with its orthogonal component in terms of peak values. From the 30 recorded ground motions, a correlation coefficient of PGA of two horizontal components is found to be 0.77. The PGA of orthogonal components of artificial ground motion is determined so that the correlation coefficient is about the same. Figure 5.2 presents the PGAs of both components of artificial ground motions and recorded ground motions. Figure 5.3 presents the displacement response spectra of component 1 of these ground motions. It should be emphasized that the above is not an exhaustive study of phase and peak parameter correlations in strong motion, but rather a brief assessment of the suite of records, both natural and artificial, to achieve a degree of consistency in the fragility relationships.

Vulnerability analyses of structures usually require a large number of dynamic analyses. Each dynamic analysis may take from a few hours to a few days depending on the level of discretization of a structural model and the number of time steps used in the analysis. Most ground motions, either recorded or artificial, include accelerations whose intensity is small enough to be neglected from the structural point of view. Thus, by trimming those insignificant accelerations at the start and the end of ground motion records, the total analysis time can be significantly reduced. In this study, the duration of ground motion is selected based on Arias intensity of 0.001% and 95% in addition to engineering judgment.

Table 5.2 Recorded ground motions selected for vulnerability analysis

Date	Earthquake	M	Station	Distance, km	PGA,g	
					Comp. 1	Comp. 2
1/17/1994 12:31	Northridge	6.7	14403 LA - 116th St School	41.9	0.21	0.13
2/9/1971 14:00	San Fernando	6.6	24278 Castaic - Old Ridge Route	24.9	0.32	0.27
10/18/1989 0:05	Loma Prieta	6.9	58262 Belmont - Envirotech	49.9	0.11	0.11
1/17/1994 12:31	Northridge	6.7	24157 LA - Baldwin Hills	31.3	0.24	0.17
11/8/1980 10:27	Trinidad, California	7.2	1498 Rio Dell Overpass, E Ground	71.9	0.16	0.13
6/28/1992 11:58	Landers	7.3	23559 Barstow	36.1	0.13	0.14
9/20/1999 1:47	Chi-Chi, Taiwan	7.6	CHY022	71.6	0.07	0.04
9/20/1999 1:47	Chi-Chi, Taiwan	7.6	CHY079	55.0	0.05	0.04
6/28/1992 11:58	Landers	7.3	23 Coolwater	21.2	0.42	0.28
4/25/1992 18:06	Cape Mendocino	7.1	89509 Eureka - Myrtle & West	44.6	0.15	0.18
1/17/1994 12:31	Northridge	6.7	Featherly Park - Pk Maint Bldg	84.2	0.10	0.10
10/18/1989 0:05	Loma Prieta	6.9	1678 Golden Gate Bridge	85.1	0.23	0.12
10/18/1989 0:05	Loma Prieta	6.9	1678 Golden Gate Bridge	85.1	0.12	0.23
1/17/1994 12:31	Northridge	6.7	14196 Inglewood - Union Oil	44.7	0.09	0.10
1/17/1994 12:31	Northridge	6.7	Beverly Hills - 12520 Mulhol	20.8	0.62	0.44
1/17/1994 12:31	Northridge	6.7	24400 LA - Obregon Park	37.9	0.36	0.56
1/17/1994 12:31	Northridge	6.7	24400 LA - Obregon Park	37.9	0.56	0.35
1/17/1994 12:31	Northridge	6.7	24278 Castaic - Old Ridge Route	22.6	0.57	0.51
2/9/1971 14:00	San Fernando	6.6	80053 Pasadena - CIT Athenaeum	31.7	0.09	0.11
7/21/1952 11:53	Kern County	7.4	283 Santa Barbara Courthouse	87.0	0.09	0.13
10/18/1989 0:05	Loma Prieta	6.9	47189 SAGO South - Surface	34.7	0.07	0.07
4/25/1992 18:06	Cape Mendocino	7.1	89530 Shelter Cove Airport	33.8	0.23	0.19
4/25/1992 18:06	Cape Mendocino	7.1	89530 Shelter Cove Airport	33.8	0.19	0.23
9/20/1999 1:47	Chi-Chi, Taiwan	7.6	TCU034	33.0	0.25	0.11
9/20/1999 1:47	Chi-Chi, Taiwan	7.6	TCU045	24.1	0.51	0.47
9/20/1999 1:47	Chi-Chi, Taiwan	7.6	TCU047	33.0	0.41	0.30
9/20/1999 1:47	Chi-Chi, Taiwan	7.6	TCU047	33.0	0.30	0.41
9/20/1999 1:47	Chi-Chi, Taiwan	7.6	TCU095	43.4	0.38	0.71
1/17/1994 12:31	Northridge	6.7	24605 LA - Univ. Hospital	34.6	0.49	0.21
2/9/1971 14:00	San Fernando	6.6	290 Wrightwood - 6074 Park Dr	60.3	0.06	0.04

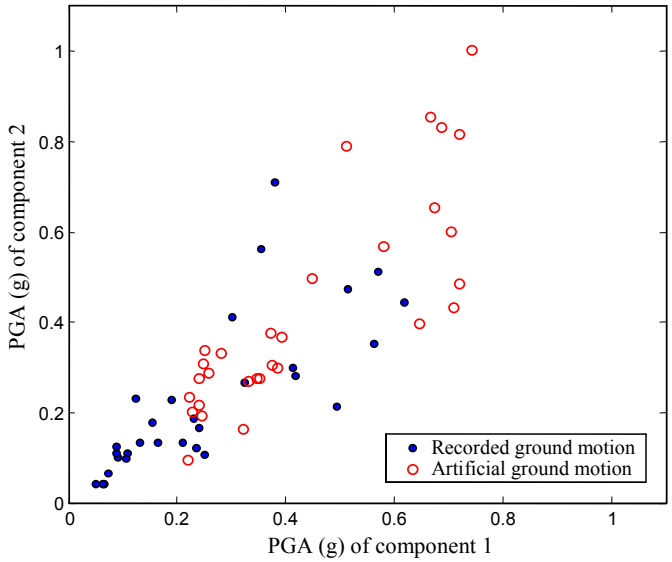

Figure 5.2 Distribution of PGAs in recorded and artificial ground motions

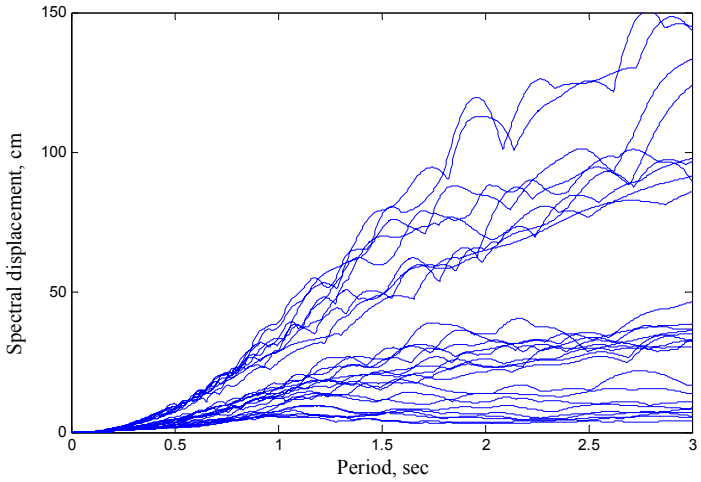

(a) Artificial ground motions

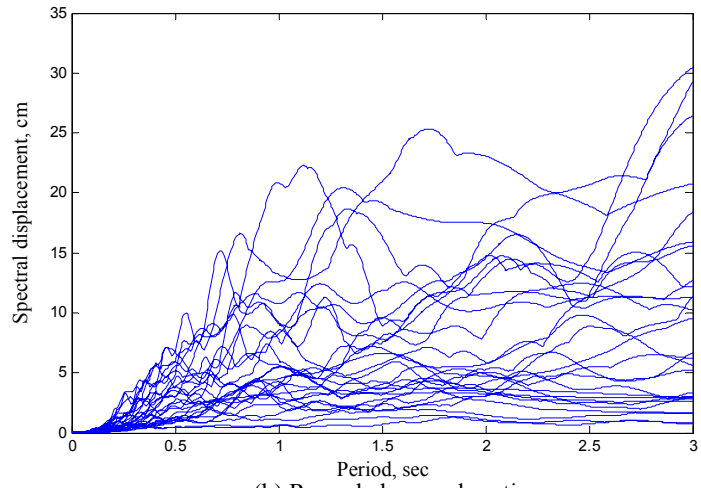

(b) Recorded ground motions

Figure 5.3 Spectral displacement of selected ground motions, Component 1

5.4 Bridge Configuration and Soil Profile

The selected bridge consists of three bents and four spans of continuous steel girders, as illustrated in Figure 5.4. The deck is supported on fixed bearings at a bent 2 and on expansion bearings at bents 1, 3, and abutments. Span lengths are 14 m at side spans and 18 m at center spans. Each bent consists of three circular piers supported by a pile cap and 10 steel piles. The piles at bent 2 are battered toward abutments to resist moment transferred from longitudinal movement of the deck. Abutments are supported on six steel piles, two of which are battered toward the bridge. Five boring tests were conducted at the site, as shown in Figure 5.5. The boring test results showed that bedrock is located at an average depth of 4.57 m (15 ft) below the bottom of pilecaps. The soil layers consist predominantly of very stiff to hard clays. Due to lack of soil parameters required for numerical soil model, standard dynamic properties of stiff clay are used.

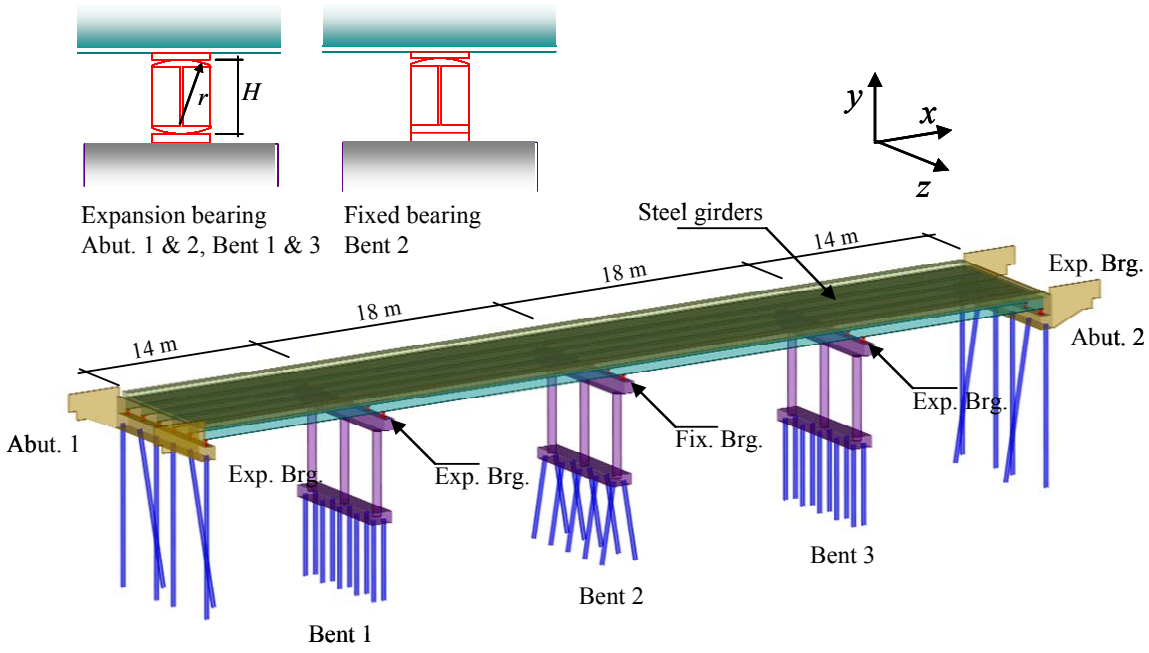

Figure 5.4 Configuration of the reference bridge

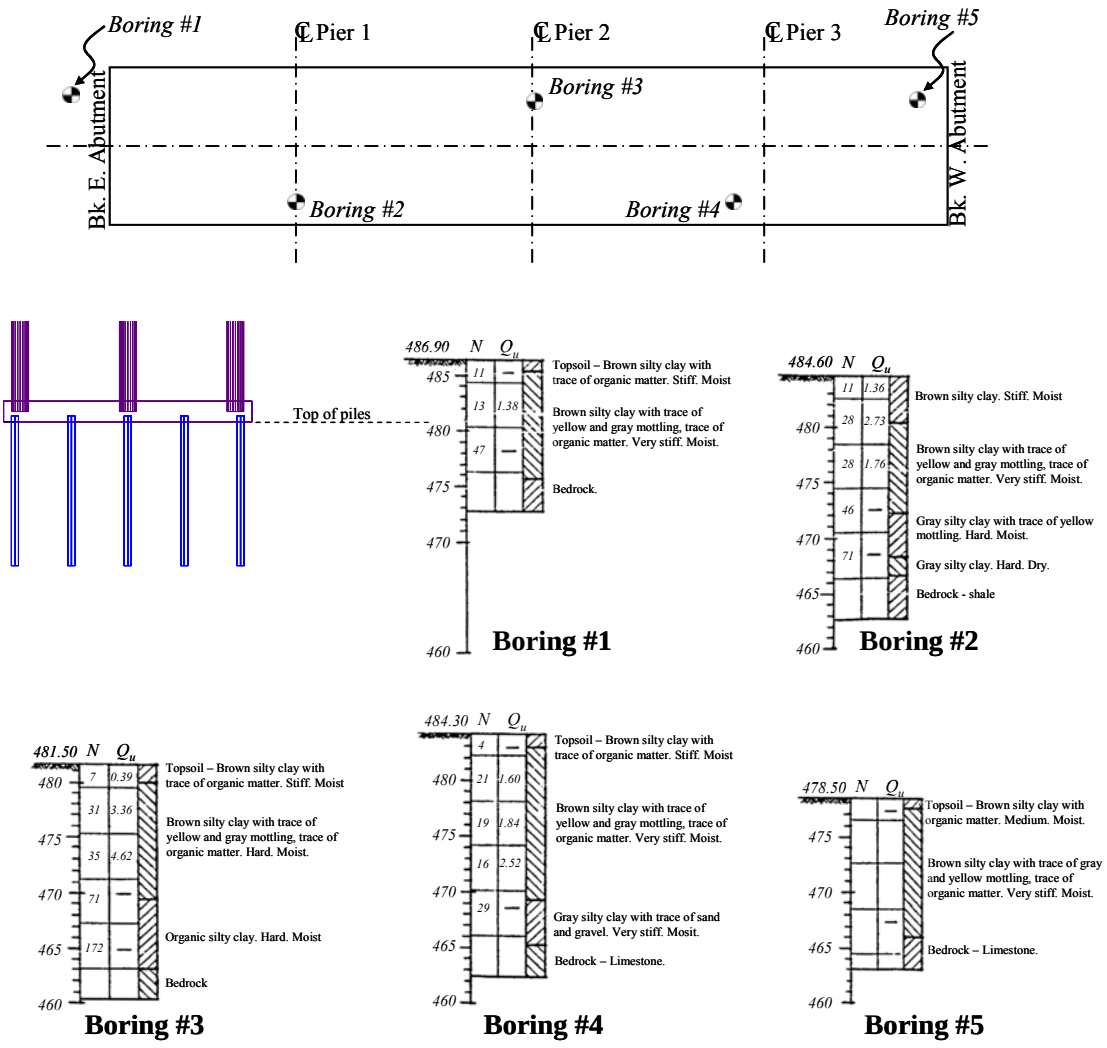

Figure 5.5 Borehole test results of the bridge site

5.5 Analytical Model of the Reference Bridge

A bridge can fail with various failure modes. For the reference bridge, the possible failure modes include unseating of superstructure in transverse or in longitudinal direction, which was frequently observed from past earthquakes, bent failures in transverse direction, and abutment failures in transverse or longitudinal directions. Bent failures in longitudinal direction are unlikely to happen for the reference bridge, as the expansion bearings relive displacement demand and abutments limit the longitudinal movement of the superstructure. To estimate the damage from these failure modes, it is essential to run analysis in both directions.

The bridge is analyzed with four approaches of SSI. The first approach assumes that abutments and pile groups are all fixed. The second approach includes lumped springs representing foundations and abutments to account for flexibility and hysteretic energy dissipation. The spring properties are estimated based on a method frequently used in practice. The third approach adopts lumped springs estimated from an analysis of a three-dimensional FE model of soil-foundation system. In the fourth approach, multiplatform analyses are conducted to combine three-dimensional FE geotechnical and structural models. This approach takes into account the flexibility and nonlinearity of soil and foundation, with less assumption than the third approach. In all of these approaches, bearings and gaps are modeled in detail as those elements critically affect the bridge response. Table 5.3 summarizes the analytical models used in the four approaches.

5.5.1 Bents and Steel Girders

A superstructure of the reference bridge consists of concrete decks on top of six continuous steel girders. Substructure consists of three piers supported by steel pile foundations. The dimension and configuration of a typical bent and foundation is presented in Figure 5.6. The steel girders, decks, cross beams of bents, and piers are modeled in ZEUS-NL using cubic frame elements, as shown in Figure 5.7. Fiber-based elements are used to model each frame element.

Table 5.3 Analytical models of bridge components for four approaches

Bridge components		Approach 1 Fixed	Approach 2 Conventional	Approach 3 FE	Approach 4 Multiplatform
Bearings	Fixed Bearings	Longitudinal and transverse direction: Tri-linear model based on the test by Mander et al. (1996)			
	Expansion Bearings	Longitudinal direction: Theoretical derivation of geometric stiffness in addition to the 5% of friction from Mazroi et al. (1983) Transverse direction: Tri-linear model based on the test by Mander et al. (1996)			
Frame elements		Fiber-based element in ZEUS-NL			
Abutments		Fixed	Lumped spring using practical approach by Caltran (2004) and Maroney (1995)	Lumped spring from FE embankment and abutment model	Multiplatform analysis
Foundations		Fixed	A single pile analysis using LPile (Ensoft, 2005) and consider group effect	Lumped spring from FE foundation model	Multiplatform analysis

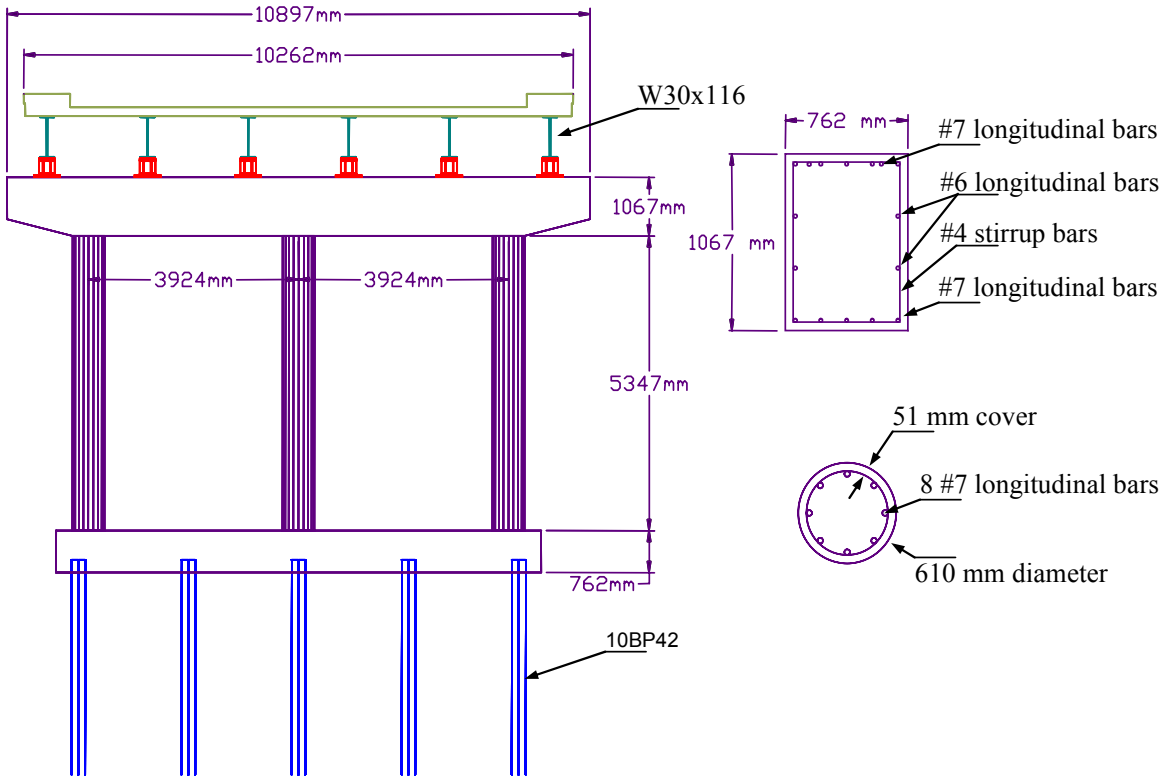

Figure 5.6 Configuration of typical bents and foundations

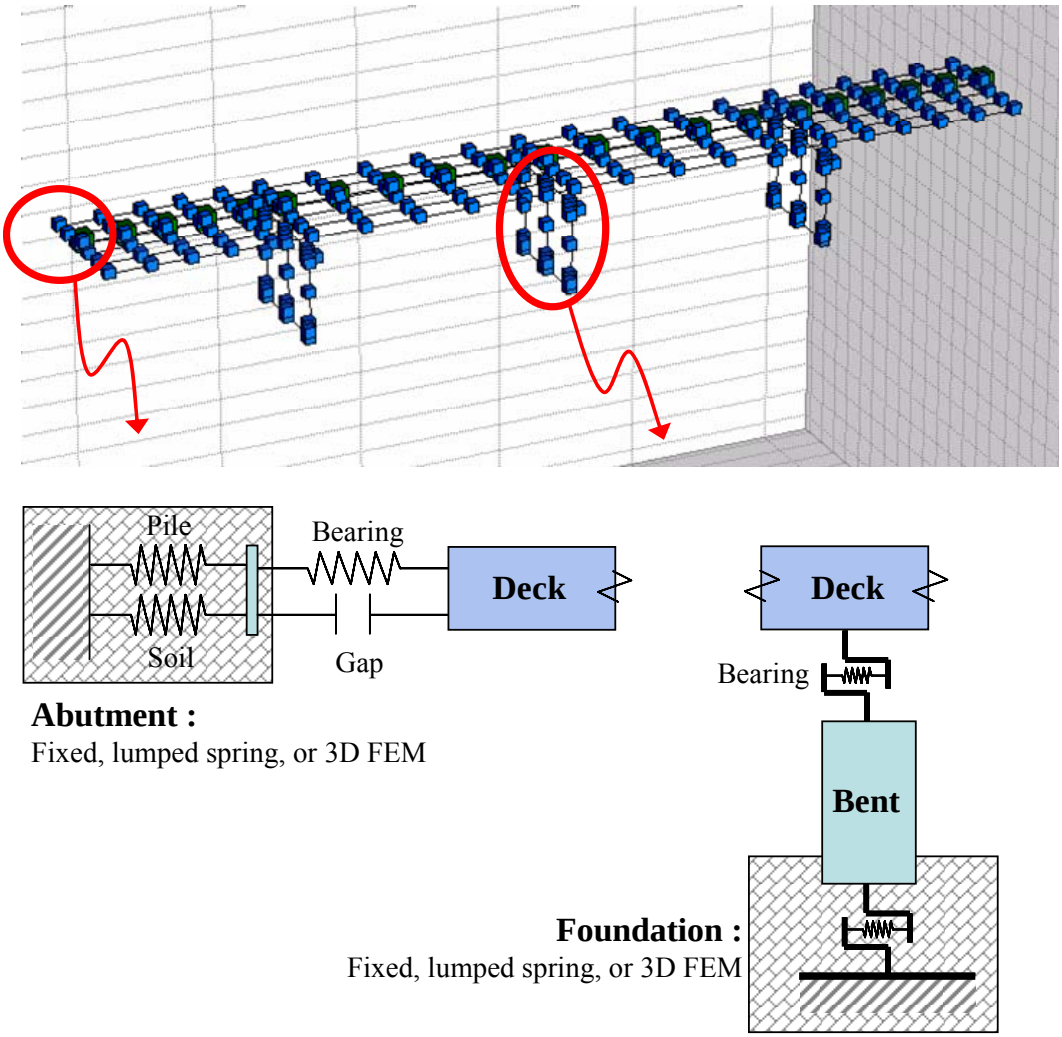

Figure 5.7 FE model of the bridge and connectivity of structural components

5.5.2 Bearings and Gap Models

Two types of bearings are used in the bridge as shown in Figure 5.4. The expansion bearings are typical segmental rocker-type bearings where the radius of bearing surface, (r), is larger than the half of the bearing height, (H/2), between two contacting surfaces. The longitudinal stiffness of this type of bearing increases with the increase of relative displacement between two contacting surfaces. In addition to this stiffness from geometry, there exists frictional resistance between bearings and bearing plates. Mazroi et al. (1983) tested the friction of circular bearings in various conditions: clean (as-built) condition, rusted condition, and with debris on bearing surface. When there is debris at the

contacting surface between bearings and bearing plates, 5% of friction was measured. In this study, the longitudinal stiffness of expansion bearings is defined as 5% of friction in addition to stiffness from the geometry of bearings. Refer to Appendix A.1 for the derivation of bearing stiffness. Figure 5.8 presents the hysteretic behavior of expansion bearings in a longitudinal direction.

Mander et al. (1996) tested various types of bearings taken from existing bridges. Among the tested bearings, the low-type bearing is expected to have similar response characteristics with transverse behavior of bearings of the reference bridge, as all of these bearings are restrained by pintles and pintle holes. The study showed that the behavior of bearings in a transverse direction is controlled by the contact and separation of pintles to bearing plates and bearing plates to anchor bolts. Until the gaps between these elements are consumed, constant friction is observed. Then, the resisting force increases with the increase of displacement. Figure 5.9 compares the test result of low-type sliding bearings and the behavior of the idealized trilinear model. With a lack of further experimental data, the behavior of fixed bearings in transverse and longitudinal directions and the behavior of expansion bearing in a transverse direction are assumed to be similar with the transverse direction test of low-type bearing by Mander et al (1996).

The response of a bridge against earthquake loading can significantly influenced by the opening and closing of the gap between the deck and abutments. The drawings of the bridge shows that there exist 38 mm of gap between the deck and abutments at the temperature of 50°F. Neglecting the variation of the length of a superstructure with temperature variation, the gaps are modeled as asymmetric springs such that the spring has no resistance on tensile loading, and they become stiff when the gap closes. The hysteretic behavior of a gap element used in the bridge model is shown in Figure 5.10.

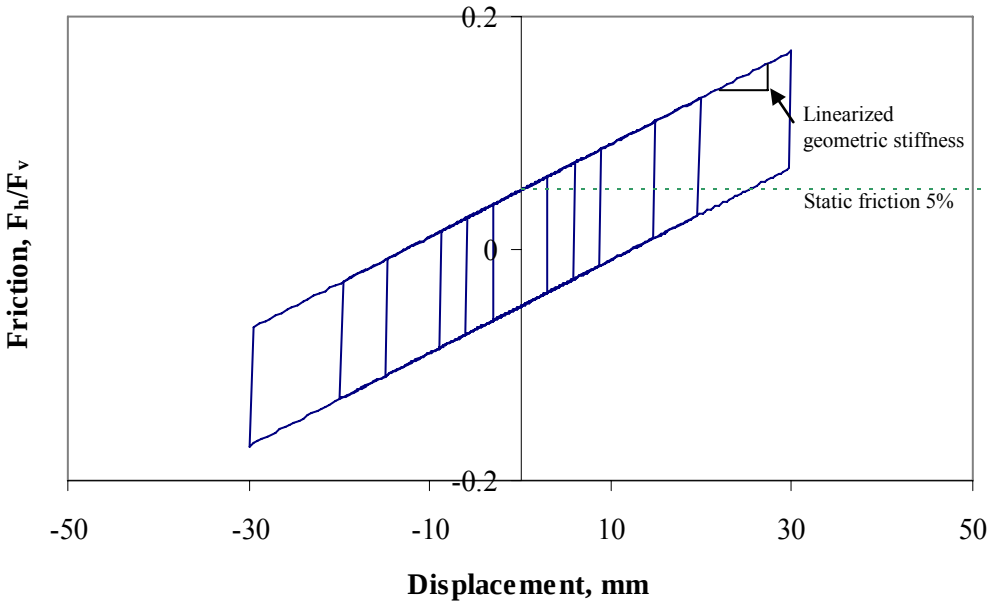

Figure 5.8 Expansion bearing model in longitudinal direction

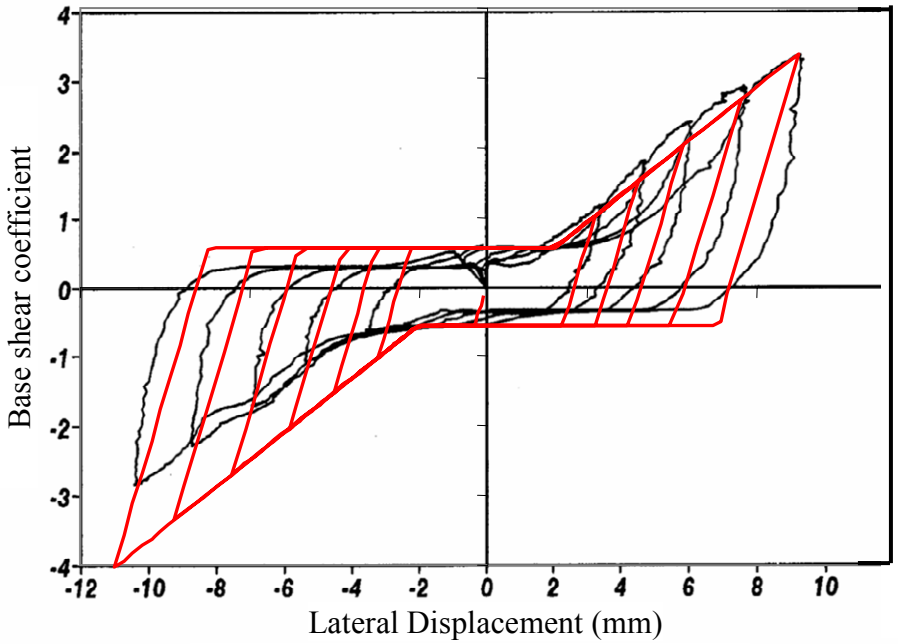

Figure 5.9 Low-type bearing behavior in transverse direction
(low-type sliding bearing in transverse direction, Mander 1996)

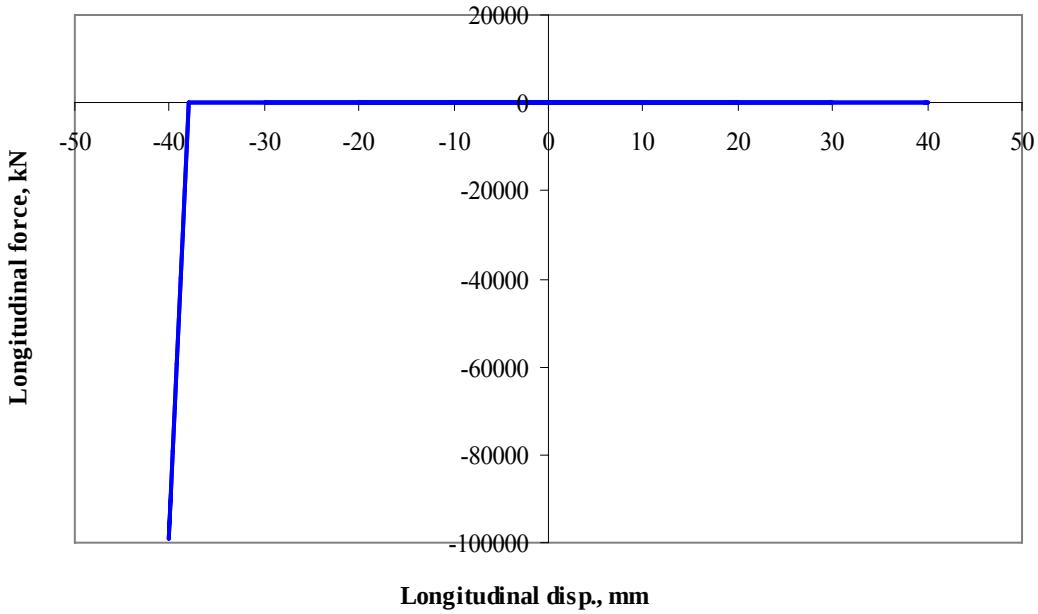

Figure 5.10 Hysteretic behavior of a gap element

5.5.3 Abutment and Foundation

5.5.3.1 Approach 1: Fixed Foundation Assumption

It is assumed herein that abutments and foundations are fixed. This approach allows the investigation of the failure modes of a bridge with rigid boundary conditions and compares it to the failure modes of a bridge with flexible boundary conditions.

5.5.3.2 Approach 2: Lumped Springs Derived from Conventional Methods

The foundation stiffness and strengths are evaluated using pile analysis application, LPile (Ensoft Inc., 2005). The nonlinear response of a single pile is obtained from the LPile analysis. The pile group effects are considered using *p*-multipliers by Brown and Reese (1985). The summary of model properties used for the single pile analysis is given in Appendix A.2. Figure 5.11 shows the hysteretic behavior of the pile group.

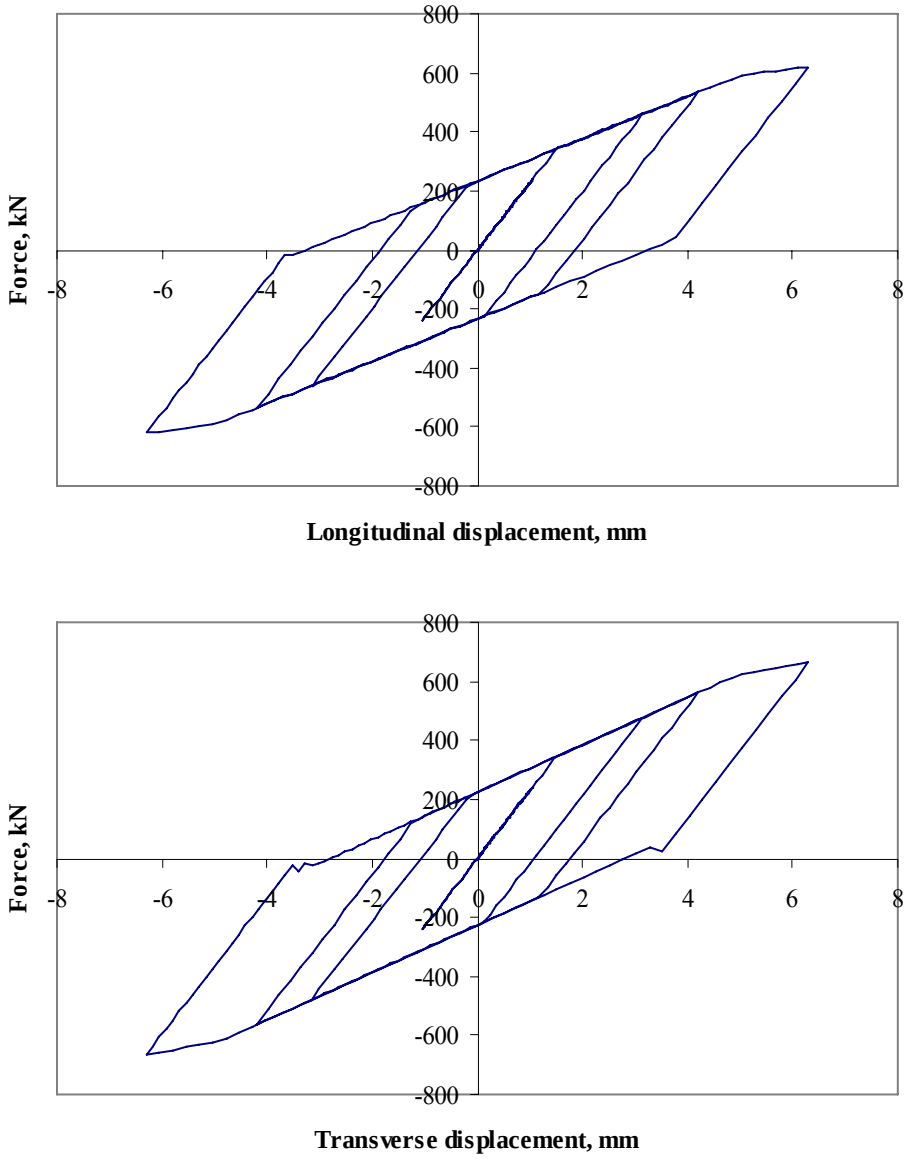

Figure 5.11 Hysteretic behavior of a pile group from Approach 1

Stiffness and strength of abutments consist of the contribution of piles and abutment. The contribution of piles supporting abutments is approximated from LPile analysis. The passive and active stiffness of abutments is approximated from the full-scale abutment test by Maroney (1995). Figure 5.12 shows the hysteretic behavior of the abutment used in the simplified model. In an active longitudinal direction, only the pile contributes to the stiffness of an abutment, while in passive longitudinal direction (compression on soil), passive soil pressure contributes to the resistance. In the transverse

direction, the stiffness of an abutment is assumed to be 50% of the stiffness of an adjacent bent, following Caltran's Design Criteria (2004). The stiffness and strength of pile in the transverse direction is from the LPile analysis. Details of the stiffness calculations are given in Appendix A.3.

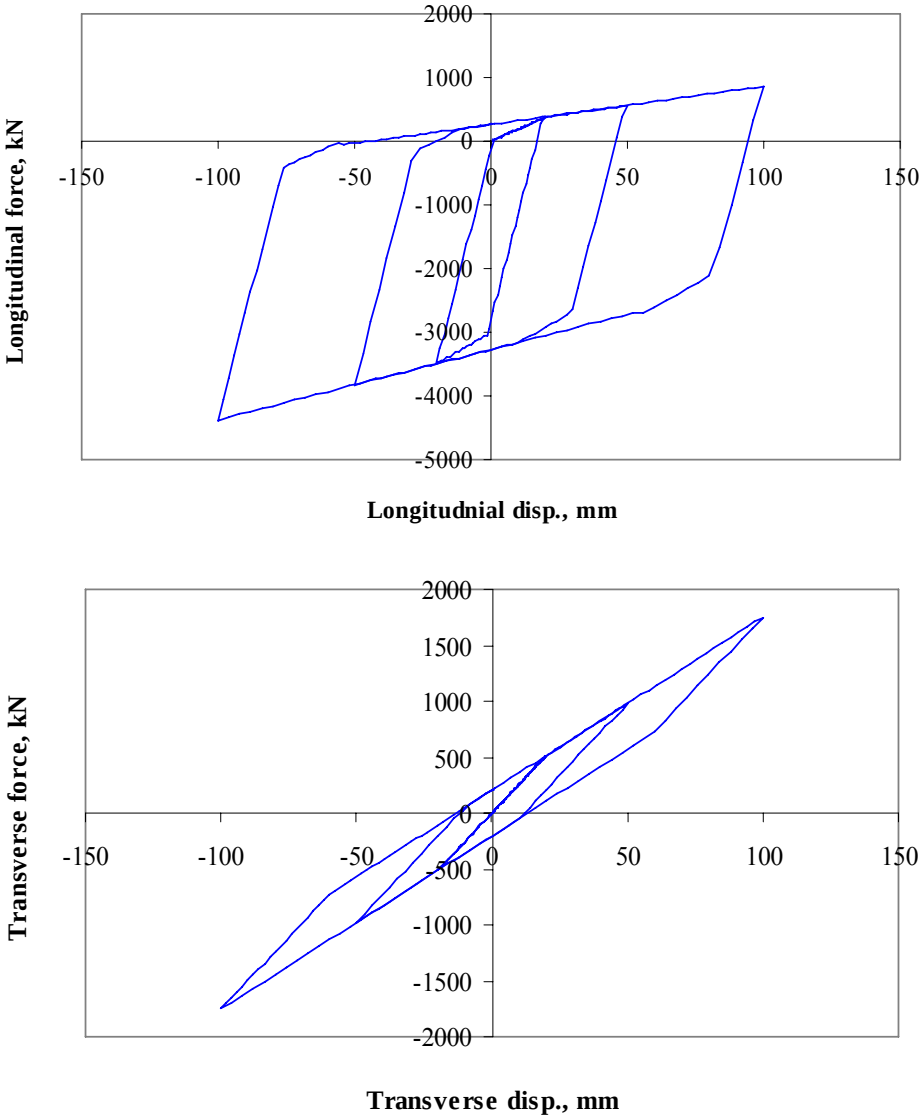

Figure 5.12 Hysteretic response of abutment from Approach 1

5.5.3.3 Approach 3 and 4: FE Foundation Model

In these approaches, soil-pile-foundation systems of the bridge are modeled in a three-dimensional FE analysis package, OpenSees, using realistic soil material models. The

mesh of the FE model is refined such that the computational cost is affordable with minimal loss of accuracy. A parametric study for bents 1 and 3 showed that the global load-deformation relationships of the soil-pile-foundation model with a fine mesh of 5,510 elements and with a coarse mesh of 1,400 elements are very similar. The reduction in analysis time per each time step is significantly reduced from 128.46 to 6.3 sec when it was run on a desktop with Pentium IV 2.6 GHz and 1GB of RAM. Similar mesh refinement studies are conducted for foundation of bent 2 and embankments. Figure 5.13 presents the final mesh with number of elements and nodes. Based on the boring log data shown in Figure 5.5, all soil materials are assumed to be pressure-independent. The stiffness and strengths of foundations identified from pushover analyses of these models are used in Approach 3. In Approach 4, these models are combined with structural model in ZEUS-NL using the multiplatform analysis framework UI-SimCor.

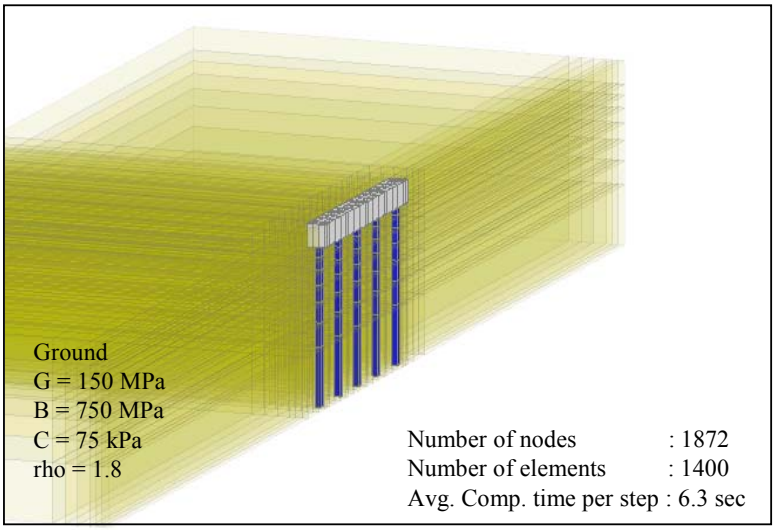

(a) FE model of Bent 1 and 3

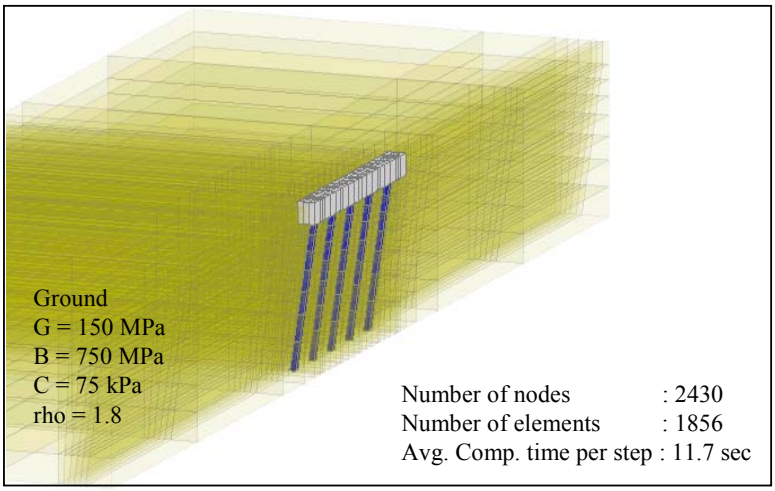

(b) FE model of Bent 2

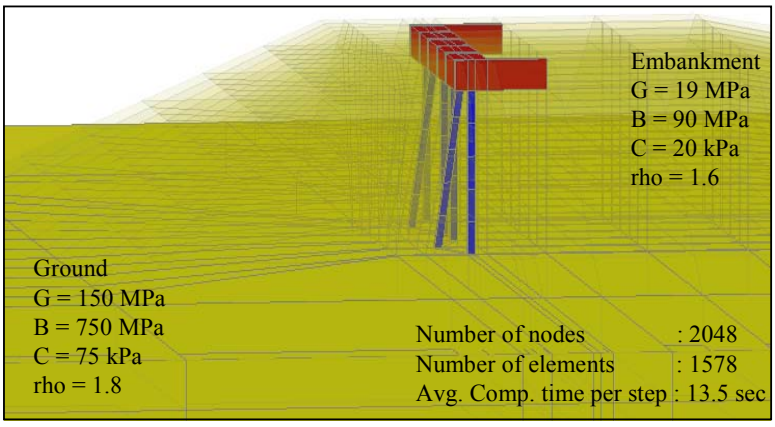

(c) FE model of Abutment and Embankment

Figure 5.13 FE soil-pile-foundation models

5.6 Sample Results from Multiplatform Simulation

A sample response of the reference bridge under the 1994 Northridge Earthquake (24278 Castaic - Old Ridge Route Station) is presented in this section. The bridge is analyzed using multiplatform simulation by combining abutment and embankment models in OpenSees, as shown in Figure 5.13, and a structural model in ZEUS-NL, as shown in Figure 5.7.

5.6.1 Dynamic Properties of the Reference Bridge

Fundamental periods of the bridge are estimated using initial stiffness of bridge components. The first transverse mode of vibration is 0.20 sec., and the first longitudinal mode of vibration is about 0.54 sec. The longitudinal period is longer than the transverse period due to gaps between superstructure and abutments, expansion bearings, and bents, which is more compliant in longitudinal direction than in transverse direction. It is expected that the fundamental periods will increase significantly as the stiffness of the bearings decrease after bearings start to develop friction and lose stiffness. After a super structure contacts an abutment in the longitudinal direction, however, it is expected that the fundamental period will decrease due to the high stiffness of abutments. These complexities justify the use of sophisticated nonlinear analysis over simplified methods. Figure 5.14 presents longitudinal input ground motion and transverse input ground motion alongside acceleration response spectrum and fundamental period of the reference bridge.

5.6.2 Bridge Response Under High Intensity Motion

The longitudinal response of the reference bridge subjected to ground motion in Figure 5.14 (a) is presented in Figure 5.15. The displacement history of deck and abutments, as shown in Figure 5.15 (a), shows that the abutment deforms only in a negative direction when relative displacement of deck and abutment is larger than the gap width, 38 mm. Small portion of negative plastic deformation of abutment is restored due to elastic rebound. The bearings on abutment do not deform more than a gap width in a negative

direction, although it can freely displace in a positive direction. Figure 5.15 (c) presents the hysteresis curve of embankment plotted with deck displacement. It is observed that at small displacement, expansion bearings transfer forces with a bilinear hysteresis curve, as modeled in Figure 5.8. As displacement increases in a negative direction and a superstructure hits the abutment, the reaction from abutment and embank increases. The response of the abutment and embankment system is in the nonlinear range. The response of expansion bearings on bent 1, Figure 5.15 (d), shows that the relative displacement of bearings is large enough to reach initial friction force. The fixed bearings deform very little due to high vertical force and corresponding large frictional force. The peak displacement of the deck in a longitudinal direction is about 100 mm. The peak displacements of bents are about 72 mm for bents 1 and 3, and 99 mm for bent 2. Note that the displacement of the bent 2 is similar to the deck displacement due to the fixed bearing on bent 2. The displacement of bents 1 and 3 are smaller than the deck displacement. The difference is not big, though, due to relatively large initial stiffness of expansion bearings in comparison with the flexibility of bents 1 and 3 in a longitudinal direction.

The response of the reference bridge in a transverse direction is presented in Figure 5.16. In a transverse direction, bearings transfer a large force, as shown in Figure 5.16 (d). Thus, the bridge deck and abutments behave in a similar manner, as shown in Figure 5.16 (a). The peak displacement of the deck is about 43 mm, which is much less than the displacement in the longitudinal response. Figure 5.16 (c) presents highly nonlinear responses of the embankment-abutment system. It is expected that a simplified model of this complex behavior introduces a large approximation. The transverse response of bearings on abutment, bents 1 and 2 are presented in Figure 5.16 (d), (e), and (f), respectively. It is observed that the bearings on abutment deform much larger than the bearings on bents 1 and 2. This large deformation is due to relatively low vertical force on the abutment (266 kN) in comparison with the vertical force on bents 1 (932 kN) and 2 (993 kN). The peak transverse displacement of bents 1 and 2 are 43 and 44 mm, respectively.

The analysis in the example shows that the most probable failure mode of the reference bridge is failure of the bearings on the abutment in a transverse direction.

Bearings on bents 1, 2, and 3 in a transverse direction are unlikely to be damaged. Bents in a transverse direction and abutments may lead to the failure of bridge. The probabilistic assessment of the vulnerability of the bridge is presented in the following sections.

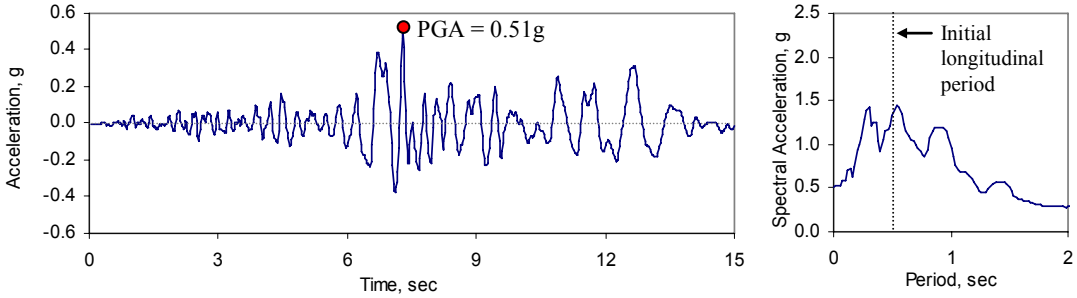

(a) Longitudinal input ground motion

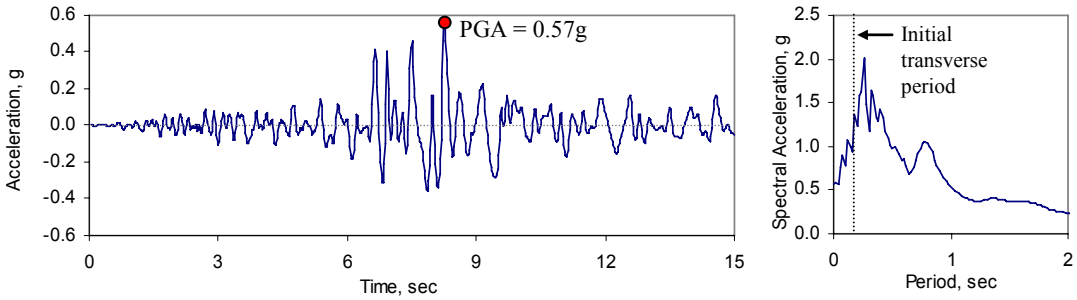

(b) Transverse input ground motion

Figure 5.14 Input ground motion for example analysis

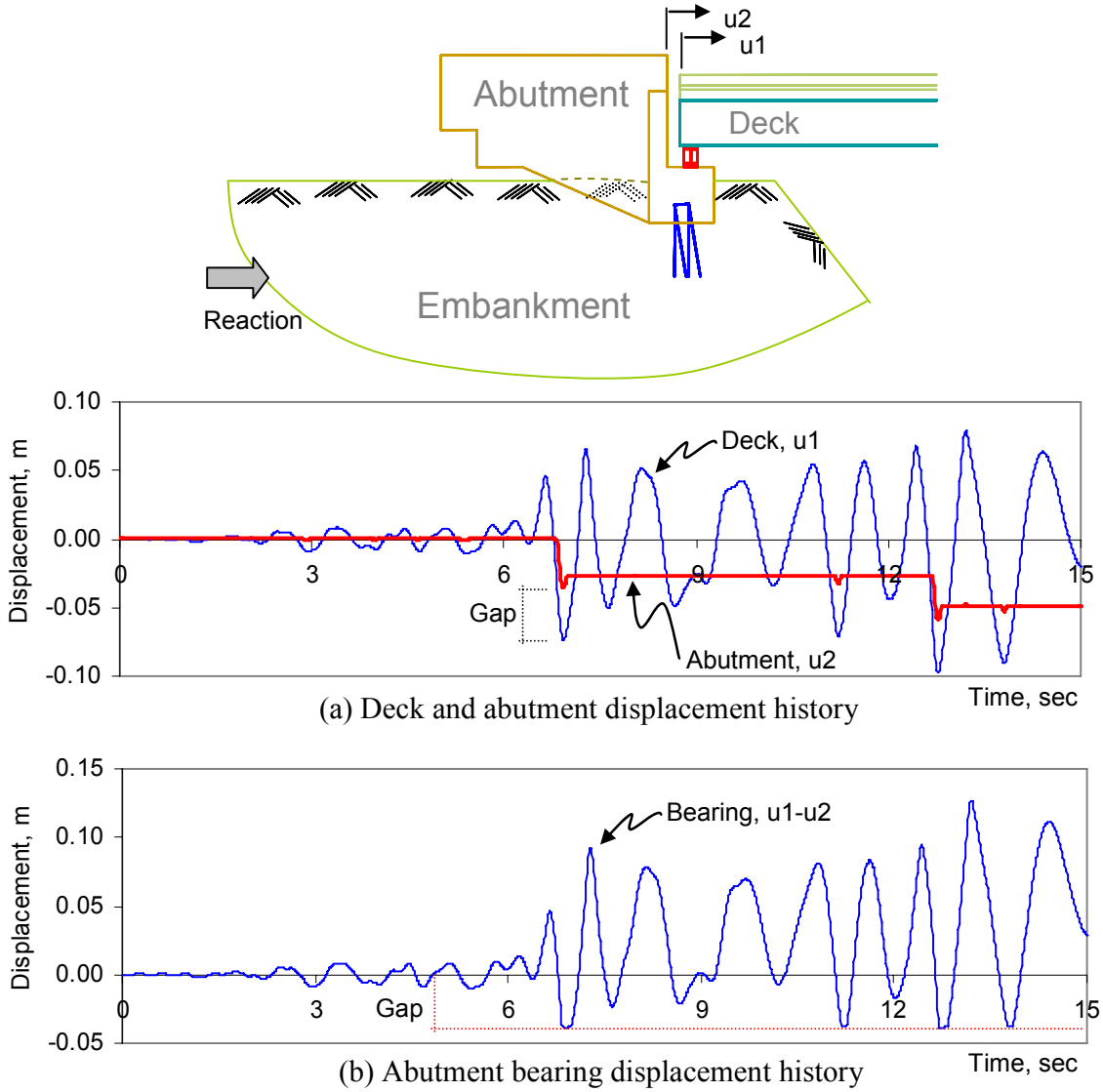

Figure 5.15 Longitudinal response of the reference bridge
(continued on next page)

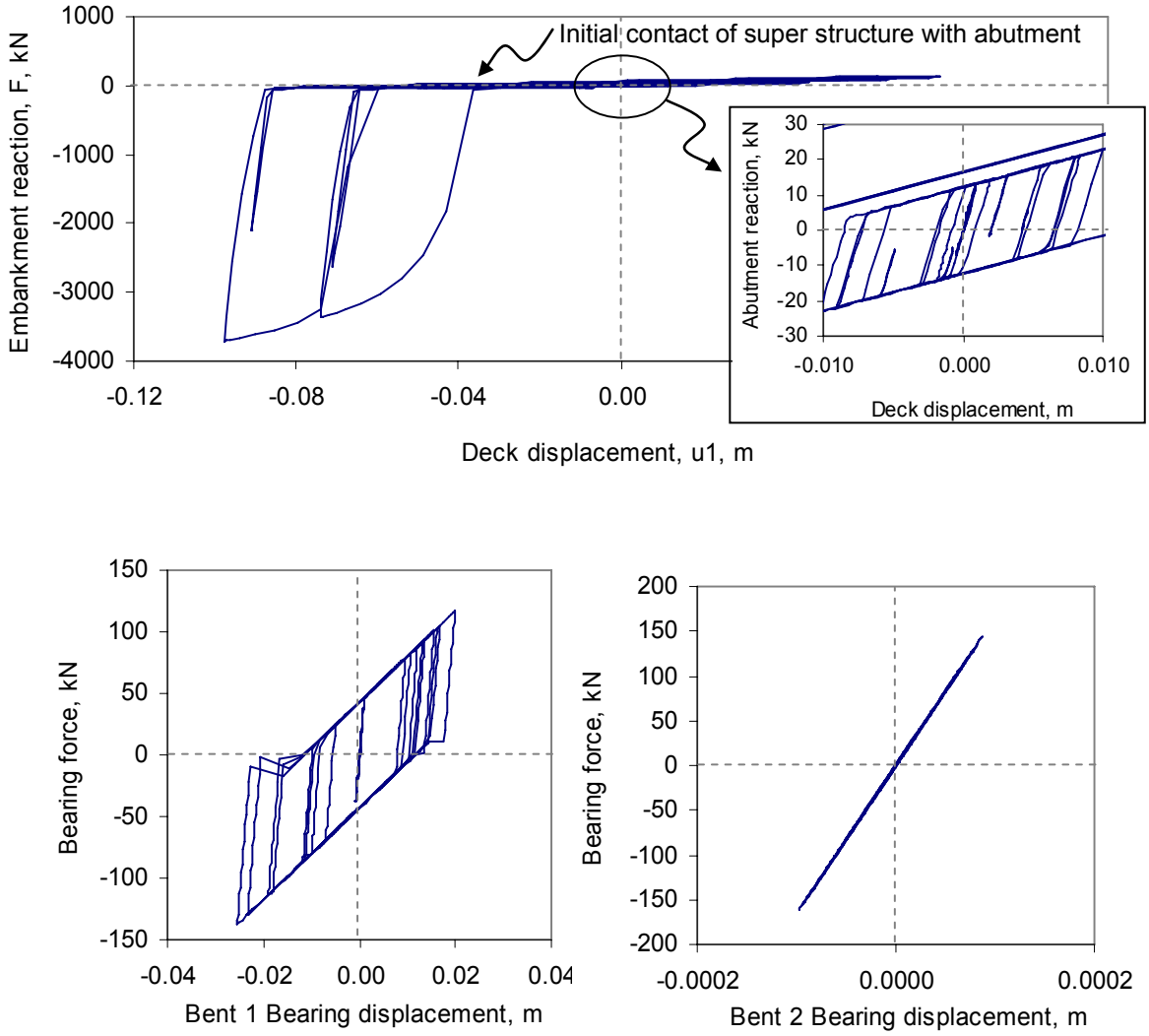

Figure 5.15 Longitudinal response of the reference bridge – *continued*

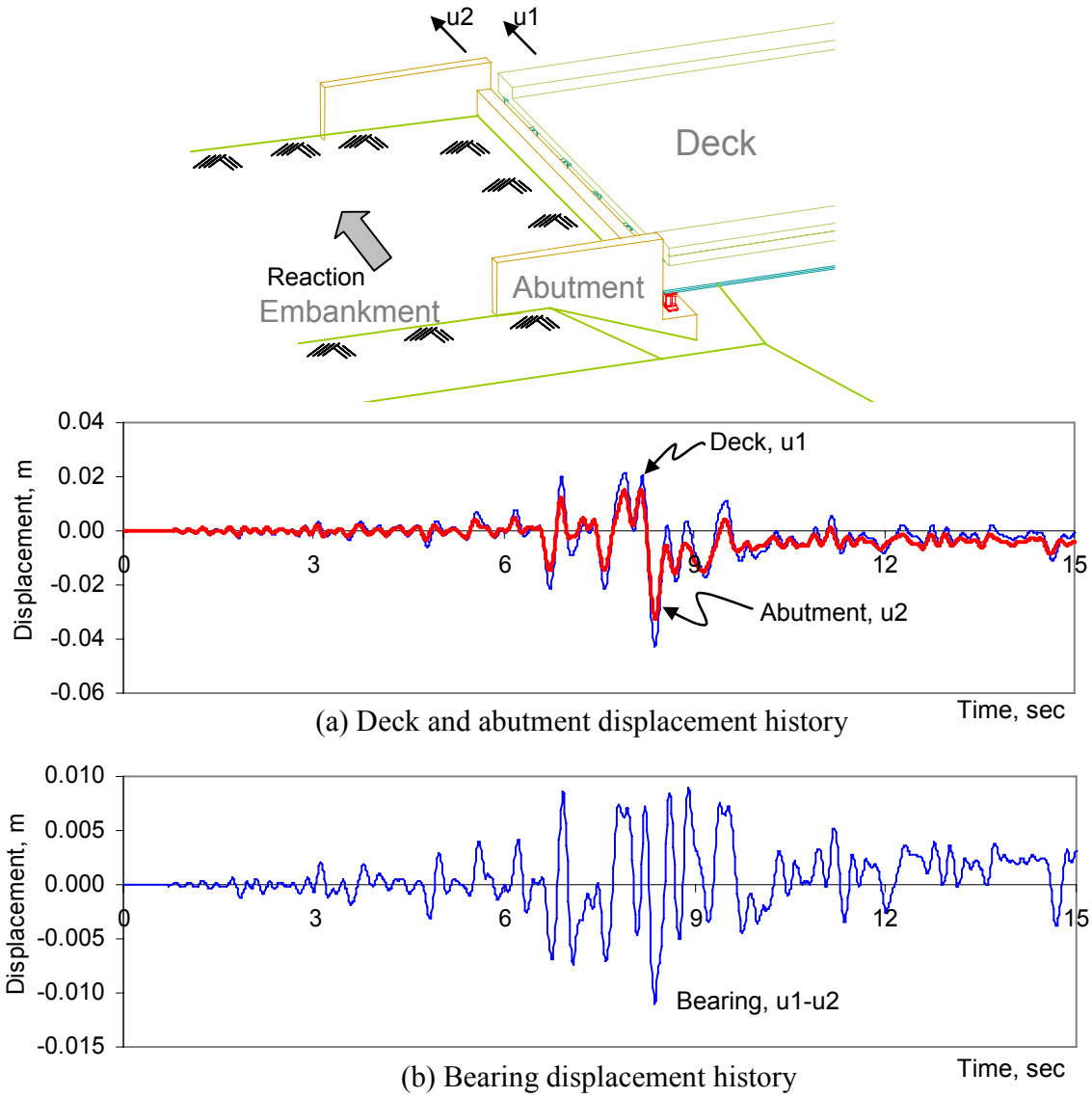

Figure 5.16 Transverse response of the reference bridge
(continued on next page)

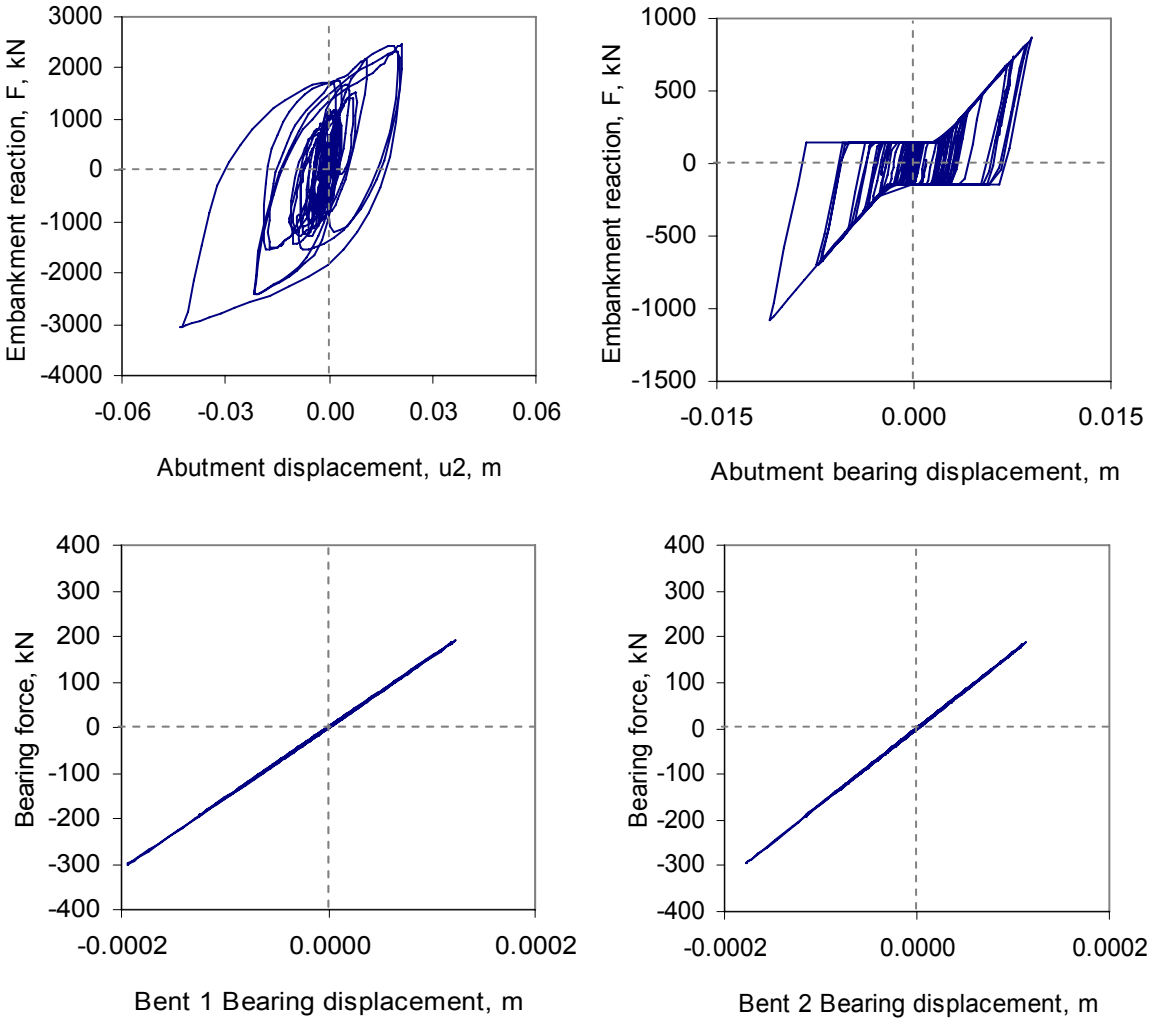

Figure 5.16 Transverse response of the reference bridge – *continued*

5.7 Random Variables in Seismic Supply and Demand

The uncertainties in structural and geotechnical models are considered based on the published literature. Following Section 2.4.4.1, the mean values and COVs of concrete ultimate stress are assumed to be 33.6 MPa and 18.6%, and those of steel yield stress are assumed to be 337 MPa and 10.7%.

Soil material properties involve more random parameters than concrete or steel. Jones et al. (2002) noted that the COV of unconfined compressive strength, S_u, of clay varies between 22 and 33%. In this study, it is assumed that the COV of S_u is 25%. In the same literature, the COV of shear wave velocity and soil density is reported as 17.8%

($\delta_{v_s} = 0.178$) and 9% ($\delta_\rho = 0.09$). The shear wave velocity (v_s), density of a soil medium (δ), and shear modulus (G) are related with the following equation:

$$G = v_s^2 \rho \tag{5.1}$$

Taking the logarithm of both sides yields

$$\log G = 2 \log v_s + \log \rho \tag{5.2}$$

Assuming that the shear modulus, shear wave velocity, and density follow log-normal distribution, the standard deviation of logarithm of each variable, ζ , is related with following equation:

$$\zeta_G{}^2 = 2^2 \zeta_{v_s}{}^2 + \zeta_\rho{}^2 \tag{5.3}$$

where $\zeta_\bullet$ is the standard deviation of log of $\bullet$. The standard deviation of a logarithm of a random variable, ζ , is related with COV, δ , in the following relationship:

$$\zeta^2 = \ln(1 + \delta^2) \tag{5.4}$$

From the equations (5.3) and (5.4), the COV of shear modulus is estimated as 0.38. Note that the randomness of geotechnical material is much larger than that of engineered material such as steel and concrete. It is anticipated that the share modulus of soil affects the stiffness of foundation most significantly. The same COV is also assumed to define the randomness of the stiffness of lumped soil springs in Approach 2 and 3.

The uncertainty in seismic hazard is accounted for by using 60 ground motions, as discussed in Section 5.3. Thirty of them are from recorded ground motions from sites with similar soil condition and epicentral distances with the site of the reference bridge. The remaining 30 records are artificially generated by Fernández and Rix (2006a). Table 5.4 summarizes the COV of random variables used in the geotechnical-structural model.

Table 5.4 Random variables in analytical models

Properties	COV	Reference
Concrete strength, MPa	0.186	Barlett and Macgregor (1996)
Steel yield strength, MPa	0.107	Mirza and MacGregor (1979)
Soil unconfined compressive strength	0.25	Jones et al. (2002)
Soil shear modulus	0.38	From COV of v_s (Romero and Rix, 2001) and rho (Jones et al., 2002)
Stiffness of lumped foundation springs	0.38	
Ground motion	Thirty recorded motions and thirty artificial motions	Fernández and Rix, 2006a

5.8 Capacity Limit States of Bridge Components

The failure of bearings, bents, and abutments are considered in this section. The capacities of these components are estimated from literature reviews, geometry of components, shear strengths, and pushover analyses. High COVs are assigned to the capacity limits that do not have clear failure criteria.

5.8.1 Capacities of Bearings

5.8.1.1 Transverse Direction Mean Capacity

The failure mechanisms of fixed and expansion bearings in transverse directions are expected to be similar to those of low-type bearings tested by Mander et al. (1996), as all of them are restrained by pintles and pintle holes. The test by Mander et al. showed that the low-type fixed bearing has constant friction up to a displacement of 3 to 4 mm, as shown in Figure 5.9. This slippage occurs at interfaces between bearing plates and between bearings and structural elements. After the displacement of 3 to 4 mm, it is anticipated that the pintles, pintle holes, or anchor bolts start to be damaged. Thereafter, the serviceability limit state for the transverse displacement is defined as 4 mm for

bearings in a transverse direction. After 4 mm of displacement, the bearings begin to develop a high resistance.

The damage control limit state is estimated from the shear strength of pintles. Each support consists of six bearings that have two pintles. Thus, a total of 12 pintles transfer lateral forces. Assuming that the pintle is made of A992 steel (F_y = 50 ksi), the lateral shear capacity of bearings are approximated as follows:

$$F_v = 0.6F_y A = 0.6(50)(14.8) = 144\,kip = 640\,kN \tag{5.5}$$

where A is the total sectional area subjected to shear force, 14.8 in^2. The shear strength of 640 kN corresponds to the base shear coefficient of 2.5. The numerical model in Figure 5.9 reaches the base shear at a displacement of 7 mm. Therefore, the damage control state of the fixed bearings in the transverse direction is defined from the abutment bearings as 7 mm.

Experiments by Mander et al. (1996) showed that pintles yielded and the bearing started to lose lateral resistance at a displacement of 20 mm. At this displacement, the base shear coefficient of 4 was achieved. In the transverse bearing model in Figure 5.9, the base shear coefficient of 4 is reached at a displacement of 11 mm in the model. Considering the experimental result that the bearing does not develop further resistance after the base shear coefficient of 4, the collapse prevention limit state for the transverse direction is defined as 11 mm.

5.8.1.2 Longitudinal Direction Mean Capacity

The three limit states in the longitudinal direction for fixed bearings are assumed to be same as those in the transverse direction. Therefore, 4, 7, and 11 mm of limit states are adopted. The expansion bearings are designed so that they do not damage in longitudinal direction unless bearings are unseated with excess displacement. Thus, it is assumed that the expansion bearings in the longitudinal direction do not contribute to the serviceability and damage control limit state of the bridge system. The collapse of an expansion bearing in the longitudinal direction will occur when the bearing overturns. As the expansion bearing used in the reference bridge rolls, it is assumed that the collapse prevention limit

state of expansion bearings in the longitudinal direction is the same as the seat width of the bearing plate, 230 mm.

5.8.1.3 Uncertainties in Capacity Limit States of Bearings

The mean capacities of bearings are not deterministic. Uncertainties arise from the fact that the mean capacities are determined from experiments whose specimens are not the same as the bearings used in the reference bridge. Even if identical specimens are used, repeated experiments will not provide identical results. Moreover, the numerical model of structural systems is not well-calibrated under high-intensity motion. And existence of vertical ground motion will significantly influence the capacities of bearings. These uncertainties must be accounted for in a systematic way.

It is certain that results from structural analyses under low-intensity ground motion are more confident than the results under high-intensity ground motion. Therefore, smaller COVs at a low-capacity limit state are adopted more readily than those at a high-capacity limit state. In this regard, Nielson (2005) assumed a COV of 0.25 for lower limit states and 0.5 for upper limit states. In this study, COVs of 0.25, 0.50, and 0.75 are adopted for serviceability limit states, damage control limit states, and collapse prevention limit states, respectively. The selection of these COVs is purely based on engineering judgment. More thorough definition of limit states and probabilistic assessment of these limit states remain for future study.

5.8.2 Capacity Limit States of Bents

The limit states of bents are determined from pushover analysis of a bent in longitudinal and transverse directions. From static analysis, it is observed that each bent supports approximately 950 kN of dead load. Pushover analyses under an axial load of 950 kN were conducted to estimate limit states of the bents. Displacement is applied at the top of bents. Three limit states in both directions are defined as drift at the first yield of steel in tension, achievement of global maximum strength, and achievement of core concrete strain of 0.01, for serviceability, damage control, and collapse prevention limit states,

respectively. The core concrete strain of 0.01 corresponded to 25% loss of core concrete stress, which resulted in a significant reduction in member strength. Based on these criteria, the limit state in the transverse direction is defined as 36 mm (0.6%), 92 mm (1.5%), and 260 mm (4.2%) for the three limit states. In the longitudinal direction, the limit states are defined as 72 mm (1.2%), 124 mm (2.0%), and 500 mm (8.0%). Note that the bent has much larger displacement capacity in the longitudinal direction as it behaves as a cantilever. The bent in the transverse direction has smaller displacement capacity as cross beams restrain the rotation of top of each pier. The bent is rather slender and long elements that are governed by flexural failure. The estimation of yielding of reinforcements and peak strength can be confidently conducted with fiber-based frame analysis software. Therefore, the COV of bents for serviceability and damage control limit states is assumed to be 0.1. On the contrary, the COV of collapse prevention limit states is assumed as 0.5, as the collapse of a structure cannot be predicted with confidence.

5.8.3 Capacities of Abutments

Abutments can be divided into two general classifications for seismic analysis: monolithic and seat-type abutments. In monolithic abutments, the superstructure of a bridge is monolithically connected to abutments. Thus, when it is necessary to transfer large forces to an embankment, the monolithic abutment is the best choice. During seismic action, the bridge and abutments behave together, mobilizing soil in the embankments. In seat-type abutments, the forces from the super structure are transferred through bearings. Longitudinally there is a gap between the super structure and the abutments.

The abutments of the reference bridge are seat-type abutments. Abutments can fail due to large deformation in transverse direction or in longitudinal direction. In seat-type abutments, the pounding of a superstructure on the back wall of the abutment can break the joint between the abutment and the back wall, imposing extensive, passive pressure on the backfill of the abutments. In the Caltrans procedure, two values of the acceptable abutment deformations are considered: 25 mm (1 inch) and 61 mm (2.4

inches). The first represents the deformation at which the soil pressure reaches its peak value of 369 kPa (7.7 ksf), and the latter represents the limiting value corresponding to the incipient damage to the abutments (Caltrans, 1988 and 1989). The displacement capacities of abutments are assumed as 25 and 61 mm for serviceability limit state and damage control limit state, respectively.

Padgett and DesRoches (2005) conducted a survey in which practitioners in department of transportations participated. The survey results indicated that it is unlikely to achieve complete failure of abutments from earthquakes. In most seat-type abutments, however, the abutment back wall is designed to resist the soil pressure of filled soil. When a large impact from the super structure of a bridge is imposed to the back wall, the back wall may fail, which can impose severe disruption on traffic. The displacement limit of abutment failure in the longitudinal direction is assumed as the displacement when the shear strength of abutment back wall is reached. The shear strength of the abutment back wall is approximated as below:

$$V_c = \sqrt{f_c^{'}} / 6 \cdot b \cdot d = \sqrt{33.6} / 6 \cdot (12.9) \cdot (0.42) = 5.2MN \qquad (5.5)$$

where b is the assumed length of shear failure and d is the effective thickness of the back wall, as shown in Figure 5.17. From the FE analysis of the embankment, abutment, and supporting pile system, the shear strength of 5.2 MN is reached at the abutment displacement of 0.075 m. Hence, the collapse prevention state of abutment in the longitudinal direction is assumed as 75 mm. The transverse movement of abutments also disrupts traffic due to the relative displacement between the bridge and abutment as well as settlement of backfill soil. Without further information about failure criteria in the transverse direction, the limit state for longitudinal direction is adopted as the limit state for the transverse direction. The COVs of abutment capacity is assumed to be 0.5 for all three limit states, as these are not based on experiments of similar abutment configurations. Table 5.5 summarizes the mean capacity limit of bridge components and their COVs.

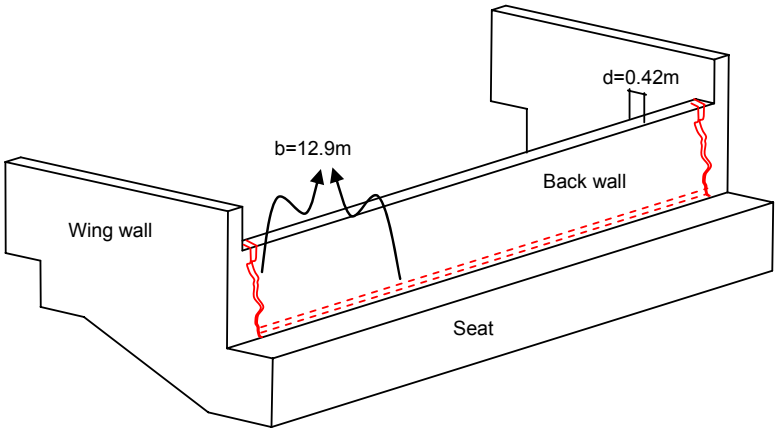

Figure 5.17 Assumed shear failure mode of abutment backwall

Table 5.5 Capacity limit states

Properties		Serviceability		Damage Control		Collapse Prevention		Reference
		Mean	COV	Mean	COV	Mean	COV	
Transverse Direction	Fixed bearing, mm	4	0.25	7	0.5	11	0.75	Mander et al. (1996)
	Expansion bearing, mm	4	0.25	7	0.5	11	0.75	Mander et al. (1996)
	Bent deformation, mm	36	0.1	92	0.1	260	0.5	Pushover analysis of bent
	Abutment movement, mm	25	0.5	61	0.5	75	0.5	Caltran (1988, 1989)
Longitudinal Direction	Fixed bearing, mm	4	0.25	7	0.5	11	0.75	Mander et al. (1996), Geometry of bearing
	Expansion bearing, mm	N/A	N/A	N/A	N/A	230	0.50	Geometry of bearing
	Bent deformation, mm	72	0.1	124	0.1	500	0.5	Pushover analysis of bent
	Abutment movement, mm	25	0.5	61	0.5	75	0.5	Caltran (1988, 1989) & shear strength of backwall

5.9 Vulnerability Simulation

The vulnerability curves of the reference bridge are derived using the SAC-FEMA Method introduced in Section 2.2. The seismic demand of bridge components and their correlation coefficients are estimated from nonlinear response history analyses of the reference bridge. As the closed-form estimation of system vulnerability with various failure modes is not readily achievable, MCS are applied based on the distribution of seismic demands of bridge components and their correlation coefficients. This two-step approach, estimating component demands and aggregating the demands through MCS, may not be applicable to highly nonlinear system. Therefore, in Section 5.9.1, the two-step approach is compared with full MCS for which no probabilistic distributions are assumed and system failure probability is directly estimated from nonlinear response history analysis. Bridges with conventional foundation springs are used in this verification.

Fragility curves of the reference bridge are presented in Section 5.9.2. Seismic demands of bridge components from various approaches in Table 5.3 are compared. Finally, the system vulnerability curves from different approaches are presented in Section 5.9.3

5.9.1 Numerical Verification of SAC-FEMA Method

The SAC-FEMA method introduced in Chapter 2 is adopted to derive vulnerability curves of a bridge system. The method considers only single-failure mode. As a bridge structure may fail with several failure modes, the failure probability of a system should be estimated from the seismic demands and capacities of various components. Nielson (2005) estimated seismic demand of each component using the SAC-FEMA method and its correlation coefficient. Then, much larger sets of seismic demands are randomly generated based on the probabilistic distributions of seismic demands of bridge components. Failure probability of a system is numerically estimated from these randomly generated seismic demands. This approach requires nonlinear response history analysis at the stage of estimating seismic demands on bridge components. Thereafter, the results are extrapolated to estimate system failure probability.

It is worthwhile to verify the accuracy of this approach with full MCS because the responses of bridge components in transverse and longitudinal directions are highly independent, and defining probabilistic distribution and the correlation coefficient of highly nonlinear and independent components seems not suitable. Therefore, the system vulnerability curves from the SAC-FEMA method are compared with those from the full MCS.

The full MCS requires many analysis results at each prescribed PGA level, while the SAC-FEMA approach allows the use of ground motion intensities scaled at arbitrary PGA levels. To conduct a fair comparison, 60 ground motions are scaled at PGAs from 0.1 to 1g with 0.1g intervals. This scaling of ground motion is not appropriate, as the frequency content of ground motions of large earthquake is different of those from small earthquakes. However, the investigation of this section (Section 5.9.1) is solely for the comparison of the two different simulation approaches. Accordingly, the vulnerability curves derived from this section do not represent the vulnerability curve of the reference bridge. Vulnerability curves of the reference bridge are presented in Section 5.9.2.

5.9.1.1 The SAC-FEMA Method

The seismic demand of each component is estimated from 600 simulations comprised of 60 ground motions at 10 PGA scales. Figure 5.18 presents an example of seismic demand on abutment bearings where raw data from nonlinear response history analysis, median demand curve, and ±1 standard deviation of median demand curve are compared. The median curve is obtained by fitting Equation (2.4) to the raw data from nonlinear response history analysis. The estimated component demands and their correlations are utilized to generate a large number of seismic demand values of all components. Five thousand samples are generated, which is sufficiently large to minimize the error from sample size. These generated seismic demands, which are not from nonlinear response history analysis, are utilized to estimate system vulnerability. The same number of structural capacities is generated based on Table 5.5. System failure is judged by comparing the seismic demand and the structural capacity. Table 5.6 presents how the system vulnerability is estimated from seismic demands of all components. Note that in

the shaded cells, the seismic demands of components are randomly generated based on component seismic demands and their correlation coefficients.

5.9.1.2 Full MCS

The full MCS is basically the same as the previous procedure except that the seismic demands of components are directly obtained from nonlinear response history analysis. Consequently, the number of samples to estimate system failure probability is limited to the number of nonlinear response history analysis. To account for the uncertainties in the component capacity, 60 samples of capacities are generated following the mean and COV of component capacity in Table 5.5. Sixty sets of capacity and demand are compared to define whether the system has failed or not. System failure probability in the full MCS is also determined following the procedure in Table 5.6, in which the seismic demands in the shaded cells are from nonlinear response history analysis.

5.9.1.3 Comparison of Vulnerability Curves from SAC-FEMA Approach and Full MCS

Figure 5.19 compares the system vulnerability curves from two approaches. Note that the two methods give practically identical vulnerability curves. The MCS shows more fluctuation than the SAC-FEMA approach, as the failure probability is estimated from 60 samples, while the SAC-FEMA method used 5,000 samples to estimate the probability of system failure. This comparison verifies that the SAC-FEMA approach can be applied to a system with multiple failure modes.

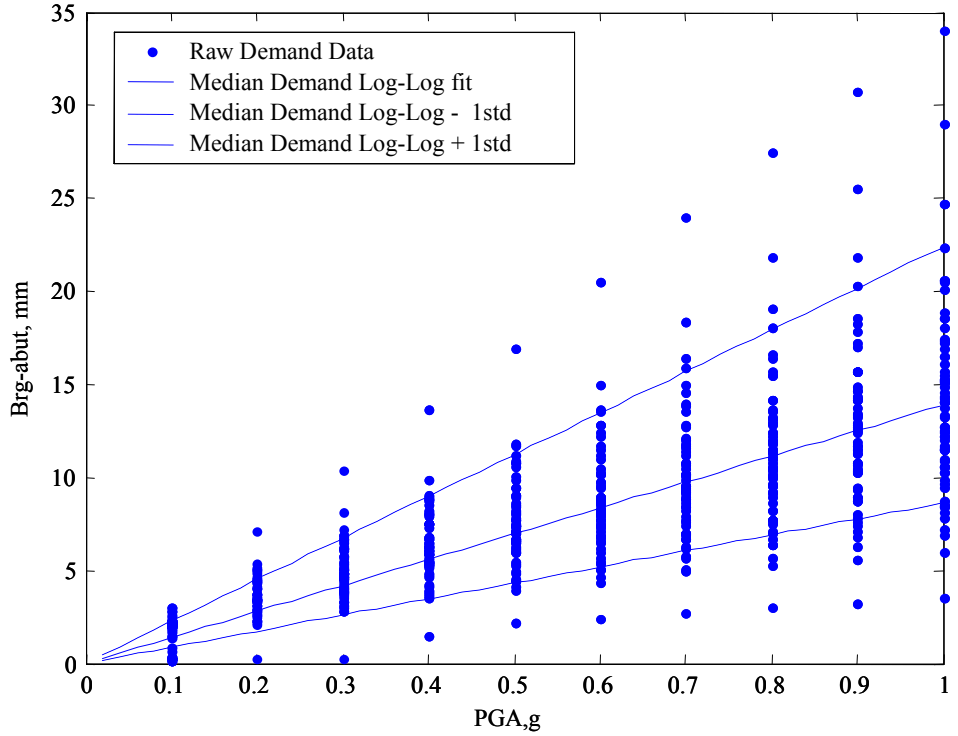

Figure 5.18 Seismic demand on abutment bearings in transverse direction

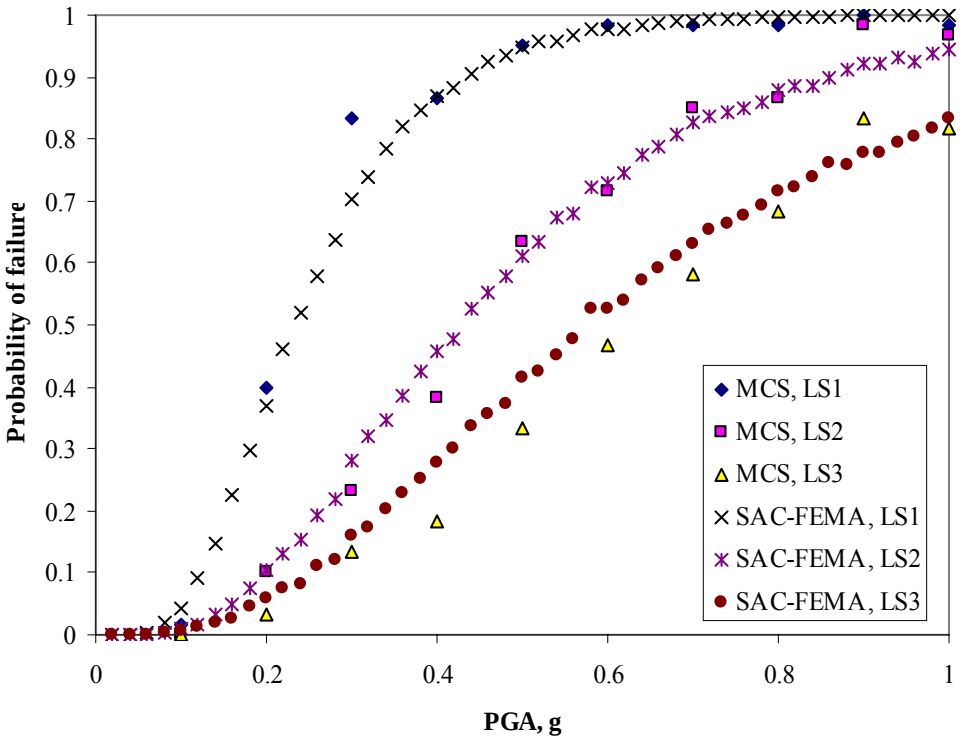

Figure 5.19 SAC-FEMA approach and vulnerability curves from full MCS

Table 5.6 Estimation of failure probability of a bridge system

PGA = 0.5 g

Sample			1	2	3	…	60
Longitudinal demand	Bent, mm	D	80.128	70.301	129.875	…	71.907
		C1	70.196	82.370	75.368	…	80.110
		C2	113.730	120.400	128.488	…	126.296
		C3	282.390	494.435	304.488	…	258.694
	Abutment, mm	D	40.138	30.319	90.934	…	32.039
		C1	21.903	36.078	14.695	…	31.323
		C2	36.208	131.630	60.539	…	63.305
		C3	59.737	78.277	111.650	…	81.042
	Fixed Bearings, mm	D	0.088	0.088	0.099	…	0.074
		C1	4.242	3.584	2.430	…	4.350
		C2	13.577	11.437	10.675	…	14.425
		C3	10.387	24.180	15.429	…	9.250
	Expansion Bearings, mm	D	84.056	68.935	149.081	…	70.675
		C1	N/A	N/A	N/A	…	N/A
		C2	N/A	N/A	N/A	…	N/A
		C3	495.177	231.446	381.158	…	229.497
Transverse demand	Bent, mm	D	40.237	32.616	80.678	…	44.766
		C1	35.098	41.185	37.684	…	40.055
		C2	84.380	89.329	95.330	…	93.703
		C3	146.843	257.106	158.334	…	134.521
	Abutment, mm	D	30.048	22.859	71.686	…	35.188
		C1	21.903	36.078	14.695	…	31.323
		C2	36.208	131.630	60.539	…	63.305
		C3	59.737	78.277	111.650	…	81.042
	Fixed Bearings, mm	D	0.175	0.156	0.239	…	0.170
		C1	4.242	3.584	2.430	…	4.350
		C2	13.577	11.437	10.675	…	14.425
		C3	10.387	24.180	15.429	…	9.250
	Expansion Bearings, mm	D	9.026	8.210	8.144	…	8.474
		C1	1.848	3.237	2.303	…	3.004
		C2	12.249	14.643	19.750	…	9.131
		C3	30.141	14.088	23.201	…	13.969

Serviceability State, $P_f = sum(D_{,any} > C1_{,any}) / 60$	if $D_{,any} > C1_{,any}$	1	1	1	…	1
Damage Control, $P_f = sum(D_{,any} > C2_{,any}) / 60$	if $D_{,any} > C2_{,any}$	1	0	1	…	0
Collapse Prevention, $P_f = sum(D_{,any} > C3_{,any}) / 60$	if $D_{,any} > C3_{,any}$	0	0	0	…	0

Note D: Seismic demand on component
C1: Serviceability limit state
C2: Damage control limit state
C3: Collapse prevention limit state

5.9.2 Seismic Demand of Bridge Components

The intensity measure and seismic demand of structural components are related by the following equation:

$$\hat{D} = aIM^{b} \tag{5.6}$$

where *IM* is the intensity measure and *a* and *b* are regression parameters. $\hat{D}$ indicates a median seismic demand. Equation (5.6) is an identical form with Equation (2.5), except that *PGA* is used as an intensity measure. As the relationship between seismic intensity and seismic demand is not deterministic, a term that accounts for uncertainty is introduced in Equation (5.7).

$$D = \left(aIM^{b}\right)\varepsilon \tag{5.7}$$

where ε is a random variable with a mean of 1. Assuming that ε follows lognormal distribution, logs of both sides yield the following:

$$\ln D = \ln\left(a\right) + b\ln\left(IM\right) + \ln\left(\varepsilon\right) \tag{5.8}$$

From nonlinear history analyses of bridge systems, the seismic demands, D, can be obtained for a given ground motion with intensity of IM. By running regression analysis, the parameters a and b can be determined such that mean of the residual, $\ln(\varepsilon)$, is close to zero. The standard deviation of $\ln(\varepsilon)$ is a dispersion of seismic demand of component, β_D. The estimated demand parameters of bridge components for different SSI approaches are summarized in Table 5.7 and qualitative summary of seismic demands are provided in Table 5.8. Figure 5.20 presents median demand curves. The following can be observed from the seismic demands on bridge components using different SSI approaches.

- Transverse bridge response, Figure 5.20 (a), (c), (e), (g), and (i)
    - The differences between various SSI approaches are much larger in the transverse than in the longitudinal direction. In the transverse direction, the bearings on abutments transfer forces even at low-intensity levels. Thus, the characteristics of embankment models affect the bridge response directly.

- When it is assumed that embankments and abutments are fixed, the seismic demand on abutment bearings is higher than those from other approaches. The seismic demand on other bearings and bents is lower than those from different approaches. The fixed abutment assumption tends to limit structural response but increases the demand on the connecting elements of structure and fixed boundary.
- The seismic demands from multiplatform simulation and from FE-lumped spring are different, but the differences are not significant. The conventional approach, for which foundation properties are estimated from LPile analysis and abutment properties are based on Caltran (2004), shows significantly different seismic demand.

- Longitudinal bridge response, Figure 5.20 (b), (d), (f), (h), and (j)
  - The conventional-spring approach, FE-lumped spring approach, and multiplatform simulation resulted in similar seismic demand for all bearings and bents at low PGA levels. The similarity is attributed to the existence of gaps and expansion bearings on abutments which minimizes the interaction between embankments and bridge. If the bridge is constructed with monolithic abutments, the different SSI approaches may result in different longitudinal seismic responses.
  - The fixed-base approach shows distinctly different demand for all structural components, as shown in Figure 5.20 (b), (d), (f), and (h). Assuming fixed boundary in longitudinal direction underestimates demand on components.
  - The seismic demand on abutments is very similar for the FE soil spring approach and multiplatform simulation, while differences are observed in comparison to the conventional spring model, as shown in Figure 5.20 (j). The difference results from the use of different properties of soil springs rather than from modeling assumptions.
  - For structural components, the rate of demand increase tends to decline with increasing PGA, as demonstrated in Figure 5.20 (b), (d), (f), and (h). On the contrary, the rate of demand increase on abutments tends to

increase, as shown in Figure 5.20 (j). At low-seismic intensity, the demand on structural components is nearly proportional to the input motion intensity. At a certain PGA level, the superstructure starts to impact the abutments, which limits structural response and activates abutment response.

- The seismic demand on bearings of bent 2 is very low, as shown in Figure 5.20 (f). Due to high axial force, the bearings exhibit high frictional resistance. Low seismic demand on fixed bearings is also observed in the sample analysis in Figure 5.15.

The seismic demand of bridge components in Table 5.7 can be combined with the component capacity in Table 5.5 to estimate component vulnerability using Equation (2.11). Even though the component vulnerability can be estimated in closed form, the closed-form assessment of system failure probability is not straightforward. Thus, large numbers of seismic demand values are generated following the demand distribution in Table 5.7. The correlation coefficient of component demand, Table 5.9, shows that all components in the same direction are highly correlated, with correlation coefficients in the range of 0.85 to 1.0. The correlation between component responses in the transverse and longitudinal directions is lower than those in the same direction. This difference mainly results from the use of different ground motion in the two directions.

Table 5.7 Seismic demands on bridge components

Approach	Parameter	Abutment		Brg. Abut		Brg. Bent 1, 3		Brg. Bent 2		Bent	
		Trans	Long	Trans	Long	Trans	Long	Trans	Long	Trans	Long
Fixed	a	N/A	N/A	28.533	63.171	0.160	17.485	0.154	0.073	34.203	59.746
	b	N/A	N/A	1.318	0.479	0.915	0.730	0.866	0.327	1.226	0.461
	β_D	N/A	N/A	0.280	0.487	0.202	0.717	0.196	0.324	0.247	0.488
Conv.	a	66.212	46.965	14.973	99.494	0.290	24.837	0.267	0.089	83.121	101.115
	b	0.990	1.337	1.014	0.681	0.656	0.858	0.656	0.395	0.993	0.676
	β_D	0.412	0.817	0.502	0.516	0.260	0.758	0.261	0.354	0.382	0.519
FE	a	35.454	66.326	20.713	110.20	0.242	28.637	0.239	0.099	66.081	96.845
	b	1.078	2.375	0.755	0.717	0.700	0.936	0.710	0.452	1.058	0.664
	β_D	0.557	1.806	0.198	0.554	0.231	0.767	0.213	0.358	0.343	0.539
Multiplat form	a	44.349	70.416	18.741	124.70	0.224	26.926	0.207	0.093	62.981	95.654
	b	1.352	2.398	0.957	0.767	0.780	0.914	0.776	0.427	1.238	0.662
	β_D	0.511	1.818	0.289	0.607	0.270	0.779	0.268	0.359	0.434	0.556

Table 5.8 Qualitative comparison of seismic demand on bridge components

Component		Fixed	Conventional	FE	Multiplatform
Transverse direction	Abutment	N/A	Higher than FE	Similar	
	Bearings on abutment	Highest at large PGA level	Low	High	Lowest
	Bearings on bent 1 and 3	Lowest	Highest	Similar	
	Bearings on bent 2	Lowest	Highest	High	Low
	Bent	Lowest	Highest	Similar	
Longitudinal direction	Abutment	N/A	Higher than FE up to .7 g	Very similar	
	Bearings on abutment	Lowest	Similar. Distinctively larger than Fixed approach		
	Bearings on bent 1 and 3	Lowest	Similar. Distinctively larger than Fixed approach		
	Bearings on bent 2	Lowest	Similar. Distinctively larger than Fixed approach		
	Bent	Lowest	Similar. Distinctively larger than Fixed approach		

Note: Relative seismic demand is qualitatively described as lowest, low, high, and highest.

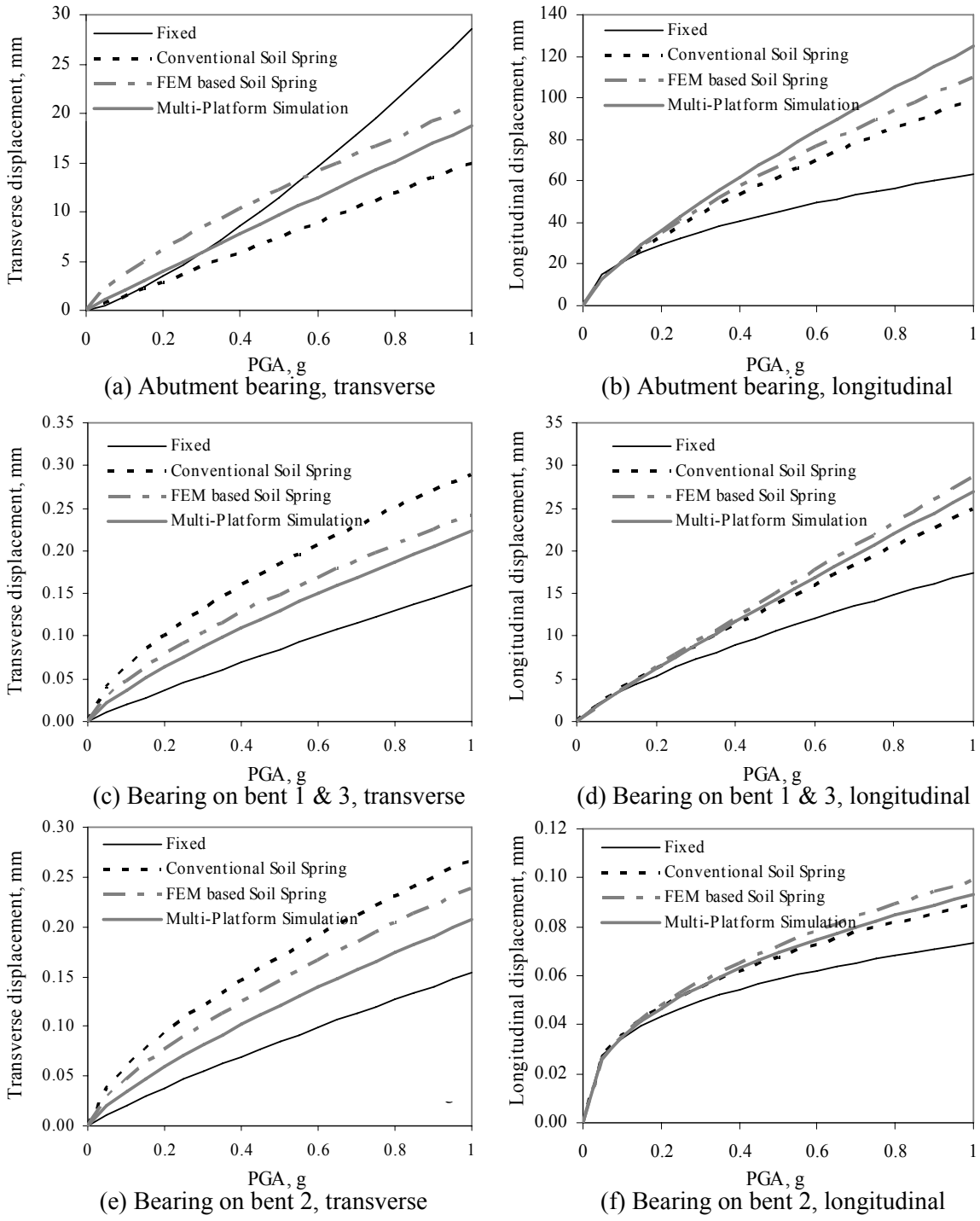

(a) Abutment bearing, transverse

(b) Abutment bearing, longitudinal

(c) Bearing on bent 1 & 3, transverse

(d) Bearing on bent 1 & 3, longitudinal

(e) Bearing on bent 2, transverse

(f) Bearing on bent 2, longitudinal

Figure 5.20 Median seismic demand on bridge components
(continued on next page)

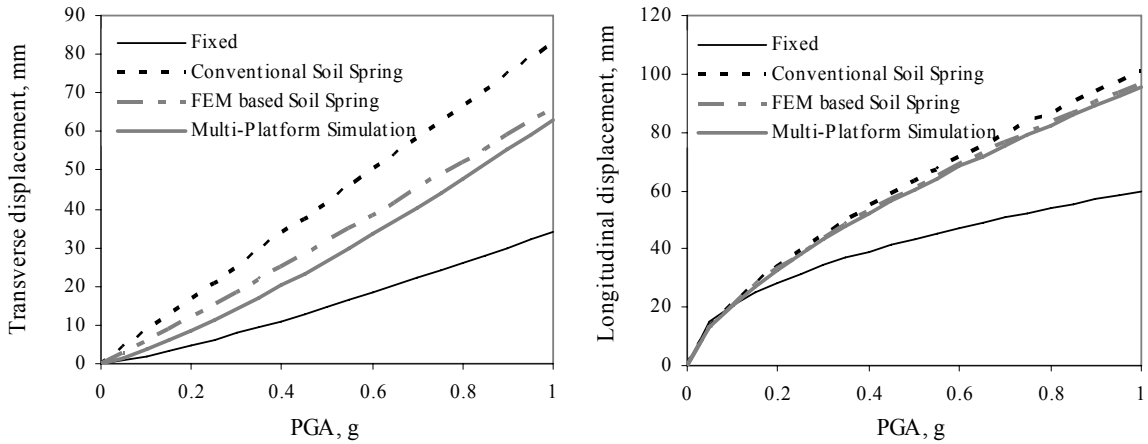

(g) Bents, transverse (h) Bents, longitudinal

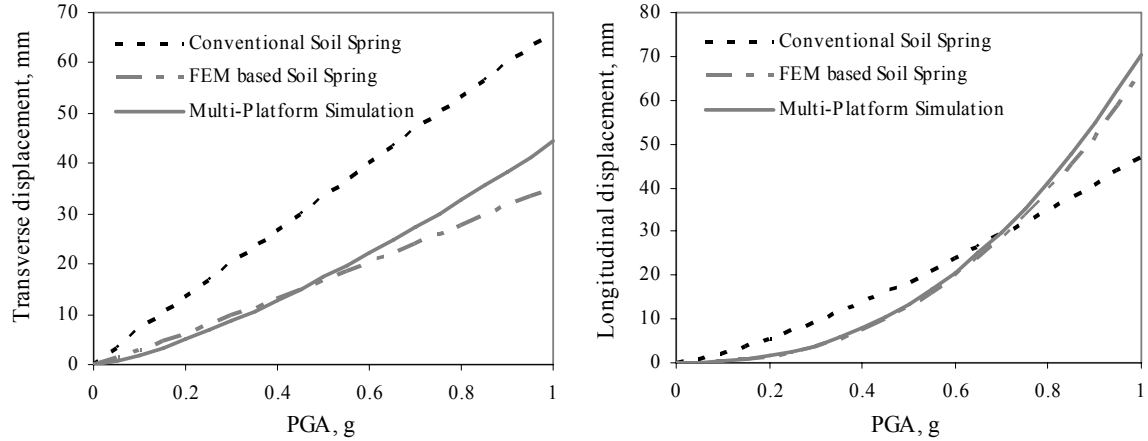

(i) Abutments, transverse (j) Abutments, longitudinal

Figure 5.20 Median seismic demand on bridge components – *continued*

Table 5.9 Correlation coefficients of seismic demands of bridge components

(a) Fixed foundation model

Fixed		Transverse					Longitudinal				
		Comp. 01	Comp. 02	Comp. 03	Comp. 04	Comp. 05	Comp. 01	Comp. 02	Comp. 03	Comp. 04	Comp. 05
Transverse	Comp. 01	N/A	N/A	N/A	N/A	N/A	N/A	N/A	N/A	N/A	N/A
	Comp. 02	N/A	1.000	0.992	0.983	0.989	N/A	0.540	0.542	0.550	0.528
	Comp. 03	N/A	0.992	1.000	0.995	0.993	N/A	0.509	0.514	0.523	0.495
	Comp. 04	N/A	0.983	0.995	1.000	0.996	N/A	0.502	0.509	0.520	0.488
	Comp. 05	N/A	0.989	0.993	0.996	1.000	N/A	0.537	0.541	0.551	0.524
Longitudinal	Comp. 01	N/A	N/A	N/A	N/A	N/A	N/A	N/A	N/A	N/A	N/A
	Comp. 02	N/A	0.540	0.509	0.502	0.537	N/A	1.000	0.992	0.993	1.000
	Comp. 03	N/A	0.542	0.514	0.509	0.541	N/A	0.992	1.000	0.994	0.990
	Comp. 04	N/A	0.550	0.523	0.520	0.551	N/A	0.993	0.994	1.000	0.991
	Comp. 05	N/A	0.528	0.495	0.488	0.524	N/A	1.000	0.990	0.991	1.000

(b) Conventional foundation model

Conventional		Transverse					Longitudinal				
		Comp. 01	Comp. 02	Comp. 03	Comp. 04	Comp. 05	Comp. 01	Comp. 02	Comp. 03	Comp. 04	Comp. 05
Transverse	Comp. 01	1.000	0.858	0.987	0.984	0.995	0.775	0.758	0.680	0.694	0.750
	Comp. 02	0.858	1.000	0.893	0.896	0.901	0.732	0.799	0.761	0.766	0.798
	Comp. 03	0.987	0.893	1.000	0.999	0.992	0.771	0.746	0.689	0.704	0.743
	Comp. 04	0.984	0.896	0.999	1.000	0.991	0.765	0.741	0.685	0.700	0.738
	Comp. 05	0.995	0.901	0.992	0.991	1.000	0.788	0.772	0.700	0.712	0.766
Longitudinal	Comp. 01	0.775	0.732	0.771	0.765	0.788	1.000	0.846	0.805	0.825	0.849
	Comp. 02	0.758	0.799	0.746	0.741	0.772	0.846	1.000	0.979	0.980	0.998
	Comp. 03	0.680	0.761	0.689	0.685	0.700	0.805	0.979	1.000	0.994	0.985
	Comp. 04	0.694	0.766	0.704	0.700	0.712	0.825	0.980	0.994	1.000	0.986
	Comp. 05	0.750	0.798	0.743	0.738	0.766	0.849	0.998	0.985	0.986	1.000

(c) FEM-based lumped spring foundation model

FEM Based		Transverse					Longitudinal				
		Comp. 01	Comp. 02	Comp. 03	Comp. 04	Comp. 05	Comp. 01	Comp. 02	Comp. 03	Comp. 04	Comp. 05
Transverse	Comp. 01	1.000	0.891	0.922	0.921	0.935	0.553	0.548	0.521	0.542	0.537
	Comp. 02	0.891	1.000	0.989	0.984	0.988	0.642	0.612	0.583	0.610	0.593
	Comp. 03	0.922	0.989	1.000	0.997	0.991	0.625	0.589	0.562	0.589	0.571
	Comp. 04	0.921	0.984	0.997	1.000	0.992	0.629	0.593	0.568	0.595	0.575
	Comp. 05	0.935	0.988	0.991	0.992	1.000	0.647	0.636	0.608	0.634	0.620
Longitudinal	Comp. 01	0.553	0.642	0.625	0.629	0.647	1.000	0.862	0.849	0.865	0.844
	Comp. 02	0.548	0.612	0.589	0.593	0.636	0.862	1.000	0.991	0.997	0.998
	Comp. 03	0.521	0.583	0.562	0.568	0.608	0.849	0.991	1.000	0.994	0.994
	Comp. 04	0.542	0.610	0.589	0.595	0.634	0.865	0.997	0.994	1.000	0.996
	Comp. 05	0.537	0.593	0.571	0.575	0.620	0.844	0.998	0.994	0.996	1.000

(d) Hybrid simulation model

Hybrid		Transverse					Longitudinal				
		Comp. 01	Comp. 02	Comp. 03	Comp. 04	Comp. 05	Comp. 01	Comp. 02	Comp. 03	Comp. 04	Comp. 05
Transverse	Comp. 01	1.000	0.808	0.907	0.904	0.914	0.659	0.626	0.563	0.591	0.595
	Comp. 02	0.808	1.000	0.935	0.938	0.923	0.588	0.579	0.561	0.577	0.568
	Comp. 03	0.907	0.935	1.000	1.000	0.995	0.623	0.623	0.577	0.603	0.598
	Comp. 04	0.904	0.938	1.000	1.000	0.995	0.623	0.622	0.576	0.603	0.598
	Comp. 05	0.914	0.923	0.995	0.995	1.000	0.628	0.632	0.576	0.604	0.604
Longitudinal	Comp. 01	0.659	0.588	0.623	0.623	0.628	1.000	0.858	0.829	0.840	0.826
	Comp. 02	0.626	0.579	0.623	0.622	0.632	0.858	1.000	0.984	0.992	0.994
	Comp. 03	0.563	0.561	0.577	0.576	0.576	0.829	0.984	1.000	0.995	0.993
	Comp. 04	0.591	0.577	0.603	0.603	0.604	0.840	0.992	0.995	1.000	0.997
	Comp. 05	0.595	0.568	0.598	0.598	0.604	0.826	0.994	0.993	0.997	1.000

5.9.3 System Vulnerability Curves

The vulnerability curves of the reference bridge are numerically estimated from randomly generated component demands following the statistical distribution in Table 5.7 and the correlation coefficients in Table 5.9. To utilize the vulnerability curves for loss estimation, it is necessary to represent the vulnerability curves in a functional form. As the vulnerability curves of bridge components are based on lognormal distribution, the system vulnerability curves are most likely to fit well in lognormal cumulative distribution function. To determine lognormal parameters of system fragility curves, regression analysis is conducted for the numerically estimated vulnerability points. Figure 5.21 presents an example of system vulnerability curves fitted into lognormal cumulative distribution function. Table 5.10 summarizes the system vulnerability curves in terms of median and standard deviation in log space.

Table 5.10 Regression analysis result of proposed vulnerability curves

SSI Approach	FIXED			CONVENTIONAL		
Limit state	LS1	LS2	LS3	LS1	LS2	LS3
μ	-1.507	-1.069	-0.725	-1.496	-0.876	-0.532
σ	0.287	0.414	0.551	0.505	0.590	0.661

SSI Approach	FE			Multiplatform		
Limit state	LS1	LS2	LS3	LS1	LS2	LS3
μ	-2.199	-1.479	-0.989	-1.675	-1.123	-0.770
σ	0.409	0.624	0.756	0.383	0.523	0.633

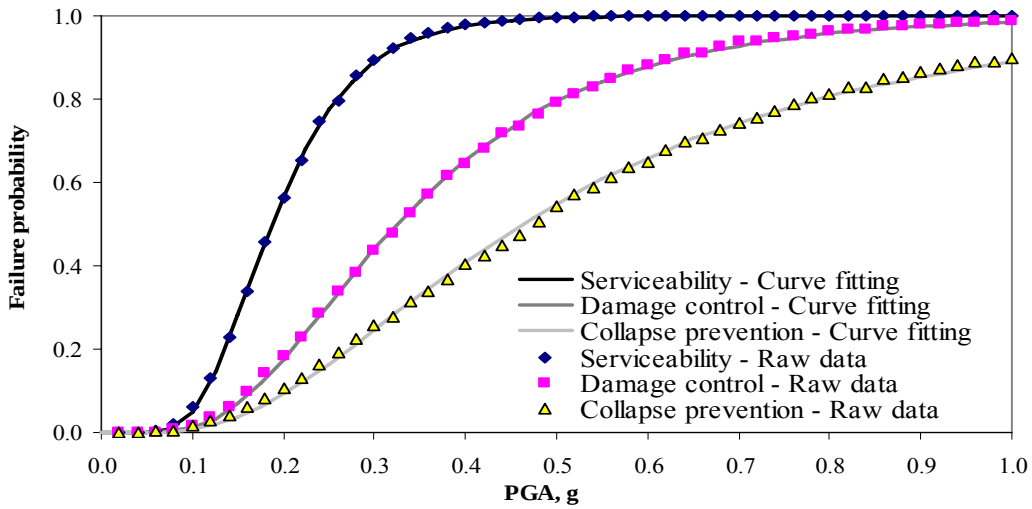

Figure 5.21 Curve fitting of system vulnerability curve

Figure 5.22 through 5.25 present fragility curves of bridge components and system fragility curves estimated from seismic demand of bridge components. Bridge components that do not contribute to the failure probability of bridge systems are not included in the figure.

When it is assumed that embankments and foundations are fixed, as shown in Figure 5.22, the most vulnerable bridge components are abutments bearings in a transverse direction. All other components are not vulnerable and do not contribute to the failure probability of the bridge system. This observation is consistent with the seismic demand of bridge components shown in Figure 5.20 and Table 5.8, which show that the seismic demand of all bridge components except abutment bearings in transverse directions are the lowest when abutments and foundations are fixed.

Figure 5.23 presents component and system fragility curves of a bridge whose foundations are assumed as lumped springs derived from a conventional method. In this system, the abutment bearings in the transverse direction are still the most vulnerable components. However, other components, such as abutments and bents in transverse and longitudinal direction also contribute to the system failure probability.

Figure 5.24 presents the fragility curves of the reference bridge whose foundations are modeled as lumped springs determined from an FE analysis of each foundation. Figure 5.25 shows vulnerability curves from a multiplatform simulation. In all limit states, the abutment bearings in the transverse direction are the most vulnerable component. For the serviceability and the damage control limit states, the abutment and bent in the transverse directiondirection and the abutment and bent in the longitudinal direction contribute to the system failure. For the collapse prevention limit state, bents do not contribute to the failure probability due to their large displacement capacity. As the limit state of expansion bearings in the longitudinal direction are defined only for collapse prevention system conditions, those components contribute to the system failure probability.

The USGS United States Geological Survey (USGS) recommends the seismic hazard of a bridge site to be 0.19, 0.38, and 0.87g for 10, 5, and 2% probabilities respectively, of exceedance in 50 years. Figure 5.25 shows the seismic hazards are overlapped with failure probabilities. System failure probabilities for each seismic hazard

level are summarized in Table 5.11. For ground earthquakes with 10% exceedance probability in 50 years, the probability of reaching serviceability limit states is 51%. For 5% exceedance probability in 50 years, the damage control limit state is about 62%. And for 2% ground motion, the collapse prevention limit state is about 84%. Therefore, when a structure with the studied bridge configuration is subjected to improvement, the abutment bearings should be replaced with bearings with larger transverse displacement capacity in transverse direction, such as elastomeric bearings. Otherwise, the use of restrainers is recommended.

Table 5.11 Failure probability of the bridge subjected to seismic hazard of the site

PE in 50 years	Serviceability	Damage control	Collapse prevention
10%	0.51	0.15	0.08
5%	0.97	0.62	0.38
2%	1.00	0.97	0.84

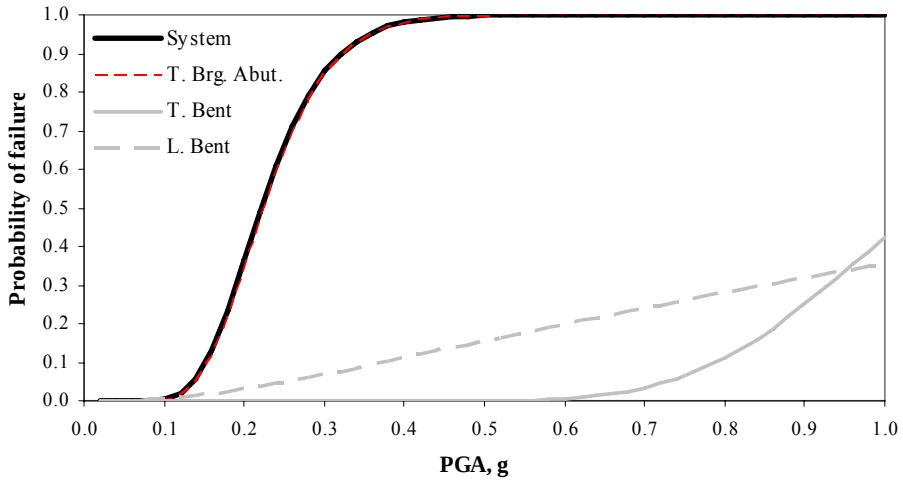

(a) Serviceability limit state

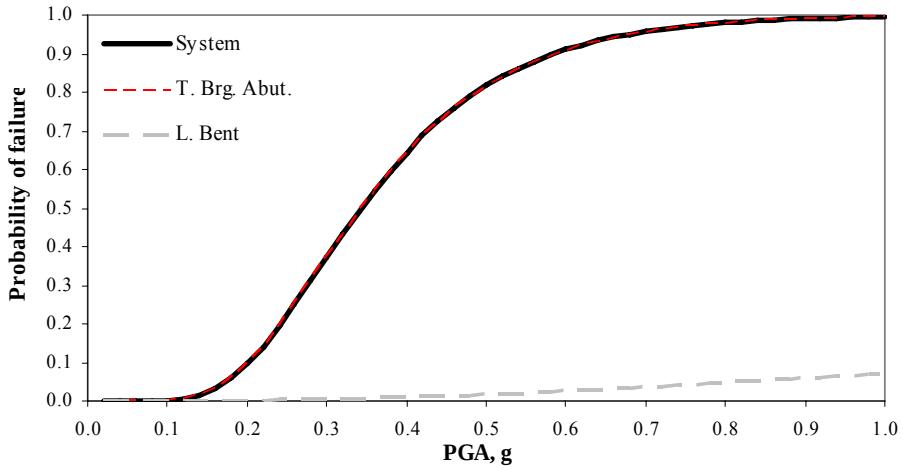

(b) Damage control limit state

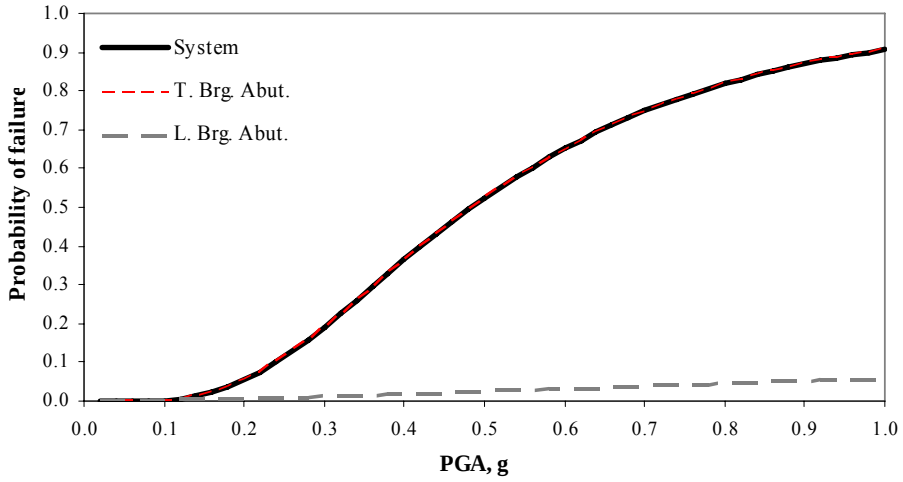

(c) Collapse prevention limit state

Figure 5.22 Vulnerability curves – Fixed foundation model

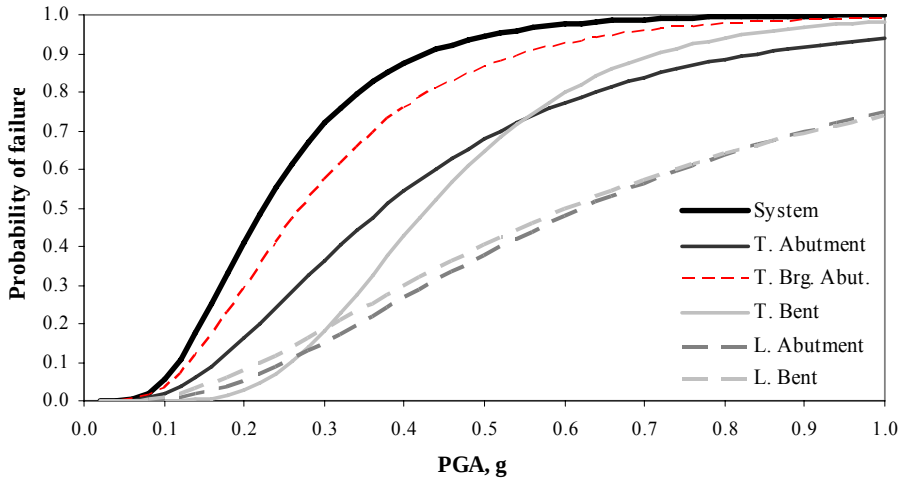

(a) Serviceability limit state

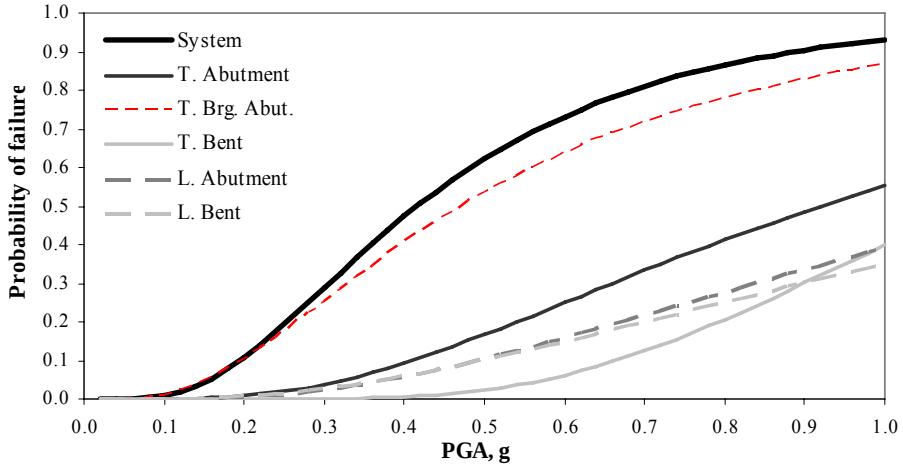

(b) Damage control limit state

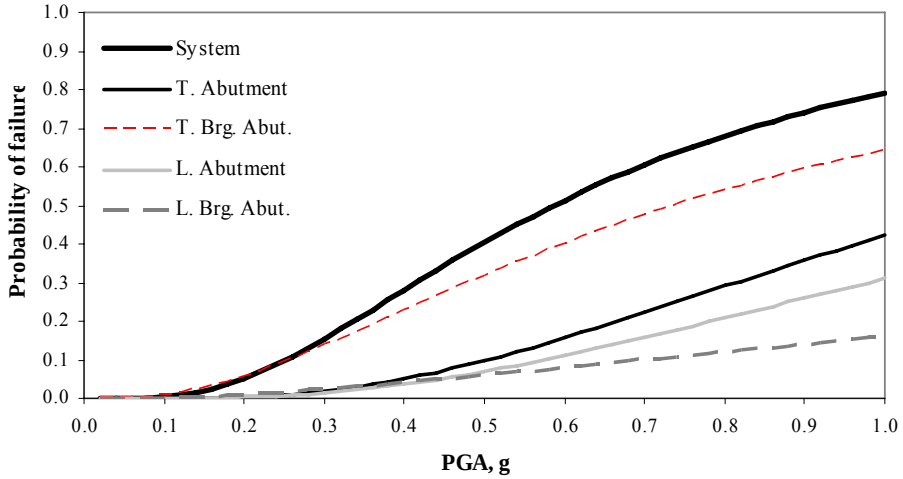

(c) Collapse prevention limit state

Figure 5.23 Vulnerability curves – Conventional foundation model

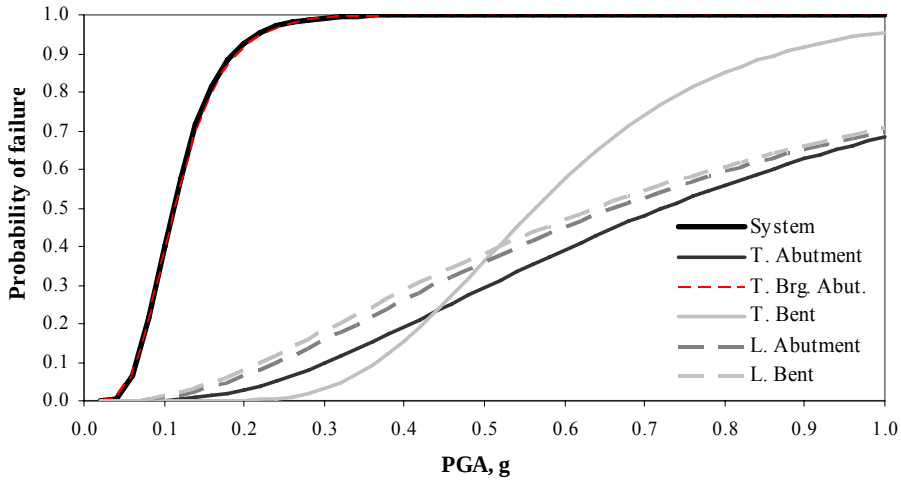

(a) Serviceability limit state

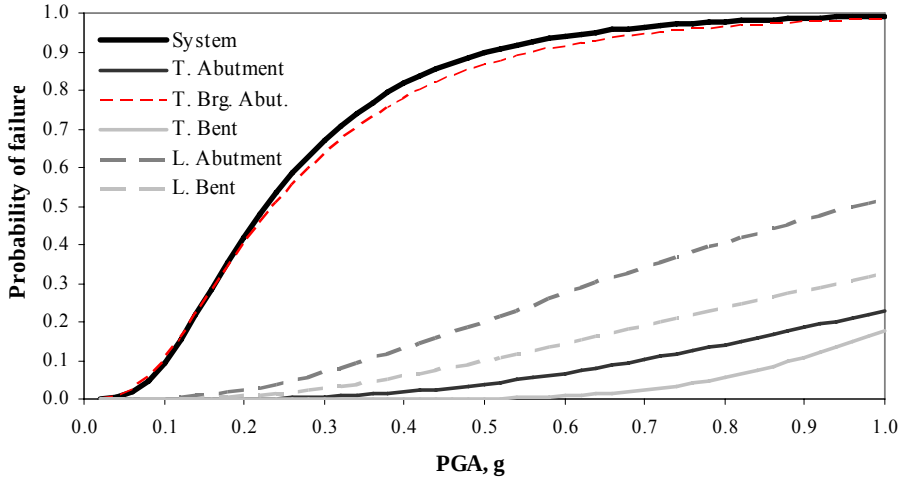

(b) Damage control limit state

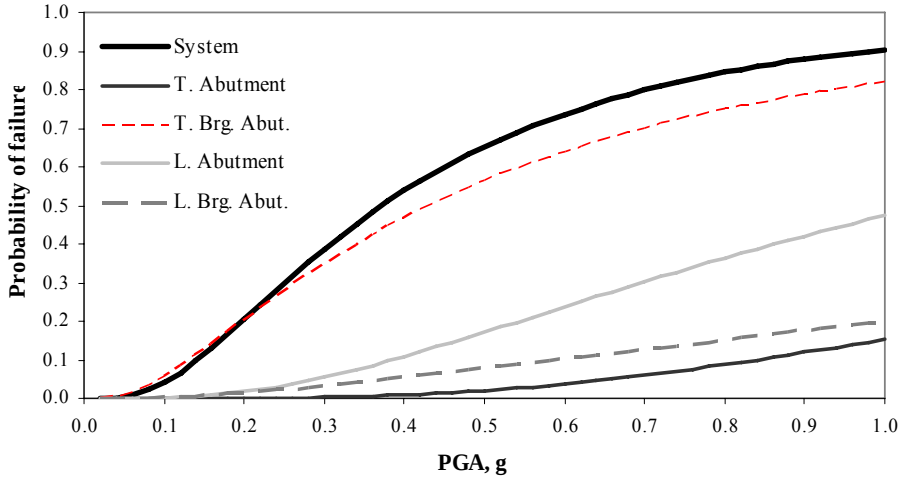

(c) Collapse prevention limit state

Figure 5.24 Vulnerability curves – FE foundation model

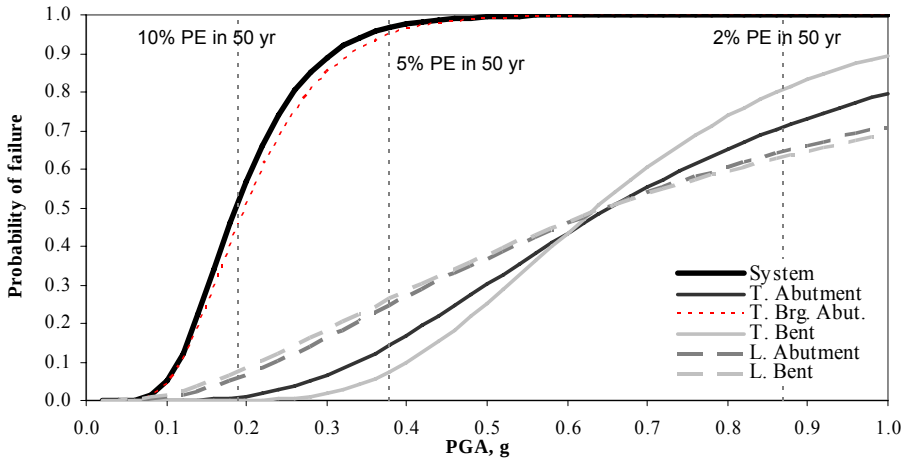

(a) Serviceability limit state

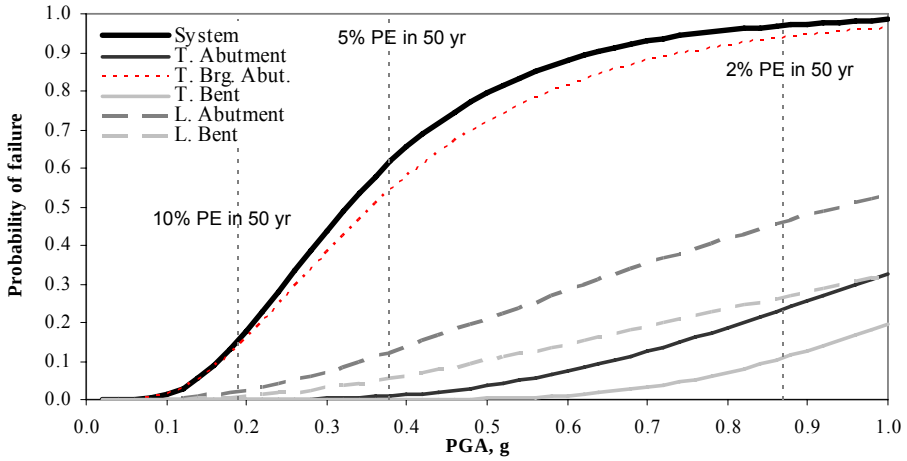

(b) Damage control limit state

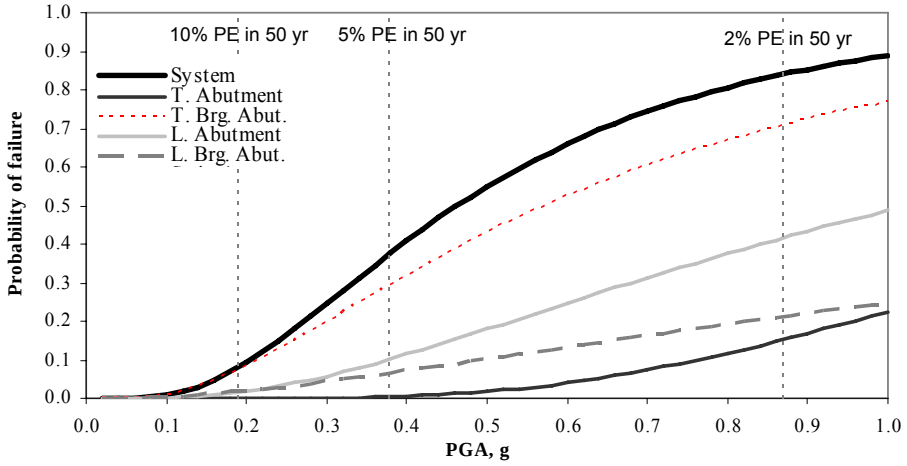

(c) Collapse prevention limit state

Figure 5.25 Vulnerability curves – Multiplatform foundation model

5.10 Summary and Discussions

In this chapter, vulnerability curves for a reference bridge in the Central and Eastern U.S. are derived. Four different approaches are used to consider soil-structure interaction: (a) Abutment and foundations are assumed to be fixed, (b) Abutment and foundations properties are estimated from conventional method are assumed to be lumped springs, (c) Abutment and foundations whose properties are estimated from FE analysis are assumed as springs, and (d) Multiplatform analysis is utilized.

The SAC-FEMA simulation method is compared with the full MCS. The two methods resulted in similar fragility curves. The full MCS might be the most realistic estimation of system failure probabilities because it does not need to include assumptions in probability distribution and aggregation of component failure probability. However, with computational advantages in the SAC-FEMA simulation method and negligible differences in derived fragility curves, the SAC-FEMA method is adopted in this study.

The fragility curves from the four methods for SSI analysis show that system failure probability is mostly governed by failure probability of abutment bearings. When it is assumed that foundations are fixed, the bridge response in the longitudinal direction is limited to gap width. Thus, failure probabilities of longitudinal components are negligible. In the transverse direction, the bearings on abutments are damaged, as abutments are assumed to be fixed. The other three approaches show similar trends, except that contributions from other components are increased.

The four different approaches resulted in slightly different fragility curves. It is difficult to conclude which method reflects reality most accurately. But in terms of accuracy, the multiplatform approach can be considered as the most accurate, as the method is verified from measured response of instrumented bridge in Section 4.3. In addition, the FE model for multiplatform approach does not need large assumptions. The second reliable method is the use of lumped springs estimated from the FE analysis of foundations. This method does not account for the coupling effect between different DOFs, and hysteretic response is simplified as a trilinear response. The conventional method for foundation springs may be useful as a starting approximation in design process. But due to sweeping assumptions, the method may not result in reliable performance evaluation. Assuming fixed foundations for bridges is not recommended

because the method overestimates the failure probability of elements adjacent to fixed boundaries. In terms of computational costs and modeling efforts, the multiplatform simulation is the most expensive, followed by the lumped spring from the FE model and the conventional method, and then the fixed foundation.

As a reference application, failure probability of the reference bridge is estimated for the earthquake hazard of the bridge site. The probability of reaching serviceability, damage control, and collapse prevention limit state against 10, 5, and 2% probability of exceedance seismic hazard are about 51, 62, and 84%, respectively. As the bridge does not satisfy performance criteria, the use of bearings at abutments, with large displacement capacity or restrainers to restrict deck movement in the transverse direction is recommended.

CHAPTER 6

CONCLUSIONS AND RECOMMENDATIONS FOR FUTURE RESEARCH

The objective of this project is to assess the seismic vulnerability of bridges with consideration of soil-structure interaction (SSI) using distributed simulation. Each subcomponent of the simulation process, such as soil and foundation model, soil-structure interaction model, and vulnerability simulation procedures, is carefully verified with reliable data as shown in Figure 1.1. The structural analysis platform is verified with measured response data of a structure tested on a shaking table. The geotechnical analysis platform is verified with in-situ tests of laterally loaded piles. The soil-structure interaction system is verified using a heavily instrumented bridge that experienced several sets of actual earthquake motions. To run soil-structure-interaction analysis, a multiplatform simulation framework is developed that also allows a geographically distributed hybrid simulation. Several application examples of the developed framework are also introduced. A reference bridge in the Central and Eastern U.S. is selected to derive fragility curves. Fragility analysis of the bridge is conducted using four different SSI representations. Conclusions are drawn in the various chapters and sections. Herein, the main conclusions are reiterated, followed by suggestions for future developments on the system and component levels.

6.1 Summary of Conclusions

6.1.1 Verification of Numerical Models and SSI Effects

Structures are designed to behave in the inelastic range under earthquake ground motion in order to dissipate seismic energy and reduce construction costs. The materials of the structural system, such as concrete, and the geotechnical system are highly inelastic. Thus numerical model of these systems should be verified with reliable data, such as experiments or measurements from actual earthquake events. In this study, a shaking

table-tested structure, laterally loaded piles in cohesionless and cohesive soil, and an instrumented highway overcrossing bridge are used for the verification studies. The following is a summary of findings from the verification studies:

Benchmark structure

- The response from the numerical model is compared with measurements from the shaking table test. The reinforced concrete frame structure is modeled with fiber-based, beam-column elements with nonlinear material properties. The response from the numerical model is similar to that from the shaking table test.
- Through the comparison of the dynamic analysis with shaking table experimental results at various ground motion levels, it is concluded that using the same level of damping for elastic and inelastic ranges may result in an unconservative result at a large-response amplitude range.

Laterally Loaded Piles

- Numerical models of a single pile in cohesionless and cohesive soils are verified with field test results. The analytical results are in good agreement with test results. The deformation of soils and hysteretic behaviors of a pile in cohesionless soil and soil are significantly different due to the different nature of soil properties.
- The verification study suggests that the sophisticated 3D material model can represent field conditions with good accuracy. If computational power and resources for FE modeling allow, the soil and foundation system can be represented by the FE model, as the simplified method includes sweeping assumptions and extrapolations.

MRO Bridge

- Multiplatform analytical simulation is applied to the MRO Bridge. The analysis results show good agreement with recorded data, thus confirming the potential of the multiplatform approach for SSI analysis.
- The analytical mode shapes and fundamental periods of the entire system are close to those identified from recorded ground motion using transfer functions.

The good agreement of mode shapes proves that the stiffness and effective mass of the embankment is correctly estimated and that the transverse response of a bridge is mainly controlled by the response of the embankment.

- The stiffness of the inelastic model of the central pier pile group is within the range of the stiffness from previous studies. Owing to the different approaches adopted, however, the range of stiffness values is wide, and cannot be easily narrowed.

The above-referenced verification studies prove that the adopted modeling approach for the structure, soil-foundation system, and soil-structure-interacting system is reliable. The verified framework is applied to derive fragility curves of a reference bridge typical of the Central and Eastern U.S.

6.1.2 Development of Advanced Analysis Environment

The state-of-the-art geotechnical and structural analysis environments are combined with a hybrid simulation framework. This framework was designed to draw on the diverse resources of the earthquake engineering research world. For instance, the framework divides geotechnical and structural systems into several substructured modules that can be modeled analytically or experimentally. The framework can handle any combination and number of ZEUS-NL (MAE Center analysis platform), OpenSees (PEER Center analysis platform), ABAQUS, Vetor2, and FedeasLab modules that can, in turn, be combined with a number of experimental specimens. This framework was verified through various simulations. Four application examples are introduced: A three-site hybrid test, MRO Bridge simulation, MISST project, and a high-rise complex structure. Theses application examples show promising potential of the developed framework.

6.1.3 Vulnerability Curve Derivation Procedure

The derivation of vulnerability curves is affected by many factors, including the vulnerability analysis method, input ground motions, and the definition of random

variables and performance limit states. A three-story OMRCF is used as a reference structure to compare the vulnerability curves from various methods. The following is a summary of findings from the benchmark study.

- The selected ground motion sets mainly affect the derived vulnerability curves when PGA is used as an intensity measure. Thus, scrupulous consideration is required when ground motions are selected for a vulnerability analysis.
- When spectral acceleration is used as an intensity measure, the variability of the derived vulnerability curves dropped dramatically.
- The concrete ultimate strength affects the structural response from small ground motion level because the concrete elastic modulus is related to the ultimate strength.
- The yield strength of steel has little effect on the structural response at low ground motion levels.
- At high ground motion levels, material properties contribute to the variability in structural response, but the variability is much smaller than that due to ground motion variability.
- The SAC-FEMA approach, Monte-Carlo Simulation, and Response Surface Method results in similar vulnerability curves.

The study shows effects of various parameters in vulnerability simulation. Considering that the SAC-FEMA approach is reliable and computationally efficient, the vulnerability curves of a reference bridge in the Central and Eastern U.S. is derived using the SAC-FEMA method.

6.1.4 Vulnerability Analysis of Bridges with SSI Consideration

The reference bridge analyzed in this research is a multi-span, continuous steel girder bridge. The bridge is supported on seat-type abutments and bents with three reinforced concrete piers. The abutment and embankment model affects the transverse response of the bridge significantly, while it has a minor influence on the longitudinal response. The following is a summary of the findings from the vulnerability analysis of the reference bridge:

- The different SSI approaches affect the transverse more than the longitudinal response. In the transverse direction, the bearings on abutments transfer forces even at low-intensity levels. Thus, the characteristics of the embankment model affect the bridge response directly.
- When it is assumed that embankments and abutments are fixed, the transverse seismic demand on abutment bearings is higher than other approaches. The fixed abutment assumption tends to limit the structural response in the transverse direction, but it increases the demand on the connecting elements between structure and boundary.
- The conventional spring and the FE-based lumped spring approaches, and multiplatform simulation results in very similar longitudinal seismic demand for all bearings and bents at low PGA levels. This similarity results from gaps and expansion bearings on abutments which minimizes the interaction between the embankments and bridge. The fixed-base approach shows distinctively different longitudinal seismic demand for all structural components. The fixed boundary in the longitudinal direction underestimates the demand on components.
- For structural components, the rate of demand increment tends to decrease with increasing PGA. On the contrary, the rate of demand increment on abutments tends to increase with increasing PGA. At low seismic intensity, the demand on structural components is nearly proportional to intensity. But at a certain PGA level where the superstructure contacts abutments, the structural response is restricted while the abutment response is activated.
- The fragility curves from the four methods of SSI analysis show that system failure probability is mostly governed by the failure probability of abutment bearings.
- The four different approaches result in slightly different fragility curves. It is difficult to conclude which method reflects reality most accurately due to lack of fragility relationship from actual earthquakes. However the multiplatform approach can be considered as most accurate, as the method is verified from measured response of instrumented bridge.

- The second most reliable method is lumped springs estimated from the FE analysis of foundations. This method, however, does not account for the coupling effect between different DOFs, and the hysteretic response is simplified as a trilinear response.
- The conventional method for foundation springs may be useful as a starting approximation in the design process. But due to the sweeping assumptions underlying it, the method may not result in a reliable performance evaluation. Assuming a fixed foundation for bridges is not recommended because the method overestimates the failure probability of elements adjacent to fixed boundaries.
- As a reference application, the failure probability of the reference bridge is estimated for the earthquake hazard of the bridge site. The probability of reaching serviceability, damage control, and collapse prevention limit state against seismic hazard with 10, 5, and 2% probability of exceedance in 50 years is about 51, 62, and 84%, respectively. If a retrofit project is conducted, it is recommended that abutment bearings be replaced with bearing possessing larger displacement capacity, such as elastomeric pads. Otherwise, the use of restrainers is recommended.

6.1.5 Summary

In this study, structural and geotechnical analysis methods are rigorously verified. A multiplatform simulation framework is developed for the purpose of soil-structure-interaction analysis. The framework can be extended to geographically distributed hybrid simulation. The vulnerability curves of a reference bridge in the Central and Eastern U.S. are derived. The methodologies and developed simulation frameworks will be of great interest to those involved in running advanced analyses and hybrid testing-analysis investigations. The derived vulnerability curves with advanced simulation method can be utilized for seismic loss assessment packages such as MAEviz and HAZUS.

6.2 Recommendation for Future Research

There are issues that have not been deeply investigated within the scope of this study. Many of those issues are left unresolved either due to lack of computational resources at the current state of computational environments, or due to the lack of data and their probabilistic distributions. There is also room for improvement in analysis methodologies. The following is a short list of suggested future research:

- Limit states of structural components critically affect the derived vulnerability function. The definition of limit states in a quantitative manner and their relation to actual functionality of the structure is still a wide-open subject. Many researchers in vulnerability derivation define limit states based on their judgment. More experimental data and more field surveys are required to estimate reliable capacity limit states and their probability distributions.
- Vulnerability curves have been developed by many researchers. In the development process, earthquake-induced structural damage data are generated from seismic analysis. With the development of increases in computational power, more sophisticated seismic analyses will be available. In addition, large earthquakes occur every few years. Thus, rather than discarding the structural analysis results after developing vulnerability curves, it is worthwhile to develop a database of structural damage observations so that new data may be used to update the existing vulnerability curves. The new data can be either analysis results or field surveys from earthquakes.
- In this study, only kinematic SSI is accounted for and surface motions are used as input. In large structures with deep and massive foundations, not only kinematic but also inertial SSI significantly affect the structural response. For this type of structure, it is insufficient to consider only kinematic SSI against surface ground motion. There are attempts to consider these interactions in the frequency domain, which is also inaccurate due to the necessary linearization of the intrinsically nonlinear problem. It is worthwhile to investigate this issue with practical applications.
- The cyber infrastructure dramatically evolves with time. The communication speeds over networks and the capacity and processing speed of computational

hardware are increasing. In the field of civil engineering, more and more institutions are equipped with experiment facilities. Analysis tools are being developed which simulate actual structures more accurately than ever. To fully explore these environments in the near term, it is recommended that a simulation portal be developed that can utilize the best features of all of these research environments.

The seismic performance evaluation of a structure comprises many subcomponents. In this study, much effort is devoted to the rigorous verification of models and methodologies using available experimental and observationaldata. In fact, the most realistic method for seismic performance evaluation might be instrumenting a target structure with a dense array of sensors, calibrating analytical and/or experimental models with measurement from the sensors, running hybrid simulation using the recorded ground motion from the site, and evaluating seismic performance from the fully calibrated model. Future efforts in this direction will decrease the uncertainties in numerical and experimental model dramatically, increase the reliability of seismic performance and vulnerability of structures, and therefore, improve public safety in future disasters.

APPENDICES

A. Horizontal Stiffness of Segmental Rocker

The geometric stiffness of horizontal rocker is derived from moment equilibrium as shown in Figure A.1. The stiffness is a function of the radius of bearing (R), the radius of rotation (r), and the rotation angle (θ). Figure A.2 shows the geometric stiffness of various R/r ratio as a function of the relative displacement of two plates. As expected, when R/r = 1, no force is required to roll the bearing, assuming that friction does not exist between contacting surfaces. As the radius of bearing becomes larger than that of rotation, the force required to move plates increases as the horizontal force equilibrates the moment caused by vertical forces. For the bearings used in the bridge in Section 5, when the relative displacement is less than 50 mm, the geometric stiffness is nearly linear, as shown in Figure A.3. For the modeling of expansion bearings, the linearized stiffness is used.

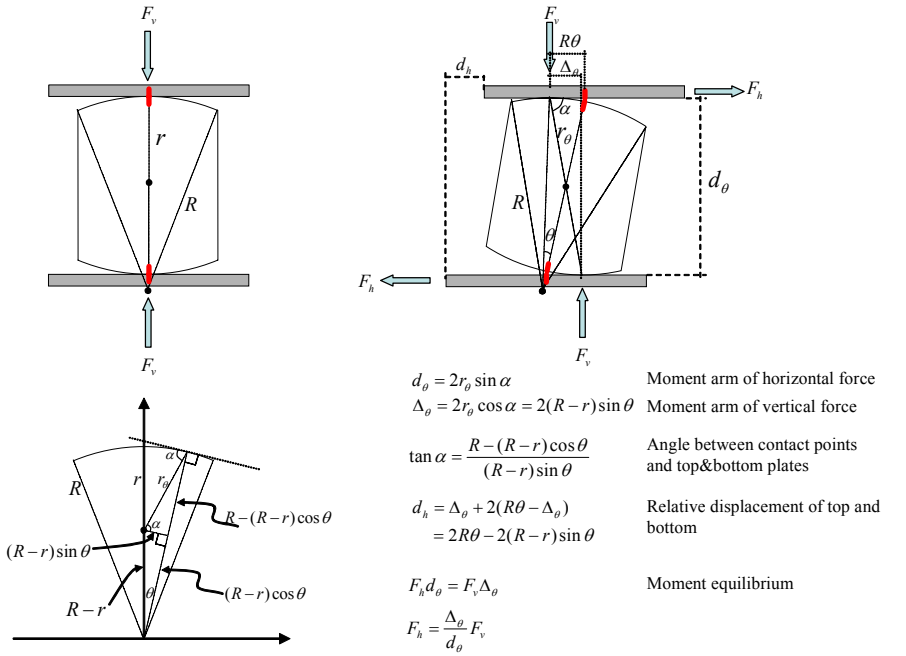

$d_\theta = 2r_\theta \sin\alpha$ Moment arm of horizontal force

$\Delta_\theta = 2r_\theta \cos\alpha = 2(R-r)\sin\theta$ Moment arm of vertical force

$$\tan\alpha = \frac{R-(R-r)\cos\theta}{(R-r)\sin\theta}$$ Angle between contact points and top&bottom plates

$$d_h = \Delta_\theta + 2(R\theta - \Delta_\theta)$$
$$= 2R\theta - 2(R-r)\sin\theta$$ Relative displacement of top and bottom

$F_h d_\theta = F_v \Delta_\theta$ Moment equilibrium

$$F_h = \frac{\Delta_\theta}{d_\theta} F_v$$
$$= \frac{1}{\tan\alpha} F_v$$
$$= \frac{(R-r)\sin\theta}{R-(R-r)\cos\theta} F_v$$

When the radius of bearing, R, is equal to radius of rotation, r, $F_h = 0$.
When the radius of bearing, R, is infinite, F_h = infinite.

Figure A.1 Derivation of geometric stiffness of segmental rocker

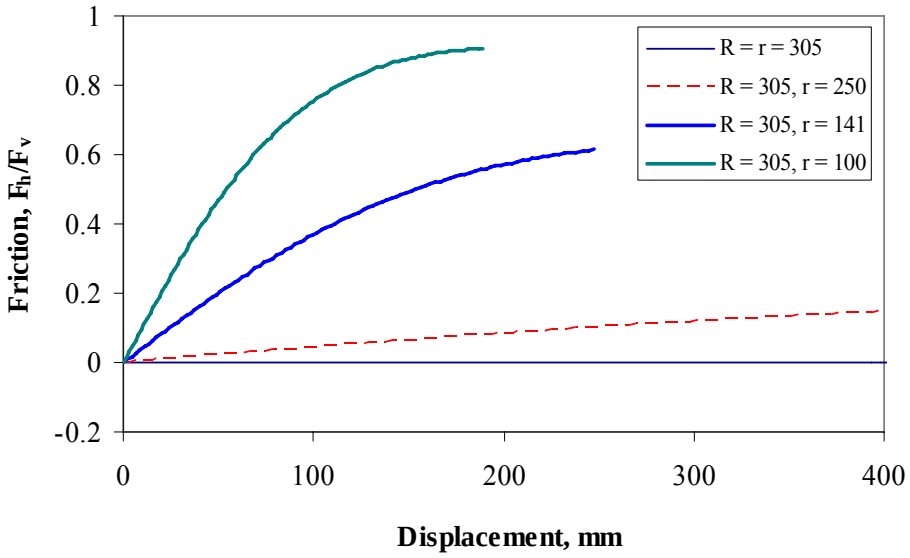

Figure A.2 The geometric stiffness as a function of relative displacement

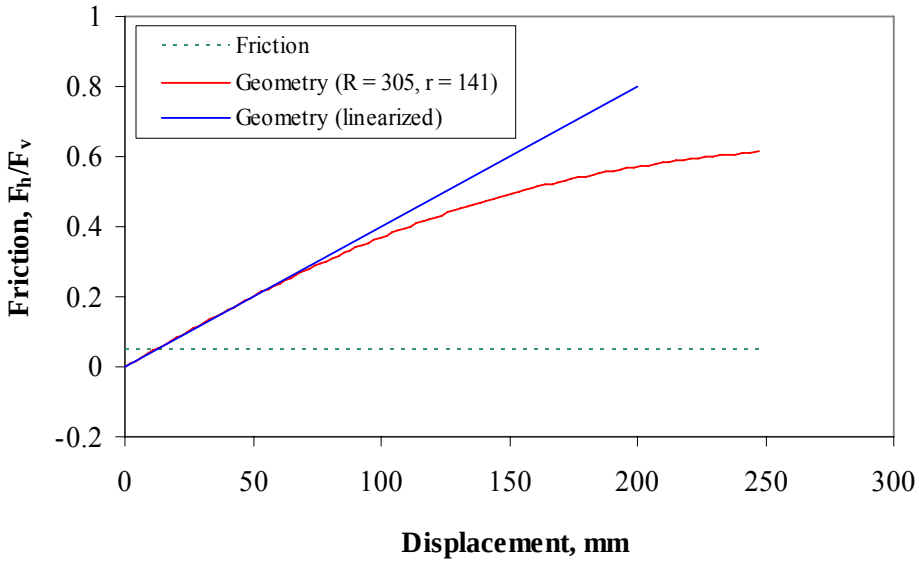

Figure A.3 Linearization of the geometric stiffness at small displacement range

B. Evaluation of Foundation Stiffness in Simplified Approach

A summary of the properties used for the LPile analysis is given below. Figure B.1 shows the load-deformation curve of a single pile.

Longitudinal direction

Pile properties

Pile Length:	4.57 m (180 in)
Diameter:	0.26 m (10.075 in, top flange width of HP10x42)
Cross sectional area:	80 cm^2 (12.4 in^2)
Moment of inertia:	$8.741x10^{-5}$ m^4 (210 in^4)
Modulus:	199948 N/mm^2 (29,000,000 lb/in^2)

Batter angle is neglected.

Assumed that pile behaves in elastic range.

Soil properties

Type:	Stiff clay with free water (Reese)
Layer depth:	4.57 m (180 in)
Unit weight:	17.6 kN/m^3
Cohesion:	75 kPa

Transverse direction

Identical to input properties in longitudinal direction except Moment of inertia of pile is 1.72 cm^4 (71.7 in^4).

Group effects

By Brown and Reese (1985), multipliers from 3x3 pile group in stiff clay

3D spacing, the multipliers: 0.7, 0.6, 0.5

Longitudinal direction: Pile spacing 762mm/256mm = 3

➔ Use multiplier of 0.7 and 0.6

Transverse direction: Pile spacing: 2057/256 = 8

➔ Pile spacing is large. The group effect is neglected.

Foundation stiffness with pile groups

Single pile stiffness and strength

$$K_{x,0} = 80\,kN/mm\,,\ K_{x,1} = 25\ kN/mm\,,\ \ K_{x,2} = 25\ kN/mm$$

$$K_{z,0} = 60\,kN/mm\,,\ K_{z,1} = 15\ kN/mm\,,\ \ K_{z,2} = 15\ kN/mm$$

Longitudinal spring properties (Foundation #1~#3)

$$K_{x,0} = 0.7\times(80\times5) + 0.6\times(80\times5) = 520\,kN/mm$$

$$K_{x,1} = 163\ kN/mm\,,\ \ K_{x,2} = 163\ kN/mm$$

Transverse spring properties (Foundation #1~#3)

$$K_{z,0} = 10\times60 = 600\,kN/mm$$

$$K_{z,1} = 150\ kN/mm\,,\ \ K_{z,2} = 150\ kN/mm$$

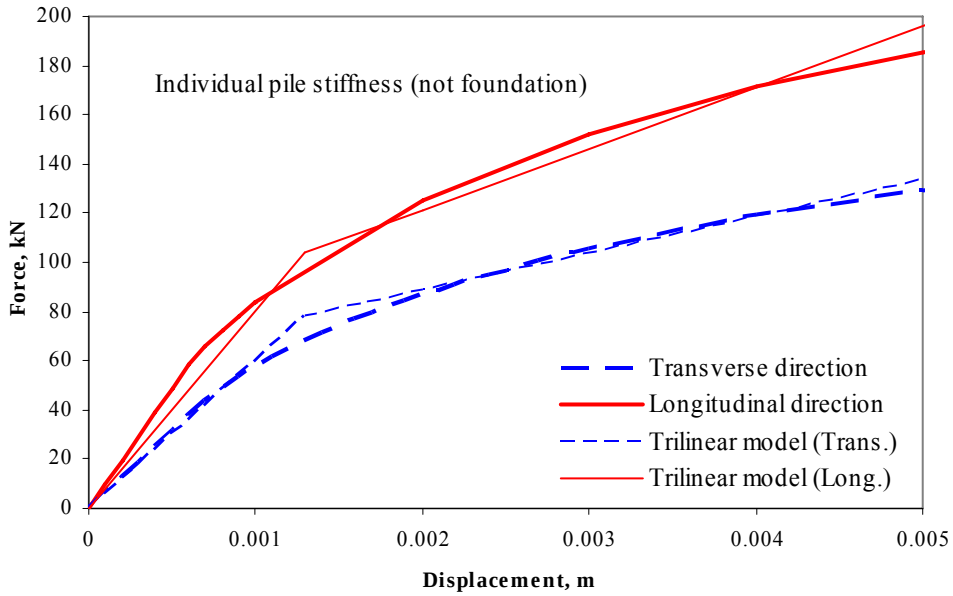

Figure B.1 Load-deformation curve of a single pile in stiff clay and linearization with tri-linear model

C. Evaluation of Abutment Stiffness in Simplified Approach

The stiffness and strength of abutments consists of the contribution from the pile and the abutment. The stiffness of the pile is estimated from the analysis using LPile. Since the pile spacing is large, the group effect is ignored. Figures C.1 and C.2 show the components of the stiffness and strength in longitudinal and transverse directions, respectively. The contribution of the pile is estimated from the linearization of the LPile analysis result. The contribution of the abutment is approximated from a full-scale abutment test that is adopted in the Caltran's Seismic Design Criteria (2004).

Pile stiffness

Longitudinal direction

Pile properties

Pile Length:	10.16 m (400 in)
Diameter:	0.26 m (10.075 in, top flange width of HP10x42)
Cross sectional area:	80 cm^2 (12.4 in^2)
Moment of inertia:	5.0 cm^4 (210 in^4)
Modulus:	199948 N/mm^2 (29,000,000 lb/in^2)

Batter angle is neglected.

Assumed that pile behaves in the elastic range.

Soil properties

Type:	Soft clay (Matlock)
Thickness:	10.16 m (400 in)
Unit weight:	17.6 kN/m^3
Cohesion:	20 kPa

It is assumed that the soil in embankment is softer than the soil in bridge foundation.

Evaluated spring properties

$$K_{x,0} = 6 \times 3.2 = 19.2\, kN/mm$$

$$K_{x,1} = 6 \times 1 = 6\, kN/mm$$

$$K_{x,2} = 6 \times 0.25 = 1.5\, kN/mm$$

Transverse direction

Identical to input properties in longitudinal direction except Moment of inertia of pile is 1.72 cm^4 (71.7 in^4).

Evaluated spring properties

$$K_{z,0} = 6 \times 2.3 = 13.8\, kN/mm$$

$$K_{z,1} = 6 \times 0.6 = 3.6\ kN/mm$$

$$K_{z,2} = 6 \times 0.25 = 1.5\ kN/mm$$

Abutment stiffness

Longitudinal direction

Based on passive earth pressure tests and the force deflection results from large-scale abutment testing at UC-Davis (Maroney, 1995), the initial embankment fill stiffness is

$$K_i \approx 11.5\ \ (kN/mm)/m$$

The initial stiffness shall be adjusted proportional to the backwall height as below.

$$K_{abut} = K_i \times w \times \left(\frac{h}{1.7}\right)$$

$$K_{abut} = K_i \times w \times \left(\frac{h}{1.7}\right) = 11.5 \times (10.2) \times \left(\frac{2.15}{1.7}\right) = 148.3\, kN/mm$$

The maximum passive pressure based on the ultimate static force developed in the full-scale abutment testing conducted at UC-Davis (Maroney, 1995) is 239 kPa.

$$P_{bw} = A_e \times 239kPa \times \frac{h_{bw}}{1.7}$$

$$P_{bw} = A_e \times 239kPa \times \frac{h_{bw}}{1.7} = 12.65 \times 239 \times \frac{2.15}{1.7} = 3823\, kN$$

$$A_e = 1.24 \times 10.2 = 12.65\ m^2$$

where A_e is effective abutment area = $h_{bw} \times w_{bw}$

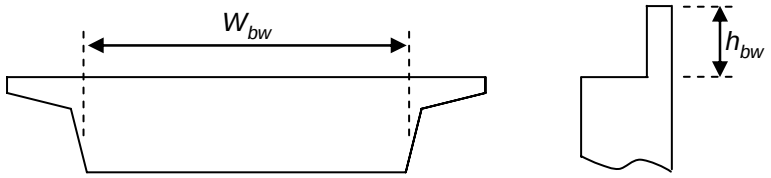

For seat abutments the back wall is typically designed to break off in order to protect the foundation from inelastic action. The area considered effective for mobilizing the backfill longitudinally is equal to the area of the back wall (Caltrans, 2004). The ultimate deformation is suggested as 10% of abutment height (h = 2.15 m) for cohesive soil and 6% for cohesionless soil. In the reference bridge, 8% (172 mm) of back wall height is adopted. It is assumed that the abutment behaves linear perfectly plastic in compression and has no strength in tension.

Transverse direction

Caltran's Design Criteria (2004) proposed that a nominal transverse spring, K_{nom}, of abutment can be assumed to be equal to 50% of the transverse stiffness of the adjacent bent in the elastic demand assessment models. When the footings of bents are assumed to be fixed, the transverse bent stiffness is 23.8 kN/mm. Hence,

$K_{abut,transverse} = 11.9 kN/mm$

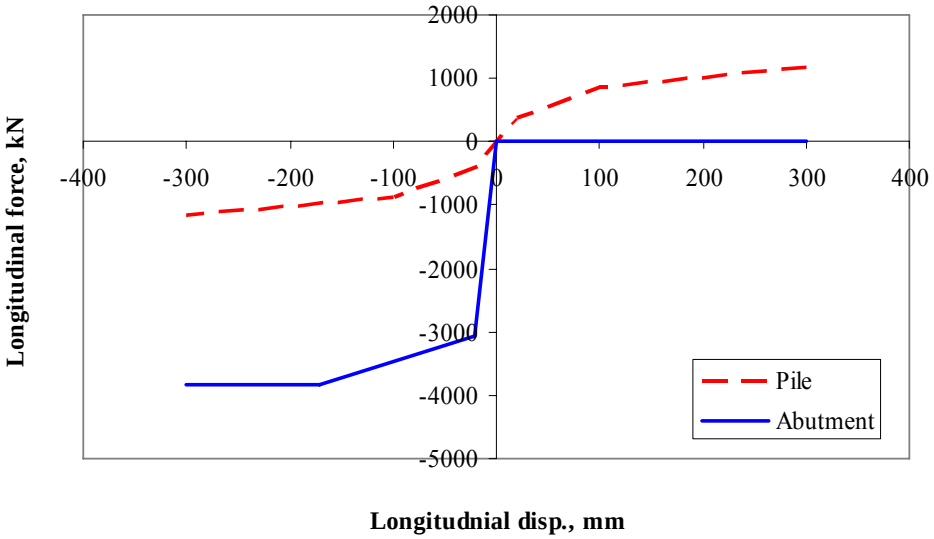

Figure C.1 Contribution of pile and abutment on longitudinal stiffness

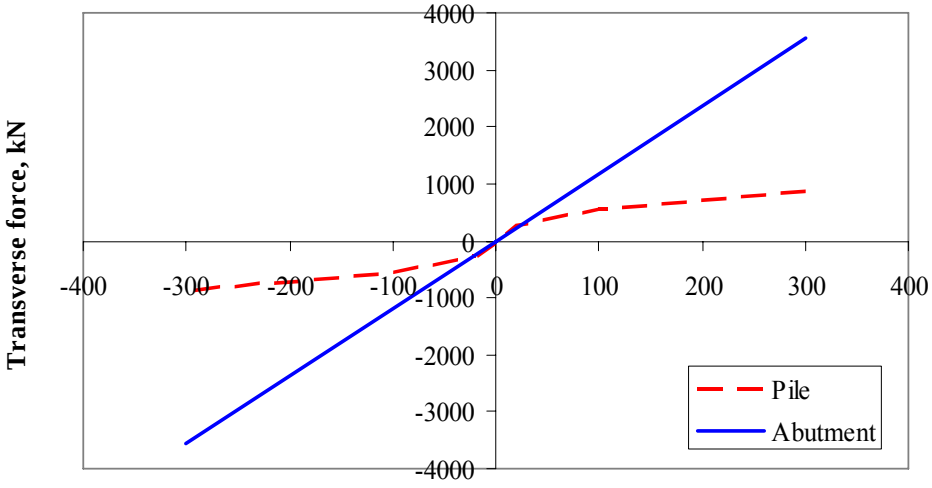

Figure C.2 Contribution of pile and abutment on transverse stiffness

REFERENCES

ACI (1989). "Building code requirements for structural concrete and commentary (318-89)", American Concrete Institute, Detroit, Michigan.

ACI (2002). "Building code requirements for structural concrete and commentary (318-02)", American Concrete Institute, Detroit, Michigan.

Anderson, D. G. (2003). *Laboratory Testing of Nonlinear Soil Properties: I & II*. prepared by CH2M HILL, Bellevue, Washington for the Lifeline Research Program, Pacific Earthquake Engineering Research Center, University of California at Berkeley, December.

API (1991). *Recommended Practice for Planning, Designing, and Constructing Fixed Offshore Platforms*, American Petroleum Institute, Washington D.C.

Aschenbrener, T. B. and Olson, R. E. (1984). "Prediction of Settlement of Single Piles in Clay," *Proceedings of Symposium on Analysis and Design of Pile Foundation*, ASCE, San Francisco, pp. 41-58.

ATC-13 (1985). *Earthquake Damage Evaluation Data for California*, Applied Technology Council, Redwood City, Palo Alto, California.

ATC-40 (1997). *Seismic Evaluation and Retrofit of Concrete Buildings*, Applied Technology Council, Redwood City, Palo Alto, California.

Badoni, D. and Makris, N. (1996). "Nonlinear Response of Single Piles under Lateral Inertial and Seismic Loads," *Soil Dynamics and Earthquake Engineering*, Vol. 15, pp. 29-43.

Badoni, D. and Makris, N. (1997). "Analysis of the Nonlinear Response of Structures Supported on Pile Foundations," Earthquake Engineering Research Center, *Report No. UCB/EERC-97/07*.

Barlett, F. M., and MacGregor, J. G. (1996). "Statistical analysis of the compressive strength of concrete in structures," *ACI Material Journal*, 93(2), 158-168.

Bommer, J. J. and Martinez-Pereira, A. (1999). "The effective duration of earthquake strong motion," *Journal of Earthquake Engineering*, 3(2): 127-172.

Bondonet, G., and Filiatrault, A. (1997). "Frictional Response of PTFE Sliding Bearings at High Frequencies," *Journal of Bridge Engineering*, 2(4):139-148.

Borzi, B., Calvi, G. M., Elnashai, A. S., Faccioli, E., and Bommer, J. J. (2001). "Inelastic spectra for displacement-based seismic design," *Soil Dynamics and Earthquake Engineering*, 21(1):47-61.

Bowles, J. E. (1996). *Foundation Analysis and Design*, McGraw-Hill, New York.

Bracci, J. M., Reinhorn, A. M.,and Mander, J. B. (1992). "Seismic Resistance of Reinforced Concrete Frame Structures Designed only for Gravity Loads: Part I-Design and Properties of a One-Third Scale Model Structure.", *Technical Report NCEER-92-0027.*

Broderick, B. M., Elnashai, A. S. (1994). "Seismic resistance of composite beam–columns in multi-story structures, part 2: analytical model and discussion of results," *Journal of Construct Steel Research*, 30(3):231–58.

Brown, D. A., and Reese, L. C. (1985). *Behavior of a large-scale pile group subjected to cyclic lateral loading*, Report to the Minerals Management Services, U.S. Dept. of Interior, Reston, VA. Dept. of Research, FHWA, Washington DC and U.S. Army Engineer Waterways Experiment Station, Vicksburg, Mississippi.

Caltrans (1988). *Memo to Designers 5-1,* California Department of Transportation, Division of Structures, Sacramento, CA, Septermber.

Caltrans (1989). *Bridge Design Aids 14-1,* California Department of Transportation, Sacramento, CA, October.

Caltrans (2004). *Seismic Design Criteria*, Version 1.3.

Carrion, J., and Spencer, B. F. (2006). "Real-Time Hybrid Testing Using Model-Based Delay Compensation," Proceedings of 4th International Conference on Earthquake Engineering, Taipei, Taiwan, Oct 12-13.

Chen, C.-H., Lai, W.-C., Cordova, P., Deierlein, G. G., and Tsai, K.-C. (2003). "Pseudo-Dynamic Test of Full-Scale Rcs Frame:Part 1 - Design, Construction and Testing," *Proceedings of International Workshop on Steel and Concrete Composite Constructions*, Taipei, Taiwan, 107-118.

Chopra, A.K. (2000). *Dynamics of structures: Theory and applications to earthquake engineering*, 2nd ed., Prentice Hall, Englewood Cliffs, New Jersey.

Chopra, A. K., and Goel, R. K. (1999). *Capacity-Demand-Diagram Methods for Estimating Seismic Deformation of Inelastic Structures: SDF Systems*, Report No. PEER-1999/02, Pacific Earthquake Engineering Research Center, University of California, Berkeley.

Chryssanthopoulos, M. K., Dymiotis, C., and Kappos, A. J. (2000). "Probabilistic evaluation of behaviour factors in EC8-designed R/C frames," *Engineering Structures*, 22(8):1028-1041.

Combescure, D. and Pegon, P. (1997). "α-Operator Splitting time integration technique for pseudodynamic testing. Error propagation analysis," *Soil Dynamics and Earthquake Engineering,* Vol. 16, pp. 427-443.

Constantinou, M. C., Mokha, A., and Reinhorn, A. M. (1990). "Teflon bearings in base isolation II: Modeling," *Journal of Structural Engineering*, 116(2), 455–474.

Cornell, C. A., Jalayer, F., Hamburger, R. O., and Foutch, D. A. (2002). "Probabilistic Basis for 2000 SAC Federal Emergency Management Agency Steel Moment Frame Guidelines," *Journal of Structural Engineering*, 128:526-533.

Cox, W. R., Reese, L. C., and Grubbs, B. R. (1974). "Field Testing of Laterally Loaded Piles in Sand," *Offshore Technology Conference*, Dallas, Texas, 459-472.

Coyle, H. M. and Reese, L. C. (1966). "Load Transfer for Axially Loaded Piles in Clay," *Journal of the Soil Mechanics and Foundations Division*, ASCE, Vol. 92, No. SM2, pp. 1-26.

Cremer, C., Pecker, A., and Davenne, L. (2002). "Modeling of Nonlinear Dynamic Behaviour of a Shallow Strip Foundation with Macro-Element," *Journal of Earthquake Engineering*, 6(2):175-211.

CSI Inc. (2005). "SAP2000 – Structural analysis program, Computers and Structures," Berkeley, California.

Das, B. M. (2003). *Principles of Foundation Engineering*, Thomson Learning.

de Felice, G., Giannini, R., and Pinto, P.E. (2002). "Probabilistic Seismic Assessment of Existing R/C Buildings: Static push-over versus dynamic analysis," London, UK. 12th European Conf. on Earthquake Engineering.

Dermitzakis, S.N. and Mahin, S.A. (1985). "Development of substructuring techniques for on-line computer controlled seismic performance testing." *Report UCB/EERC-85/04*, Earthquake Engineering Research Center, University of California, Berkeley.

Desai, C. S., Zaman, M. M., Lightner, J. G., and Siriwardane, H. J. (1984). "Thin-layer Element for Interfaces and Joints," *International Journal for Numerical and Analytical Methods in Geomechanics*, 8:19-43.

Dimig, J., Shield, C., French, C., Bailey, F., and Clark, A. (1999). "Effective force testing: A method of seismic simulation for structural testing." *Journal of Structural Engineering*. 125(9):1028-1037.

Douglas, B. M., Maragakis, E., and Vrontinos, S. (1991). "Parameter identification studies of the Meloland Road Overcrossing." *Proceedings of the Pacific Conference on Earthquake Engineering*, Auckland, New Zealand, 105–116.

Drosos, V.A. (2003). *Synthesis of Earthquake Ground Motions for the New Madrid Seismic Zone,* MS thesis, Georgia Institute of Technology, Atlanta, GA.

Duncan, J. M., Evans, L. T., and Ooi, P. S. K. (1994). "Lateral load analysis of single piles and drilled shafts," *Journal of Geotechnical Engineering*, 120(5), 1018-1033.

Ellingwood, B. R., and Wen, Y. K. (2005). "Risk–benefit-based design decisions for low-probability/high consequence earthquake events in Mid-America," *Progress in Structural Engineering and Materials*, 7:56-70.

El-Naggar, M. H. and Novak, M. (1996). "Nonlinear Analysis for Dynamic Lateral Pile Response,"*Journal of Soil Dynamics and Earthquake Engineering*, 15:223-244.

Elnashai, A. S. (1984). "Non-linear analysis of composite tubular joints," Ph. D. Dissertation, Imperial College, London.

Elnashai, A. S. (2003). "Next generation vulnerability functions for RC structures," *Proceeding of Response of Structures to Extreme Loading*, Toronto, 3-6 Aug.

Elnashai, A. S., Borzi, B., and Vlachos, S. (2004). "Deformation-based vulnerability functions for RC bridges," *Journal of Structural Engineering and Mechanics*, 17(2)

Elnashai, A. S., Elghazouli, A.Y. (1993). "Performance of composite steel/concrete members under earthquake loading, Part I: Analytical model," *Earthquake Engineering and Structural Dynamics*, 22(4):314-345.

Elnashai, A. S., Elghazouli, A. Y. and Dowling, P.J. (1990). "Verification of pseudo-dynamic testing of steel members," *Journal of Constructional Steel Research*, 16:153-161.

Elnashai, A. S., Izzuddin, B. A. (1993). "Modeling of material nonlinearities in steel structures subjected to transient dynamic loading," *Earthquake Engineering and Structural Dynamics*, 22:509-532.

Elnashai, A. S., Papanikolaou, V. and Lee, D. (2002). *ZEUS NL – A System for Inelastic Analysis of Structures*, Mid-America Earthquake Center, University of Illinois at Urbana-Champaign, Program Release Sept.

Ensoft Inc. (2005). "LPile Plus Student Edition Electronic Documentation." Austin, Texas.

Erberik, M. A. and Elnashai, A. S. (2004). "Fragility Analysis of Flat-Slab Structures," *Engineering Structures*, 26(7):937-948.

Fan, C.-C. (1996). *The Behavior of Laterally Loaded Single Piles and Group Piles in Sand*, Ph. D. thesis, University of Illinois at Urbana-Champaign .

FEMA-273 (1997). *NEHRP guidelines for seismic rehabilitation of buildings*, Federal Emergency Management Agency, Washington D.C.

FEMA-350 (2000). *Recommended Seismic Design Criteria for New Steel Moment-Frame Buildings*, Federal Emergency Management Agency, Washington D.C.

Fernández, J. A. and Rix, G. J. (2006a). "Soil Attenuation Relationships and Seismic Hazard Analyses in the Upper Mississippi Embayment," Submitted to *Bulletin of the Seismological Society of America*, September.

Fernández, J. A. and Rix, G. J. (2006b). "Seismic Hazard Analysis – Preliminary results, Seismic retrofit study of bridge A-1700 Route I-155, Pemiscot county", Georgia Institute of Technology, Atlanta, Georgia.

Filippou , F. C. and Constantinides, M. (2004). *FEDEASLab Getting Started Guide and Simulation Examples*, Technical Report NEESgrid-2004-22.

Gazetas, G. (1991). "Formulae & Charts for Impedance Functions of Surface and Embedded Foundations," *Journal of Geotechnical Engineering*, 117(9):1363-1381.

Gehrig, D. (2004). *Guide to the NEESgrid Reference Implementation*. NEESgrid TR-2004-04

Ghaboussi, J., Yun, G., and Hashash, Y. M. A. (2004). "A Novel Predictor-Corrector algorithm for substructure pseudo dynamic testing," *Earthquake Engineering and Structural Dynamic,* 35: 453-476.

Green, R. A., Obermeier, S. F., and Olson, S. M. (2005). "Engineering geologic and geotechnical analysis of paleoseismic shaking using liquefaction effects: field examples." *Engineering Geology*, 76:263-293.

Haukaas, T. (2003). *Finite element reliability and sensitivity analysis of hysteretic degrading structures*. Ph.D. Thesis, Department of Civil and Environmental Engineering, University of California, Berkeley.

Heydinger, A. G. (1989). "Prediction of Driven Pile Behavior Using Load Transfer Functions." *Predicted and Observed Axial Behavior of Piles*, Geotechnical Special Publication No. 23, ASCE, pp. 117-128.

Hibbit, H. D., Karlsson, B. I., and Sorensen (2001). *ABAQUS theory manual. Version 6.2.*

Inel, M., and Aschheim, M. A. (2004). "Seismic Design of Columns of Short Bridges Accounting for Embankment Flexibility." *Journal of Structural Engineering*, 130(10):1515-1528.

Jeong, S. H. and Elnashai, A. S. (2004a). "Analytical assessment of an irregular RC frame for full-scale 3D pseudo-dynamic testing, Part I: Analytical model verification," *Journal of Earthquake Engineering*, 9 (1): 95-128.

Jeong, S. H. and Elnashai, A. S. (2004b). "Analytical assessment of an irregular RC frame for full-scale 3D pseudo-dynamic testing, Part II: Condition assessment and test deployment," *Journal of Earthquake Engineering*, 9 (2): 265-284.

Jeong, S. H. and Elnashai, A. S. (2005). "Analytical Assessment of an Irregular RC Frame for Full-Scale 3D Pseudo-Dynamic Testing. Part I: Analytical Model Verification," *Journal of Earthquake Engineering*, 9(1), 95-128.

Jeong, S. H. and Elnashai, A. S. (2006). "Probabilistic fragility analysis parameterized by fundamental response quantities," *Engineering Structures* (in press).

Ji, J., Kwon, O., Elnashai, A. S., and Kuchma, D. (2007) "Multi-resolution distributed finite element simulation for complex structural system", Earthquake Spectra, submitted on March, (in review)

Jones, A. L., Kramer, S. L., and Arduino, P. (2002). "Estimation of uncertainty in geotechnical properties for performance-based earthquake engineering," *PEER Report 2002/16.*

Kagawa, T. and Kraft, L. M., Jr. (1980a). "Seismic p-y Response of Flexible Piles," *Journal of the Geotechnical Engineering Division*, ASCE, 106(GT8):899-918.

Kagawa, T. and Kraft, L. M., Jr. (1980b). "Lateral Load-Deflection Relationship of Piles Subjected to Dynamic Loadings," *Soils and Foundations*, 20(4):19-36.

Kappos, A., Pitilakis, K., Stylianidis, K., Morfidis, K. and Asimakopoulos, D. (1995) "Cost-benefit analysis for the seismic rehabilitation of buildings in Thessaloniki, based on a hybrid method of vulnerability assessment," *Proceedings of the Fifth International Conference on Seismic Zonation*, Vol. I, 406-413, Nice, France, October 17-19.

Kornkasem, W., Foutch, D. A., and Long, J. H. (2003). "Seismic Behavior of Pile-Supported Bridges." *CD-ROM Release 03-05*, MAE Center.

Kraft, L. M., Ray, R. P., and Kagawa, T. (1981). "Theoretical t-z Curves," *Journal of the Geotechnical Engineering Division*, ASCE, 107(GT11):1543-1561.

Kramer, S. L. (1996). *Geotechnical Earthquake Engineering*, Prentice Hall, First Edition.

Kwon, O. and Elnashai, A. S. (2006). "Multi-platform simulation of highway over-crossing bridge with consideration of soil-structure-interaction," Journal of Structural Engineering, ASCE, submitted on October (in review)

Kwon, O., Elnashai, A. S., and Spencer, B. (2005). "A framework for multi-site distributed simulation and application to complex structural systems," *Journal of Earthquake Engineering*, 9(5):741–753.

Lam, I. P. and Martin, G. R. (1986). *Seismic Design of Highway Bridge Foundations, Vol. II: Design Procedures and Guidelines*, Federal Highway Administration.

Lupoi, G., Franchin, P., Lupoi, A., and Pinto, P.E. (2004). "Seismic fragility analysis of structural systems," *Proceedings of 13th World Conf. on Earthquake Engineering*, Vancouver BC, Canada. Paper 4008.

Mander, J. B., Kim, D.-K., Chen, S. S., and Premus, G. J. (1996). *Response of Steel Bridge Bearings to Reversed Cyclic Loading,* Technical Report NCEER-96-0014, National Center for Earthquake Engineering Research.

Maragakis, E. A., Douglas, B. M., and Abdel-Ghaffar, S. M. (1994). "An Equivalent Linear Finite Element Approach for the Estimation of Pile Foundation Stiffnesses." *Earthquake Engineering and Structural Dynamics*, 23:1115-1124.

Maroney, B. H. (1995). *Large Scale Bridge Abutment Tests to Determine Stiffness and Ultimate Strength under Seismic Loading*, PhD thesis, University of California, Davis.

Martinez-Rueda and Elnashai, A. S. (1997). "Confined concrete model under cyclic load," *Materials and Structures*, 30(197):139–147.

Matlock, H. (1970). "Correlations for Design of Laterally Loaded Piles in Soft Clay," *Proceedings of 2nd Annual Offshore Technology Conference*, Houston, Texas, pp. 577-594.

Mazroi, A., Wang, L. L., and Murray, T. M. (1983). *Effective Coefficient of Friction of Steel Bridge Bearings*, Transportation Research Record 903.

McCallen, D. B., and Romstad, K. M. (1994). "Dynamic Analyses of a Skewed Short-Span, Box-Girder Overpass." *Earthquake Spectra*, 10(4):729-756.

McKenna, F. and Fenves, G. L. (2001). *The OpenSees command language manual, version 1.2*. Pacific Earthquake Engineering Research Center, Univ. of California at Berkeley.

Mirza, S. A., and MacGregor, J. G. (1979). "Variability of Mechanical Properties of Reinforcing Bars," *Journal of structural division*, Vol.105, No.ST5.

Molina, F. J., Verzeletti, G., Magonette, G., Buchet, P., and Geradin, M. (1999). "Bi-Directional Pseudodynamic Test of a Full-Size Three-Story Building," *Earthquake Engineering and Structural Dynamics*, 28:1541-1566.

Mosalam, K. M., Ayala, G., White, R. N., and Roth, C. (1997). "Seismic fragility of LRC frames with and without masonry infill walls," *Journal of Earthquake Engineering*, 1(4):693-720.

Mosher, R. L. (1984). "Load-Transfer Criteria for Numerical Analysis of Axially Loaded Piles in Sand, Part I: Load-Transfer Criteria," Final Report to U.S. Army Engineer Division, Lower Mississippi Valley, Vicksburg, Missouri.

Mwafy, A. M., Elnashai, A. S. and Yen, W-H. (2006a). "Implications of design assumptions on capacity estimates and limit states of multi-span curved bridges", submitted to *Journal of Bridge Engineering.*

Mwafy, A. M., Elnashai, A. S. and Yen, W-H. (2006b). "Comparative assessment of the designed and as-built simulations of complex bridges subjected to increasing earthquake intensities", submitted to *Journal of Bridge Engineering.*

Nakashima, M. and Kato, H. (1987). "Experimental error growth behavior and error growth control in on-line computer test control method," Building Research Institute, *BRI-Report No. 123*, Ministry of Construction, Tsukuba, Japan.

Nakashima, M., Kato, H., and Takaoka, E. (1992). "Development of Real-Time Pseudo Dynamic Testing," *Earthquake Engineering and Structural Dynamics*, 21(1):79-92.

National Science Foundation, (2000). Network for earthquake engineering simulation (NEES): system integration, program solicitation. *Report NSC00-7*, U.S.A.

Negro, P., Pinto, A. V., Verzeletti, G., and Magonette, G. E. (1996). "PsD Test on Four-Story R/C Building Designed According to Eurocodes," *Journal of Structural Engineering*, 122(12):1409-1471.

Newmark, N.M. and Rosenblueth, E. (1971). *Fundamentals of Earthquake Engineering*. Englewood Cliffs, N.J., Prentice-Hall.

NIBS (1999). *HAZUS, Earthquake Loss Estimation Technology*, Technical Manual prepared by the National Institute of Buildings Sciences (NIBS) for the Federal Emergency Management Agency (FEMA).

Nielson, B. G. (2005). *Analytical Fragility Curves for Highway Bridges in Moderate Seismic Zones*, PhD thesis, Georgia Institute of Technology, Atlanta, Georgia.

Nogami, T. and Konagai, K. (1987). "Dynamic Response of Vertically Loaded Nonlinear Pile Foundations," *Journal of the Geotechnical Engineering Division*, ASCE, 113(2):147-160.

Nogami, T. and Konagai, K. (1988). "Time Domain Flexural Response of Dynamically Loaded Single Piles," *Journal of Engineering Mechanics*, 14(9):1512-1525.

Norris, G. M., and Sack, R. L. (1986) "A seismic analysis: Meloland Overcrossing during the 1979 earthquake." *Proceedings of 'soil properties evaluation from centrifuge models and field performance'*, Nashville, Tennessee, 88-107.

Olson (1990). "Axial load capacity of steel pipe piles in sand," *Proceedings of Offshore Technology Conference*, Houston, Texas, pp. 17-24.

O'Neill, M. W. and Murchison, J. M. (1983). *An Evaluation of P-Y Relationships in Sands*, A report to the American Petroleum Institute (PRAC 82-41-1), University of Houston, University Park, Houston, Texas.

Orsini, G (1999). "A model for buildings' vulnerability assessment using the parameterless scale of seismic intensity (PSI)," *Earthquake Spectra*, 15(3):463-483.

Padgett, J. E. and DesRoches, R. (2005). "Survey of Bridge Inspectors for Highway Bridge Damage-Functionality Relationships." Georgia Institute of Technology, Unpublished Work).

Pan, P., Tada, M., and Nakashima, M. (2005). "Online hybrid test by internet linkage of distributed test-analysis domains," *Earthquake Eng. Struct. Dyn.*, 34:1407-1425.

Pearlman, L., D'Arcy, M., Johnson, E., Kesselman, C., and Plaszczak, P. (2004). "NEESgrid Teleoperation Control Protocol (NTCP)," *Technical Report NEESgrid-2004-23*, http://it.nees.org/.

Pinho, R. (2000). *Selective Repair and Strengthening of RC Buildings*. PhD thesis, Imperial College, London.

Pinho, R., and Elnashai, A. S. (2000). "Dynamic Collapse Testing of a Full-Scale Four Story RC Frame," *ISET Journal of Earthquake Technology*, 37(4):143-163.

Pinto, P. E., Giannini, R., and Franchin, P. (2004). *Seismic Reliability Analysis of Structures*. IUSS Press.

Price, T. E. (1997). *Influence of embankment/superstructure interaction on the seismic response of bridges*, PhD thesis, Univ. of Washington, Seattle.

Priestley, M.J.N., Seible, F., and Calvi, G.M. (1996). *Seismic design and retrofit of bridges*, Wiley, New York.

Randolph, M. F. and Wroth, C. P. (1979). "Analysis of Deformation of Vertically Loaded Piles," *Journal of the Geotechnical Engineering Division*, ASCE, 104(GT12): 1465-1488.

Reese, L. C., Cox, W. R., and Grubbs, B. R. (1967). "Lateral load tests of instrumented piles in sand at Mustang Island," a report to Shell Development Company, Houston, Texas.

Reese, L. C., Cox, W. R., and Koop, F. D. (1975). "Field Testing and Analysis of Laterally Loaded Piles in Stiff Clay." *Offshore Technology Conference*, Dallas, Texas, 671-690.

Reese, L. C. and O'Neill, M. W. (1988). *Drilled Shafts: Construction Procedures and Design Methods*, U.S. Department of Transportation, Federal Highway Administration, Office of Implementation, McLean, Virginia.

Reese, L. C. and O'Neill, M. W. (1989). *Criteria for the Design of Axially Loaded Drilled Shafts*, Research Report 89-11F, Center for Highway Research, the University of Texas, Austin, Texas.

Reese, L. C. and Welch, R. C. (1975). "Lateral Loading of Deep foundations in Stiff Clay," *Journal of Geotechnical Engineering Division*, ASCE, 101(GT7):633-649.

Reinhorn, A. M., Barron-Corvera, R., and Ayala, A.G. (2001). "Spectral evaluation of seismic fragility of structures, Structural safety and reliability," (ICOSSAR 2001).

Romero, S. M., and Rix, G. J. (2001).. "Ground motion amplification of soils in the upper mississippi embayment." GIT-CEE/GEO-01-1, Georgia Institute of Technology.

Rossetto, T. and Elnashai, A. S. (2003). "Derivation of vulnerability functions for European-type RC structures based on observational data," *Engineering Structures*, 25(10):1241-1263.

Sawada, T., Hirao, K., Yamamoto, H. and Tsujihara, O. (1992). "Relation between maximum amplitude ratio and spectral parameters of earthquake ground motion," *Proceedings of 10th World Conference on Earthquake Engineering*, Madrid, Spain, 2:617-622.

Schellenberg, A. and Mahin, S. (2006). "Integration of Hybrid Simulation within the General-Purpose Computational Framework OpenSees," *Proceedings of the 100th Anniversary Earthquake Conference Commemorating the 1906 San Francisco Earthquake*.

Schotanus, M. I. J., Franchin, P., Lupoi, A., and Pinto, P. E. (2004). "Seismic fragility analysis of 3D structures," *Structural Safety*, 26:421-441.

Seed, H. B., and Idriss, I. M. (1970). "Soil moduli and damping factors for dynamic response analyses." *UCB/ERRC-70/10*, Earthquake Engineering Research Center, University of California, Berkeley, California.

Shing, B. and Manivannan, T. (1990). "On the accuracy of an implicit algorithm for pseudodynamic tests," *Earthquake Engineering and Structural Dynamics*, 19: 631-651.

Shing, B., Vannan, M.T., and Cater, E. (1991). "Implicit time integration for pseudodynamic tests," *Earthquake Engineering and Structural Dynamics*, 20: 551-576.

Spencer Jr., B. F., Elnashai, A. S., Park, K., and Kwon, O. (2006a). *Hybrid Test Using UI-SimCor, Three-Site Experiment*, Final report to NEESit for Phase I project of hybrid simulation framework development, University of Illinois at Urbana-Champaign.

Spencer Jr., B. F., Elnashai, A., Kuchma, D., Kim, S., Holub, C., and Nakata, N. (2006b). *Multi-Site Soil-Structure-Foundation Interaction Test* (MISST). University of Illinois at Urbana-Champaign.

Sweet, J., and Morrill, K. B. (1993). "Nonlinear soil-structure interaction simulation of the Painter Street Overcrossing," *Proceedings of 2nd Annual Caltrans Seismic Research Workshop*, Sacramento, California.

Takahashi, Y. and Fenves, G. L. (2006). "Software framework for distributed experimental-computational simulation of structural systems," *Earthquake Engineering and Structural Dynamics*, 35:267-291.

Takanashi , K., and Ohi, K. (1983). "Earthquake response analysis of steel structures by rapid computer-actuator on-line system, (1) a progress report, trial system and dynamic response of steel beams." *Bull. Earthquake Resistant Struct. Research Center* (*ERS*), Inst. of Industrial Sci., Univ. of Tokio, Tokio, Japan, 16:103-109.

Takanashi, K., Udagawa, K., Seki, M., Okada, T. and Tanaka, H. (1975). "Nonlinear earthquake response analysis of structures by a computer-actuator on-line system," *Bull. of Earthquake Resistant Structure Research Centre*, No.8, Institute of Industrial Science, University of Tokyo, Japan.

TDOT (2004). "Bridge inspection report", State of Tennessee Department of transportation, Bridge no. 23I01550001.

Trifunac, M. D. and Brady, A. G. (1975). "A study on the duration of strong earthquake ground motion," *Bulletin of the Seismological Society of America*, 65(3):581-626.

Tsai, K., Hsieh, S., Yang, Y., Wang, K., Wang, S., Yeh, C., Cheng, W., Hsu, C., and Huang, S. (2003). Network Platform for Structural Experiment and Analysis (I). *NCREE-03-021*, National Center for Research on Earthquake Engineering, Taiwan.

USGS (2006). "Earthquake Hazards Program Website." http://earthquake.usgs.gov/, Date Accessed: August 31, 2006.

Vecchio F. J. and Collins M. P. (1986). "The modified compression field theory for reinforced concrete elements subjected to shear," ACI Structural Journal 83(2): 219–31.

Vecchio, F. J. and Wong, P. (2003). *VecTor2 and FormWorks Manual.* http://www.civ.utoronto.ca/vector/, University of Toronto, Toronto, Canada.

Veneziano, D., Casciati, F., and Faravelli, L. (1983). "Method of seismic fragility for complicated systems," *Proc. of the 2nd Committee of Safety of Nuclear Installation (CNSI)*. Specialist Meeting on Probabilistic Methods in Seismic Risk Assessment for NPP, Lawrence Livermore Laboratory, CA.

Vijayvergiya, V. N., Hudson, W. R., and Reese, L. C. (1969). *Load Distribution for Drilled Shaft in Clay Shale*, Research Report 89-5, Univ. of Texas, Austin, 193p.

Vucetic, and Dobry, R. (1991). "Effect of soil plasticity on cyclic response," *Journal of Geotechnical and Geoenvironmental Engineering*, 117(1).

Wang, S., Kutter, B. L., Chacko, J. M., Wilson, D. W., Boulanger, R. W., and Abghari, A. (1998). "Nonlinear Seismic Soil-Pile-Structure Interaction," *Earthquake Spectra*, 14(2): 377-396.

Watanabe, E., Sugiura, K., Nagata, K., Yamaguchi, T., and Niwa, K. (1999). "Multi-phase Interaction Testing System by Means of the Internet," *Proceedings of 1st International Conference on Advances in Structural Engineering and Mechanics*, Seoul, Korea, 43-54.

Watanabe, E., Kitada, T., Kunitomo, S. and Nagata, K. (2001). "Parallel pseudodynamic seismic loading test on elevated bridge system through the Internet." *The Eight East Asia-Pacific Conference on Structural Engineering and Construction*, Singapore, December.

Wen, Y. K., Ellingwood, B. R., and Bracci, J. (2004). *Vulnerability Function Framework for Consequence-based Engineering*, Mid-America Earthquake Center Project DS-4 Report, April.

Wen, Y. K., Ellingwood, B. R., Veneziano, D., and Bracci, J. (2003). *Uncertainty Modeling in Earthquake Engineering*, Mid-America Earthquake Center Project FD-2 Report, January.

Werner, S. D., Beck, J. L., Katafygiotis, L., and Nisar, A. (1993). "Seismic Analysis of Meloland Road Overcrossing Using Calibrated Structural and Foundation Models." *Proceedings of Structural Engineering in Natural Hazards Mitigation*, Irvine, California.

Werner, S. D., Beck, J.L., and Levine, M.B. (1987). "Seismic response evaluation of Meloland road overpass using 1979 Imperial valley earthquake records," *Earthquake Engineering and Soil Dynamics* 15: 249–74.

Wilson, J. C., and B. S. Tan. (1990a). "Bridge abutments: formulation of simple model for earthquake response analysis," *Jour. of Eng. Mechanics* 116(8):1828–1837.

Wilson, J. C., and B. S. Tan. (1990b). “Bridge abutments: accessing their influence on earthquake response of Meloland Road Overpass,” *Journal of Engineering Mechanics* 116(8):1838–1856.

Wolf, J.P. (1997). “Spring-Dashpot-Mass Models for Foundation Vibrations,” *Earthquake Engineering and Structural Dynamics*, 26:931-949.

Yang, Z., Elgamal, A., and Parra, E. (2003a). “Computational model for cyclic mobility and associated shear deformation,” *Journal of Geotechnical and Geoenvironmental Engr*. 129 (12):1119-1127.

Yang, Z., He, L., Bielak, J., Zhang, Y., Elgamal, A., and Conte, J. (2003b). “Nonlinear seismic response analysis of a bridge site subject to spatially varying ground motion.” *16th ASCE Engineering Mechanics Conference*, University of Washington, Seattle, July 16-18.

Yang, Z., Lu, J. and Elgamal, A. (2005). “OpenSees Geotechnical Simulation Capabilities and User Manual”, University of California San Diego, http://cyclic.ucsd.edu/opensees/.

Zhang, J. and Makris, N. (2001). “Seismic Response Analysis of Highway Overcrossings Including Soil-Structure Interaction,” *PEER Report 2001/02.*

Zhang, J. and Makris, N. (2002). “Seismic Response Analysis of Highway Overcrossings Including Soil Structure Interaction,” *Earthquake Engineering and Structural Dynamics*, Vol. 31 pp.1967-1991.

Zhu, T. J., Heidebrecht, A. C. and Tso. W. K. (1988). “Effect of peak ground acceleration to velocity ratio on ductility demand of inelastic systems,” *Earthquake Engineering and Structural Dynamics*, 16:63-79.